VISCOELASTIC PROPERTIES OF HEAVY OILS

A Dissertation

Presented to

the Faculty of the Department of Earth and Atmospheric Sciences

University of Houston

In Partial Fulfillment

of the Requirements for the Degree

Doctor of Philosophy

By

Maria Alejandra Rojas Luces

May 2010

VISCOELASTIC PROPERTIES OF HEAVY OILS

Maria Alejandra Rojas Luces

APPROVED:

Dr. John Castagna

Dr. Christopher Liner

Dr. De-hua Han

Dr. Azra Tutuncu

Dean, College of Natural Sciences and Mathematics

Acknowledgements

I would like to express my deepest thanks to my advisor, Dr. John Castagna, for his guidance and invaluable academic advice that contributed to significantly improve the quality of this work as well as my career.

My special thanks to Dr. De-hua Han for supplying some of the heavy oil samples to be analyzed in this study, but especially for his encouragement, advices, and recommendations that helped me to successfully finish this dissertation.

My sincerest appreciation goes to my committee member, Dr. Azra Tutuncu, for her invaluable input throughout the process of completing this thesis. Thanks to her help, I was able to carry out some of the rheological measurements.

My stay at the University of Houston and the research that led to this dissertation was funded by a scholarship from Shell Oil Company.

Finally, and most importantly, I would like to deeply thank my family for their support and love. I want to especially thank my mom, Rafaela, for her patience, dedication, optimism, and unconditional love. They have always believed in me, no matter how hard it seems to be and no matter the distance between us.

VISCOELASTIC PROPERTIES OF HEAVY OILS

An Abstract of a Dissertation

Presented to

the Faculty of the Department of Earth and Atmospheric Sciences

University of Houston

In Partial Fulfillment

of the Requirements for the Degree

Doctor of Philosophy

By

Maria Alejandra Rojas Luces

May 2010

Abstract

Rheological low frequency measurements were carried out to analyze the viscoelastic properties of four heavy oil samples taken from different reservoirs. At room conditions, the heavy oil samples exhibit non-Newtonian or viscoelastic behavior since they have a viscous component, typical of Newtonian fluids, and an elastic component. The latter becomes very important for temperatures below 30°C, and for seismic to ultrasonic frequencies. Above this temperature, the viscous component increases significantly in comparison to the elastic component, and for seismic frequencies heavy oils can be considered as Newtonian fluids.

The glass point temperature estimated by the Differential Scanning Calorimeter method varied approximately from -40°C to -50°C. Likewise, the liquid point temperature varied from 60°C to 20°C according to the sample.

A new viscosity model based on the concept of activation energy was derived to predict viscosity in terms of frequency and temperature for temperatures below 60°C. Above this temperature, viscosity becomes Newtonian and no shear thinning is observed. The activation energy was found to be independent of temperature but dependent on frequency. It varies from 800 J/mol to 1800J/mol according to frequency.

A new frequency-temperature dispersion model was derived to address the variation of the complex shear modulus (G*) with frequency and temperature for the heavy oil samples. This model fits the measured data well for seismic and sonic frequencies with a correlation coefficient of 0.99. However, the model overpredicted G* at ultrasonic frequencies.

The power-law attenuation model accurately (correlation coefficient above 0.99) predicts, for all samples, the variation of attenuation coefficient with frequency and temperature measured by the rheological measurements, and only requires one parameter.

On the heavy and extra-heavy oil samples analyzed in this study, the causality link demonstrated by the Kramers – Kronig relations is evident for frequency, strain, and viscosity factors.

Finally, a heavy oil carbonate reservoir was modeled using finite element modeling and well-log data to generate 3D fracture and vug porosity cubes. It was found that fracture porosity derived from P-wave data has a higher magnitude than S-wave results, but in a qualitative sense, both results showed similar changes in fracture porosity over the field.

Table of Contents

Part 3 Frequency Dispersion in Viscoelastic Media: Analysis of Low and High Frequency Measurements

List of Tables

Part 2

Part 3

Part 4

List of Figures

Part 1

Part 2

Part 3

Part 4

Part 1

Introduction

The need to characterize fluid flow and viscoelastic properties of unconventional reservoirs, such as heavy and extra-heavy oils, has increased significantly in the last decade. The demand for crude oil has increased substantially in these years and new sources of energy are urgently sought. On the other hand, the fact that heavy oil accumulation is close to 3,396 billion barrels of original oil in place, whereas extra-heavy oil reserves are about 5,505 billion barrels of original oil in place worldwide (Meyer et al., 2007) are definitely powerful incentives to study, explore and produce heavy oil reservoirs (Figure 1.1).

Heavy and extra-heavy oil result from the degradation of conventional oil; during this process hydrogen-rich, low molecular weight compounds such as paraffins and naphtenes are reduced significantly, leaving the two other types of compounds: resins and asphaltenes. These are characterized by high molecular weight (rich in nitrogen, sulfur, and oxygen), branching and entanglement, which translate into high viscosity and modulus.

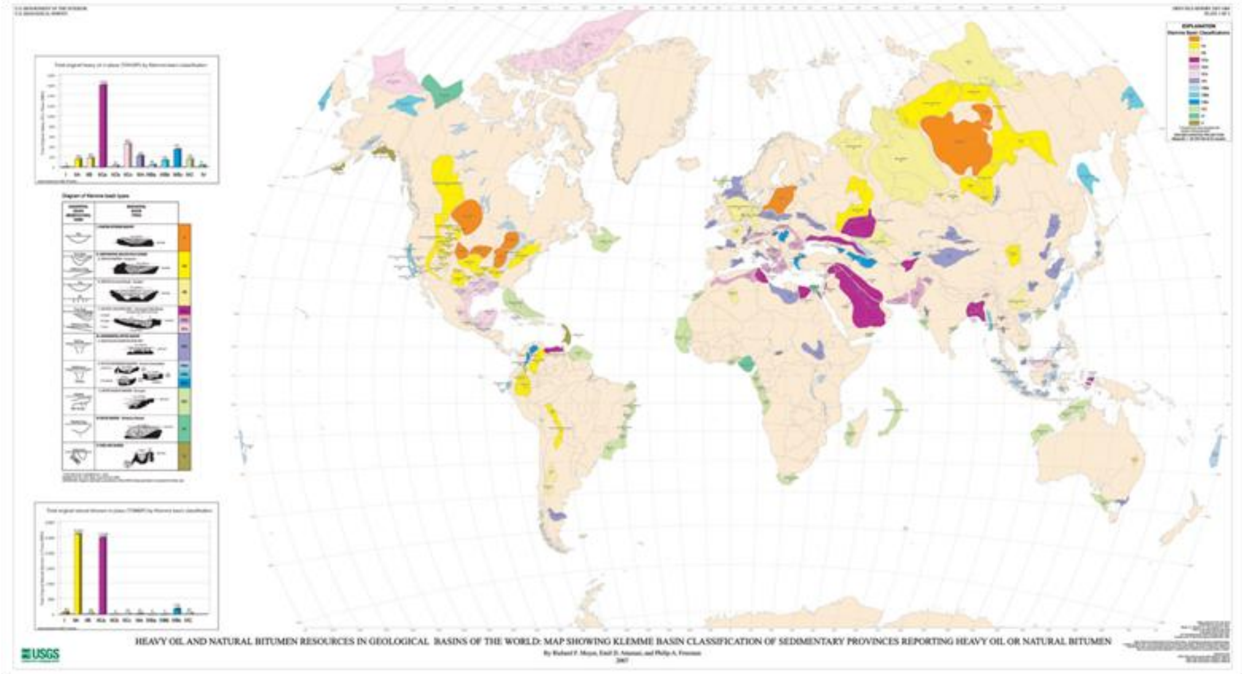

Figure 1.1. Heavy and extra-heavy oil distribution in the world. Meyer et al., 2007

There have been many attempts in the past to estimate viscosity of heavy oils through empirical relations that correlate viscosity with density and temperature. However, these correlations might work for temperatures above room conditions but they are very inaccurate in the low temperature regime (below 20°C), showing differences in the range of hundred thousand centipoises. Partially, this is due to the lack of viscosity measurements at that temperature range. This certainly represents a major problem since in-situ conditions of many reservoirs coincide with that temperature range. Beggs and Robinson model (1975), DeGuetto model (DeGuetto et al., 1995), and Bennison model (1998) are only some of the examples.

Heavy oil properties are particularly dependent on frequency and temperature changes. According to its rheological properties, it can be considered as a non-Newtonian viscoelastic fluid, which means stress and strain are not linearly correlated. Viscoelastic fluids are also time dependent, they require some time before being able to release the applied stress; therefore, such materials have an elastic component, which makes them able to support shearing.

Viscoelastic fluids have a bit more complicated nomenclature since the stress - strain relation can be explained by harmonic functions, leading to complex properties. The real part is given by the elastic component while the imaginary part corresponds to the viscous component. Also, adding more difficulty, the elastic energy component varies with time (increasing or decreasing) but the viscous component always decreases. Rheology is the science that studies the flow and deformation of mostly non-Newtonian fluids, such as heavy and extra heavy oils.

The emergence of shear wave modulus and shear wave dispersion is certainly a characteristic of heavy oils, which has an obvious impact on the elastic velocities. Previous ultrasonic measurements (Han et al., 2007) have shown that velocity dispersion might be significant for heavy oils at in-situ conditions. Once temperature increases, the heavy oil becomes Newtonian and viscosity becomes independent of frequency, entering into the liquid phase, here velocity dispersion is negligible (Han et al., 2007).

The need for a rock physics model able to correlate the major factors: viscosity, frequency, temperature, modulus and attenuation that also assumes heavy oil as a Non-Newtonian fluid is obvious and clear. It is necessary to understand that the role that fluid properties play on a heavy oil reservoir is fundamental. Behura et al. (2007) showed that the variation of shear modulus with frequency of a heavy oil saturated rock is consistent with the variation endured by the heavy oil. Consequently, the rheological properties of heavy oil most likely dominate the possible change with temperature and frequency endured by the rock.

This dissertation has been divided in three main parts that correspond to three different investigations; however, they all have in common the analysis of viscoelastic properties of heavy oils and their subsequent application on a heavy oil carbonate field.

In this dissertation, firstly, as the basis of this research, general rheological concepts including viscoelasticity, difference between Newtonian and non-Newtonian fluids, and oscillatory shear are introduced. Also, previously published viscosity and viscoelastic models currently used in the industry are reviewed. The next section explains the rheological low frequency measurements carried out for heavy oil samples using a shear rheometer and the measurements of the glass point temperature using a calorimeter. The corresponding laboratory techniques and results are also analyzed. Finally, a new viscoelastic model to model complex viscosity of heavy oils is presented.

The second part discusses frequency dispersion models suitable for heavy oil. It introduces the static and dynamic moduli concepts and the different factors that influence intrinsic attenuation. A review of some of the frequency dispersion models found in the literature is presented, which will be very helpful to understand the variation of the shear modulus with frequency resulting from the rheological low frequency measurements and the ultrasonic acoustic measurements. The new frequency – temperature dispersion model is presented and comparison with both datasets is analyzed.

Attenuation models are also discussed and the selection of one model for heavy oils is recommended. The causality link between attenuation and frequency dispersion explained through the Kramers – Kronig relations, is evident for frequency changes but also for strain and viscosity.

The third and last part, introduces the finite element modeling as the method of choice when modeling complicated geometries as the pore space of a rock. Different effective medium theories are briefly reviewed and compared with the numerical modeling that is based on the partition theory (Huet, 1990). The next part introduces the heavy oil carbonate reservoir through the dataset available, mainly well-log information, and a brief review of the geological formations. Subsequently, a new methodology that makes use of numerical modeling and well-log information is presented to qualitatively characterize the porous space (fractures or vugs) of the heavy oil carbonate reservoir. Finally, 3D fracture and vug porosity subsurface models are analyzed.

This dissertation ends, in Part 5, with the major conclusions obtained from all three main investigations.

Part 2

Modeling of Complex Viscosity as a Function of Frequency and Temperature for Heavy Oils

In this chapter complex viscosity of heavy oils is modeled as a function of temperature and frequency, which are some of the most important factors controlling viscosity. Laboratory measurements for four extra-heavy oil samples have been carried out using a shear rheometer to measure the complex viscosity, complex shear modulus (real and imaginary parts) while changing temperature and frequency. The results were modeled using the time-temperature superposition principle widely used in rheological applications and a modified expression of the Eyring's rate reaction equation with very good results and small errors. The chapter introduces the geological origin of heavy oils and its effect on the chemical composition. Then, an explanation of concepts used in Rheology and a review of their mathematical background is presented. The next section reviews empirical models currently used in the industry to estimate viscosity of heavy and extra-heavy oils. Experimental setup and laboratory techniques to rheologically characterize these fluids are presented in the fourth part. Finally, I present the mathematical expression to estimate complex viscosity in heavy oils.

2.1 Heavy and Extra-Heavy Oil

Physical properties such as density, viscosity and specific gravity are used to classify petroleum. According to the USGS, heavy oils have API gravity between 10° and 20° and a dead oil viscosity between 100 cp and 10,000 cp (Figure 2.1) while according to the American Petroleum Institute, extra-heavy oil has API gravity below 10 degrees. The API gravity correlates the density of a crude oil (ρ_o) with the density of water. The expression to estimate API gravity is:

$$API\ gravity = \frac{141.5}{\rho_o} - 131.5 \tag{1}$$

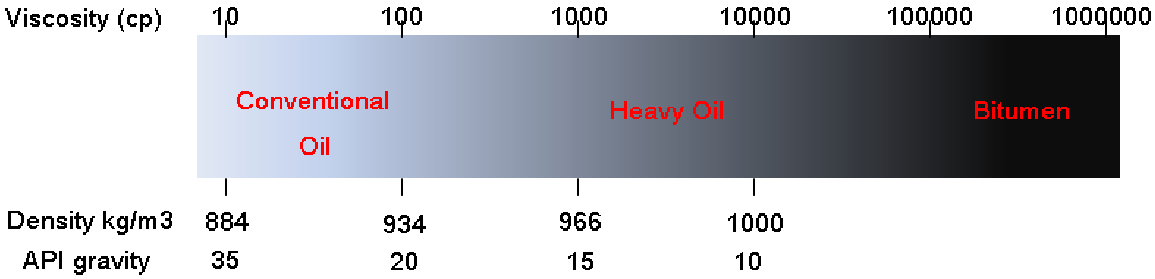

Figure 2.1. Classification of petroleum based on physical properties. Speight, 1999.

Heavy oil in response to bacterial degradation, water washing, loss of volatiles, and inorganic oxidation, loses the low molecular weight compounds (paraffins and naphtenes) leaving the high molecular aggregates such as resins and asphaltenes (Meyer et al., 2007). After these natural processes, oil becomes highly viscous, black or dark brown, with a deficiency of hydrogen and a high proportion of asphaltic molecules, nitrogen, sulfur, and oxygen are substituted in the carbon network, which notably increase the molecular weight of the compound.

According to Ruhl (1982), biochemical degradation is responsible for the enrichment of heavy oils in asphaltic compounds (six times approximately) and in aromatic content (up to 40% to 70%). Also, Ruhl observed in oil samples from different reservoirs from Western Canada basin that as they become shallower, API gravity increases, salinity decreases, and sulfur also increases. Similar conditions have been observed in the Eastern Venezuela basin.

The composition of heavy oils is characterized by an increase in resins, asphaltenes, and aromatic compounds and a notable decrease on alkanes. Table 2.1 shows the composition of heavy oil samples through SARA (Saturates – Aromatics – Resins - Asphaltenes) analysis taken from reservoirs around the world.

Table 2.1. Composition of some heavy oil samples in comparison to conventional oils. Tissot and Welte, 1984.

Locations	**Number of samples**	**Asphaltenes (wt. %)**	**Resins (wt. %)**	**Aromatics (wt. %)**	**Saturates (wt. %)**
Athabasca	15	23.3	28.6	32.2	15.9
Wabasca	7	21.6	30.6	32.1	15.6
Peace River	3	48.7	23.2	20.5	7.6
Cold Lake	7	20.6	28.0	30.5	20.9
Tar sands (Venezuela)	9	22.1	37.6	26.0	14.3
Heavy Oils (Venezuela)	5	12.6	32.4	36.4	18.6
Average	**46**	**22.9**	**30.6**	**30.4**	**16.1**
Conventional oil – various origin	**517**	**14.2**		**28.6**	**57.2**

Heavy oils, regardless of source, have a very high molecular weight; high molecular branching and entanglement due to the high proportion of resins and especially asphaltene compounds.

Asphaltenes become more complex as result of polymerization when they are subjected to burial diagenesis or thermal maturation; this has a clear effect on moduli but also on viscosity, which relates to the size and abundance of the aggregates.

Increasing temperature reduces entanglement by breaking chemical bonds; therefore, viscosity and moduli decrease. Drastic changes occur, especially at low temperatures (below room temperature), where a rearrangement of the molecular aggregates is assumed. On the other hand, as frequency increases, molecules elongate in order to align with the fluid flow; and this change in shape lowers apparent viscosity (Ferry, 1980).

Several studies have published the correlation between the sum of weight fraction of asphaltenes and resins on viscosity and density (Figure 2.2). A considerable increase in viscosity is observed when there is a deficiency of aromatics and alkanes but an abundance of resins and asphaltenes (Tissot and Welte, 1984).

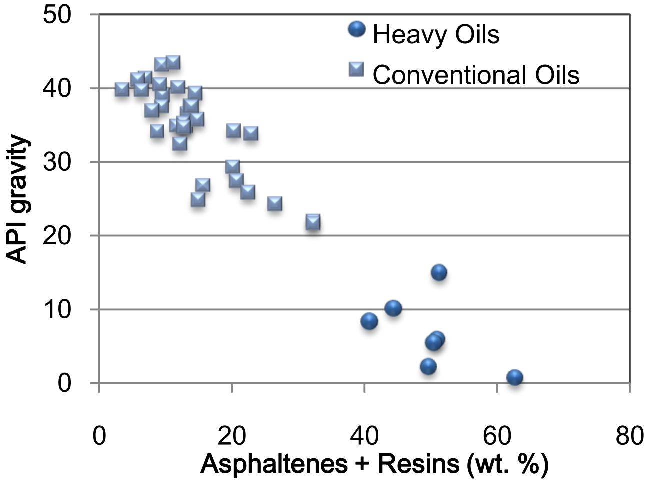

Figure 2.2. Impact of aliphatics compounds on API gravity. Data of Speight, 1999.

2.2 Literature Review - Rheological Concepts

2.2.1 Viscosity

Rheology can be defined as the study of the flow and deformation of materials under various kinds of stress-strain conditions, embracing elasticity, viscosity, and plasticity. Usually, rheological measurement is considered as the most sensitive method for material characterization because it takes into account chemical, mechanical, and thermal properties of the fluid flow.

Viscosity is intrinsically correlated with the concept of laminar flow: the movement of one layer of fluid with respect to another with no transfer of matter from one to the other. Viscosity is the measure of the resistance to flow or internal friction between these layers. The greater the friction, the greater the amount of force (shear) required to generate this movement. Highly viscous fluids require more force to move than less viscous materials.

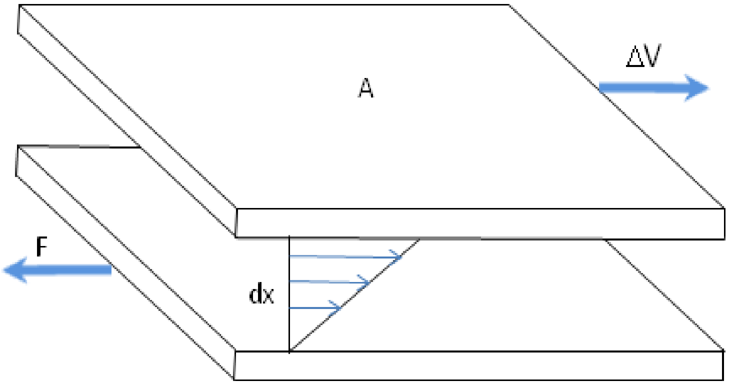

Figure 2.3. Schematic representation of a fluid being sheared between two parallel plates, one stationary (bottom) and one moving (upper).

Viscosity can be explained using Figure 2.3. Two parallel plates of fluid of equal area A are separated by a distance d and are moving in the same direction at a relative velocity ΔV. The velocity gradient, dv/dx, is a measure of the shearing the liquid experiences and is thus called *shear strain rate or shear rate* ($\dot{\gamma}$). It is given in units of *reciprocal second* (sec^{-1}). The term F/A indicates the force per unit area required to produce the shearing action. It is referred to as *shear stress* (σ). Using these simplified terms, viscosity may be mathematically defined by the following formula:

$$\sigma = \eta\dot{\gamma} \qquad (1)$$

where η is the shear viscosity. Sometimes, it is referred as the coefficient of viscosity but in reality it can be a function of the shear rate. The term of viscosity should be used for Newtonian fluids, such as water and gasoline, while complex viscosity corresponds to the more complex and numerous group of non-Newtonian fluids.

2.2.2 Newtonian vs. Non-Newtonian Fluids

Newton assumed that for all fluids the shear stress is directly proportional to the shear rate and therefore viscosity is independent of shear strain rate and shear time. These fluids therefore are called Newtonian. At a given temperature the viscosity of a Newtonian fluid will remain constant regardless of the shear rate. Newtonian fluids (referred to as Newtonians) are not, unfortunately, as common as the more complex group of non-Newtonian fluids. Table 2.2 shows approximate viscosities of some common fluids.

Table 2.2. Approximate viscosities of some Newtonian and non-Newtonian fluids at room temperature. Shear rate is not available.

Fluid	Approx. viscosity (Pa.s)
Air	10^{-5}
Water	10^{-3}
Lubricating oil	10^{-1}
Glycerol	10^{0}
Liquid honey	10^{1}
Corn syrup	10^{3}
Bitumen	10^{9}
Molten glass	10^{12}

Non-Newtonians are unable to immediately regain their original (random) state once stress is applied; they require some time to relax back to their original state. This time is referred to as Relaxation time (τ). Therefore, when the shear strain is varied, the shear stress doesn't vary in the same proportion. Viscosity will change as shear rate is varied, meaning the experimental procedure will have an effect on the measured viscosity. Non-Newtonian flow is characterized by a mixture of molecules with different shapes and sizes; this distribution will determine how much force is required to move them. At each specific rate of shear, the alignment may be different and more or less force may be required to maintain motion.

Three types of non-Newtonian fluids are recognized depending on the change of shear stress with shear rate (Figure 2.4). Heavy oils are considered pseudo-plastic or shear-thinning fluids since viscosity decreases as shear rate increases. This occurs when high molecular weight molecules are untangled and oriented by the flow. The viscosity curve for a shear-thinning fluid includes two plateau regions that occur at very low and very high shear rates (Figure 2.5).

These are known as the upper and lower Newtonian regions. At the lower region, where the shear rate is the lowest, the viscosity attains its highest value, usually referred as zero-shear viscosity (η_0).

Other types of fluids are dilatant, for which viscosity increases as shear rate increases, and Bingham fluids, which need to achieve a yield stress to allow fluid flow.

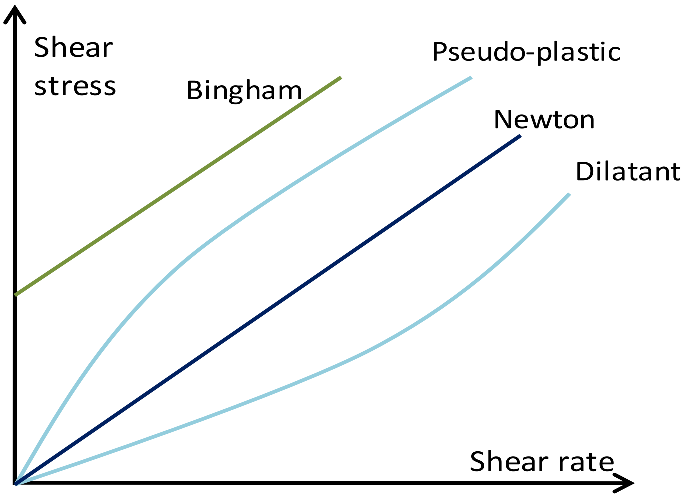

Figure 2.4. Newtonian and non-Newtonian flow behavior independent of shearing time (from Wang et al., 2005).

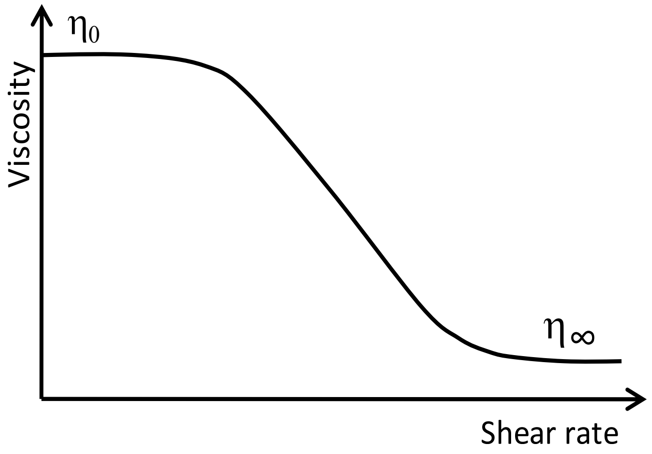

Figure 2.5. Viscosity curve of a shear-thinning fluid (from Wang et al., 2005).

The SI unit of viscosity is the pascal-second (Pa·s) while the cgs unit is the *poise* (P), which is equal to 1 $g \cdot cm^{-1} \cdot s^{-1}$. See the Appendix A for a table of units for the viscoelastic parameters. Viscosity is regarded by many as the most important property to characterize heavy oils and also to distinguish them from conventional oils. This property depends heavily on temperature, shear rate, and to a lesser degree on pressure:

- **Temperature**

  Some materials like heavy oils are especially sensitive to temperature. In fact, the higher the viscosity the stronger the temperature dependence; therefore, a relatively small variation in temperature can result in a significant change in viscosity. For most applications, the temperature range of interest is between 0°C to 100°C. The viscosity of Newtonian (and also viscoelastic) fluids decreases with increasing temperature following the Arrhenius equation in the case of gases and Eyring's equation for liquids (more on this in Section 2.5):

  $$\eta = Ae^{-B/T} \tag{2}$$

  where T is the absolute temperature and A and B are constants of the fluid.

- **Pressure**

  Viscosity of liquids increases exponentially with isotropic pressure (Barnes et al., 1989). However, most applications measure the viscosity at atmospheric pressure in which case the pressure effect is ignored. In the case of extra-heavy oil reservoirs, since they are located at shallow depths, the pressure effect can also be ignored; however, a pressure rise from atmospheric to 0.5 GPa, can cause a viscosity change of four orders of magnitude (Barnes et al., 1989).

- **Shear Rate**

  Most fluids exhibit non-Newtonian behavior; therefore, it is necessary to fully understand the effects of variations in shear rate when analyzing experimental rheological data. The approximate shear rate is estimated by the ratio of the velocity of the fluid flow by a characteristic dimension of the geometry in which it is flowing (thickness of the fluid). Usually, the term shear rate is used for steady shear flow whereas for dynamic viscosities, frequency would be the appropriate term.

2.2.3 Linear Viscoelasticity

Viscoelastic materials have the abilities of storing energy, as in the case of elastic materials, but also to dissipate energy, as in the case of viscous fluids when subjected to a stress field. They also exhibit a time dependence that is absent from any of the constitutive relations of elasticity theory (Christensen, 2005), meaning they can have a delayed response between the stress applied and the consequent deformation. The relaxation time (τ) can be defined as the time needed for the molecules subjected to a stress - strain field to relax back to its original state once the field is removed.

A viscoelastic material is linear when the strain output of the sum of two arbitrary stresses applied at different times equals the sum of the strain output of each individual stress (Findley et al., 1989). This is known as the Boltzmann Superposition principle and can be mathematically represented with the following expression:

$$\varepsilon[\sigma_1(t) + \sigma_2(t - t_1)] = \varepsilon[\sigma_1(t)] + \varepsilon[\sigma_2(t - t_1)] \tag{3}$$

where ε represents deformation and σ_1 and σ_2 the stresses applied at two different consecutive times. On the other hand, it is also known the elastic general relation between stress and strain fields for anisotropic materials:

$$\sigma_{ij} = C_{ijkl}\varepsilon_{kl} \tag{4}$$

where the strain field can be expressed in terms of displacement components as:

$$\varepsilon_{kl} = \frac{1}{2}\left(u_{k,l} + u_{l,k}\right) \tag{5}$$

Therefore, in order to obtain the general relation for linear viscoelastic materials, equation (4) is substituted into the continuous form of equation (3), as follows:

$$\sigma_{ij}(t) = \int_{-\infty}^{t} C_{ijkl}\,(t - \tau)\,\frac{d\varepsilon_{kl}(\tau)}{d\tau}\,d\tau \tag{6}$$

where σ_{ij} and ε_{kl} are the second rank stress and strain tensors respectively. C_{ijkl} is the fourth order elastic stiffness tensor that represents the basic properties of the material dependent of time (Christensen, 2005).

Equation 6 can be re-written in direct notation for shear stress as:

$$\boldsymbol{\sigma}(t) = \int_{-\infty}^{t} \boldsymbol{G}\,(t - \tau)\dot{\varepsilon}(\tau)d\tau \tag{7}$$

where $\sigma(t)$ is the shear stress that changes with time (or frequency), $\varepsilon(t)$ is the shear strain rate and G is the shear modulus. Intuitively, recent strains would be more important than those from longer ago, so for t > 0, **G**(t) is a positive monotonically decreasing function of time where deformation started a long time ago at t =-∞.

We can also use harmonic functions to describe the stress-strain relation, in which case the modulus become complex. If the strain is a harmonic function of time, then equation 6 becomes:

$$\boldsymbol{\sigma}(t) = \mathbf{G}^{*}(\dot{\omega})\varepsilon_0 e^{i\omega t} \qquad (8)$$

where **G***(ω) is the complex shear modulus, composed by a real (G'(ω)) and an imaginary part (G"(ω)).

The important concept of structural relaxation will be used extensively at the end of this chapter. As mentioned previously, viscoelasticity is the delayed response of a material subjected to a stress or strain applied; however, structural relaxation is the delayed response of the material to temperature changes (Scherer, 1986). They are both intrinsically related in the case of heavy oils, since they both deal with the rearrangement of the molecules as the free volume decreases with temperature.

2.2.4 Oscillatory Shear

Experimentally, the different parameters can be measured through dynamical rheological measurements, which consist of subjecting the material to a continuously oscillating strain (γ) over a range of frequencies and measuring the peak value of the stress (σ) and the phase difference (δ) between the stress and strain.

In order to explain the elastic and viscous properties of a material, let us consider a small cubical volume of material under shear stress, which will shift its shape to a parallelogram (Figure 2.6). The change in shape has two components, elastic deformation E and slippage or viscous deformation S. The elastic deformation is accompanied by storage of elastic energy, while slippage is associated with a continuous input of viscous energy. When the force is removed, the deformed material undergoes a partial recovery of shape as the elastic energy is recovered but the shape change due to slippage is permanent.

In a time-varying flow, the elastic energy component varies with time, either increasing or decreasing, while the viscous energy is always decreasing. Consequently, the relation between the time-varying force and velocity of the flow of the volume material reflects both the elastic and viscous properties of the material.

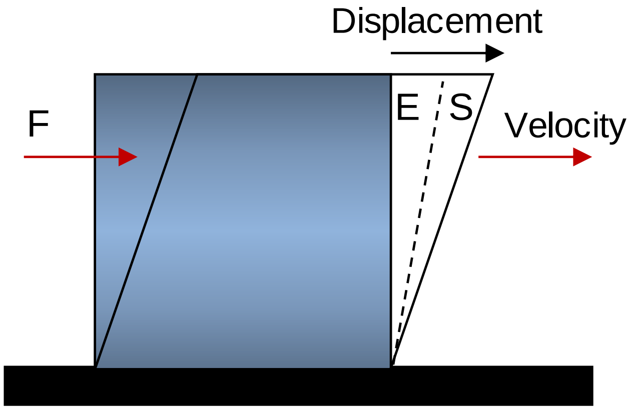

Figure 2.6. Cubic volume material before and after shear stress. The shear strain rate is a function of the displacement which is composed by an elastic component and a viscous component.

If the material behaves as an ideal elastic material, the resulting stress is proportional to the strain amplitude and the stress and strain signals are in phase, as predicted by Hooke's Law.

For an ideal viscous material, the stress is proportional to the strain rate (also called shear rate) and the stress is 90° out of phase with strain. For viscoelastic materials, the phase lag (δ) between stress and strain rate occurs somewhere between 0° (elastic) and 90° degree (viscous). The phase lag is actually a measure of the attenuation of the fluid or quality factor (Q). The quality factor is infinite for purely elastic materials and zero for completely attenuative (viscous) materials. Their correlation is given by:

$$Q = \frac{1}{tan\delta} \tag{9}$$

where:

$$\tan\delta = \frac{G''}{G'} \tag{10}$$

where Q is inversely proportional to the attenuation (Aki and Richards, 2002).

Figure 2.7 shows the sinusoidal functions of shear rate (γ) and shear stress (σ) corresponding to a fluid in small-amplitude oscillatory shear deformation. The components of the shear stress can be described in terms of these energies: the viscous stress is the rate of energy dissipation per unit volume, per unit shear rate. The elastic stress is the maximum energy stored during the cycle per unit volume, per unit strain.

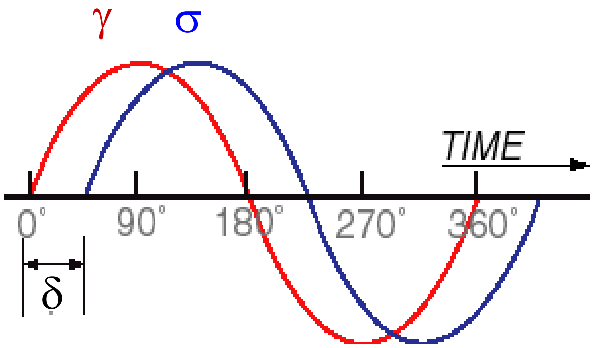

Figure 2.7. Viscoelastic materials show a phase lag (δ) between the shear stress (blue) and shear strain rate (red).

Letting strain be a harmonic function of time:

$$\varepsilon(t) = \alpha \sin \omega t \tag{11}$$

where ε is the shear deformation, ω is the angular frequency, and α is the amplitude, which must be kept small to ensure that the Boltzmann superposition principle is applicable. Then, the shear strain rate could be written as follows:

$$\dot{\varepsilon}(t) = \alpha\omega \cos \omega t \tag{12}$$

Substituting equation (11) into (7):

$$\boldsymbol{\sigma}(t) = \int_{-\infty}^{t} \mathrm{G}\,(t-\tau)\alpha\omega\cos\,(\omega\tau)d\tau \tag{13}$$

Transforming this integral by assuming s = t-τ:

$$\boldsymbol{\sigma}(t) = \alpha\omega \int_0^\infty \boldsymbol{G}\,(s)\cos\,\big(\omega(t-s)\big)ds \tag{14}$$

If the expression cos(ω(t-s)) is the real part of exp(iω(t-s), then:

$$\begin{aligned}\boldsymbol{\sigma}(t) &= \alpha\omega Re \int_0^\infty \boldsymbol{G}\,(s) \exp\big(i\omega(t-s)\big)ds \\ &= \alpha\omega Re \left[exp(i\omega t) \int_0^\infty \boldsymbol{G}\,(s) \exp(-i\omega s)ds\right]\end{aligned} \tag{15}$$

The integral on the right-hand side, has no dependence on t, this complex expression is defined by convention as the complex shear modulus G*:

$$G^* = i\omega \left[\int_0^\infty \boldsymbol{G}\,(s) \exp(-i\omega s)ds\right] \tag{16}$$

Or in terms of its real and imaginary parts:

$$G^* = G' + iG" \tag{17}$$

where G’ is the storage modulus G” is the loss modulus.

The storage modulus (G’) corresponds to the elastic component and it represents the ability of a material to store energy elastically. The loss modulus (G’’) or viscous component represents the ability of a material to dissipate energy while the complex modulus (G*) represents the overall resistance of a material to deformation.

$$\begin{gathered} G' = G^* cos\delta \\ G" = G^* sin\delta \end{gathered} \tag{18}$$

In the case of viscoelastic fluids, complex viscosity will be the ratio of the complex shear modulus and the angular frequency:

$$\eta^* = \frac{G^*}{\omega} \tag{19}$$

Plotting the moduli with respect to angular frequency, we observe the trends depicted on Figure 2.8. The point where both curves intersect according to Maxwell's model is $\omega\tau = 1$. At slow speeds $\omega\tau >>1$, the material approximates a viscous fluid while for high speeds ($\omega\tau <<1$), the material resembles an elastic solid.

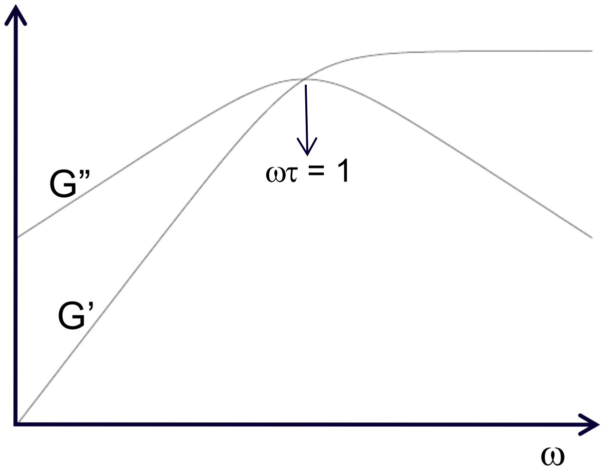

Figure 2.8. Storage modulus (G') and Loss modulus (G") with respect to frequency for a single relaxation model (from Wilson, 2006).

2.3 Dead Oil Empirical Viscosity Models

Most of the viscosity correlations used to understand the relationship between velocities and different properties are empirical; however, a correlation's reliability is valid only in a well-defined range of reservoir fluid characteristics (DeGuetto et al., 1995). Heavy oil viscosity measurements exhibit very high errors in comparison with other properties (bubble pressure, GOR, isothermal compressibility). DeGuetto suggests that this behavior is justifiable since only two input variables are used: temperature and API gravity.

Elsharkawy and Alikhan (1999) consider not taking into account the crude oil base (asphaltic, paraffinic, or mixed) as the cause for such high errors. Also, even laboratory measurements on the same high viscosity sample exhibit 10% variation when measured with different equipment. All the empirical correlations assume that the fluid is Newtonian, which is not completely valid for highly viscous fluids and temperatures below room temperature.

Extra-heavy and heavy oils usually have a small amount of gas dissolved on the crude; therefore, we will use in this study the correlations corresponding to *dead crude oil*, oil without gas in solution at atmospheric pressure (Gabitto and Barrufet, 2003). As temperature is increased, additional gas usually is expulsed from the dead oil, meaning API gravity would be different for each temperature. However, given the natural composition of heavy oils, there are very few components between C3 and C10 or in the volatile region, which means that the API gravity of the dead oil can be assumed as constant for the range of temperatures studied (Bennison, 1998).

2.3.1 Beggs and Robinson Correlation (1975)

Beggs and Robinson carried out 2533 viscosity measurements on 600 different crude oil samples. Based on their dataset, they developed correlations to calculate dead oil viscosity and undersaturated oil viscosity. They reported an accuracy of -0.64% for the equation used to estimate dead oil viscosity in comparison to their dataset, while the same correlation against literature cases exhibited an error of 114.27% (De Guetto et al., 1995). The mathematical expression provided to estimate dead oil viscosity is:

$$\begin{gathered} ln(\eta+1)=0.505y(17.8+T)^{-1.163} \\ ln(y)=5.693-\frac{2.863}{\rho_0} \end{gathered} \tag{20}$$

where η is the viscosity (centipoise), T is temperature (°C) and ρ_0 is the oil density. Usually those models are only valid for a specific temperature range; in this case, the low limit temperature is –17.8°C. However, for temperatures below 0°C, the results are questionable since viscosity approaches to infinity (Figure 2.9).

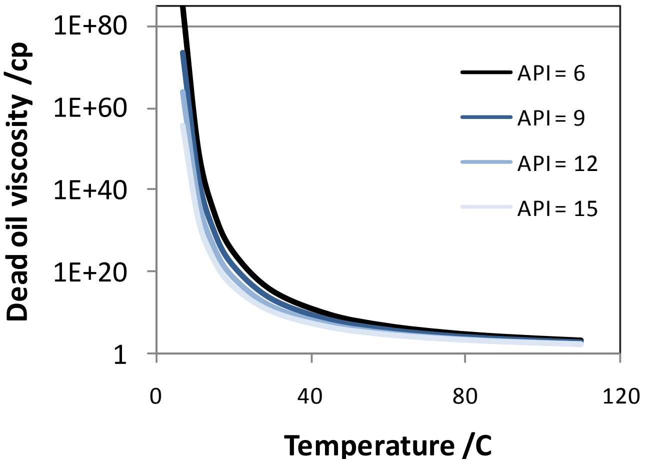

Figure 2.9. Viscosity as a function of temperature for oils with different API gravity using Beggs & Robinson (1975) correlation.

2.3.2 DeGuetto, Paone, and Villa Correlation (1995)

The objective of work by DeGuetto, Paone, and Villa (1995) was to evaluate empirical correlations for estimating dead oil viscosity, among other properties, and to develop new correlations based on 65 heavy and extra-heavy oil samples, specifically, for oils with API gravity between 6° and 22°. For extra-heavy oils (API ≤ 10°), they modified the Egbogah-Jack's correlation:

$$\eta = 10^{y} - 1 \qquad (21)$$
$$y = 10^{(1.90296 - 0.012619API - 0.61748\log(T))}$$

And for heavy oils, the empirical relation is:

$$\eta = 10^{y} - 1 \qquad (22)$$
$$y = 10^{(2.06492 - 0.01793API - 0.7022\log(T))}$$

where η is the viscosity (centipoise), T is temperature (°F) and API is the oil gravity.

2.3.3 Bennison Correlation (1998)

Using measured data from four heavy oil reservoirs in the North Sea, Bennison (1998) developed the following model to estimate viscosity based on temperature and API gravity:

$$\eta = 10^{(0.052API^2 - 2.2704API - 5.7567)} T^{(-0.0222API^2 + 0.9415API - 12.839)} \qquad (23)$$

where η is the viscosity (centipoise), T is temperature (°F), and API is the oil gravity. The curves generated with this correlation show a good agreement with the measured data for temperature less than 121°C and API gravity less than 20 degree.

All four viscosity empirical models predict a similar change of viscosity with temperature for temperatures above 15°C (Figure 2.10), since most of them have been developed based on laboratory measurements for conventional oil samples. However, for lower temperatures where the Non-Newtonian properties are more accentuated, the difference is significantly high. Also, these models do not take into account the frequency, which is crucial for geophysical applications. For that reason, the goal is to build a model capable of correlating the viscoelastic properties as a function of frequency and temperature assuming heavy oil as a Non-Newtonian fluid. In the following section, two recent models that include the frequency effect to estimate not only the complex viscosity but the compressional and shear velocity are reviewed.

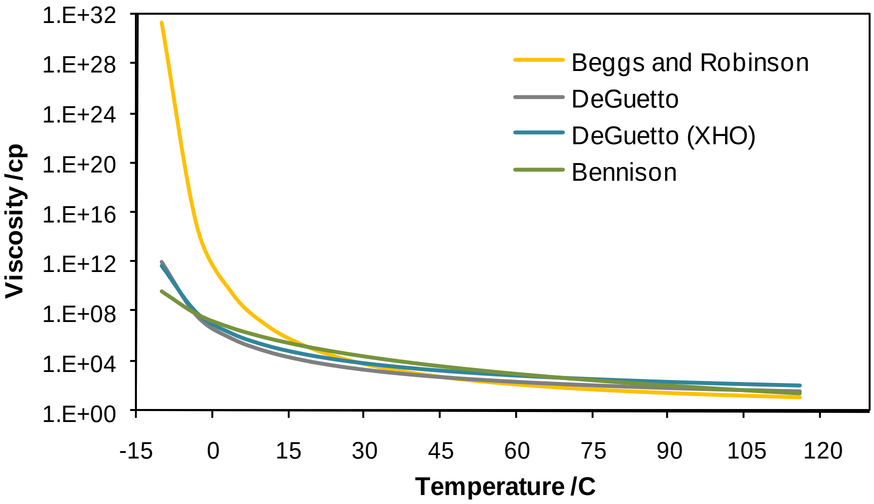

Figure 2.10. Different predicted viscosity correlations for heavy oil with API =10.

2.3.4 Han Model and Behura et al. Model

Ultrasonic laboratory measurements for heavy oils have shown that according to P-wave and S-wave velocity trend with temperature, three different phases have been recognized (Han et al., 2007). The phases are: glass-solid, quasi-solid, and fluid (Figure 2.11). Heavy oil rarely occurs in the glass-solid phase, and in the fluid phase it has essentially the same characteristics as conventional oil; therefore, most of the models focus on the quasi-solid phase since it is here where their viscoelastic properties are clearly evident.

The glass point temperature (GP) marks the transition from quasi-solid phase to glass phase, whereas the liquid point temperature (LP) is the temperature at which the transition from quasi-solid phase to liquid phase occurs (Han et al., 2007). For temperatures above the LP, the heavy oil behaves as a fluid with the following characteristics:

- Absence of shear modulus.
- Viscosity has no effect on velocities.
- P-wave and S-wave velocities have a linear relationship with temperature.

For temperatures below LP, the fluid becomes essentially Non-Newtonian, and heavy oil has the following characteristics:

- Presence of shear modulus.
- P-wave and S-wave velocities are frequency dependent.
- Velocities have a non-linear relationship with temperature.

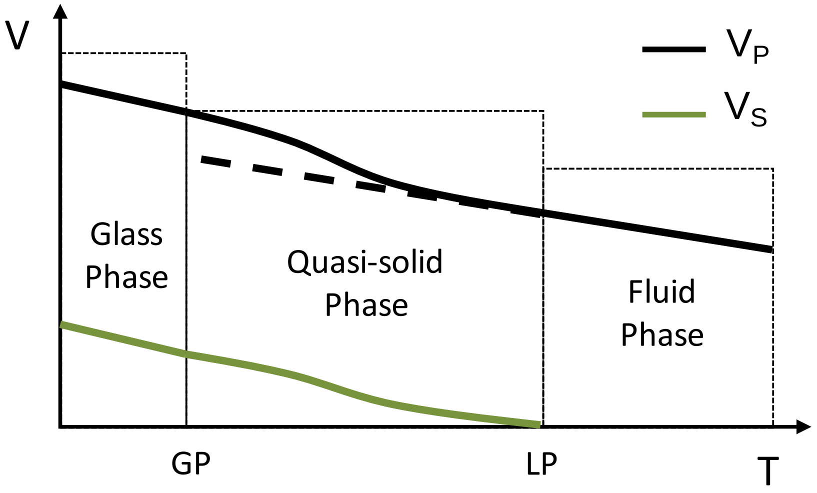

Figure 2.11. Phase behavior for heavy oils. Liquid point (LP) and Glass point (GP) are shown as well as P-wave and S-wave velocities (from Han et al., 2007).

The effect of frequency on shear wave velocity is particularly significant in the quasi-solid phase where dispersion can occur for a certain temperature and viscosity. Velocity dispersion (P and S waves) seems to be negligible for heavy oils in the liquid and glass phase (Han et al., 2007).

Behura et al., (2007) have shown for a heavy oil-saturated rock that as frequency increases, the complex shear modulus increases, which is consistent with the frequency dependence of the shear modulus for heavy oil. Consequently, the rheological properties of heavy oil dominate the possible change with temperature and frequency endured by the matrix.

They used the Maxwell model, which combines an ideal spring or elastic component (G') and a perfect dashpot or viscous component (G") connected in series. Hence, the total shear rate is the sum of shear rates of both elements.

$$G^*(\omega) = \frac{G_{max} i\omega\eta}{1 + i\omega\tau}$$

$$G'(\omega) = \frac{G_{max}(\omega\tau)^2}{1 + (\omega\tau)^2} \qquad (24)$$

$$G''(\omega) = \frac{G_{max}(\omega\tau)}{1 + (\omega\tau)^2}$$

where G* is the complex shear modulus, G' and G" are the storage modulus and the loss modulus respectively, τ is the relaxation time, and ω is the angular frequency. The shear wave modulus or rigidity at the glass point temperature (GP) is defined as μ_g, which is the same as the effective rigidity at high frequency (G_{max}). Unfortunately, the Maxwell model provides a drastic change of complex shear modulus with frequency, not observed on the laboratory measurements (Figure 2.12).

In the case of high frequencies ($\omega\tau >> 1$), the complex shear modulus tends to the rigidity at GP or infinity (G_{max} or μ_g); while in the case of low frequencies, ($\omega\tau << 1$), $G(\omega)$ tends to $i\omega\eta$, which in the time domain means that the shear stress is proportional to the time derivative of the shear deformation (shear rate), characteristic of Newtonian fluids (Gurevich, 2007). At low frequencies, the fluid has time to reach the equilibrium reducing the energy or storage modulus, while at high frequencies; the relaxation time is too short to relax the molecules/chains of hydrocarbons making the energy transfer easier. Simultaneously, energy lost by friction is lower; therefore attenuation decreases (Behura et al., 2007).

Other models have been proposed to fit properly the lab measurements; those are: Cole-Cole model (1941), Cole and Davidson model (1951), and Havriliak-Negami (H-N) model (1967). The equations for these models can be found in the Appendix B. Han et al., (2007) found the best fit when using the H-N model; however, it is necessary to take into account that the shear wave modulus of the dataset has been estimated using the GP viscosity given by DeGuetto (extra-heavy) model, which presents a lot of uncertainty in the low temperature/high viscosity range.

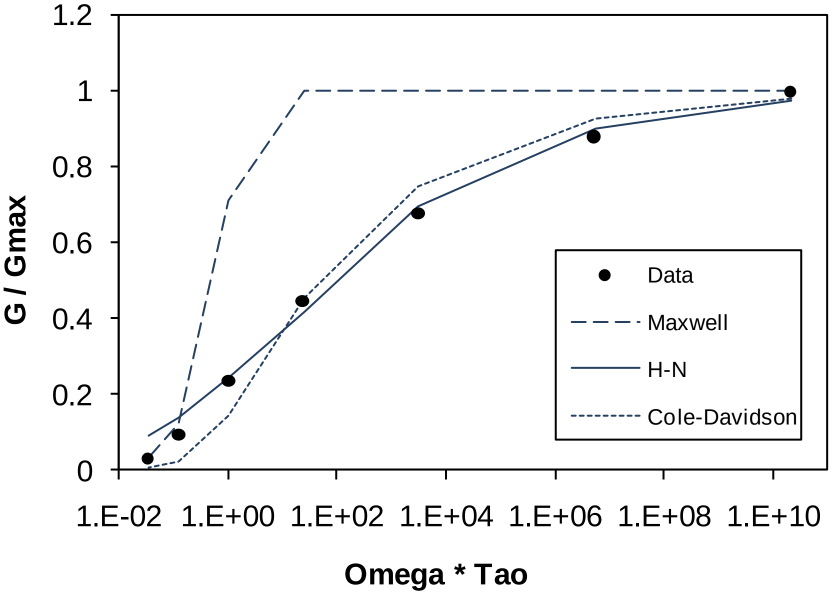

Figure 2.12. Complex shear modulus normalized by the shear modulus at high frequency as a function of $\omega\tau$. Three viscoelastic models have been used to fit the “data”. The DeGuetto (extra-heavy) model has been used to estimate the GP temperature of the data.

2.4 Rheological Measurements of Heavy Oil Samples

Low-frequency measurements were carried out using a dynamic shear rheometer to measure the rheological properties of heavy oil samples obtained from reservoirs around the world. The samples are defined as extra-heavy and heavy dead oil according to the American Petroleum Institute. One of the goals was to observe the trend of complex viscosity, shear modulus and attenuation as frequency and temperature is varied. However, in this chapter, the measurements obtained for complex viscosity will only be discussed.

Currently, I am unaware of any reliable complex viscosity measurements at low temperature (in the vicinity of the glass-point temperature) on heavy oil samples; this provides motivation for the utilization of Differential Scanning Calorimeter (DSC) method to estimate the glass point. This piece of information is crucial to model the complex viscosity expression as will be shown in section 2.5. Table 2.3 shows the densities and API gravities of the samples used in this study.

Table 2.3. Densities were measured at standard conditions.

Sample	API gravity	Density (g/cc)
Canada A	9.38	1.004
Brazil	14.27	0.971
Venezuela	10.99	0.993
Canada B	8.05	1.014

2.4.1 Differential Scanning Calorimeter Measurements

DSC is a method used for thermal analysis that is based on the quantity of heat absorbed or released by a material when goes through a physical or chemical change (Ehrenstein et al., 2004). Melting, crystallization, and glass transition are examples of phase transitions. DSC records the amount of heat required to increase the temperature of a sample and the reference calorimeter. When the sample undergoes phase transitions, more (melting) or less (crystallization) heat flows to the reference to maintain both at the same temperature. The result of a DSC experiment is again, the amount of heat absorbed or released during such transitions, given by the difference in heat flow between sample and reference calorimeter.

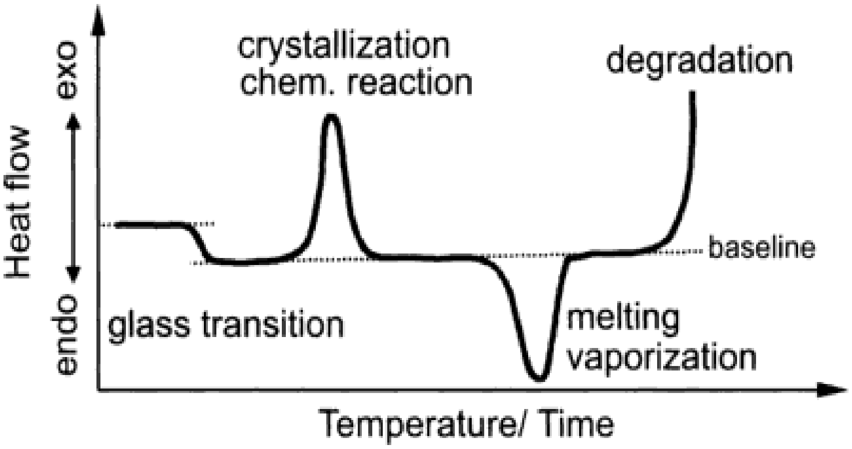

Figure 2.13. DSC curves. The glass transition is represented as a step in the baseline and not a peak since an actual phase change does not occur. Ehrenstein et al., 2004.

DSC curves (Figure 2.13) represent the change of heat flux versus temperature or versus time. Exothermic reactions are usually shown with a negative peak whereas endothermic with a positive peak. In these experiments, the interest will be on the glass transitions, which are represented as a step or an inflection point in the Q baseline.

Glass transitions, according to the IUPAC Compendium of Chemical Terminology, are a 2nd-order phase transition (not a formal phase change) where changes only in heat capacity yield a supercooled melt to have properties similar to those exhibited by crystalline materials. Also, the fact that the glass point temperature (T_G) depends on the cooling rate is evidence that it is not a thermodynamic phase change. Time and temperature are intrinsically correlated for this type of materials: the faster the cooling rate, the higher T_G. This is an evidence of a concept that will be explained later (section 2.4.4) known as the Time-Temperature Superposition Principle.

Changes of volume, enthalpy or viscosity with temperature usually reveal clearly the presence of T_G, since it represents the departure from the liquid equilibrium curve (Scherer, 1986). A plot of the logarithm (neperian) of viscosity with respect to the inverse of temperature helps to define T_G if the fluid follows the Arrhenius equation (more about this equation and activation energy, E, will be discussed in section 2.5):

$$\eta = A\,exp\left(\frac{E}{RT}\right) \qquad (25)$$

$$ln\eta = lnA + \left(\frac{E}{R}\right)\frac{1}{T}$$

where E is the activation energy, R the ideal gas constant, and T is the absolute temperature. The position of the T_G as the point where the non-equilibrium viscosity (glassy state) begins to be lower than that at the equilibrium curve is shown in Figure 15. In this region, there is not enough energy for atoms to move freely; therefore they cannot achieve the equilibrium arrangement if the cooling rate is fast enough to prevent structural relaxation. The viscosity will eventually increase until equilibrium if temperature is held constant.

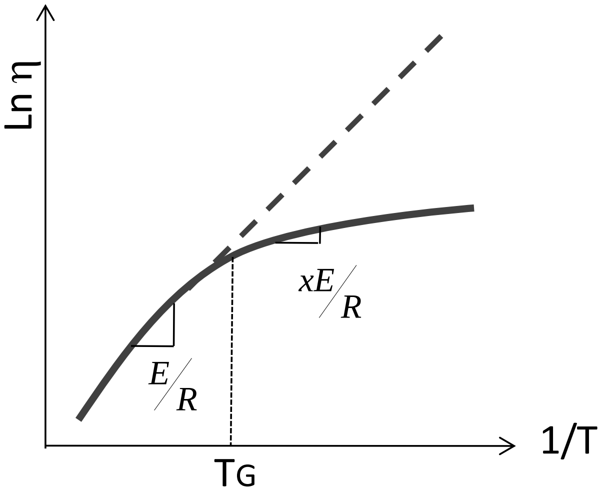

Figure 2.14. Glass point temperature for a fluid that obeys the Arrhenius equation. The viscosity decreases at non-equilibrium (from Scherer, 1986).

2.4.1.1 Evaluating T_G

One of the biggest challenges is to evaluate the location of the T_G. First, heavy and extra-heavy oils exhibit a very subtle glass point temperature due to their complex structure where each compound has a different melting point. Second, there are many conventions to choose T_G. For example, for some authors T_G is the temperature at which half of the change in c_p has occurred. For others, it is actually the temperature at which the heat curve exhibits a considerable change in their slope. In this study, the latter was chosen.

To determine the T_G, the temperature scan was started 50°C below the expected transition temperature and was continued until 50°C after the transition. This is generally done for a better evaluation of the heat flow baseline. In our case, we presumed the glass point temperature to be around -40°C based on ultrasonic velocity measurements.

The cooling rate parameter is very important; different rates were tested to properly identify the glass transition. At the beginning, a 20°C/min rate was used but the phase transition was too broad to identify T_G. Then, the rate was changed to 40°C/min in an attempt to eliminate the melting/crystallization transitions that were occurring and accentuate any changes in heat capacity (C_P) that would indicate a glass transition. However, the results were not satisfactory. The rate was slowed to 10°C/min which showed all the transitions more clearly, including T_G.

A total of 8 runs were done for each of the four samples:

1. DSC Isothermal: temperature is kept at 30°C (approximately room temperature) for one (1) minute.
2. DSC Temperature Scan: temperature of sample and reference is dropped from 30°C to -100°C.
3. DSC Isothermal: temperature is kept at -100°C for one (1) minute.
4. DSC Temperature Scan: temperature of sample and reference is increased from -100°C to 10°C.
5. DSC Isothermal: temperature is kept at 10°C for one (1) minute.
6. DSC Temperature Scan: temperature of sample and reference is increased from 10°C to -100°C.
7. DSC Isothermal: temperature is kept at -100°C for one (1) minute.
8. DSC Temperature Scan: temperature of sample and reference is finally increased from -100°C to 10°C.

For some of the samples, it was impossible to determine the glass transition; however, in Figure 2.15, three DSC curves and their respective glass point temperatures are shown. The results obtained through DSC will be used to model the response of complex viscosity with temperature and frequency in a subsequent section.

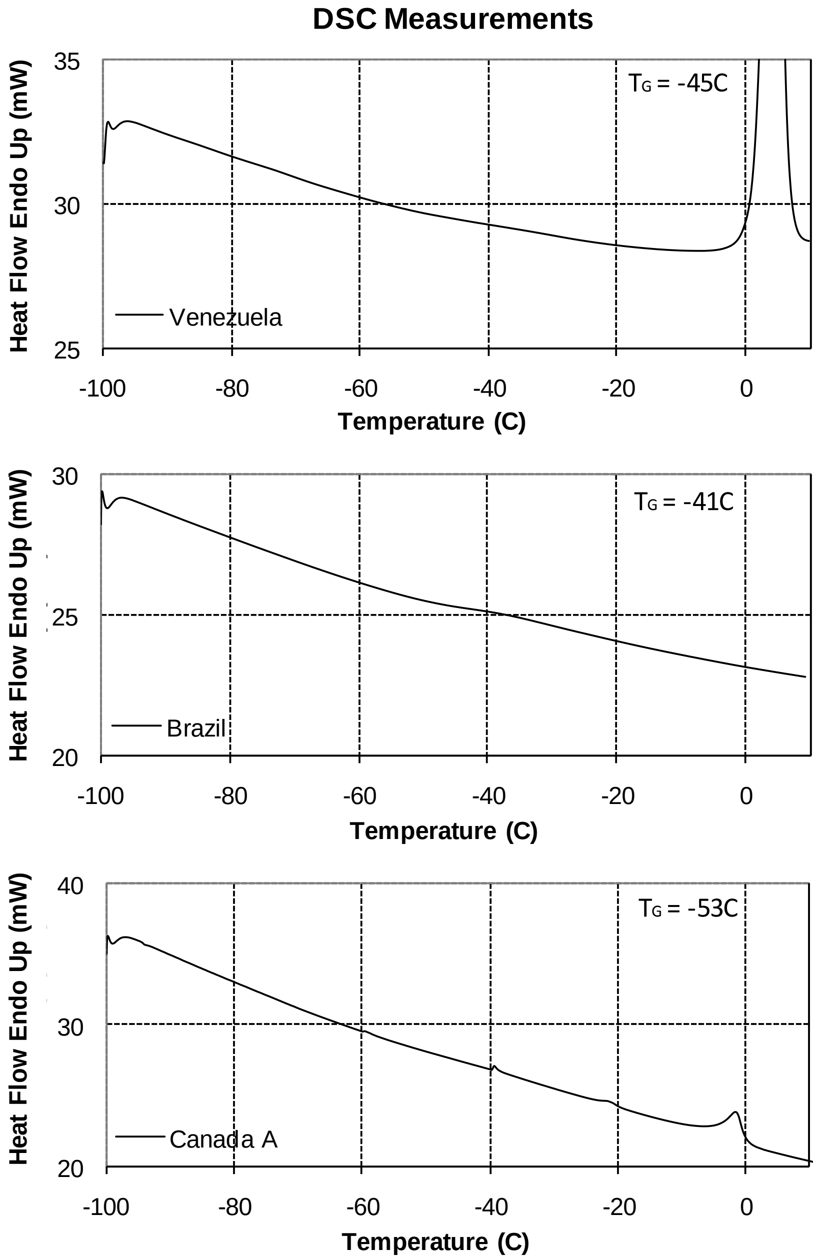

Figure 2.15. DSC curves for extra-heavy and heavy oil samples at a cooling rate of 10°C/min.

2.4.2 Dynamic Rheological Measurements using a Shear Rheometer

2.4.2.1 Experimental Setup

The dynamic rheological measurements consist of subjecting the oil sample to a continuously oscillating (sinusoidal) strain (γ) over a range of frequencies and measuring the peak value of the stress (σ) and the corresponding phase lag. This process, usually referred as Dynamic Frequency Sweep testing, is repeated for each temperature. The frequency range goes from 0.01 rad/s to 600 rad/s while the temperatures analyzed are: 0°C, 10°C, 20°C, 30°C, 40°C, 50°C, 60°C, 80°C, and 100°C. For some samples, we were not able to estimate reliably the highest temperatures or lowest frequencies, simply because at those ranges the fluid has Newtonian behavior.

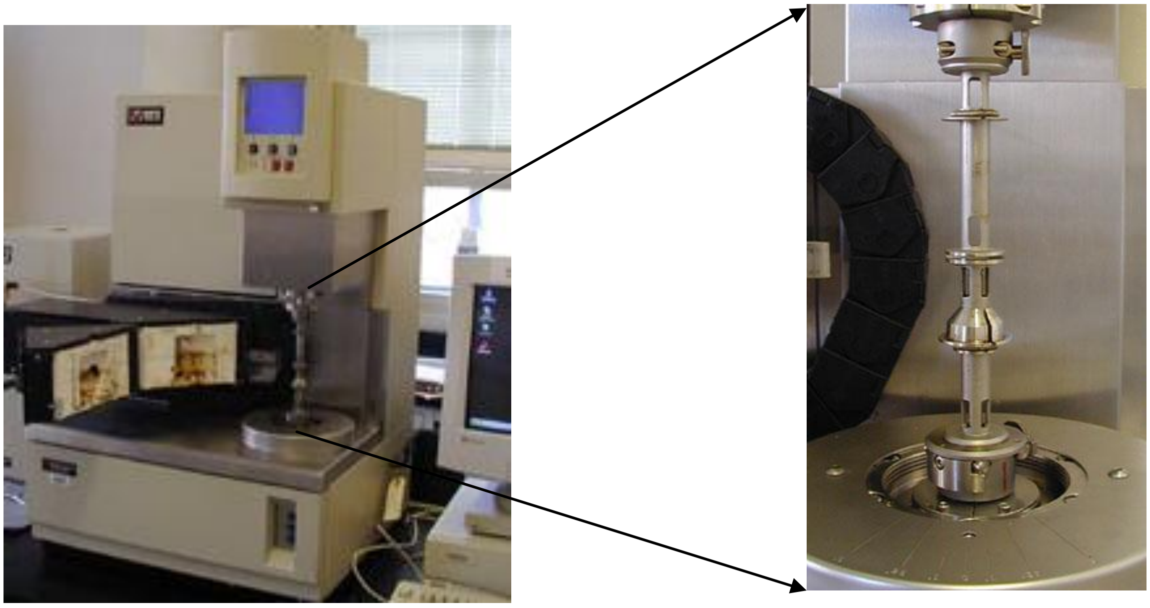

Figure 2.16. The ARES TA Rheometer. The picture to the right shows the parallel plates that surround the heavy oil sample.

Two rheometers of the controlled-strain type (input signal is the shear strain whereas the output signal is the shear stress) were used: a Physica MCR from Anton Paar and an ARES TA Rheometer. The instrument applies a translational sinusoidal displacement (x) to move the upper plate with angular frequency ω:

$$x^* = x_0 exp\ (i\omega t) \tag{26}$$

Based on displacement and the gap distance between both plates, the shear rate is calculated by:

$$\gamma \approx \frac{x^*}{h} \tag{27}$$

The lower plate transmits the harmonic shear force (F_s) resulting from the viscoelastic response of the fluid to the piezoelectric transducer:

$$F_S = F_0 e^{i(\omega t + \delta)} \tag{28}$$

Then, shear stress can easily be calculated knowing the area of the plates. In our case, the dimension of the plates was 25mm:

$$\sigma_S \approx \frac{F_S}{A} \tag{29}$$

The stress signal of a viscoelastic material can be separated into two components if we know the phase angle difference between stress and strain signals: an elastic stress that is in phase with strain, and a viscous stress that is 90° out of phase with strain. These correspond to the previously mentioned, loss and storage moduli, G” and G’ respectively.

An oscillatory test was chosen among the different rheological tests because it involves the lowest strain amplitude and preserves the structure of the fluid depending on temperature and frequency. In particular, the strain amplitude is higher for high temperatures and low frequencies. The strain amplitude in the rheological tests varies from 10^{-5} to 10^{-2} approximately. The strain amplitude is varied to keep the measurements within the region where the Boltzmann superposition principle is valid (linear viscoelastic regime). Results within this region allow comparisons between different rheometers to be made.

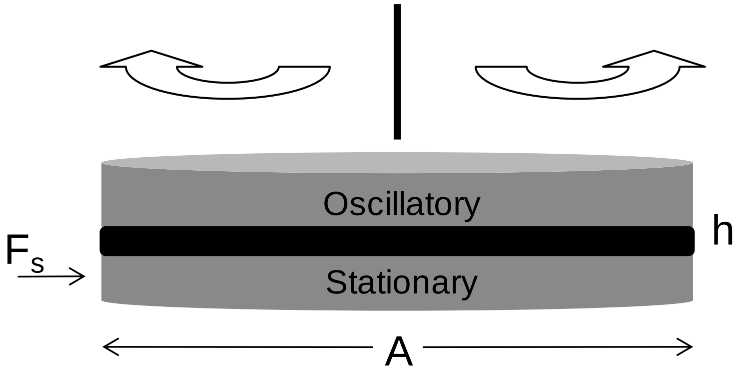

Figure 2.17. The oscillatory movement of the upper parallel plate produces a harmonic shear force that it is transmitted to the stationary lower plate due to the viscoelastic nature of the fluid. Crawford, 1998.

Some of the factors affecting rheological measurement results on bitumens could be:

- *Temperature control:* the whole sample must be at the same temperature since bitumens are highly susceptible to temperature.
- *Equipment calibration:* most rheometers require calibration at the beginning of each run. Such calibrations can be misleading, particularly since bitumens are significantly more viscous than standard fluids used for calibration.

The experimental procedure can be summarized as follows:

1. Turn on the water pump that is in charge of stabilizing the temperature.
2. Calibrate the motor.
3. Run the moment of inertia test.
4. Set the temperature. Usually, the first temperature to be studied should be in the middle of the temperature range. In this case, initial temperature was 30°C.
5. Place both plates together to equilibrate both temperatures. The main advantage of sandblasted plates is higher traction and therefore lower strain amplitude is required. A 25mm parallel plate is used.
6. Both plates should be parallel and aligned. The gap distance should be zero as well as the normal forces.
7. The sample is loaded on the bottom plate, making sure that the whole area is covered by a homogeneous layer.
8. Start the frequency sweep testing from 0.01 Hz to 100Hz.
9. Strain amplitude should be increased as temperature increases, if not increased properly, then the torque is not high (sensitive) enough and departure from the linear regime may occur. As a check, in the linear viscoelastic regime, there should be no dependence between strain amplitude and G' or G".
10. Temperature should be increased slowly, as normal forces increase with temperature, which might produce some damage to the transducer.

2.4.2.2 Results – Heavy Oil as a Viscoelastic Fluid

Resulting measurements of viscous and elastic moduli with respect to frequency at several temperatures are shown in Figure 2.18 and Figure 2.19. It can be seen that the viscous component is always higher than the elastic component, distinctive of a viscoelastic liquid. However, this difference decreases as frequency increases, until a certain frequency is reached indicating the beginning of a transition zone where higher frequencies will decrease not only the viscosity (shear thinning phenomenon) but also the elastic component (G'). Same behavior is observed at each temperature. In general, G" is proportional to ω, whereas G' is proportional to ω^2. For all the heavy oil samples, G' measurements become less reliable for temperatures above 60°C, since the viscoelasticity is lost above this temperature and the rheometer is not useful anymore. If G' is higher than G", then that temperature is referred as the glass point (T_G). However, due to limitations of the equipment, it was not possible to measure temperatures below 0°C; therefore this method cannot be used to determine T_G.

As discussed previously, the shear thinning phenomenon is observed in Figures 2.20 and 2.21. This typical behavior of viscoelastic and Non-Newtonian fluids occurs when molecules try to align themselves to the fluid flow, decreasing the viscosity as frequency increases.

Samples with the lowest API gravity, such as the Canada A and Canada B heavy oil samples exhibit a more noticeable shear thinning effect. For temperatures approximately higher than 40°C (depends on the sample), the shear thinning effect is almost lost. It can also be observed that the linear viscoelastic regime shifts to higher frequencies as temperature increases.

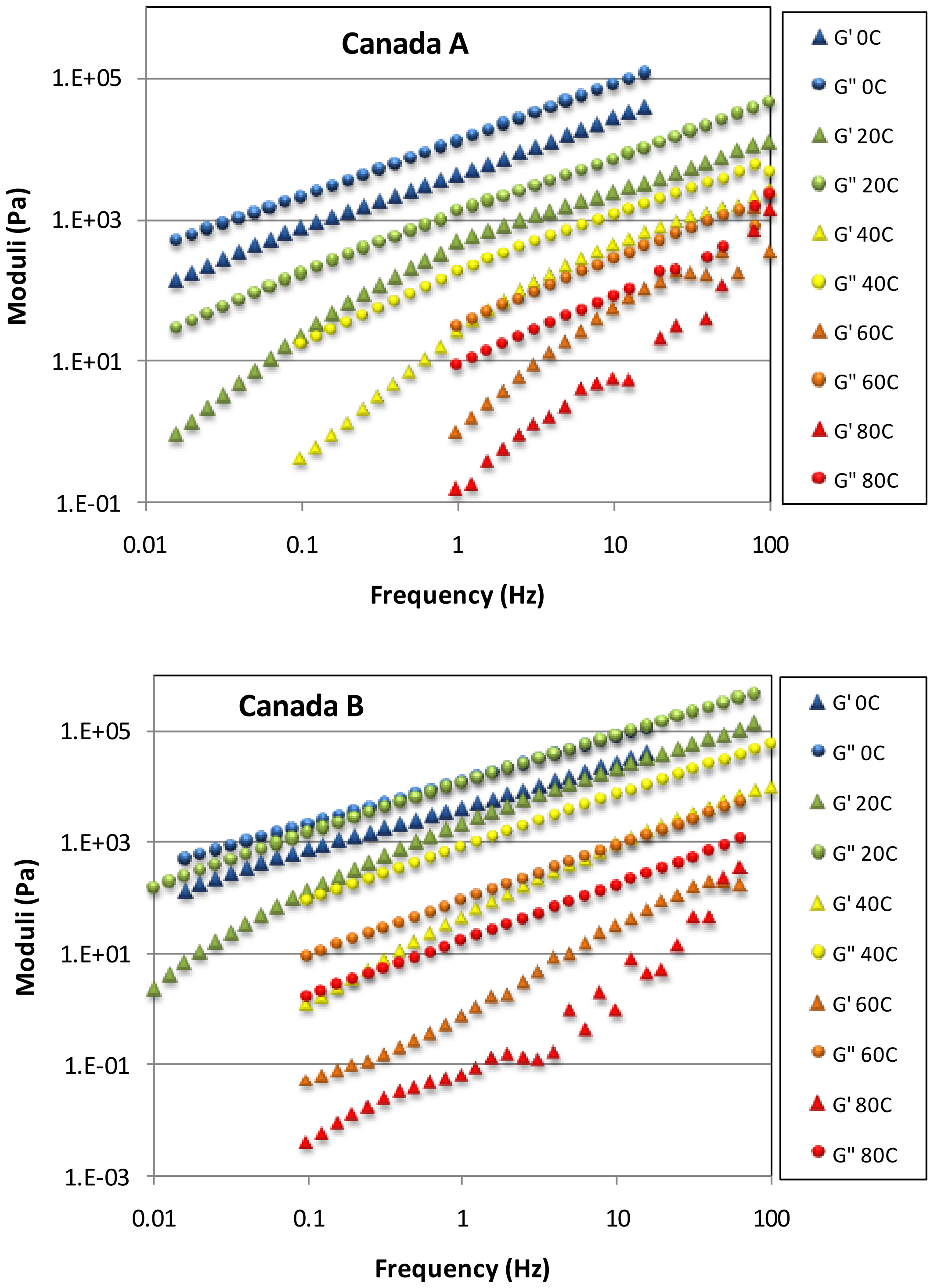

Figure 2.18. Frequency dependence of moduli for Canada A and Canada B oil samples. Typical behavior of a viscoelastic liquid is G” >G’. Filled triangles show storage modulus (G’) and filled circles are for loss modulus (G”).

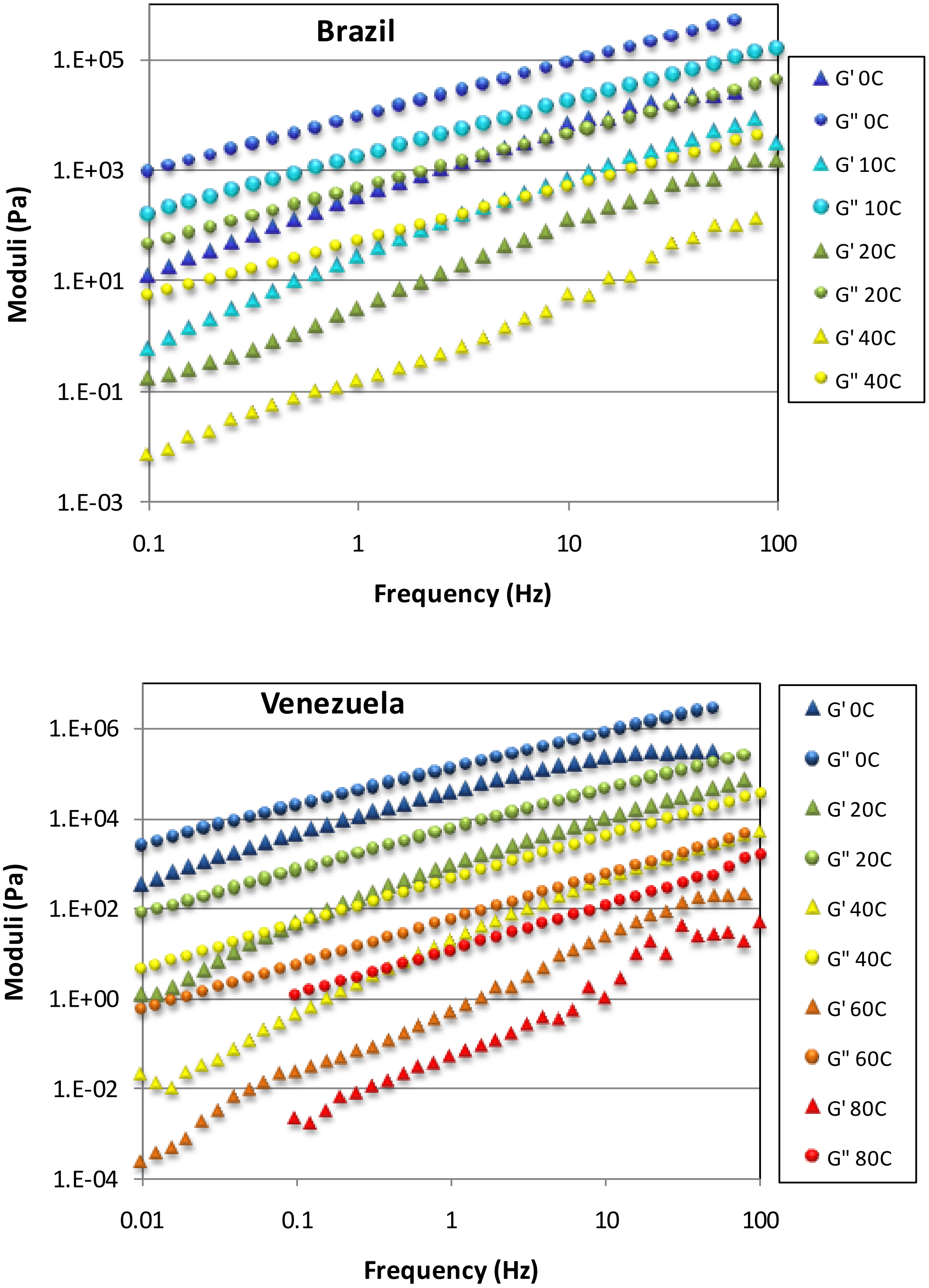

Figure 2.19. Brazil and Venezuela heavy oil samples also display the behavior of a viscoelastic liquid. Filled triangles show storage modulus (G’) and filled circles are for loss modulus (G”).

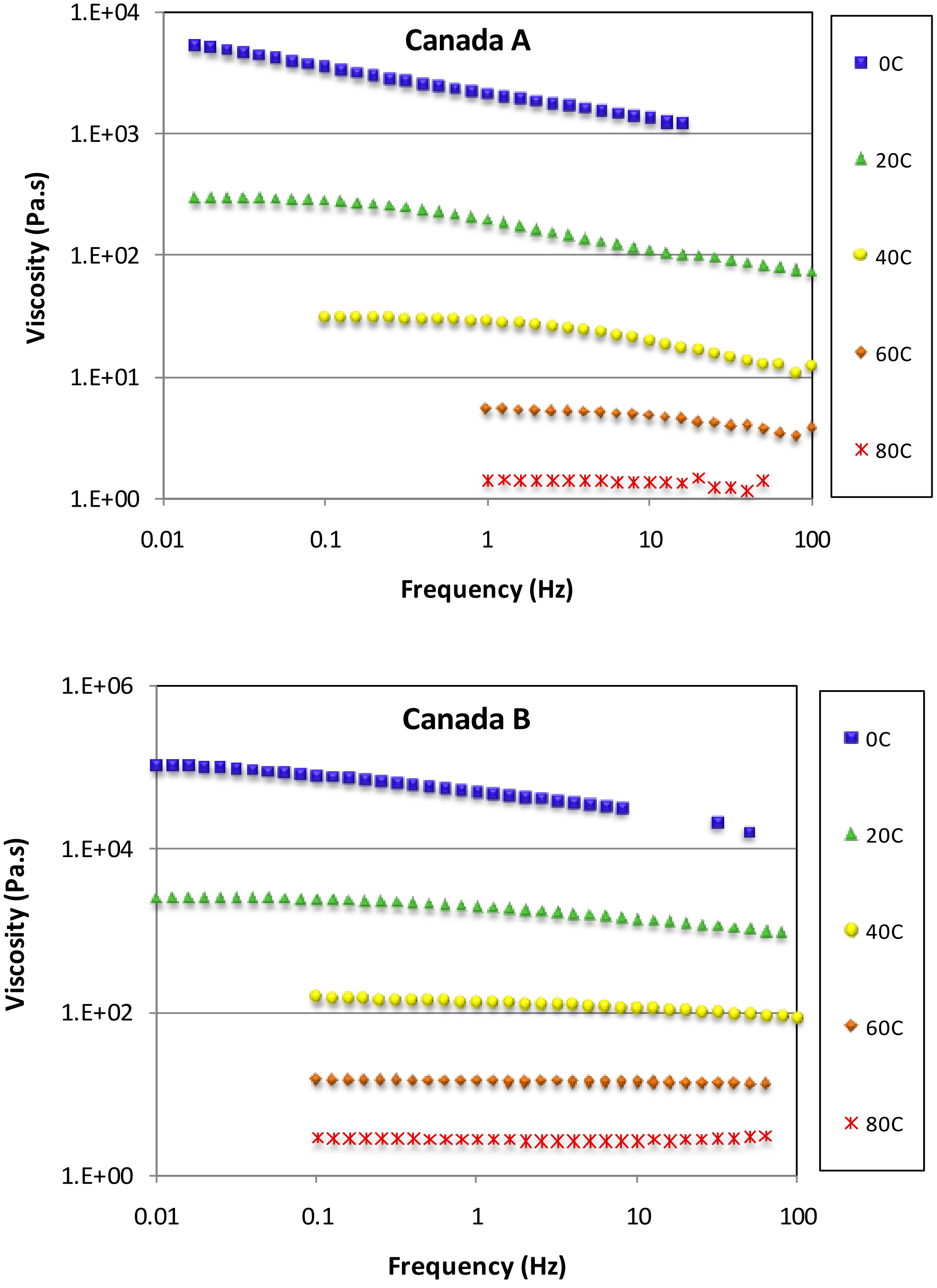

Figure 2.20. Complex viscosity versus frequency for Canada A and Canada B heavy oil samples. They both show shear thinning behavior but thinning is more accentuated in the latter.

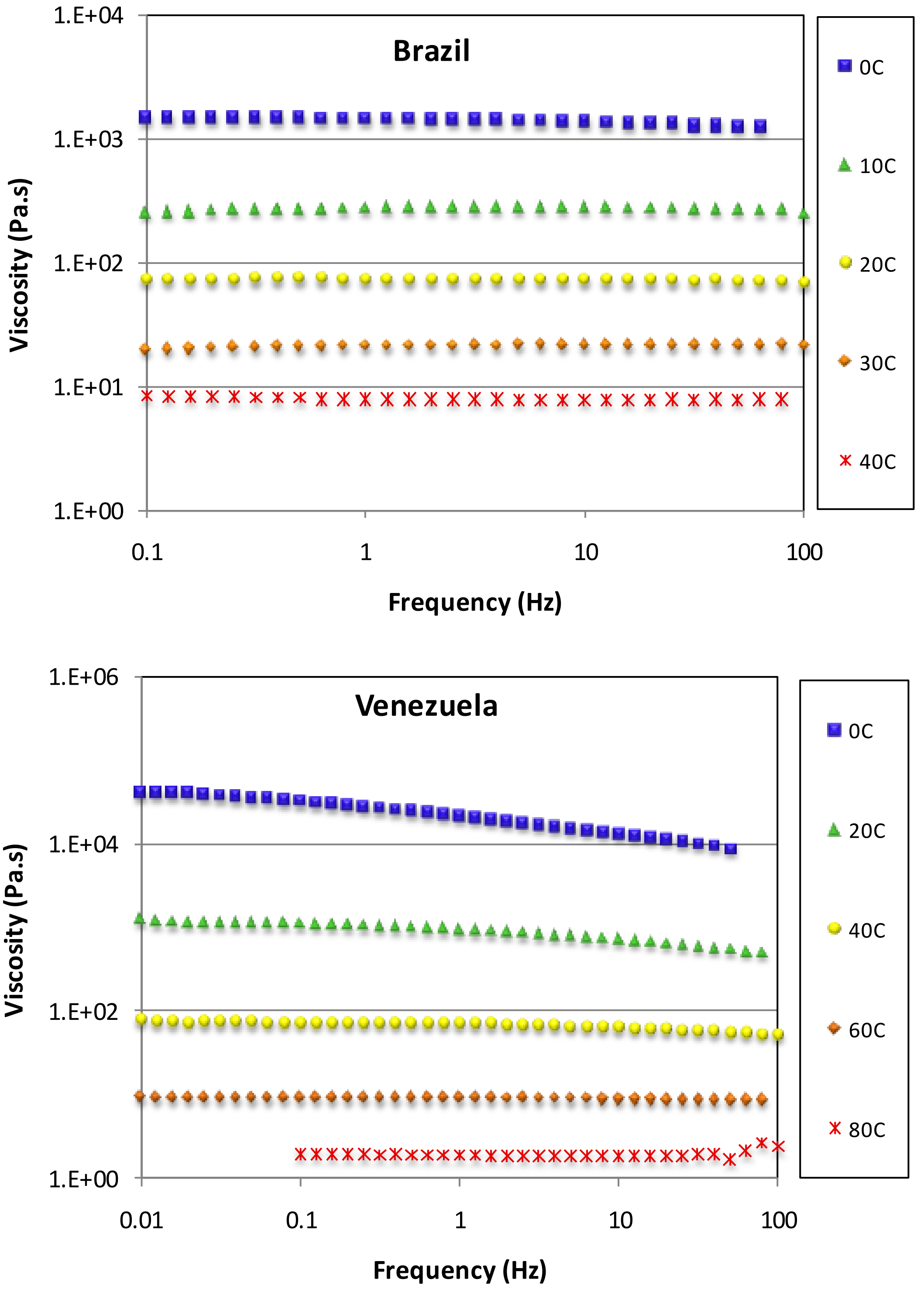

Figure 2.21. Complex viscosity versus frequency. Brazil heavy oil sample with the lowest density, and obtained from a high-pressure reservoir, indicates a very subtle shear thinning phenomenon.

2.4.3 The Liquid Point

The liquid point represents the transition between the quasi-solid and the liquid state; it can be determined by looking at the highest value on the tangent of the phase angle (tanδ) when plotted against the temperature (Yu et al., 2007). Loss tangent (tanδ) is just the ratio between the viscous and elastic modulus, which means if the elastic modulus is close to zero, tanδ will achieve its highest value.

In Figure 2.22, the liquid point varies for each sample from 20°C to 60°C. Above the LP temperature, the fluid becomes Newtonian, since G' is greatly reduced above this temperature. A similar graph of loss tangent as a function of frequency is an indication of the attenuation of the heavy oil sample. This will be shown in Part 2 where the relationship between frequency dispersion and attenuation is discussed. A change in the slope of the G' modulus with respect to temperature can also help to identify the liquid point (Figure 2.23). In fact, the LP given by G' varies also from 20°C to 60°C. It is important to note that the LP is fully dependent on frequency. Different frequencies will exhibit different LP. With the exception of the Venezuela heavy oil sample, the tested oils display a drastic change in the G' slope at the LP temperature.

Table 2.4. Liquid point for all the heavy oil samples using rheological measured data.

Sample	LP based on tan δ	LP based on G'
Canada B	60C	60C
Canada A	40C	40C
Brazil	20C	20C
Venezuela	60C	Indeterminate

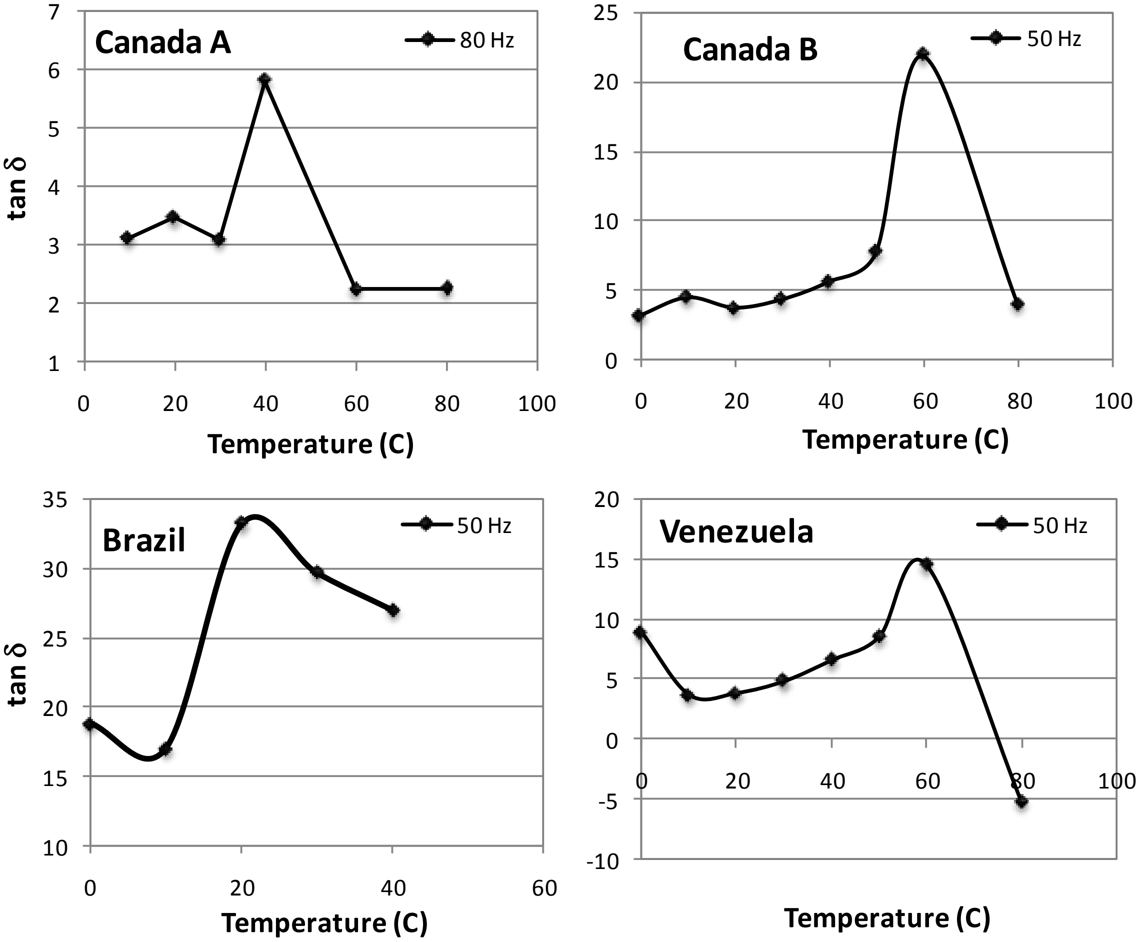

Figure 2.22. tan δ versus temperature for all four samples. The liquid point differs for each sample mainly due to their different densities.

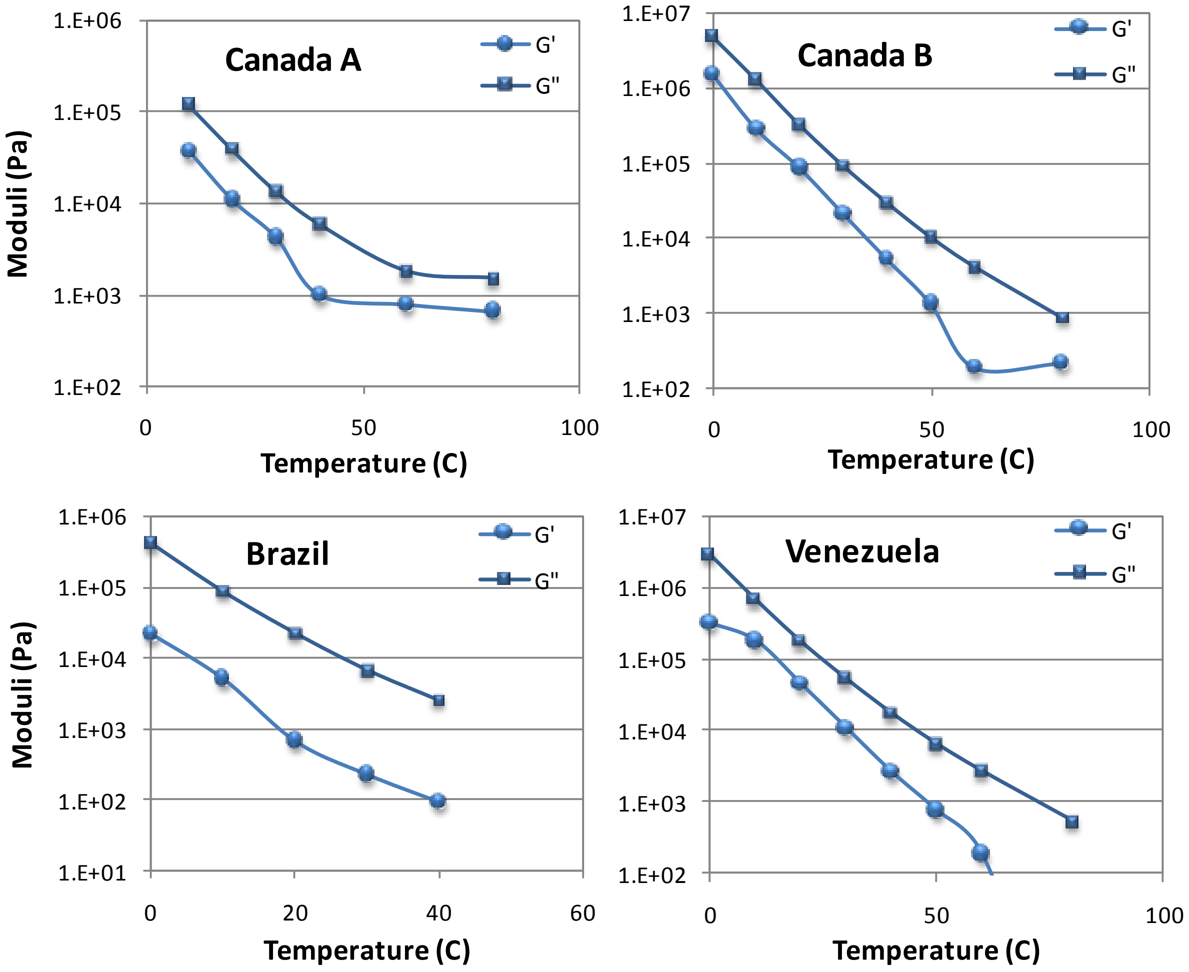

Figure 2.23. Shear modulus as a function of temperature showing the liquid point of Canada A sample. G’ agrees with the value obtained using tanδ.

2.4.4 Frequency – Temperature Superposition Principle

The frequency – temperature or time – temperature superposition principle is a very well-known method in Rheology to increase the frequency range covered by the original data. This principle is based on the fact that changes measured by the sample at *low temperatures* are similar to those caused at *high frequency* and, conversely changes measured by the sample at *high temperatures* are similar to those caused at *low frequency* (Menard, 1999).

For the so-called thermorheologically simple materials, such as heavy and extra-heavy oils, this principle can be applied; however, for crystalline or multiphasic polymers, the presence of multiple relaxation times for each temperature invalidates this approach. Therefore, it can only be used for the quasi-solid phase bounded by T_G and the isotropic or liquid phase.

Master curves are computed by collapsing all the curves to a single reference temperature (Tr) covering a range much greater than that of the original data. For example, data measured from a frequency sweep at one temperature can be shifted horizontally to complement the data measured at a different temperature. This requires a shift factor a_T (x axis) accounting for the change in the time scale (Aklonis and MacKnight, 1983). The same shift factor (a_T) was applied to G', G" and, η* for each of the samples. There are several models to estimate the shift factor; one of them is the Williams–Landel–Ferry (WLF) model (Ferry, 1980):

$$\log a_T = \frac{-C_1(T - T_r)}{C_2 + (T - T_r)} \tag{30}$$

where T is the absolute temperature, and C_1 and C_2 are constants.

A vertical shift, accounts for the change of the sample density with temperature, which in the case of heavy oils is significant:

$$\mathrm{a_V} = \frac{T_G \rho}{T \rho} \tag{31}$$

where ρ is the density of the material at a temperature T.

In summary, this principle holds if:

- Exact matching of shapes of adjacent curves (different temperatures)
- The shift factor a_T is the same for all viscoelastic functions (G', G'', η*)
- Not applicable in the vicinity of glass transition.
- Temperature dependence of a_T has a reasonable form. According to experimental data of this study, a logarithmic relationship holds between a_T and temperature:

$$\ln a_T = C_1 ln\, T + C_2 \tag{32}$$

where C_1 and C_2 are constants. The shift factor versus temperature for Canada A heavy oil sample is shown in Figure 2.24.

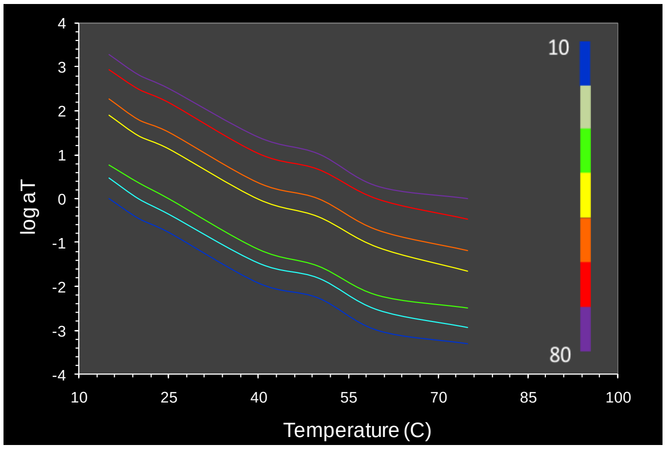

Figure 2.24. The shift factor has a logarithmic relationship with temperature for Canada A heavy oil sample. The color scale indicates the range of temperatures covered.

Using the data, it is possible to apply the Time Temperature Superposition principle (TTS) following the next 4 steps. These were applied on Canada A sample as shown in the Figure 2.25.

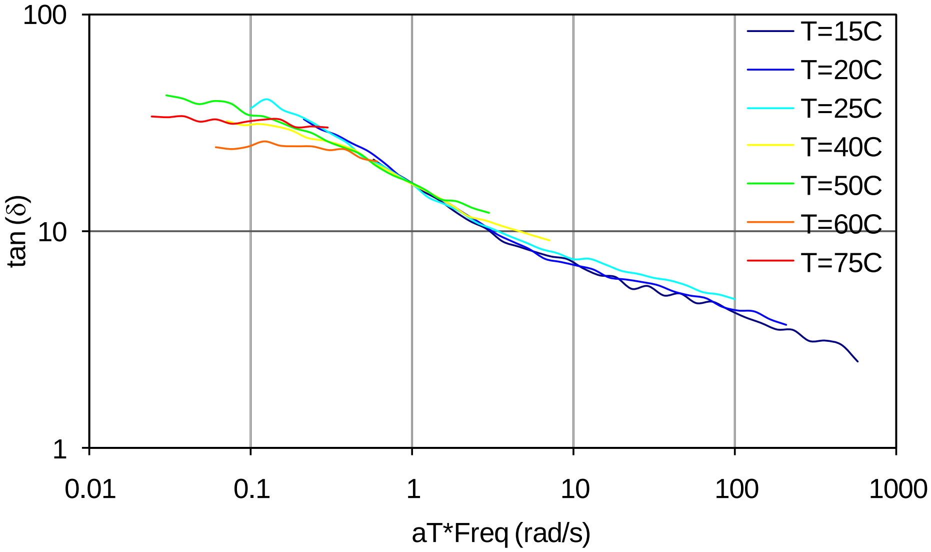

Figure 2.25a. First step: each frequency scan is multiplied by a_T in order to collapse all the curves based on the 25°C reference curve of the tanδ.

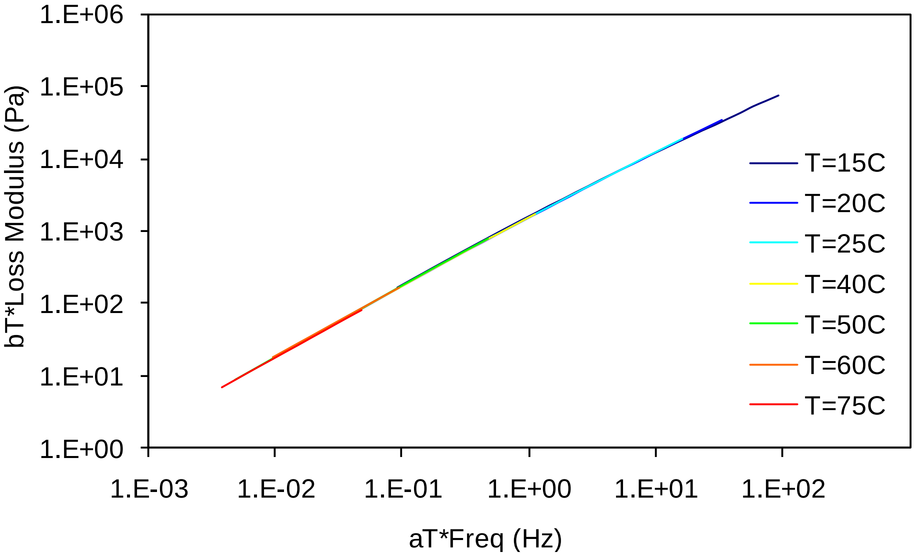

Figure 2.25b. Second step: shift factor b_T is computed by collapsing all the G” curves. A new G” is calculated.

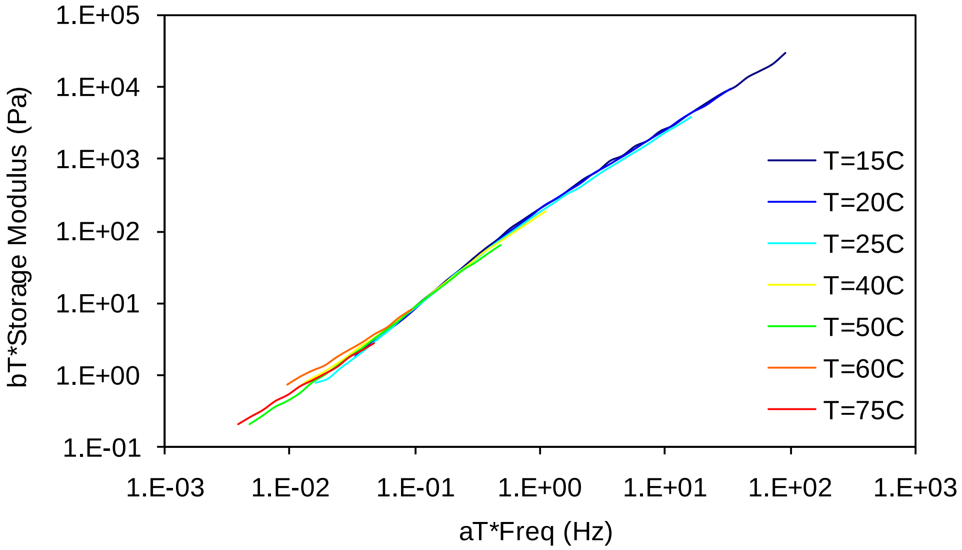

Figure 2.25c. Third step: shift factor b_T is computed by collapsing all the G' curves. A new G' is calculated.

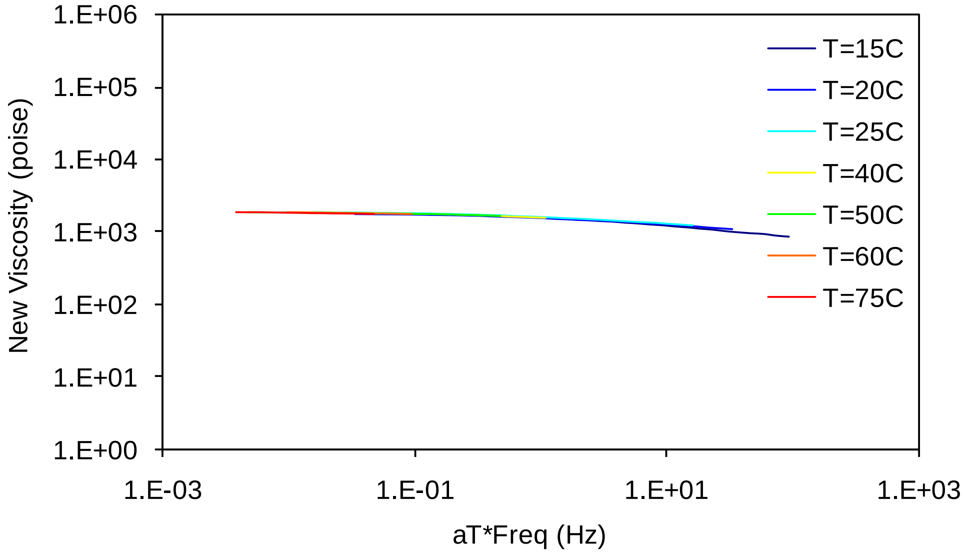

Figure 2.25d. Fourth step: the new G' and G" curves of each frequency scan are used to estimate G* and η* using equations 18 and 19. The shear thinning phenomenon is observed.

As a result of the Time Temperature Superposition Principle for G' and G" the original frequency range can be effectively increased by a factor of three. This range spans sonic and ultrasonic frequencies. For seismic frequencies, the effect of the viscous component is considerably higher than the elastic component for temperatures above 30°C, suggesting that heavy oil can be regarded as a Newtonian fluid (Figures 2.26, 2.27, 2.28, 2.29). For sonic frequencies, the Brazil heavy oil sample has a relatively small elastic component (Figure 2.28); the other heavy oil samples exhibit viscoelastic behavior.

Finally, for ultrasonic frequencies, the difference between G' and G" moduli is very small, and treatment of heavy oil as a non-Newtonian fluid should be considered.

In summary, for seismic, sonic and ultrasonic frequencies below 30°C frequency dispersion and attenuation become remarkably important. Above that temperature, G" increases significantly in comparison to G' (one order of magnitude approximately) and for seismic frequencies the Newtonian assumption might be valid.

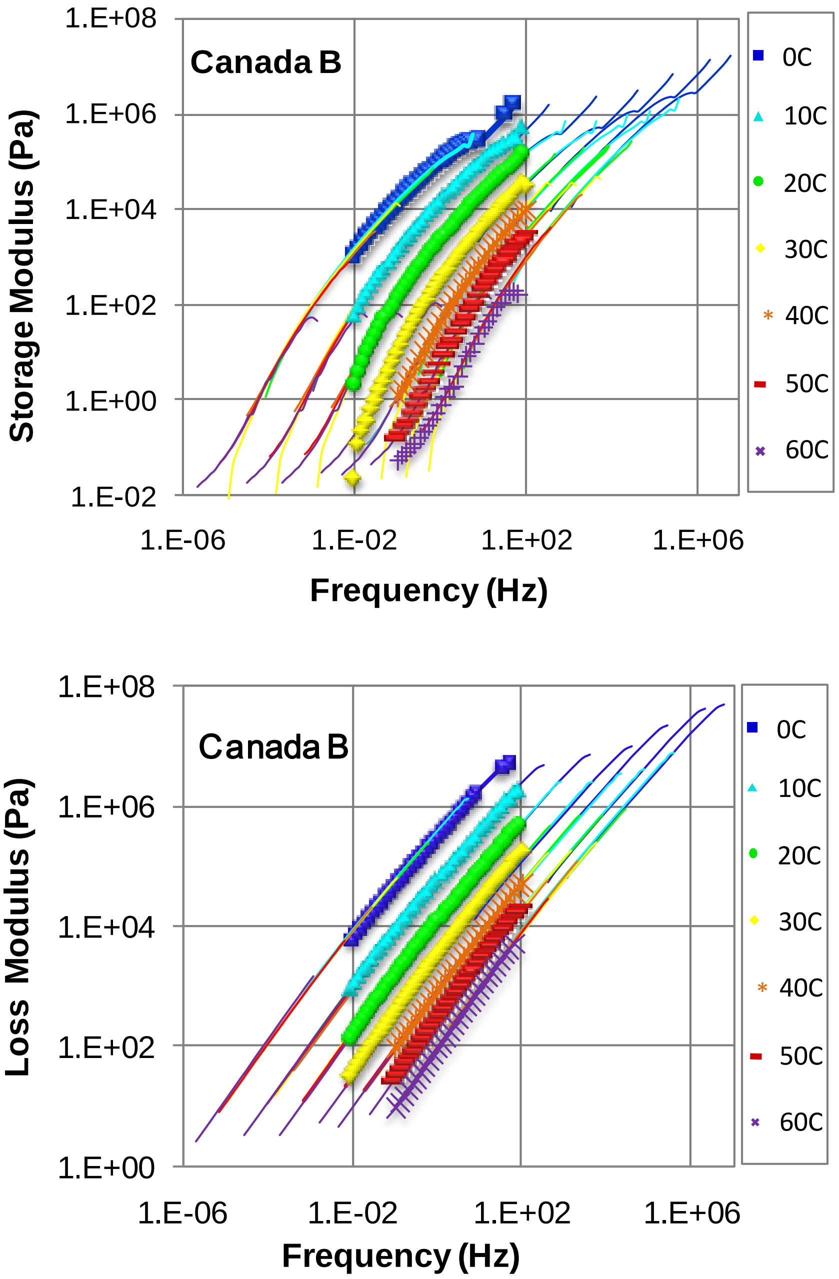

Figure 2.26. Loss and storage moduli versus frequency color code by temperature for Canada B oil sample. Data measured are represented by symbols and the result of the superposition for each temperature is illustrated by lines.

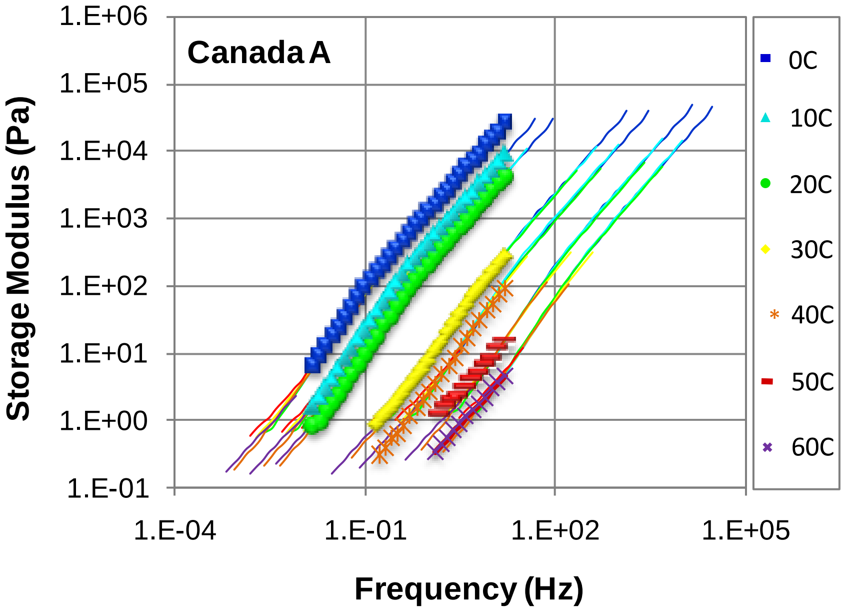

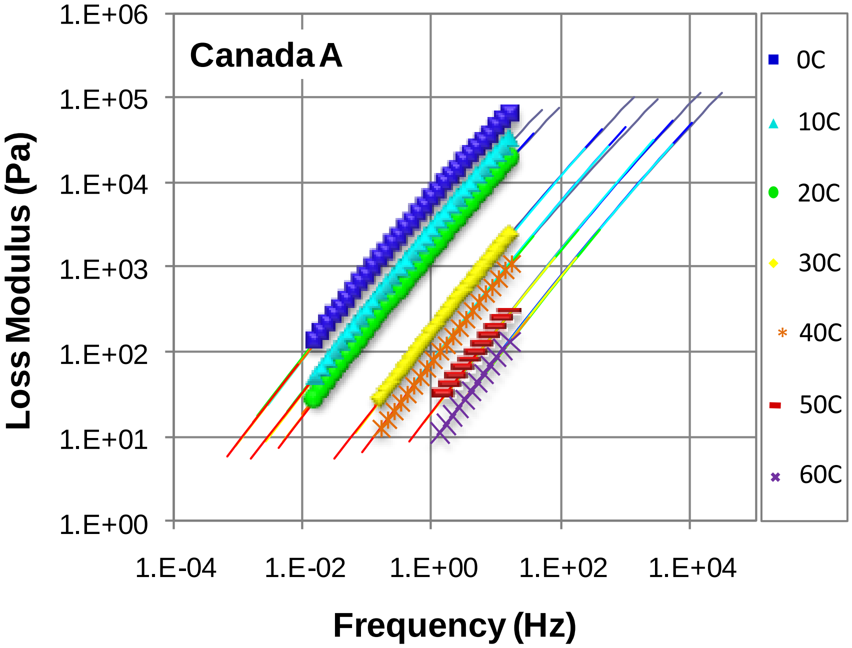

Figure 2.27. Loss and storage moduli versus frequency color code by temperature for Canada A oil sample. Data measured are represented by symbols and the result of the superposition for each temperature is illustrated by lines.

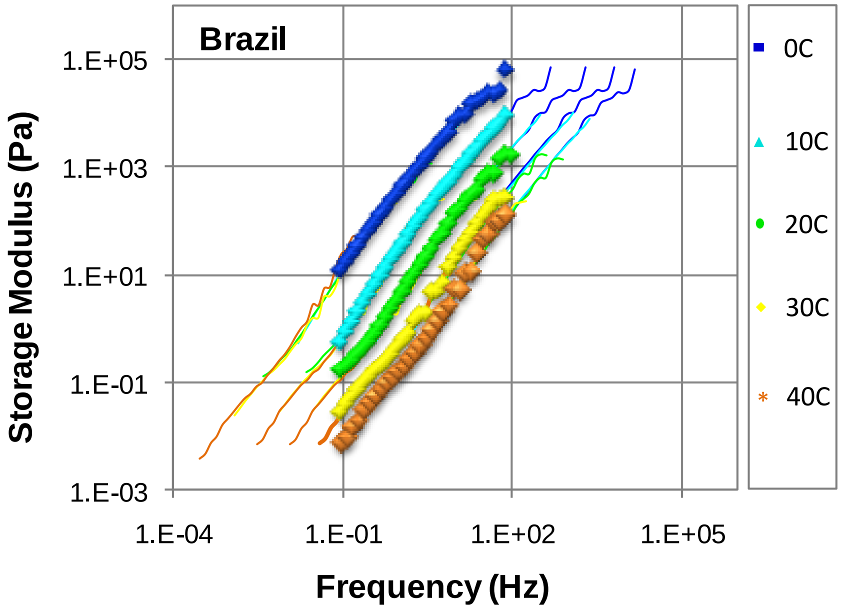

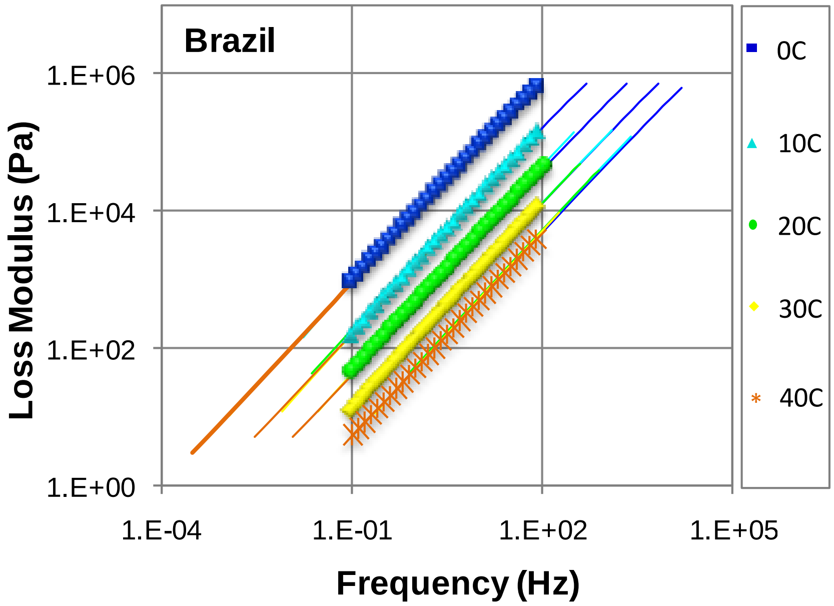

Figure 2.28. Loss and storage moduli versus frequency color code by temperature for Brazil oil sample. Data measured are represented by symbols and the result of the superposition for each temperature is illustrated by lines.

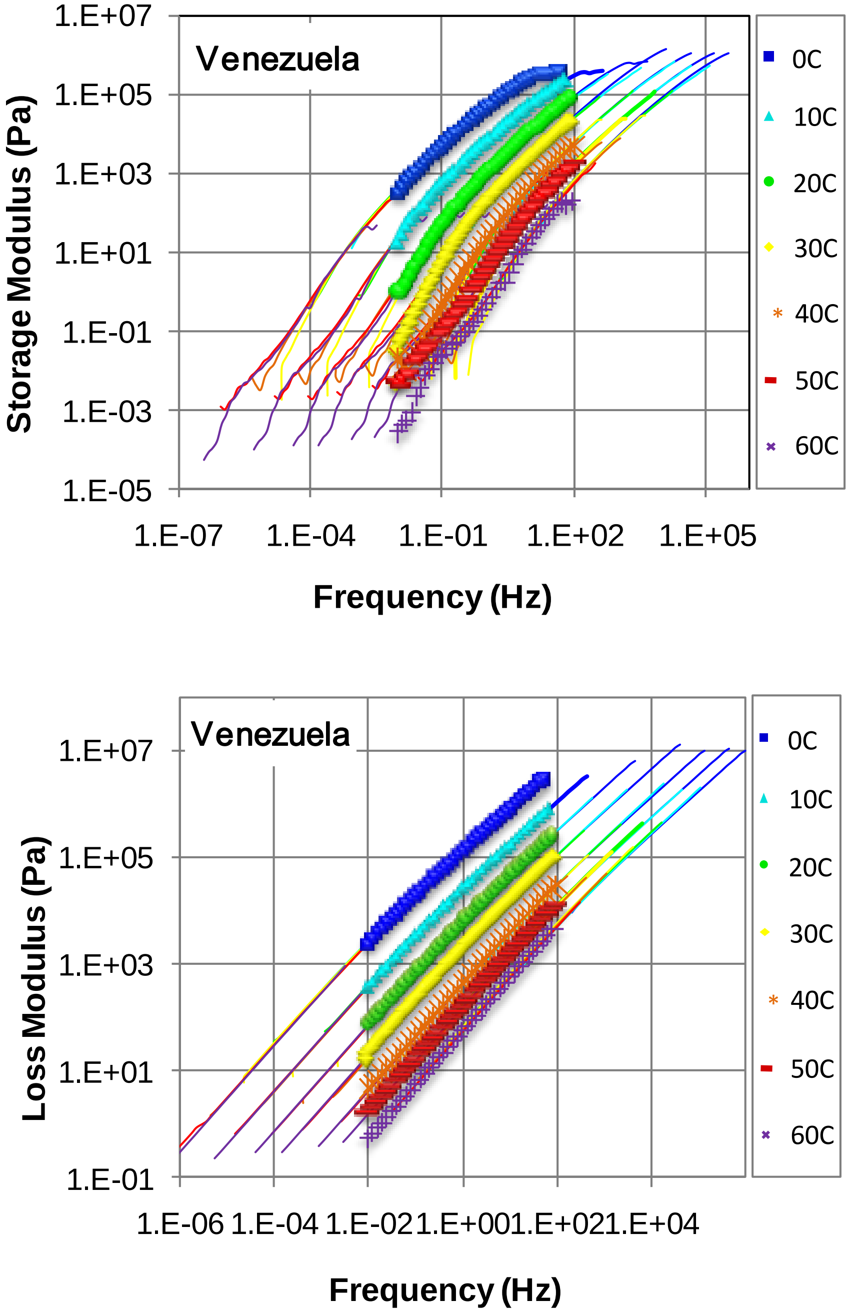

Figure 2.29. Loss and storage moduli versus frequency color code by temperature for Venezuela oil sample. Data measured are represented by symbols and the result of the superposition for each temperature is illustrated by lines.

The trend of G’ with frequency for different temperatures and for all samples shows similar relaxation time, although the theoretical plateau zones corresponding to very low frequency (viscous region) and very high frequency (elastic region) are absent (Figure 2.30).

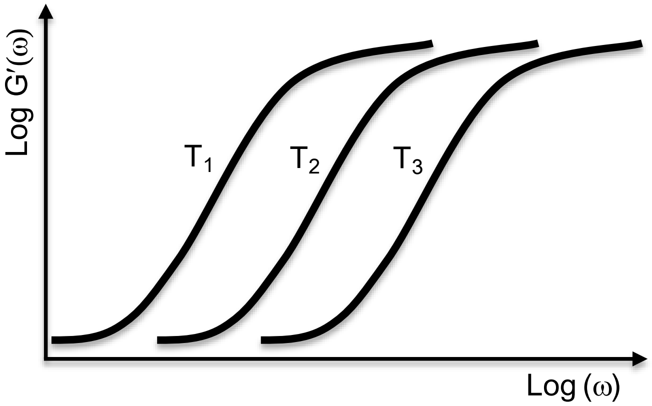

Figure 2.30. Temperature dependence of G’ as a function of frequency (from Christensen, 1971).

2.5 Modeling of Complex Viscosity (η*)

Understanding viscosity is important when dealing with simulation and optimization of reservoir production. In the literature, there are several approaches to model viscosity as a function of pressure, temperature, composition, and oil and gas gravity. However, the major problem is that the modeling becomes geographically dependent, it is mostly empirical and no standard method is available (Macias-Salinas et al., 2009).

On the other hand, the effect of temperature on the complex viscosity can be studied using Eyring's absolute rate reaction theory. This theory states that in order for a liquid molecule to move, the other surrounding molecules must move into the adjacent vacant sites to create space for the molecule to enter. To occupy the vacant space, the molecules must overcome a high potential energy region called activation energy E_a (Figure 2.31), which is symmetrical if there are no other sources in the system. Once the compound or molecules goes through the activated state, the next step is the formation of products. At a higher temperature, the molecules have higher thermal energy so they easily overcome the energy barrier and move into the adjacent vacant sites. The reaction depends not on one average internuclear distance but on all the distances (a and δ) between molecules that change as reactant molecules become into product molecules (Sadoway, 2009).

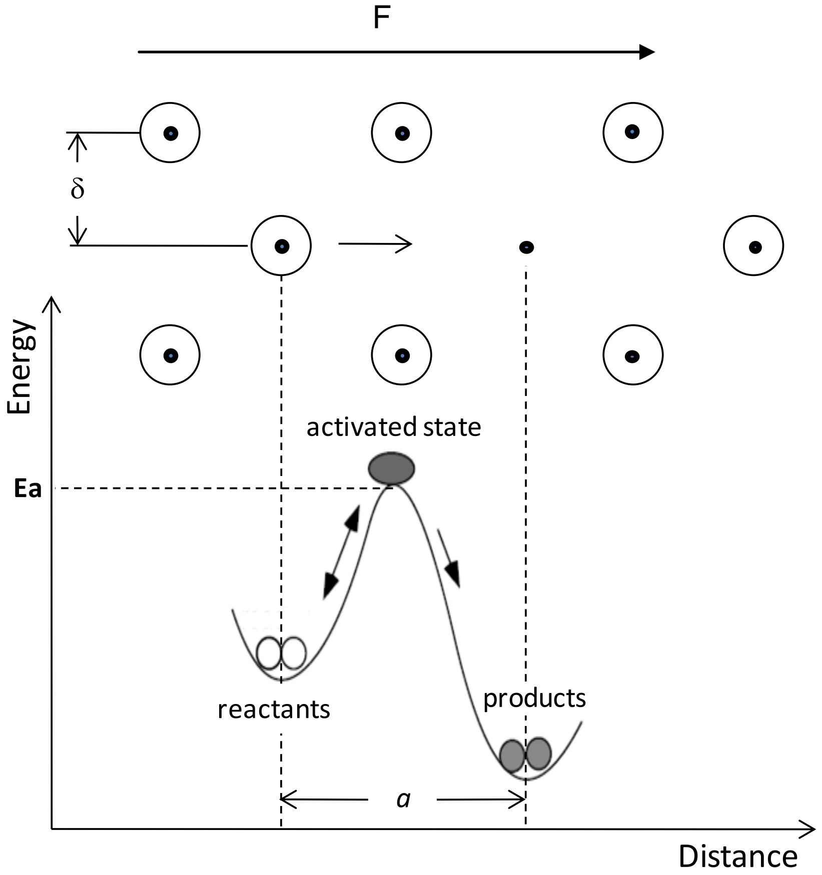

Figure 2.31. Diagram of a fluid showing the rate reaction process involved in a viscous flow. The molecule moves into an unoccupied space only if its energy is equal to the activation energy (Charm, 1962; Sadoway, 2009)

The activation energy parameter (Ea) controls the rate of molecular motion and therefore the flow of the liquids (Fan et al., 2003). The reaction rate process can occur in the presence of an external force, F, which will move molecules in one plane with respect to another. The area associated with one molecule is 1/nδ. Therefore, the work done by the external force to move a molecule a distance a/2, assuming the activation state is midway between two lattice sites is:

$$W = \frac{1}{2}\frac{aF}{n\delta} \tag{33}$$

where δ is the distance between adjacent plane of molecules, a is the distance between lattice sites and n is the number of molecules. In fact, W is the amount by which the free energy of activation is changed. In the case an external force is present, the energy potential becomes distort in two ways: through the *forward* process, where the molecule moves into a space in the direction of the applied force or *reverse* process where the molecule moves to a space in an opposite direction of the applied force. The corresponding frequencies are K_f and K_r; therefore the net velocity of the flow in the direction of the applied force is (Charm, 1962):

$$V = a\left(K_f - K_r\right) \tag{34}$$

The following derivation was based on Charm (1962):

$$K_f = K_0 exp\left(\frac{aF}{2\delta nkt}\right) \tag{35}$$
$$K_r = K_0 exp\left(-\frac{aF}{2\delta nkt}\right)$$

where K_0 will be the same as K_f or K_r if no external force is present.

Substituting equation (35) into the equation for the velocity of the net flow (34), it is possible to obtain the velocity of flow of one layer over the next one:

$$V = aK_0\left[exp\left(\frac{aF}{2\delta nkT}\right) - exp\left(-\frac{aF}{2\delta nkT}\right)\right] \tag{36}$$

which is similar to

$$V = 2aK_0\left[sinh\left(\frac{aF}{2\delta nkT}\right)\right] \tag{37}$$

The hyperbolic sine can be expressed as a Maclaurin series:

$$\sinh X = X + \frac{X^2}{3!} + \frac{X^5}{5!} \cdots \tag{38}$$

Assuming small external forces, we can substitute only for the first term:

$$V = 2aK_0 \frac{aF}{2\delta nkT} \tag{39}$$

The viscosity can then be defined as the ratio of the force per unit area to the velocity gradient between layers:

$$\eta = \frac{F}{V/_{\delta}} \tag{40}$$

$$\eta = \left(\frac{\delta}{a}\right)^2 \frac{nkT}{K_0}$$

Assuming that the frequencies follow an Arrhenius type expression (Charm, 1962):

$$K = \frac{kT}{h} exp\left(-\frac{E}{RT}\right) \tag{41}$$

where E is the activation energy, R the gas constant, k is the Boltzmann constant, h is the Planck's constant and T is the absolute temperature. Then substituting equation 40 into equation 41, we have:

$$\eta = \left(\frac{\delta}{a}\right)^2 nh\, exp\left(\frac{E}{RT}\right) \tag{42}$$

which can also be expressed as:

$$\eta = \left(\frac{\delta}{a}\right)^2 \frac{Nh}{V} exp\left(\frac{E}{RT}\right) \tag{43}$$

where N is the Avogadro constant and V is the liquid molar volume.

The above expression was proposed by Eyring and others (1941) for a Newtonian fluid since viscosity is independent of force. In Non-Newtonian flow, the applied forces are very high and we need to include more terms of the Maclaurin series when substituting the hyperbolic sine. The equation can be further simplified by assuming δ/a equal to one with no loss of accuracy (Macias-Salinas et al., 2009).

This theory is very similar to the Arrhenius' equation, and both describe the temperature dependence of reaction rate. However, Arrhenius' is applied for gas reactions whereas Eyring's equation for fluids and mixed-phase reactions. Another main difference is the latter is based on the transition state theory while Arrhenius equation was developed empirically.

Other models that use the absolute rate reaction theory to describe viscous flow are:

- **Vogel-Fulcher-Tammann**

This model correlates viscosity and temperature for glass melts, especially, for those usually called "fragile". These materials show an abrupt fall of viscosity when heated, suggesting that the structure collapses rapidly. Usually only three pairs of viscosity and temperature are needed to determine the three unknowns: A, B, and T_G:

$$\eta = A\, exp\left(\frac{B}{T - T_G}\right) \tag{44}$$

where A and B are constants of the material and T_G is the temperature at the glass point. Generally these constants are not applicable over a wide range of temperatures (Avramov, 2005).

- **Adams and Gibbs Model**

Their approach assumes that when the free volume is reduced in the vicinity of the glass transition, the motion of the viscous flow or relaxation dynamics depends on the “simultaneous rearrangement of independent regions of molecules” (Avramov, 2005). Since they are independent from each other, it is possible to describe them as a many-body problem using statistic mechanics (Leuzzi and Nieuwenhuizen, 2007). Based on this model, the relaxation time of the fluid depends on the configurational entropy, which refers to the different positions that molecules can have in the system. As temperature increases, the molecules have more “free volume” or space, therefore entropy increases (Dyre et al., 2009).

$$\eta = A\, exp\left(\frac{B}{TS}\right) \tag{45}$$

where A and B are positive constants depending on the material and S is the molar configurational entropy.

Both models are very similar to the Eyring’s equation; however, it is necessary to investigate if activation energy is independent of temperature for our heavy oil samples. Activation energy (E_a) is independent of temperature if only one relaxation time exists for the range of temperature studied; evidently, in the vicinity of the glass transition, E_a will depend on temperature. One simple way to estimate the activation energy and its dependence with temperature is to modify the Eyring’s equation by taking the natural logarithm of each side of the equation to get a linear relationship between viscosity and temperature, as follows:

$$ln\eta = lnA + \left(\frac{E}{R}\right)\frac{1}{T} \tag{46}$$

By obtaining a linear trend, the activation energy for each frequency can be estimated and it can be proven that the heavy oil samples follow an Arrhenius or Eyring's behavior, meaning that activation energy is independent of temperature.

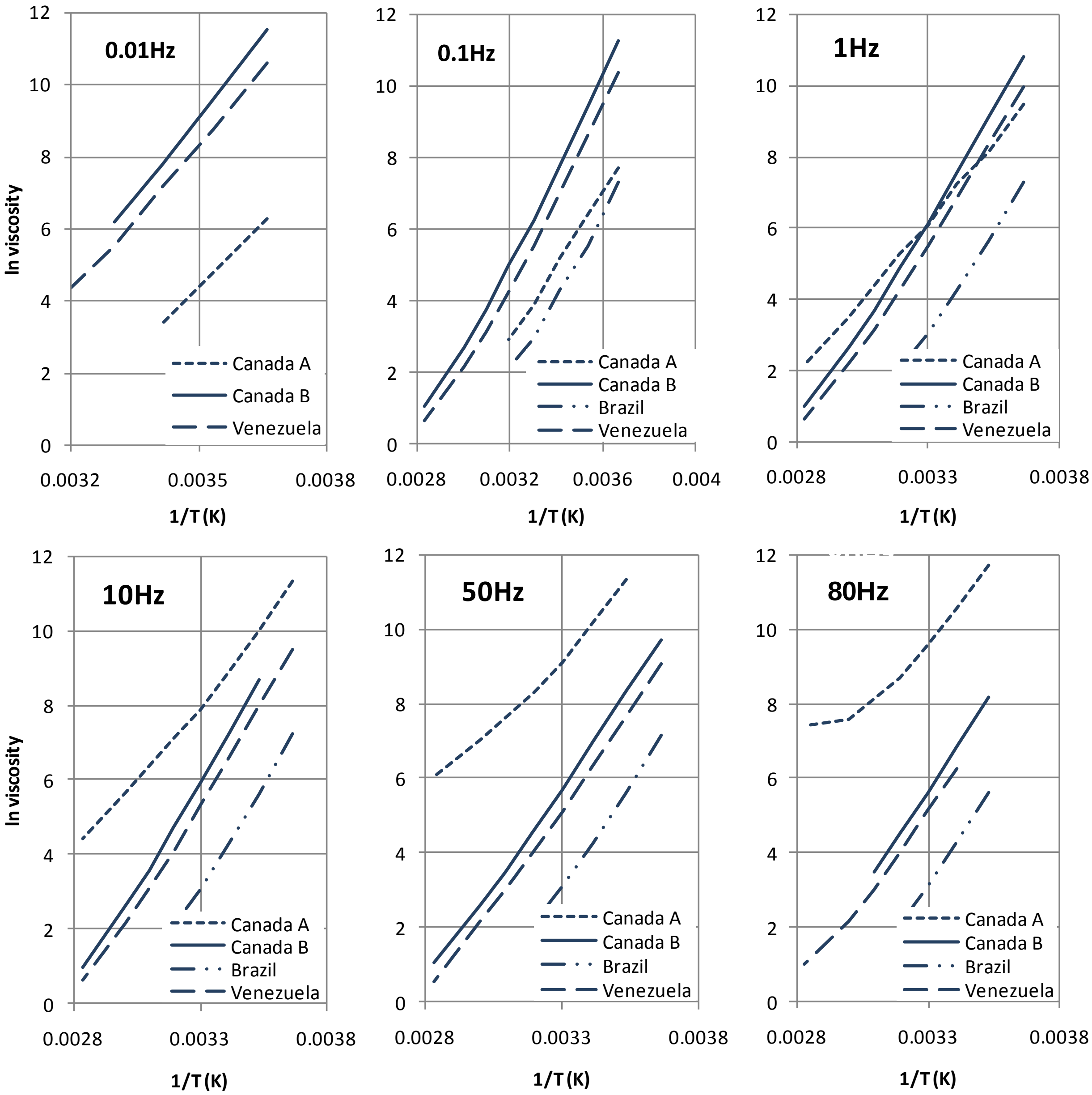

Figure 2.32. Viscosity versus temperature in Arrhenius coordinates at several frequencies for all the heavy oil samples investigated in this study.

The logarithms of viscosity as a function of the inverse of the absolute temperature given in Kelvin degrees for all heavy oil samples at six different frequencies are shown in Figure 2.32. The Canada B and Brazil heavy oil samples exhibit a linear trend between viscosity and temperature at all frequencies with a correlation coefficient greater than 0.99. The activation energy for both of these samples approximately varies between 1250J/mol (high frequency) and 1800J/mol (low frequency).

The Venezuela heavy oil sample exhibits a linear trend at all frequencies except for the measurements made at 80 Hz. Here, a subtle inflection point can be observed between 40°C and 50°C, which indicates a drop in the activation energy of approximately 20%, possibly correlated with the presence of the liquid point. However, assuming that E_a is independent of temperature (linear fit), the corresponding correlation coefficient will be about 0.992.

Lastly, Canada A heavy oil sample exhibits one activation energy for frequencies between 0.01Hz to 10Hz while at 50 Hz and 80 Hz more than one activation energy is observed for the rate reaction process. At 50 Hz, the energy barrier drops by 30%.The correlation coefficient is about 0.989 (Table 2.5). At 80 Hz there are three energy barriers for the temperature range studied: from 10°C to 40°C, from 40°C to 60°C, and from 60°C to 80°C. The corresponding activation energies are: 1080 J/mol, 690 J/mol and 122 J/mol, respectively. Fitting all measurements with a linear equation, the correlation coefficient becomes 0.938 which is sufficiently high to assume a single activation energy for the range of temperatures studied (Table 2.5).

In summary, as frequency increases, not only the energy barrier between reactants and products (activation energy) decreases, but also more than one activation energy is observed, which means that energy barriers of different height appear. According to Avramov (2005) the distribution function of energy barriers is intrinsically correlated to entropy of the system, which it is assumed to increase as frequency increases. However, for an amorphous system as the one present in heavy and extra-heavy oils, we should expect a broad distribution of activation energy heights.

Table 2.5. Activation energy (E_a) and correlation coefficient (R^2) estimated assuming a linear trend. In some cases, more than one activation energy was found based on the slope of the curve, in those cases, R^2 is equal to one.

Sample / Frequency	Canada A		Canada B		Brazil		Venezuela	
	Ea	R^2	Ea	R^2	Ea	R^2	Ea	R^2
0.01Hz	1384	1	1769	0.999	No data		1530	0.998
0.1Hz	1234	0.999	1497	0.996	1330	0.993	1424	0.994
1Hz	1060	0.999	1438	0.997	1339	0.997	1370	0.998
10Hz	989	0.995	1330	0.998	1332	0.998	1299	0.998
50Hz	898	0.989	1270	0.998	1310	0.998	1244	0.999
	1132	1						
	746	1						
80Hz	759	0.938	1293	0.999	1254	0.999	1107	0.992
	1080	1					1250	1
	691	1					905	1
	123	1						

Previously, we have dealt with the relationship between viscosity and temperature, mainly through the absolute rate reaction theory. However, frequency as well as temperature needs to be taken into account when estimating viscosity of viscoelastic fluids.

Solving the constitutive equations for viscoelastic fluids can be challenging since mechanical and transfer equations need to be solved simultaneously (Ferry, 1980). However, there are several models that can be used to correlate complex viscosity and frequency. One of them is called the Power-Law model (Ferry, 1980; Barnes et al., 1989; Aklonis and MacKnight, 1983) and it is strictly used for materials showing shear thinning. The equation for complex viscosity is:

$$\eta *= K\dot{\gamma}^{n-1} \tag{47}$$

where K is a constant, γ is the shear strain, and n is the Power–Law index.

Combining the rate reaction theory and the Power-Law model, a new model to relate complex viscosity, frequency and temperature for the quasi-solid or transition phase is derived, which is bounded by the glass point temperature (T_G) and the temperature at which we jump into the isotropic or fluid phase (T_I) and where viscoelastic behavior disappears:

$$\eta^{*} = K\omega^{n-1} exp\left[\frac{E}{R}\left(\frac{1}{T_G - T} + \frac{1}{T_I - T}\right)\right] \tag{48}$$

When modifying the Eyring's equation, it was important not only to include the frequency effect but also to properly model the significant drop on viscosity with each temperature scan characteristic of heavy oils, which was achieved by using the two terms inside of the brackets.

Using the least squares method, we proceed to calculate E, K, and n for each of the samples based on the complex viscosity, frequency and temperature data. The power-law index (n) varies between 0 and 1 for shear thinning fluids and measures the slope of the viscosity curve with respect to frequency (shear strain rate).

The non-linear fitting between the actual complex viscosity measurements and the result given by equation 48 was evaluated using the correlation coefficient (R^2), which is a statistical measure of how well the regression line fits the actual data points. Unfortunately, R^2 does not tell whether the correct regression was used or if the model can be improved by using different arrangements of independent variables.

Table 2.6. Inversion results of the complex viscosity equation. T_G represent the best fit obtained, which is very similar to the values obtained through DSC measurements ($T_{G\text{-}DSC}$). No data were obtained for $T_{G\text{-}DSC}$ in the case of Canada B heavy oil sample.

	Constant K	Activation energy E_A	$T_{G\text{-}DSC}$ (K)	T_G (K)	T_I (K)	R^2
Brazil	20.680 ± 0.413	2381.491 ± 11.205	232	232	378	0.999
Venezuela	101.151 ± 7.782	3179.391 ± 43.219	228	228	393	0.994
Canada A	18.390 ± 1.578	3130.765 ± 55.333	220	223	413	0.993
Canada B	53.483 ± 7.010	4280.823 ± 80.252		223	418	0.992

The inversion results for each sample corresponding to the activation energy (E_A), constant K, T_G, T_I, and the correlation coefficient (R^2) are shown in Table 2.6. The values shown below corresponding to T_G and T_I are the best fit found for each sample; however, the values of T_G are very similar to those obtained through the DSC measurements. The values of E_A, T_G, and T_I seem to follow a direct correlation with the density of the sample. Then, the lowest values registered correspond to Brazil heavy oil sample. In Figure 33, the relationship between activation energy and density of the sample is shown. Equation 48 fits very well our measurements with a correlation coefficient (R^2) above 0.99.

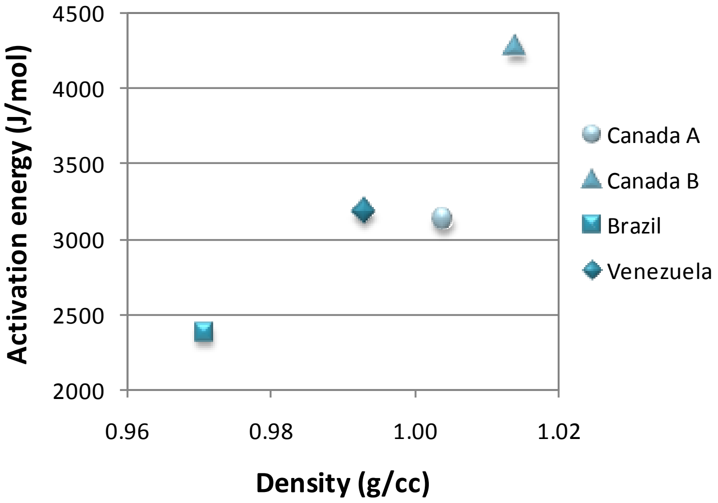

Figure 2.33. Activation energy versus oil density for heavy oil samples used in this study. Canada A heavy oil sample deviates from the linear correlation.

Equation 48 fails to properly predict complex viscosity for temperatures above 60°C since the shear thinning effect is very small (Figures 2.34-2.37). Canada A heavy oil sample exhibits the highest power-law index and therefore the highest variability in viscosity for each temperature. In fact, n varies approximately between 0.8 and 1 for all the samples. Error bars were calculated based on the standard deviation of the data for each temperature.

In summary, this equation proves to be useful to explain the effect of temperature and frequency on the estimation of viscosity. Basically, four parameters are needed: E_A, K, T_G, and T_I. Among these four parameters, T_G and T_I are very sensitive to the estimation of complex viscosity (Figure 2.38). For example, changing only T_I will affect the viscosity estimations mostly at high temperatures while changing only T_G will affect estimations mostly at the lowest temperatures (high viscosity).

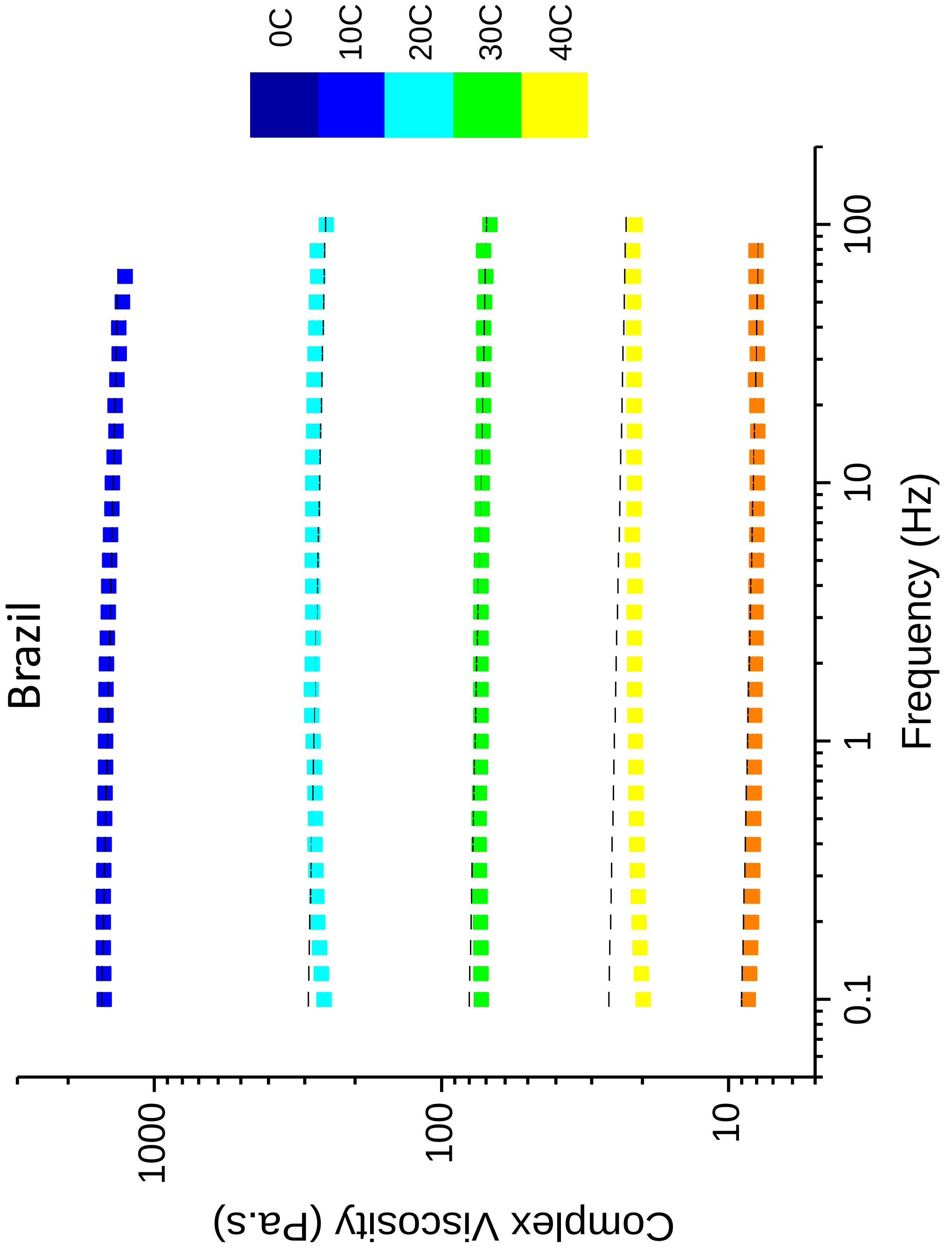

Figure 2.34. Complex viscosity as a function of frequency obtained using the inversion method for Brazil heavy oil sample. Error bars (too small to be observed) are calculated based on the standard deviation of the data for each temperature.

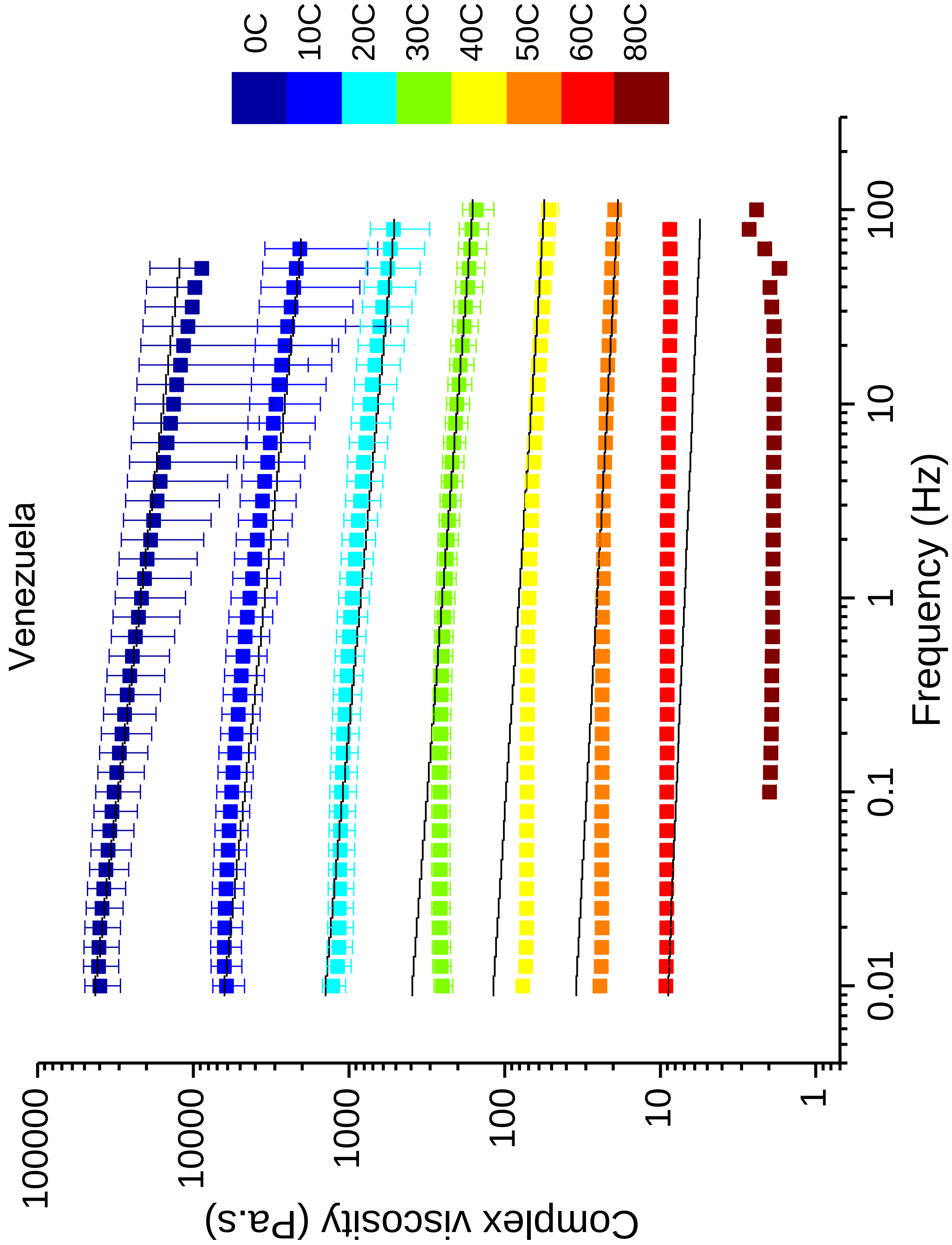

Figure 2.35. Complex viscosity as a function of frequency obtained using the inversion method for Venezuela heavy oil sample. Error bars are calculated based on the standard deviation of the data for each temperature.

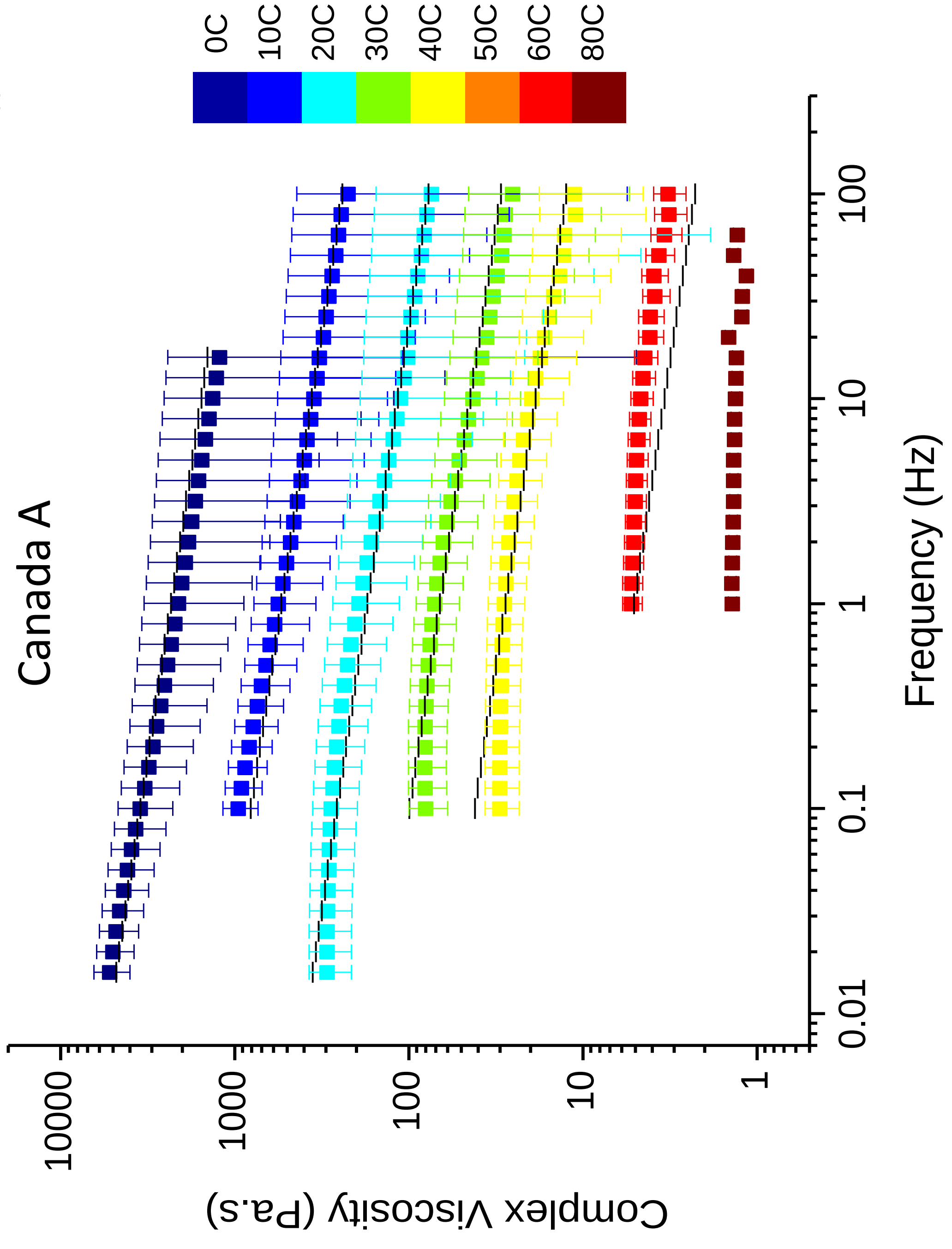

Figure 2.36: Complex viscosity as a function of frequency obtained using the inversion method for Canada A heavy oil sample. Error bars are calculated based on the standard deviation of the data for each temperature.

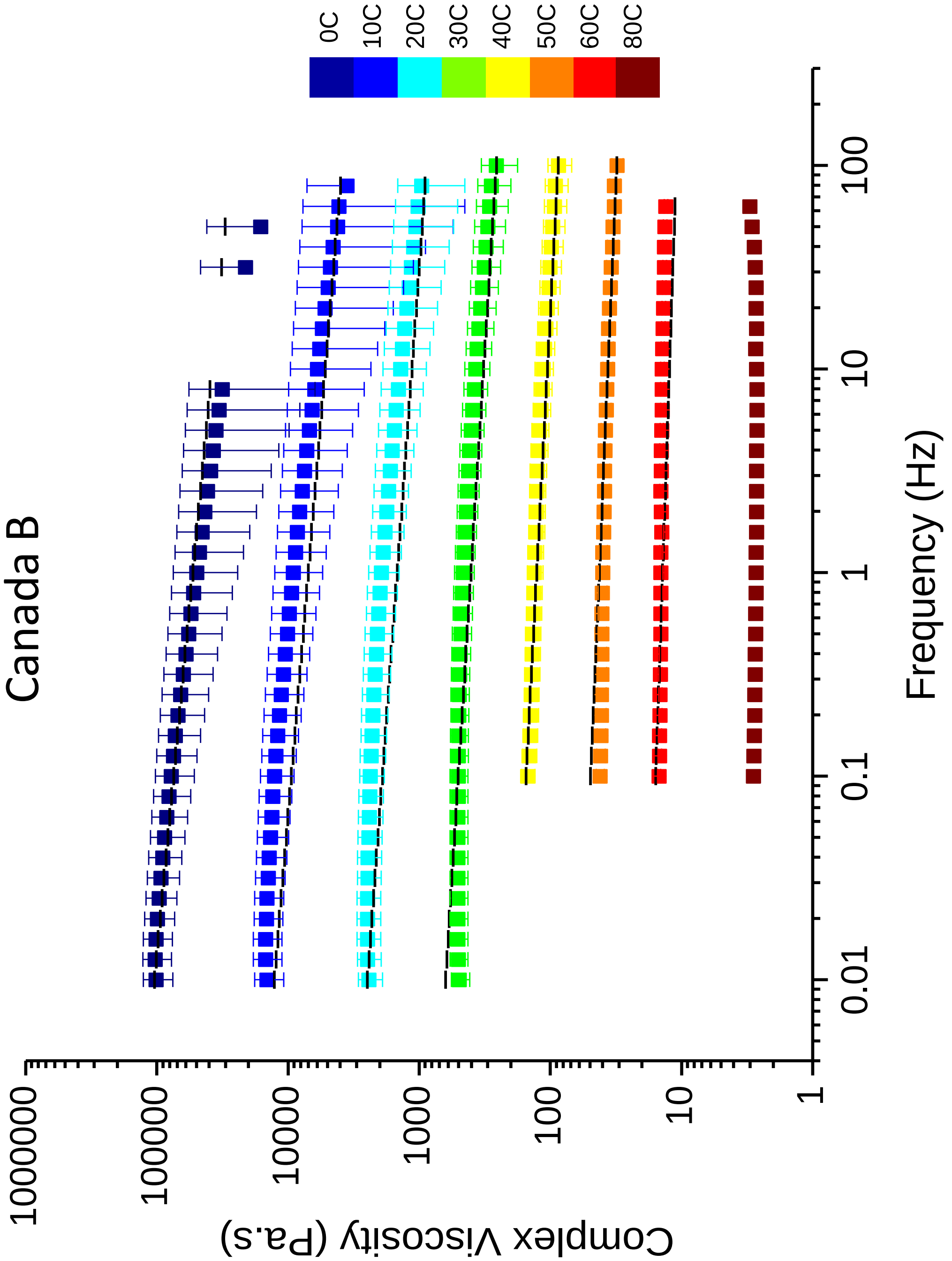

Figure 2.37: Complex viscosity as a function of frequency obtained using the inversion method for Canada B heavy oil sample. Error bars are calculated based on the standard deviation of the data for each temperature.

The constant K is the most insensitive parameter among all of them and changing it affects viscosities at different temperatures in the same manner. A 30% change in K is comparable with a 2% change in T_G or T_I. A change in E_a affects the measurements in the same way as T_G; however a change of 15% in E_a is equivalent to a 2% change on T_G (Figure 2.39). Finally, a change of 25% in *n* is shown in Figure 2.40.

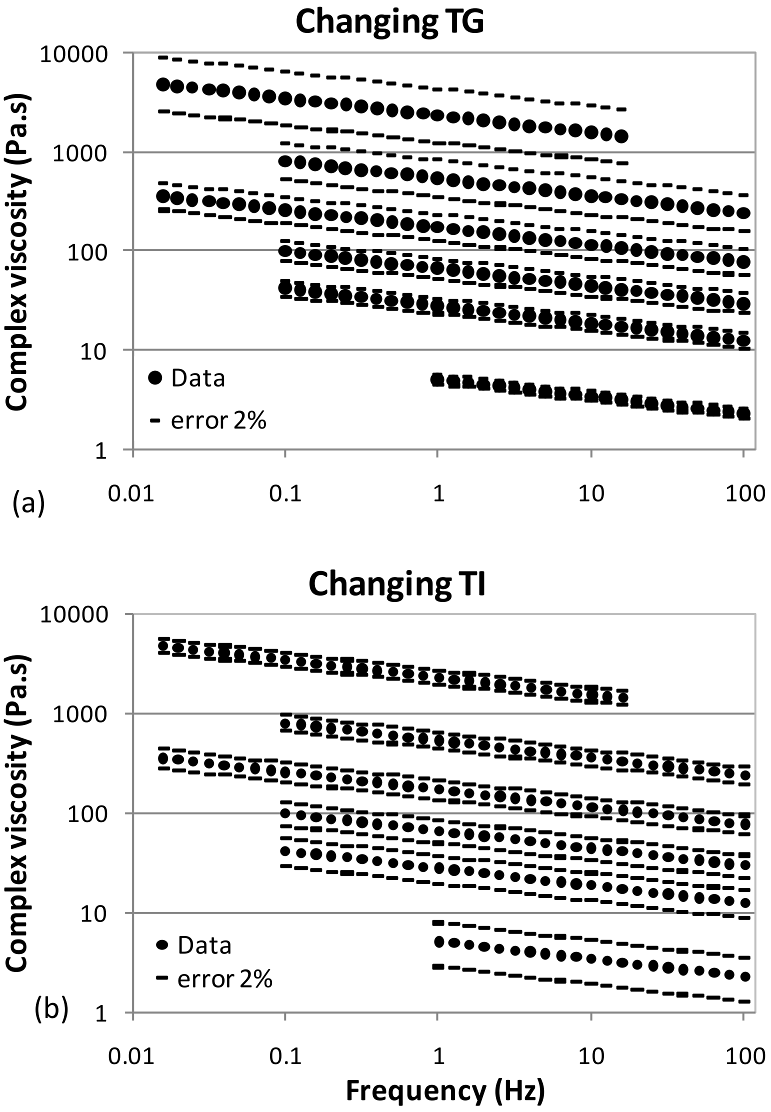

Figure 2.38: Effect of changing T_G (a) and T_I (b) values by 2% on complex viscosity. Actual measurements are denoted by the black circles.

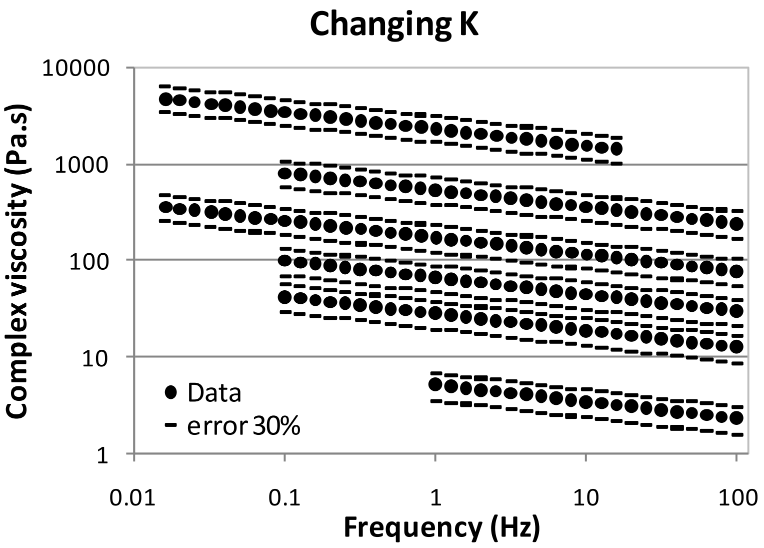

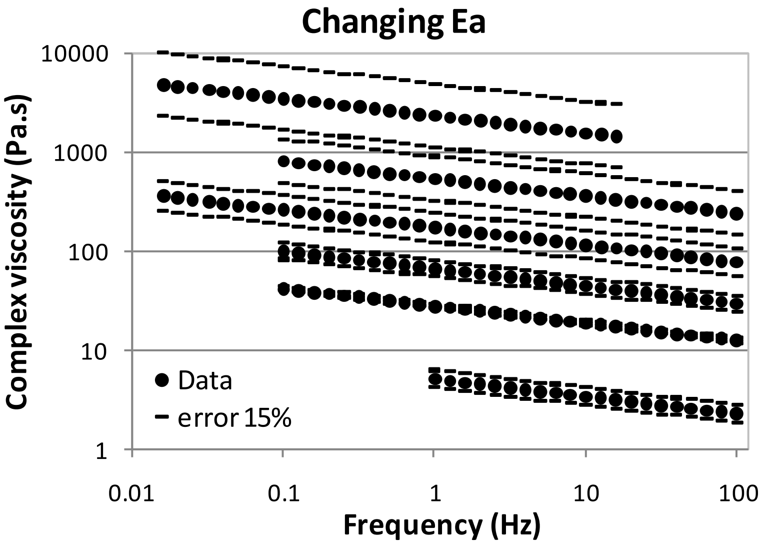

Figure 2.39: Effect of changing K (a) by 30% and E_a (b) by 15% on complex viscosity. Actual measurements are denoted by black circles. Changes in K affect all viscosities in the same way. Changes in E_a have a bigger effect on the viscosities estimated at low temperatures.

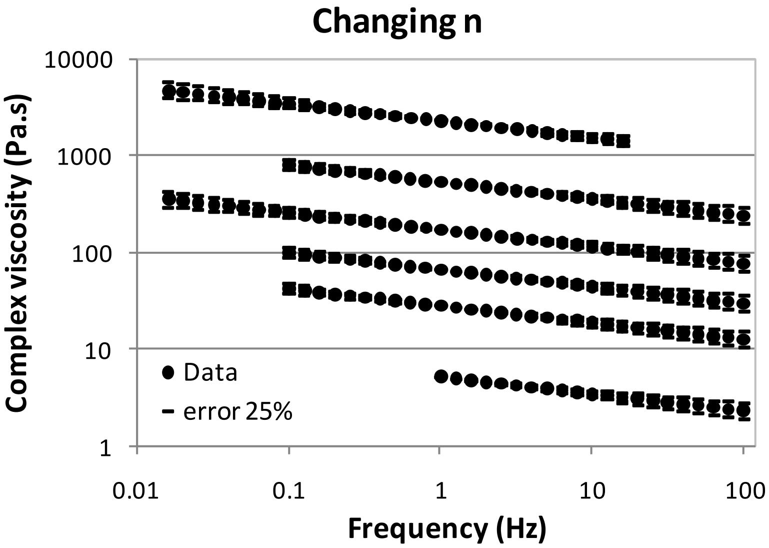

Figure 2.40: Effect of changing *n* by 25% on complex viscosity. Actual measurements are denoted by black circles. Changes in *n* do not affect significantly the viscosity, but slightly changes the slope of the curve (shear thinning phenomenon).

Part 3

Frequency Dispersion in Viscoelastic Media: Analysis of Low- and High-Frequency Measurements.

Frequency dispersion models describe and predict the variation on the elastic moduli with frequency; a typical phenomenon of viscoelastic fluids such as heavy oils. These models help to analyze the link between the low-frequency (rheological) measurements described in Part 1, and ultrasonic acoustic measurements where shear velocity and density were measured for Venezuela, Canada B, Canada A, and Brazil heavy oil samples.

Analysis of the results derived from the low-frequency and ultrasonic measurements, presents a similar challenge as analyzing static-based and dynamic-based experiments. Rock properties measured with each experiment will be greatly influenced by the characteristics of the experiment like strain amplitude and frequency; therefore, at the beginning of this section, a review of the literature will discuss static – dynamic difference in terms of how different properties such as fluid saturation, velocity/modulus, quality factor/attenuation, etc. vary according to the experiment.

Theoretically, through the Kramers – Kronig relations, it can be proven that attenuation is accompanied by frequency velocity dispersion and different models will be used in order to determine the most suitable model to describe the rheological measurements. However, it will also be shown that shear modulus dispersion does not only depend on frequency but is also evident when strain and viscosity are varied.

Finally, in this study, a rock physics model will be developed to account for the frequency dispersion observed in the shear modulus resulting from low frequency and ultrasonic measurements. Also, a simple model will be used to model attenuation variation with frequency.

3.1 Static versus Dynamic Moduli

Deformation of a sample under compression or tension as in loading and unloading is typically measured in a *static experiment* measures and it is typically considered an isothermal process. This experiment usually refers to an open system, meaning fluids in the rock can flow freely in and out of the rock. On the other hand, elastic wave velocities, with no exchange of heat in the system (adiabatic), are measured in *dynamic experiments*.

Generally, the modulus of elasticity is represented as the slope of a stress-strain plot. The modulus (static or dynamic) is given by the tangent of the stress-strain curve. Typically, it is calculated by the secant line that joins point zero with a certain point of the curve (i.e. the highest unloading cycle) (Figure 3.1).

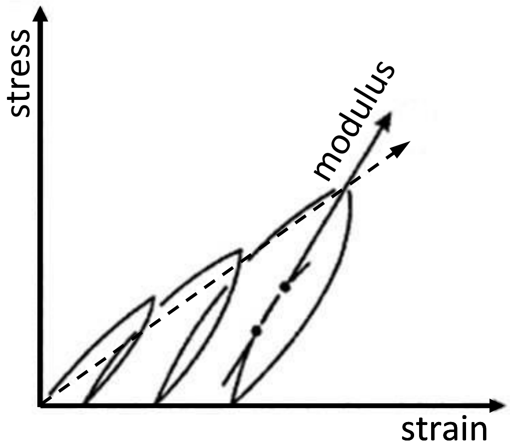

Figure 3.1. Stress versus strain plot. Both slopes (continuous or dashed line) can be used to calculate static and dynamic moduli. The difference is the level of strain, static measurements typically have larger strains and dynamic measurements have smaller strains (Barton, 2007; Tutuncu, 2010 personal communication).

In order to properly compare both experiments, a triaxial stress condition is usually recommended (Hongkui et al., 2001). In experiments involving rocks, the adiabatic/isothermal difference is generally not taken into account because the difference accounts for only 1% or 2% of the moduli difference; however, for fluids this difference is significantly more important.

The inherent or intrinsic cause of static/dynamic difference in rocks is the presence of heterogeneities (pores, cracks) and presence of fluids (Ide, 1936; Hongkui et al., 2001). In the static case, the large strain amplitude applied to the grain boundaries causes friction or sliding, which softens the rock and converts seismic energy into heat (Winkler et al., 1979; Hongkui et al., 2001). In fact, tests on common homogeneous elastic materials give similar values (less than 1% – 2%) for static and dynamic moduli (Ide, 1936; Barton, 2007). Generally, the dynamic estimated moduli are larger than the static moduli and both are linearly correlated.

Another difference between static and dynamic experiments lie in the frequency of the measurements, in other words, it depends on the time that the pore fluid needs to flow in and out of the system to remain pressure equilibrated. For instance, if the time span is very small, like in dynamic experiments, then the pore fluid has no time to escape registering higher velocities and moduli; this is defined as a closed system or undrained. However, if the pore fluid has enough time to equilibrate as in static experiments (low pore pressure), we called it an open system or drained. The definition of closed vs. open system was used by Gassmann (1951) to illustrate the difference between static and dynamic experiments (Wang, 2000).

In terms of strain amplitude, we can also discriminate between both types of experiments. When an acoustic wave propagates through a porous medium the deformation is low enough (approximately 10^{-6}m) to assume to be elastic. However, the static experiment usually requires large strains creating a non-elastic deformation of the sample (approx. 10^{-2}m).

Other studies (Hilbert et al., 1994; Plona and Cook, 1995) have shown that both types of measurements at the same frequency but at different strain amplitudes for dry rocks result in similar values for both static and dynamic moduli. However, Wilson (1985) showed that for water saturated sands, there is a small difference on the moduli estimated through static (0.001Hz) and dynamic tests (20 -110Hz).

Finally, the static/dynamic difference responds to: (1) Presence of heterogeneities and fluid on the rock. (2) Characteristics of each experiment, namely: strain amplitude and frequency.

3.2 Attenuation

Seismic waves are attenuated when propagating through an anelastic medium, due to conversion of the energy into heat. Attenuation is the result of internal friction, dislocations, etc. It seems that the principal mechanism of attenuation for dry rocks is through friction between crack or grain surfaces (Knopoff, 1964, Walsh, 1966).

According to some laboratory studies (Johnston and Toksöz, 1980a), ultrasonic measurements usually provide higher attenuation values than those estimated by resonance techniques (low frequency). However, these techniques involve different strain amplitude which might be responsible for the difference on attenuation measurement (Johnston, 1981).

For years, Q has been regarded as constant; especially for dry rocks (Knopoff, 1964; Gordon and Davis, 1968; Johnston, 1981; Toksöz et al., 1979). However, laboratory measurements have shown that there is a frequency effect for fluid saturated rocks involving viscous fluids, and even for vacuum-dry rocks (Winkler et al., 1979). In the following sections, a review of the principal factors affecting Q is presented. Table 3.1 shows some general values for compressional quality factor.

Table 3.1. Examples of Q for longitudinal or bending excitation of various solids sorted by magnitude (Barton, 2007). These values will depend on frequency and strain amplitude of the experiments among other factors. Unfortunately, they are not available for this dataset.

Material	Q_{seis}
Steel	5000
Copper	2140
Silica	1250
Glass	490
Diorite	125
Limestone	110
Lead	36
Sandstone	21
Shale	10
Celluloid	7

3.2.1 Strain Amplitude

Several studies (Knopoff, 1964; McKavanagh and Stacey, 1974; Stacey et al., 1975; Winkler et al., 1979; Stewart et al., 1983) have shown that attenuation is not only independent of frequency and strain amplitude for dry rocks but also nearly constant if strains are lower than approximately 10^{-6}. It is important to realize that this applies for solid materials since for fluids, attenuation is frequency dependent. For large strain amplitude (higher than 10^{-6}) the evidence of friction or sliding displacement in the grain boundaries appears causing a softening on the rock and converting seismic energy into heat (Winkler et al., 1979; Hongkui et al., 2001; Tutuncu et al., 1998a,b; Tutuncu and Sharma, 1992). Attenuation, as velocity, responds similarly in regards to its dependence with strain amplitude (Figure 3.2).

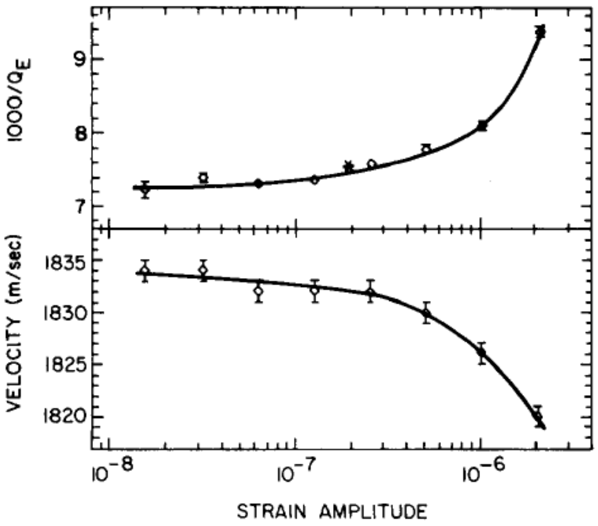

Figure 3.2. Attenuation and velocity vs. strain amplitude for dry sandstone. Winkler and Nur, 1982.

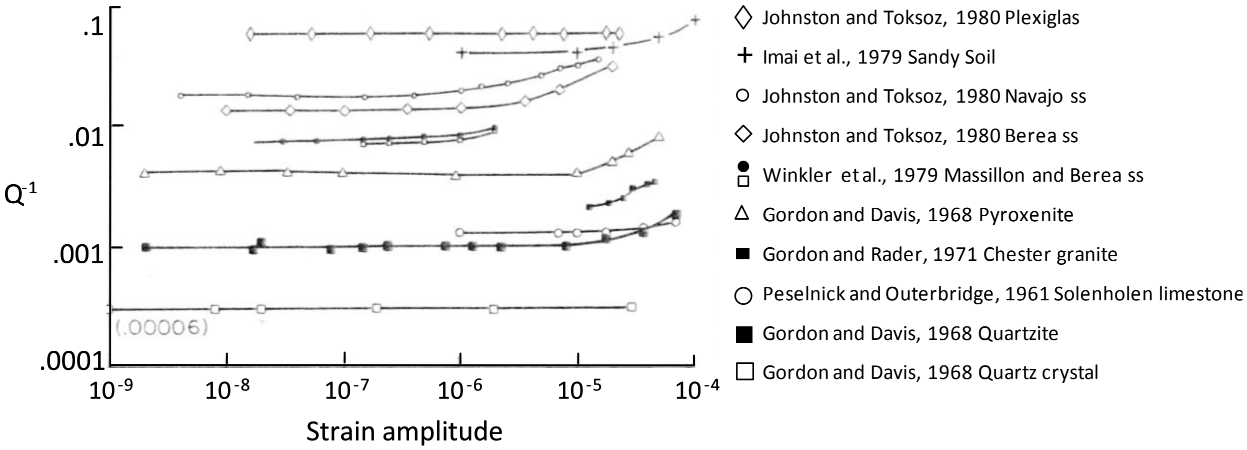

Figure 3.3. Different experiments of attenuation (P data) vs. strain amplitude. Stewart et al., 1983.

The approximate strain threshold mentioned above, results from many experiments analyzing the relation between attenuation (Q^{-1}) and strain amplitude (Figure 3.3). Winkler et al., (1979) explain that the displacement along the crack surfaces is about 10^{-8}cm, whereas the length of a crack, according to laboratory measurements, is about 10^{-2}cm (upper bound); therefore, a shear strain in the order of 10^{-6} seems to be a plausible number.

3.2.2 Fluid Saturation

Several authors (Knopoff, 1964; Nur and Winkler, 1980; Johnston and Toksöz, 1981) seem to agree that quality factor is commonly independent of frequency for homogeneous dry rock samples measured over a frequency range; however, the presence of fluid within the rocks will make attenuation frequency dependent.

Walsh (1966) explained that dry rocks suffer from attenuation when the seismic wave passes causing frictional dissipation between the crack surfaces. One of the observations that led to this was that for homogeneous materials like metals or even minerals, attenuation was significantly lower.

Johnston (1981) gave a review of how attenuation increases with the presence of volatiles (free of water) for dry rocks. Once water vapor is injected in the rock, the change in attenuation is significant. A similar approach with benzene did not provide the same result. Pandit and King (1979) showed that it is necessary to moisten the rock with several monolayers of water before observing bulk water effects; after reaching this point, the frequency dependence of attenuation was observed. Johnston (1981) explained that in some cases fluid saturated rocks might exhibit apparent constant attenuation for a certain frequency range due to superposition of flow relaxation times.

Pore fluids, such as water, change the friction between grain boundaries (Figure 3.4). In fact, only a small amount of water is needed to increase the attenuation significantly (Winkler et al., 1979). The inertial forces of the fluid (surface energy) in the microcracks will act against the energy of the passing wave, increasing attenuation mainly for ultrasonic frequencies. At lower frequencies, the squirt flow mechanism seems to be widely supported in the literature as the cause of attenuation. Scattering is another common phenomenon. For highly viscous pore fluids, viscous damping (relaxation process) clearly will vary attenuation with frequency.

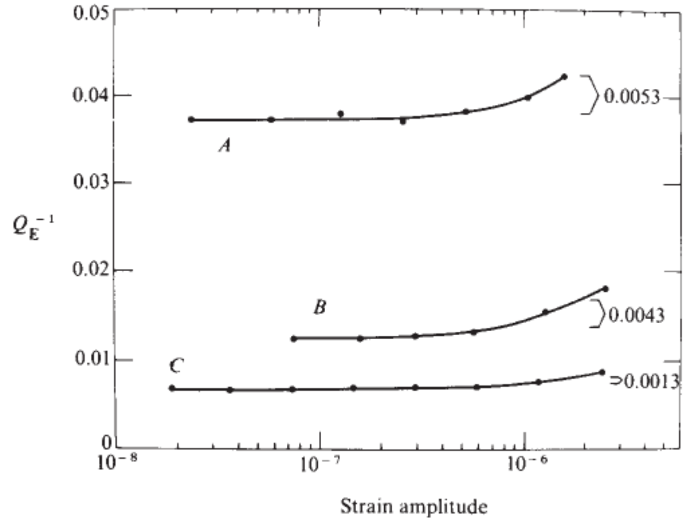

Figure 3.4. Attenuation versus strain amplitude for different degrees of saturation: A) saturated B) partially saturated C) dry. Winkler et al., 1979.

However, adding more water does not change the energy variation due to frictional effects (Winkler et al., 1979; Cadoret et al., 1998). However, Frisillo and Stewart (1980) showed how attenuation resembles the trend of velocity with gas saturation, except for high gas saturation, where the attenuation increases significantly (Figure 3.5). On the other hand, for liquids, the mechanism (intrinsic attenuation) by which the energy is lost is also dependent on frequency.

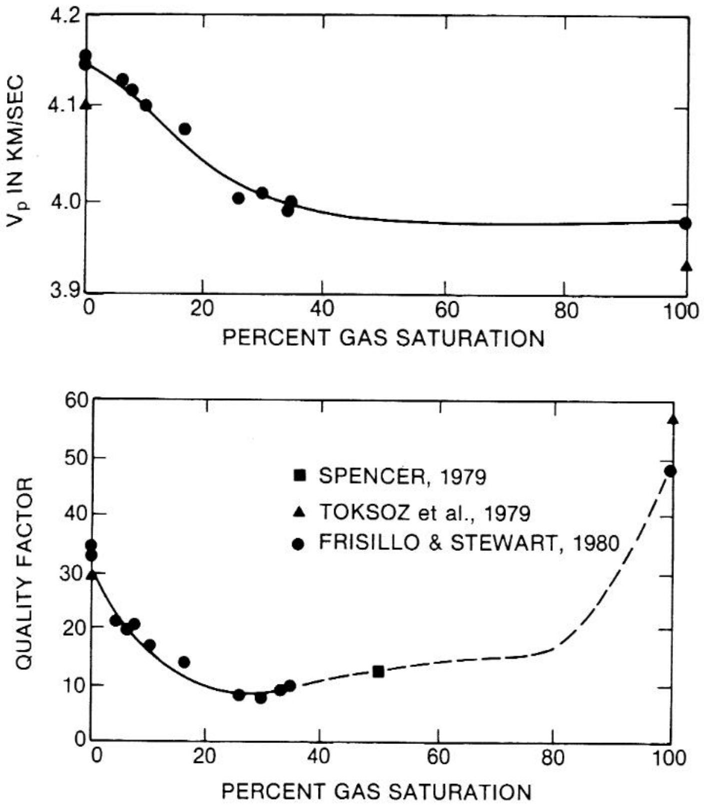

Figure 3.5. P-wave related quality factor and velocity as a function of gas saturation in Berea sandstone. Johnston, 1981.

3.2.3 Pressure

Pressure affects the quality factor of the rock (Q) by affecting directly the geometric effects or heterogeneities in the rock. Basically, as pressure increases, attenuation will decrease as cracks and pores begin to close. After certain pressure, the attenuation will remain essentially constant. For fluid-saturated rocks, the pore fluid will act against the confining pressure; therefore, the effect of pressure in fluid saturated rocks is lower than for dry or gas saturated rocks. According to Johnston (1981), the effect of pressure on extensional attenuation is more pronounced for lower frequencies than for higher frequencies for a water-saturated sandstone (Figure 3.6).

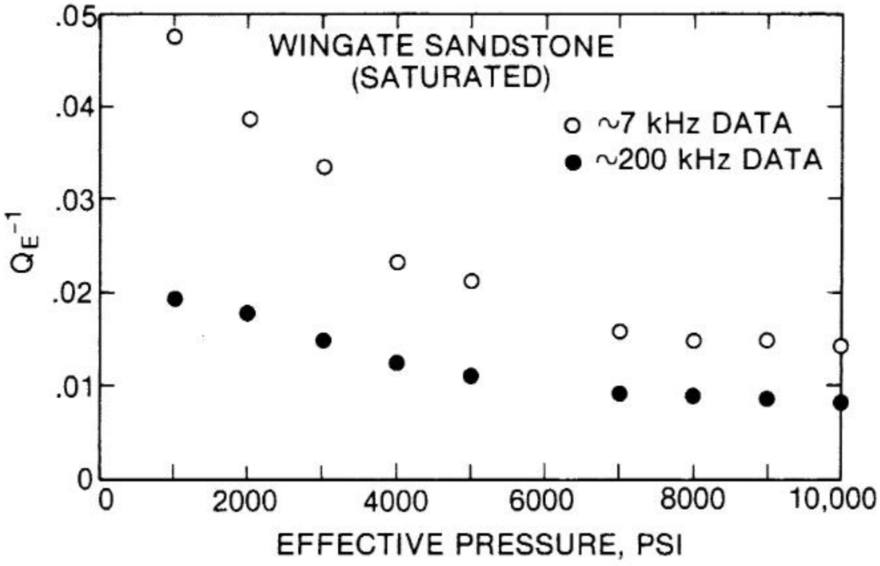

Figure 3.6. Attenuation (Young's modulus) versus effective pressure for a water-saturated sandstone at different frequencies. Johnston, 1981.

3.2.4 Temperature

Quality factor (Q) is normally regarded as independent of temperature for dry rocks for temperatures less than 150°C (Johnston, 1981). For water-saturated sandstones, limestone, and granite, Spencer (1981) showed that the attenuation peak frequency changes with pore fluid (water, ethanol, and n-decane) and temperature. These fluids have similar densities and viscosities, which make them, have approximately the same center frequency; however, the magnitudes of the attenuation peaks are different most likely due to differences in dielectrical and chemical properties and associated surfaces as measured and modeled by Tutuncu and Sharma (1992).

Next, a brief mathematical background and a few concepts regarding attenuation will be reviewed to understand the general terminology for various attenuation models.

3.2.5 Definitions

The inverse of quality factor (Q^{-1}), internal friction or anelasticity, is a parameter that denotes attenuation. Knopoff (1964) defined the intrinsic quality factor as:

$$\frac{2\pi}{Q} = \frac{\Delta \mathrm{E}}{\mathrm{E}} \tag{1}$$

where ΔE is the "energy dissipated per cycle of a harmonic excitation and E is the (peak) instantaneous elastic energy" (Barton, 2007). In rheological terms, Q is given by the inverse of tan delta or the ratio of storage modulus (stored energy) to loss modulus (dissipated energy):

$$Q = \frac{1}{\tan \delta} = \frac{\mathrm{G}'}{\mathrm{G}"} \tag{2}$$

where δ is the is the phase lag between the stress and the strain wave. Both equations 2 and 3 are equivalent (Johnston and Toksöz, 1981).

The attenuation coefficient α represents the exponential decay of the amplitude of a plane wave propagating through a homogeneous material (Johnston and Toksöz, 1981). Both parameters are related as follows:

$$\frac{1}{Q} = \frac{\alpha v}{\pi f} \tag{3}$$

where f is the frequency and v the velocity of the plane wave.

The amplitude of a plane wave can be simply described as function of the angular frequency (ω) and wavenumber (k):

$$A(x,t) = A_0 e^{i(kx-\omega t)} \tag{4}$$

However, for an attenuative wave, the wavenumber or the frequency must be a complex number. By choosing the wavenumber, the units of α will be of inverse length but if choosing frequency, the units are given in terms of inverse time. The complex wavenumber,

$$k = k_r + i\alpha \tag{5}$$

can also be expressed in terms of phase velocity and attenuation coefficient and frequency dependent:

$$k(\omega) = \frac{\omega}{c(\omega)} = \frac{\omega}{c_P(\omega)} + i\alpha(\omega) \tag{6}$$

Substituting equation (5) into the plane wave equation, we have:

$$A(x,t) = A_0 e^{-\alpha x} e^{i(kx-\omega t)} \tag{7}$$

Clearly, α represents the decay in amplitude as the wave dissipates energy. It has units of inverse length. For two positions in distance, x_1 and x_2, α takes the following form (Johnston and Toksöz, 1981):

$$\alpha = \frac{1}{x_2 - x_1} \ln\left[\frac{A(x_1)}{A(x_2)}\right] \tag{8}$$

The complex propagation velocity generates attenuation and velocity dispersion and can be described in terms of the complex modulus as:

$$c(\omega) = \frac{\omega}{k(\omega)} = \sqrt{\frac{M(\omega)}{\rho}} \tag{9}$$

where $M(\omega)$ is a complex modulus consisting of a real and an imaginary modulus:

$$M(\omega) = Re(\omega) + iIm(\omega) \tag{10}$$

Attenuation models need to obey the causality principle in order to allow for velocity dispersion.

Causality means that the cause always precedes the effect, in other words, a material is deformed only after the force is applied.

For an attenuative medium, high frequencies are commonly attenuated with distance more rapidly than low frequencies. If this occurs, the spectrum is not white anymore and the pulse spreads out since the high frequencies are lost violating the causality principle. Webb and Stacey (1982) explained that the pulse arrives at a certain distance before the wave actually travels to that point. Basically, since there is no distinct pulse, it can even arrive before initiated. This again, violates the causality principle and it is necessary to assume that attenuation varies with frequency. Then, the Fourier components of phase velocity will be adjusted in a way that their superposition cancels each other before the wave arrives (Webb and Stacey, 1982). In general, if attenuation varies with frequency, velocity dispersion must occur.

The Kramers – Krönig relations also known as dispersion relations links the imaginary and real parts of the frequency domain response. Kramers (1956) and Krönig (1926) derived a very useful expression where the real and imaginary part could be expressed each one as the Hilbert transform of the other one:

$$\begin{gathered} Re\big(\alpha_*(\omega)\big) = -Im(H(\alpha_*(\omega)) \\ Im(H\big(\alpha_*(\omega)\big) = Re\big(\alpha_*(\omega)\big) \end{gathered} \tag{11}$$

where H is the Hilbert transform.

Equation (8) can be expressed as:

$$\alpha(\omega) = -ik(\omega) + \frac{i\omega}{c_P(\omega)} \tag{12}$$

If

$$c_\infty = \lim_{\omega \to \infty} c_P(\omega) \tag{13}$$

then,

$$\alpha_*(\omega) = -ik(\omega) + \frac{i\omega}{c_\infty} \tag{14}$$

Following Kowar (2009):

$$\alpha_*(\omega) = \alpha(\omega) - i\left(\frac{\omega}{c_P(\omega)} - \frac{\omega}{c_\infty}\right) \tag{15}$$

Finally, the Kramers – Kronig relation for $\alpha(\omega)$ is:

$$\frac{\omega}{c_P(\omega)} - \frac{\omega}{c_\infty} = -H(\alpha(\omega)) \tag{16}$$

By assuming no dispersion, then the pulse will have some erroneous properties according to Aki and Richards (2000):

1) The wave will arrive at time before than zero.
2) The pulse is asymmetric, meaning the decay time is greater than the rise time.
3) The rise time is significantly larger than experiments predicts.

According to Kowar (2009) the Kramers – Krönig relation is necessary but not sufficient for causality of a wave.

3.2.6 Attenuation Models

3.2.6.1 The Kolsky – Futterman (KF) model

Kolsky (1956) modeled his experiment on polymers using a viscoelastic model with Q nearly constant with frequency. His model comes from the Maclaurin series expansion of the exponential function:

$$c_r = c_p \left|\frac{\omega_r}{\omega}\right|^{1/\pi Q} \tag{17}$$

where frequencies satisfy the condition (Kjartansson, 1979):

$$\frac{1}{\pi Q_r} \ln\left|\frac{\omega_r}{\omega}\right| \ll 1 \tag{18}$$

Futterman (1962) obtained the same formula by applying the Fourier transform to the impulse response and assuming the parameter α to be exactly proportional to frequency:

$$B(\omega) = e^{-\alpha x} e^{-i\omega x/c} \tag{19}$$

However, as was pointed out by Azimi et al., (1968), the Futterman model does not obey the causality principle when α is proportional to frequency at high frequencies (Kjartansson, 1979). Attenuation and phase velocity is given by the following equations:

$$\alpha(\omega) = \frac{|\omega|}{2 c_r Q_r} \tag{20}$$

$$\frac{1}{c_P(\omega)} = \frac{1}{c_r} + \frac{1}{\pi c_r Q_r} \ln\left|\frac{\omega_r}{\omega}\right| \tag{21}$$

where c_r and Q_r are the phase velocity and the quality factor at the reference frequency ω_r (in the seismic industry, the reference frequency is the dominant frequency of the seismic data).

3.2.6.2 The power-law Model

The power-law model is one of the nearly constant Q models (NCQ) that is not only linear but also nearly independent of frequency in a frequency band. This model satisfies the causality principle for certain power-law indexes. However, in recent years, there has been some concern regarding the validity of the Kramers – Krönig (KK) relations when using the power-law model at ultrasonic frequencies (Kowar, 2009). Though, Waters et al., (2000) showed that the dispersion relations when compared with experiments on several fluids show an agreement of less than 1m/s.

Since attenuation coefficient and phase velocity are correlated through the KK relations, the attenuation as well as the velocity dispersion varies as a power-law function or in the case of the latter, logarithmically if attenuation varies linearly with frequency (Mobley et al., 2000).

The power-law model proposed by Strick (1967) and Azimi et. al. (1968) has the following expressions for both attenuation and phase velocity:

$$\alpha(\omega) = a|\omega|^{\gamma} = a|\omega|^{1-\beta} \tag{22}$$

$$\frac{1}{c_P(\omega)} = \frac{1}{c_\infty} + a|\omega|^{-\beta} \cot\left(\frac{\pi}{2}\beta\right) \tag{23}$$

where $\beta = 1 - \gamma$ and $0 < \beta < 1$.

The quality factor can also be expressed as:

$$Q = \frac{|\omega|^{\beta}}{2ac_\infty} + \frac{1}{2}\cot\left(\frac{\pi}{2}\beta\right) \tag{24}$$

3.2.6.3 Kjartansson Model (1979)

Kjartansson (1979) made two main assumptions when deriving the constant Q (CQ) model, that is: 1) linearity and 2) frequency independence. This model is both causal and linear for frequencies varying over three orders of magnitude but it is only valid for strain amplitudes lower than 10^{-5} where both moduli and attenuation are dominated by linear effects.

The CQ model is fully parameterized by the phase velocity and quality factor (Q) and it is a special case of the power-law model, which means it can be represented by a combination of spring and dashpots. Kjartansson (1979) acknowledges that Q is not strictly independent of frequency for large losses and he offered a modification of the CQ model that is applicable for a wide range of frequencies, i.e. from seismic to ultrasonic frequencies. This is the nearly constant Q (NCQ) model.

The modulus in the CQ model is expressed as follows:

$$M(\omega) = M_0(i\omega)^{\beta} \tag{25}$$

whereas the quality factor is equal to:

$$Q = \cot\left(\frac{\pi}{2}\beta\right) \tag{26}$$

where $0 \leq \beta \leq 1$.

Finally, the phase velocity is given by (Ursin and Toverud, 2005):

$$\frac{1}{c_P(\omega)} = a|\omega|^{-\beta}\cot\left(\frac{\pi}{2}\beta\right) \tag{27}$$

3.3 Frequency Dispersion Models

3.3.1 Single Relaxation Model

The Debye model is one of the simplest models to describe frequency dispersion on fluids with single relaxation time. This model was derived at first to describe how the electric field behaves in a dielectric material. In the case of dielectrics, the polarization of the dielectric when an electric field is applied occurs over a period of time, usually called the relaxation time (τ) (Sharkov, 2003). In the case of viscoelasticity, the relaxation time refers to the time needed to release the strain, once the stress is applied.

To derive the Debye model, the function that represents the relaxation of the electrical polarization can be described as:

$$\boldsymbol{f}(\tau) = \frac{\varepsilon_0 - \varepsilon_\infty}{\tau_0} e^{-\left(\tau/\tau_0\right)} \tag{28}$$

where ε_∞ is the dielectric permittivity at high frequencies, ε_0 is the dielectric permittivity as frequency approaches to zero, and τ_0 is the characteristic time at which the dielectric loss is maximum (Sharkov, 2003).

This function will be substituted into the complex permittivity integral:

$$\dot{\boldsymbol{\varepsilon}}(\omega) = \varepsilon_\infty + \int_0^\infty \boldsymbol{f}\,(\tau) exp(j\omega\tau) d\tau \tag{29}$$

Then, the Debye model can be expressed as:

$$\dot{\boldsymbol{\varepsilon}}(\omega) - \varepsilon_\infty = \frac{\varepsilon_0 - \varepsilon_\infty}{1 + j\omega\tau} \tag{30}$$

The real and imaginary parts are:

$$\begin{aligned} \varepsilon_1(\omega) &= \varepsilon_\infty + \frac{\varepsilon_0 - \varepsilon_\infty}{1 + \omega^2\tau^2} \\ \varepsilon_2(\omega) &= \frac{(\varepsilon_0 - \varepsilon_\infty)}{1 + \omega^2\tau^2}\omega\tau_0 \end{aligned} \tag{31}$$

where τ_0 is expressed as follows:

$$\tau_0 = \frac{1}{\omega}\frac{\varepsilon_2(\omega)}{(\varepsilon_1(\omega) - \varepsilon_\infty)} \tag{32}$$

Analyzing these equations, the frequency dispersion is higher for intermediate frequencies, whereas for very low or very high frequencies, the permittivity is nearly constant with frequency.

3.3.2 Multiple Relaxation Model

For certain fluids, such as polymers, each molecule (dipole) has its own relaxation time which it could transform into a distribution function (F(τ)) if the number of relaxation times is high. Models such as Cole-Cole (1941), Cole and Davidson (1950), and Havriliak and Negami (1967) are derived for multiple relaxation times but all of them use the concept of multiple Debye-type relaxation times (Sharkov, 2003). The real and imaginary parts are given by the following expressions:

$$\frac{\boldsymbol{\varepsilon_1}(\omega) - \varepsilon_\infty}{\boldsymbol{\varepsilon_0} - \varepsilon_\infty} = \int_0^\infty \frac{F(\tau)d\tau}{1 + \omega^2\tau^2} \tag{33}$$

$$\frac{\boldsymbol{\varepsilon_2}(\omega)}{\boldsymbol{\varepsilon_0} - \varepsilon_\infty} = \int_0^\infty \frac{F(\tau)d\tau}{1 + \omega^2\tau^2}\omega\tau \tag{34}$$

Havriliak and Negami (1967) provide another modification of the Debye model. The HN model represents an asymmetric distribution of relaxation times (Figure 3.7) where at high frequencies presents a linear trend but an arc segment at low frequencies (Sharkov, 2003).

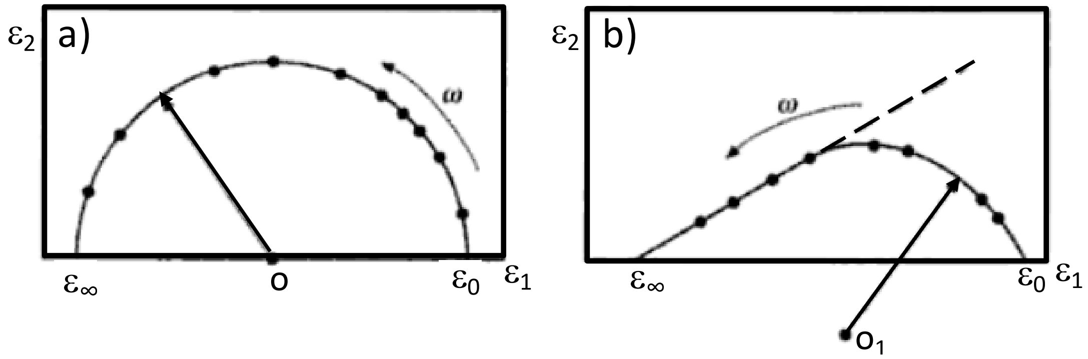

Figure 3.7. Imaginary versus real part of the complex permittivity. a) Debye model. b) Havriliak – Negami model. Sharkov, 2003.

The expression of the Havriliak – Negami model is

$$\frac{\boldsymbol{\varepsilon}(\omega) - \varepsilon_\infty}{\boldsymbol{\varepsilon_0} - \varepsilon_\infty} = [1 + (i\omega\tau_0)^{1-\alpha}]^{-\beta} \tag{35}$$

where α and β, are two empirical parameters that account for the asymmetry and broadness of the frequency spectrum (Sharkov, 2003).

3.3.3 Modified Havriliak – Negami Model

The Havriliak – Negami (HN) model will be used to describe the frequency dispersion of the complex shear modulus. Both empirical parameters (α and β) control the slope of the complex shear modulus as a function of frequency. The expression for shear modulus is given by:

$$G^*(\omega) = G'(\omega) + iG''(\omega) = [1 + (i\omega\tau_0)^{1-\alpha}]^{-\beta} \tag{36}$$

where:

$$G'(\omega) = 1 - R^{-\frac{\beta}{2}} cos(\beta\theta)$$
$$G''(\omega) = R^{-\frac{\beta}{2}} sin(\beta\theta) \tag{37}$$

and,

$$R = \left[1 + (\omega\tau)^{1-\alpha} sin\left(\frac{\pi\alpha}{2}\right)\right]^2 + \left[(\omega\tau)^{1-\alpha} cos\left(\frac{\pi\alpha}{2}\right)\right]^2 \tag{38}$$

For heavy oils, both temperature and frequency are parameters necessary to model the heavy oil response of the shear modulus. Therefore, a new model that account for frequency dispersion is derived by modifying the HN model to include the temperature effect on the relaxation time:

$$\tau_T = \frac{\eta_\infty}{G_{max}} exp\left[\frac{E}{R}\left(\frac{1}{T} - \frac{1}{T_R}\right)\right] \tag{39}$$

The T_R is the temperature at which the liquid point appears; E is the activation energy; R is the ideal gas constant and G_{max} corresponds to the modulus at the glass point temperature. Likewise, the viscosity at infinite frequencies corresponds to the glass point temperature viscosity. More on this will be explained on section 3.5.

This new model was used to describe the frequency dispersion of the shear wave modulus exhibited by the low-frequency rheological measurements and the ultrasonic acoustic measurements.

3.4 Ultrasonic Measurements

3.4.1 Velocity Measurement

The laboratory measurements were carried out by the Rock Physics Laboratory at the University of Houston. The measurements are the result of applying the conventional reflection (pulse-echo) and transmission (pulse-catch) methods to measure compressional and shear wave velocity at a frequency of 1MHz. The pulse-echo or reflection method consists of using the same transducer to generate the waves into the sample and to receive the reflected back signal from the opposite end of the sample and convert it to an electric signal. The pulse-catch method uses two (2) transducers; one at each side of the sample to transmit and receive the signal.

These methods require certain equipment: a pulse/receiver produces high voltage electrical pulses and the transducers generate high frequency ultrasonic energy. The transducer is attached to the sample through a coupling material which will enhance the transmission of the waves from the transducer to the sample. Basically, it reduces difficulties caused by the drastic impedance difference between the sample and air. The main function of a transducer is to convert electrical signals into mechanical vibrations in the case of a transmitter and mechanical vibrations into electric signals in the case of the receiver.

The key part of the transducer is a piezoelectric ceramic which polarizes itself according to an applied electric field. The shape of the piezoelectric will determine the wave mode that will generate. P transducers have a round shape and S transducers have a square shape. The thickness of the piezoelectric is directly related to the center frequency of the transducer, specifically, the thickness is equal to half the wavelength.

Buffer rods are also part of the equipment needed for ultrasonic measurements especially when working at high temperature conditions; they usually have a cylindrical shape with flat and parallel ends made of low loss materials. They are located between the transducers and the sample enclosing the fluid (Figure 3.8) with the objective of suppressing any surface effects such as wave mode conversion and diffractions (Cheeke, 2002)

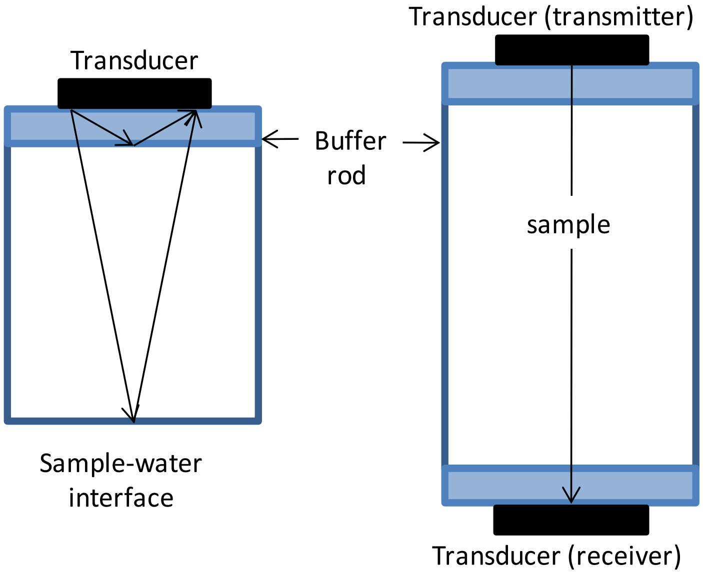

Figure 3.8. Schematic representation of pulse-echo and pulse-catch techniques for ultrasonic velocity measurement.

The velocity is calculated by dividing the length of the sample by the travel time. In the case of the pulse-echo method, a two-way traveltime should be accounted whereas the pulse-catch method only requires measuring a one-way traveltime. In addition, the travel time through the buffer needs to be subtracted from the travel time of the sample.

The pulse-catch method is recommended for highly attenuating materials and especially for shear wave velocity estimation where the amplitude of the reflected wave would be too small for a proper identification and measurement.

In order to compare the ultrasonic measurements with the low-frequency rheological measurements, the following expressions for isotropic materials that relate moduli and velocities were used:

$$V_S = \sqrt{\frac{\mu}{\rho}} \tag{40}$$

$$V_P = \sqrt{\frac{K + \left(\frac{4}{3}\right)\mu}{\rho}} \tag{41}$$

3.4.2 Density Measurement

The displacement and non-displacement method were used to measure density for heavy oils. The former method is based on the Archimedean principle, where the density can be estimated from the volume displaced by the sample in a liquid with known density (water). Following this simple equation, the density of the samples was obtained:

$$\rho_{sample} = \frac{m_T - m_C}{D_T - \left(\frac{m_C}{\rho_C}\right)} \tag{42}$$

where:

m_T: total mass (sample and container)

m_C: mass of container

D_T: displacement total

ρ_T: density of container

The non-displacement method consists of measuring the volume of a container filled with water (distilled) based on the density of the water and the mass of the water that was previously measured. The water was then replaced by the sample, weighed and the density was finally estimated.

3.4.3 Results

The ultrasonic measurement of P-wave and S-wave velocity was carried out for the same samples described in Part 1: Canada A, Canada B, Venezuela, and Brazil samples. These are dead heavy and extra-heavy oil samples whose density was measured at 15.6°C (standard conditions) to calculate the API gravity but in order to calculate velocity and modulus, the density was measured at the corresponding temperatures. The following table comprises the characteristics of the measurements for each of these samples:

Table 3.2. Temperature, pressure and density conditions for ultrasonic velocity measurements.

Fluid	Canada A	Canada B	Venezuela	Brazil
Temperature (C)	0.2 and 22.3	6 and 22.1	0.1, 4.3, 9 and 23.3	0.9, 3.3 and 22.4
Pressure	At room pressure	Varies from 300 to 1000psi	At room pressure	At room pressure
Density	Not available	Varies 0.006g/cc every 10C	Varies 0.001g/cc every 10C	Varies 0.005g/cc every 10C

Figure 3.9 shows that the shear wave velocity decreases with temperature following a logarithmic function. Unfortunately, for Canada A heavy oil sample, only two measurements were available; this makes very difficult to appreciate the true trend of the modulus with temperature for this sample. All the samples exhibit similar shear-wave velocity that ranges from 200m/s to 600m/s. It was very difficult to measure the shear-wave velocity for higher temperatures since the signal was too small. The velocity of the samples is directly correlated with the density of the sample except for Canada B heavy oil sample (Figure 3.10).

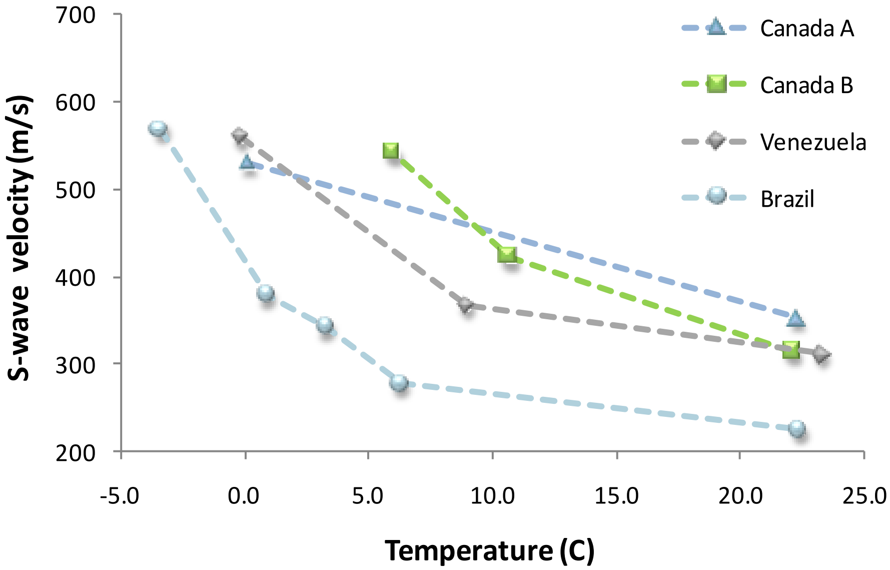

Figure 3.9. Ultrasonic shear-wave velocity with respect to temperature measured at room pressure.

In the case of P-wave velocity, the velocities also decrease as temperature increases; however, the change in slope is clear once there is a phase change, from the glass phase to the quasi-solid phase. This change was also observed in shear-wave velocity. In fact, all the samples exhibit very similar compressional velocities (Figure 3.11). For temperatures lower than 30°C approximately, the corresponding bulk modulus is higher than 2.5GPa, which is the bulk modulus for water. The compressional velocities are definitely more affected by pressure.

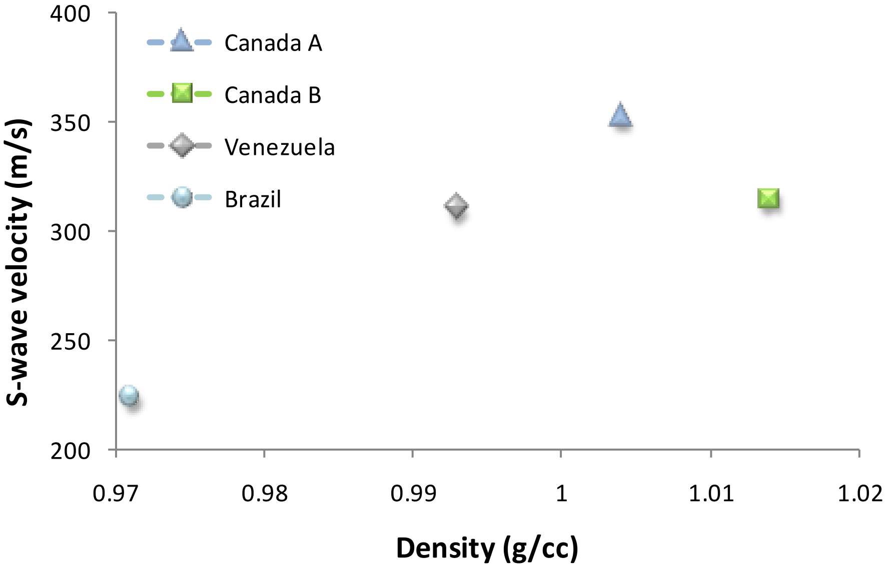

Figure 3.10. Ultrasonic shear-wave velocity with respect to bulk density measured at room temperature.

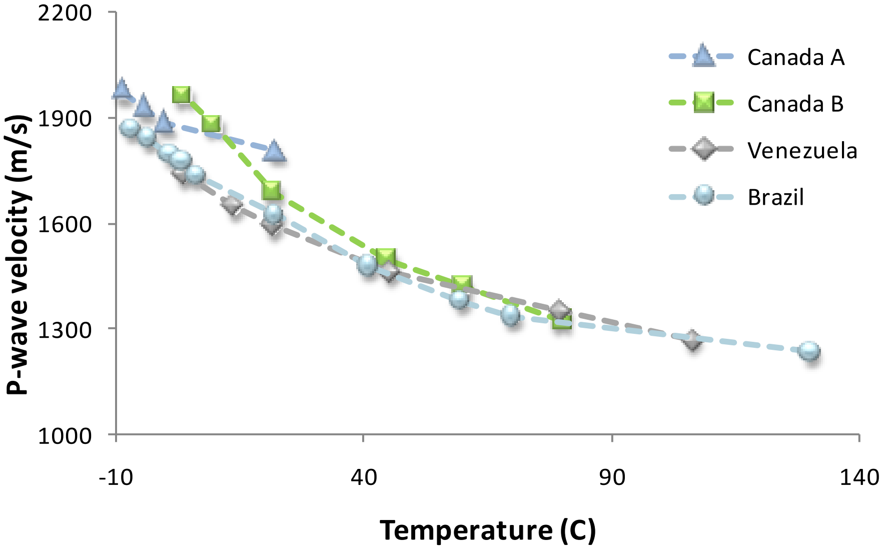

Figure 3.11. Ultrasonic P-wave velocity with respect to temperature at 500psi.

3.5 Shear Modulus at Ultrasonic and Low Frequencies

The frequency dispersion of heavy and extra-heavy oil samples is significant when ultrasonic and low-frequency measurements are compared. The latter varies from 0.001Hz to 100Hz whereas the ultrasonic measurements were carried out at 1MHz. The low-frequency rheological measurements were modified using the Frequency-Temperature superposition principle (please refer to Part 2, section 2.4.4) in order to increase the effective frequency range covered by the actual experiments.

It was also decided to compare the results given by the FLAG model that uses a modification of the Debye model but does not take into account the change of relaxation time with temperature. The FLAG model was designed by the Rock Physics Laboratory at the University of Houston based mostly on ultrasonic measurements. The analysis made for Venezuela, Brazil, Canada A, and Canada B heavy oil samples, shows that the FLAG model exhibits significantly less dispersion than the modified Havriliak – Negami model proposed in this study.

3.5.1 Venezuela Heavy Oil Sample

The new frequency – temperature dispersion model fits the rheological measurements of the Venezuela heavy oil sample as well as the shear modulus obtained through ultrasonic velocity measurements. We need to take into account that there is a small difference in temperature between both experiments and certain differences should be expected. However, the biggest difference between the new model and the ultrasonic data was found for the shear modulus at 9°C most likely due to experimental errors (the difference between ultrasonic measurements at 0°C and 9°C is very small). This is shown in Table 3.3.

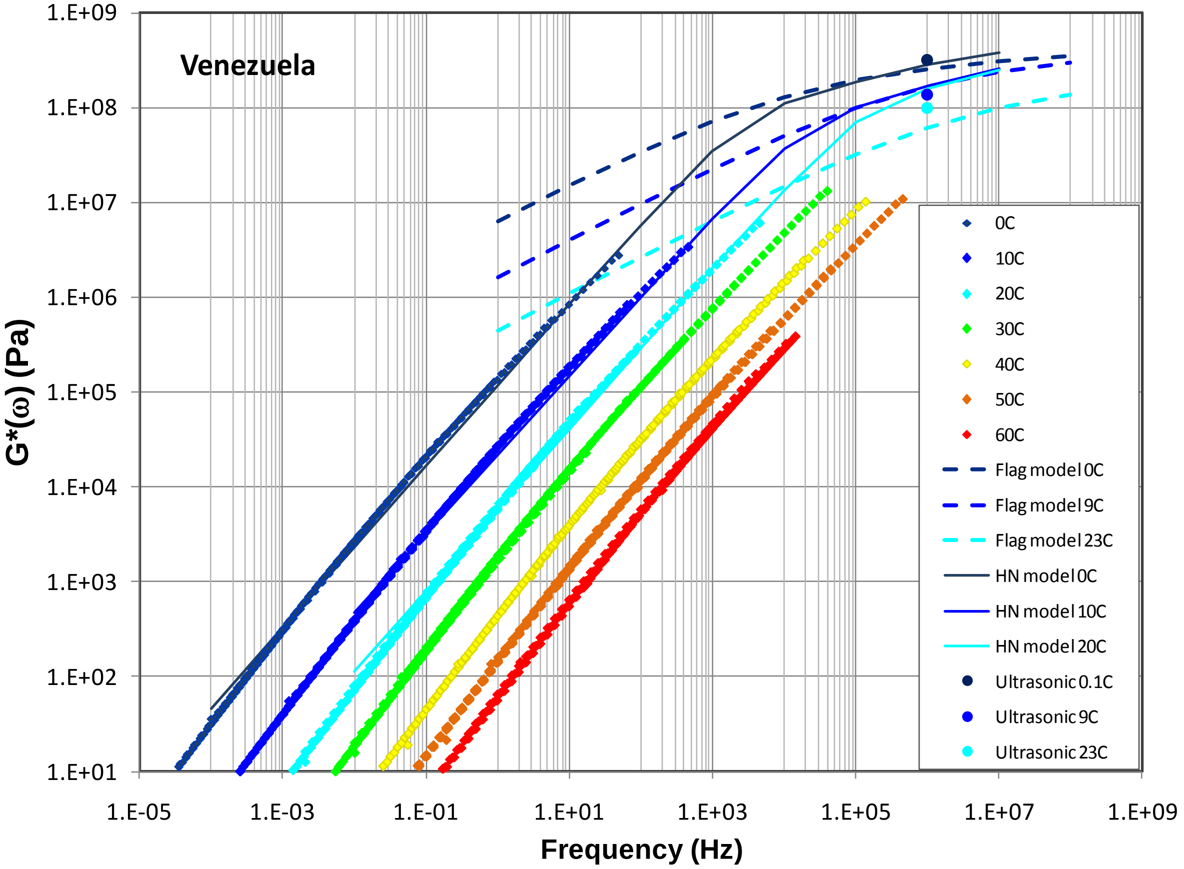

Figure 3.12. Comparison of complex shear modulus at ultrasonic and low frequencies for Venezuela heavy oil sample.

Table 3.3. Comparison of Ultrasonic, FLAG model and the new model at 1MHz. Columns 4 and 5 were calculated based on the difference in percentage between the experiment (ultrasonic) and the corresponding models. Column 1 corresponds to the temperature at which experiments were carried out.

Temperature (C)	Ultrasonic (Pa)	New model (Pa)	FLAG model (Pa)	Difference % (modified HN)	Difference % (FLAG)
0	3.21 E+08	3.18 E+08	2.56 E+08	0.7	20.28
9	1.38 E+08	1.62 E+08	1.65 E+08	17.6	20.18
23	9.80 E+07	1.1 E+08	6.10 E+07	15.6	37.75

I also estimated the ultrasonic shear modulus at the same temperatures that rheological (low-frequency) measurements were carried out that is at 0°C, 10°C and 20°C based on the logarithmic function that fits the data very well (Figure 3.13). The new model exhibits a lower error at 20°C but a higher error for 10°C (Table 3.4).

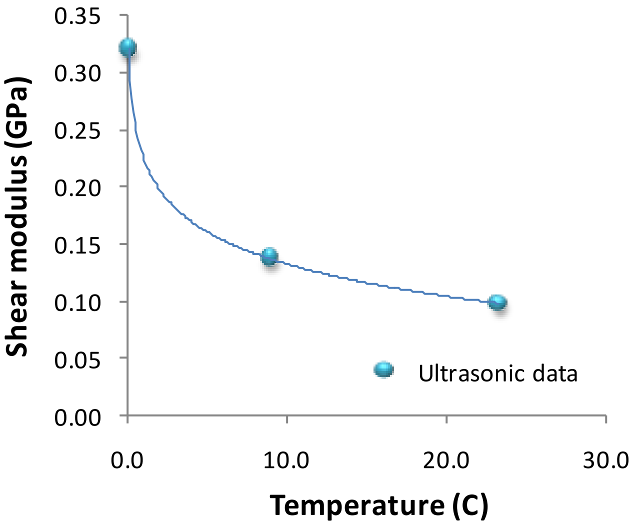

Figure 3.13. Complex shear modulus estimated from ultrasonic velocity measurements with respect to temperature. The logarithmic function was used to obtain G* at 10°C and 20°C.

Table 3.4. Comparison of Ultrasonic *(estimated)*, FLAG model and the new model at 1MHz.

Temperature (C)	Ultrasonic *estimated* (Pa)	New model (Pa)	Difference % (modified HN)
0	3.21 E+08	3.18 E+08	0.9
10	1.32 E+08	1.62 E+08	22.1
20	1.04 E+08	1.1 E+08	9.0

The new model, proposed in this study, is appropriate to describe the change of G* with frequency for frequencies higher than 0.008Hz and lower than 10Hz based on the temperature curve corresponding to 0°C (Figure 3.14). In general, this model fails to properly predict G* for very low and very high frequencies for a particular temperature. The modeled complex shear modulus (G*) is within the calculated error bars (10%) except at very low frequencies or when the modulus is too small where the new model predicts higher complex shear modulus. In summary, the proposed model fits the data well (R^2 >0.9) for a broad range of frequency and temperature (Table 3.5).

The parameters obtained as a result of the fitting procedure are summarized in Table 3.5. These parameters include the empirical constants alpha and gamma and the parameters needed to estimate the relaxation time for each temperature. Activation energy (E_a) was chosen based on the results obtained in Part 1; however, tests demonstrated that the estimation of complex shear modulus is almost insensitive to changes in E_a.

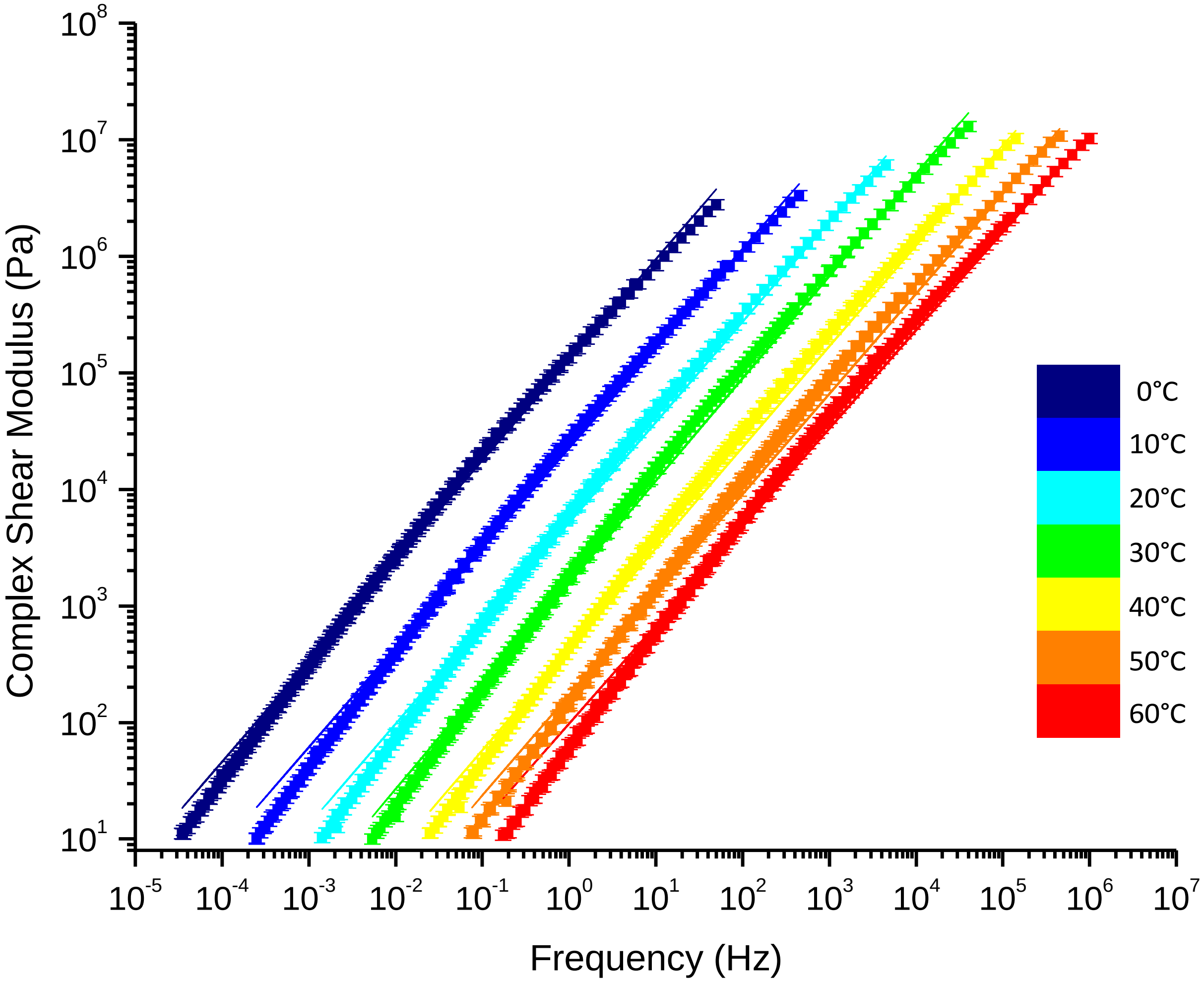

Figure 3.14. Comparison of rheological (low-frequency) measurements (filled squares) and the new model for Venezuela heavy oil sample (lines). Error bars corresponding to 10% were computed for rheological measurements. The frequency range from 0.0001Hz (0°C) to almost 100Hz (60°C) is within the error bars. The FLAG model was not compared since the difference was too large.

Table 3.5. Fitting parameters of the new model for Venezuela heavy oil sample.

T(C)	G_{max} (Pa)	η_∞ (Pa.s)	T_I (C)	E_a	Alpha (α)	Gamma (γ)	R^2
0	1 E+09	43000	30	3200	0.170 ± 0.001	0.106 ± 0.001	0.996
10	1 E+09	6200	30	3200	0.175 ± 0.001	0.101 ± 0.001	0.996
20	1 E+09	1300	30	3200	0.159 ± 0.001	0.107 ± 0.001	0.996
30	1 E+09	250	30	3200	0.155 ± 0.001	0.148 ± 0.001	0.996
40	1 E+09	75	30	3200	0.166 ± 0.001	0.109 ± 0.001	0.996
50	1 E+09	25	30	3200	0.158 ± 0.012	0.111 ± 0.001	0.995
60	1 E+09	10	30	3200	0.149 ± 0.012	0.120 ± 0.001	0.995

The temperature at which we “jump” into the isotropic phase denoted as T_I was chosen to be equal to 30°C (303°K) since it is at this temperature approximately where the elastic component of the shear modulus decrease significantly. However, the complex shear modulus estimation is almost insensitive to change on this parameter. Previously, it was mentioned that G_{max} corresponds to the maximum complex shear modulus observed even at ultrasonic measurements. A value of 1GPa was chosen as the maximum shear modulus that this sample can achieve at ultrasonic frequencies based on ultrasonic data. On the other hand, the infinite or undisturbed viscosity corresponds to the lowest frequency at which was measured based on the rheological measurements showed in Part 1. This parameter will have a significant effect on G* estimation. Finally, the empirical parameters alpha and gamma where constrained during the fitting between 0 and 1. Gamma seems to increase with temperature whereas alpha seems to decrease with temperature but no definite trend can be derived. Both, alpha and gamma variation is very small for the temperature range studied.

3.5.2 Brazil Heavy Oil Sample

The modeling study using the new proposed model offered to some extent different results for each sample. In the case of the Brazil sample, the model fits the rheological measurements with very small deviation, but it predicts significantly higher modulus than the measurements made on the sample at ultrasonic frequencies (Figure 3.15). As in the previous case, there is a small difference in temperature between ultrasonic experiments and both models (FLAG and the new model). This difference can be important close to the glass point temperature (0°C). The FLAG model over predicts the shear modulus at sonic and seismic frequencies.

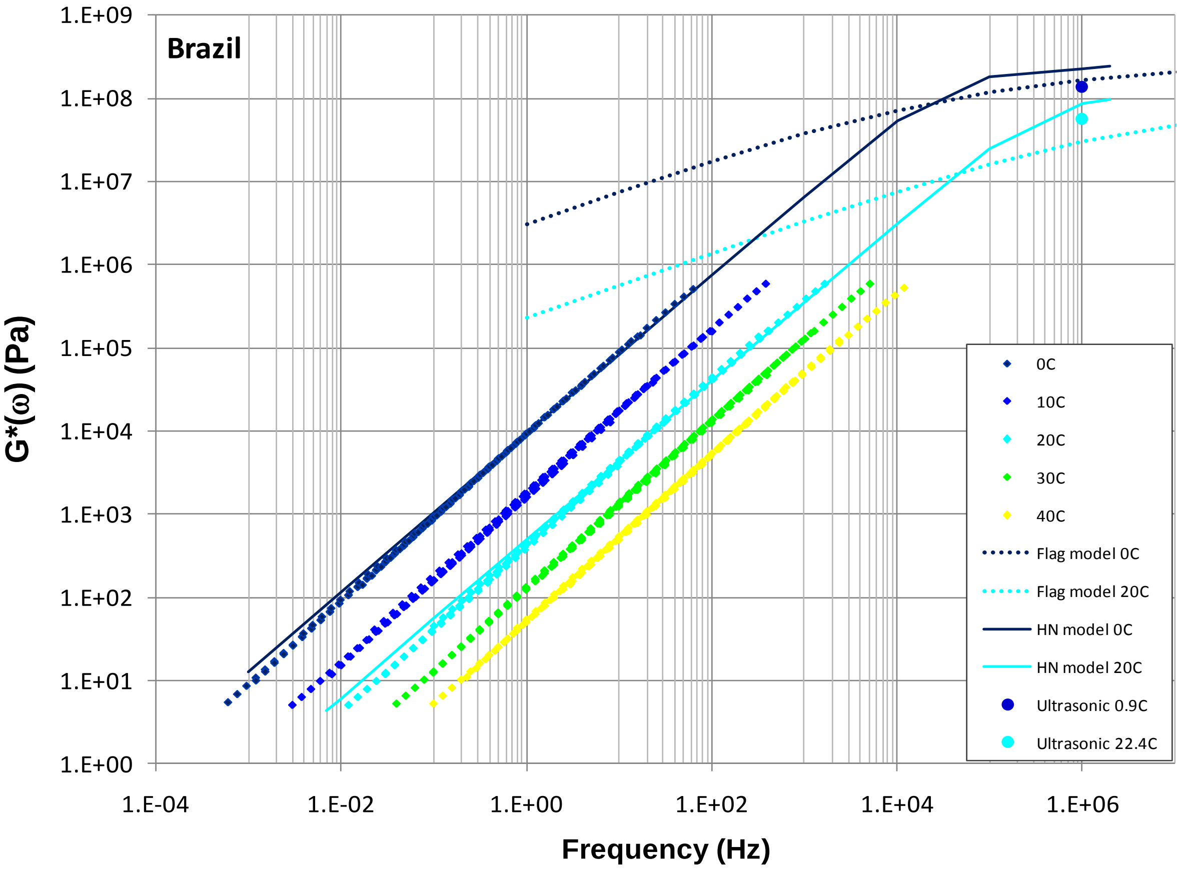

Figure 3.15. Comparison of complex shear modulus at ultrasonic and low frequencies for Brazil heavy oil sample. The model over predicts G* for both temperatures.

Once again, the ultrasonic shear modulus was estimated at the same temperatures as the rheological (low-frequency) measurements, that is, at 0°C, 10°C and 20°C. This was based on the logarithmic function that fits the shear modulus variation with temperature, which was estimated from the shear velocity measurements at ultrasonic frequencies (Figure 3.16). Using this function, the difference between the ultrasonic (estimated) data and both models can be determined. The results (Table 3.6) indicate that both models are not able to properly predict shear modulus at ultrasonic frequencies. For the new model, the errors are higher than 20% at 10°C and 20°C. However, it is necessary to consider that the ultrasonic data is predicted based only on measurements made at fewer different temperatures than the rheological measurements. Figure 3.17 shows the comparison between low-frequency and ultrasonic data estimated at the same temperatures.

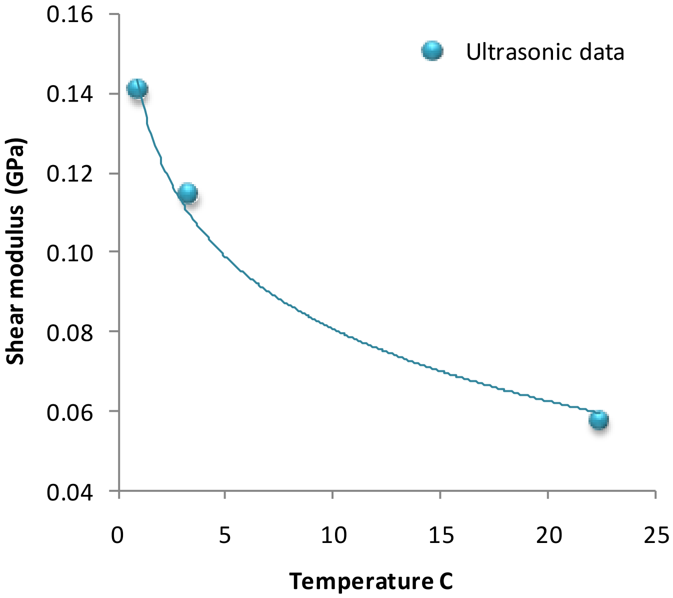

Figure 3.16. Complex shear modulus estimated from ultrasonic velocity measurements with respect to temperature. The logarithmic function was used to obtain G* at 0°C, 10°C and 20°C.

Table 3.6. Comparison of Ultrasonic *(estimated),* FLAG model and the new model at 1MHz. Columns 4 and 5 were calculated based on the difference in percentage between the experimental data, estimated at the same temperature as the rheological measurements, and the corresponding models.

Temperature (C)	Ultrasonic *estimated* (Pa)	New model (Pa)	FLAG model (Pa)	Difference % (modified HN)	Difference % (FLAG)
0	2.01 E+08	2.10 E+08	1.66 E+08	4.58	17.09
10	8.09 E+07	1.27 E+08	8.76 E+07	36.38	8.25
20	6.29E+07	8.59 E+07	3.04 E+07	26.76	51.74

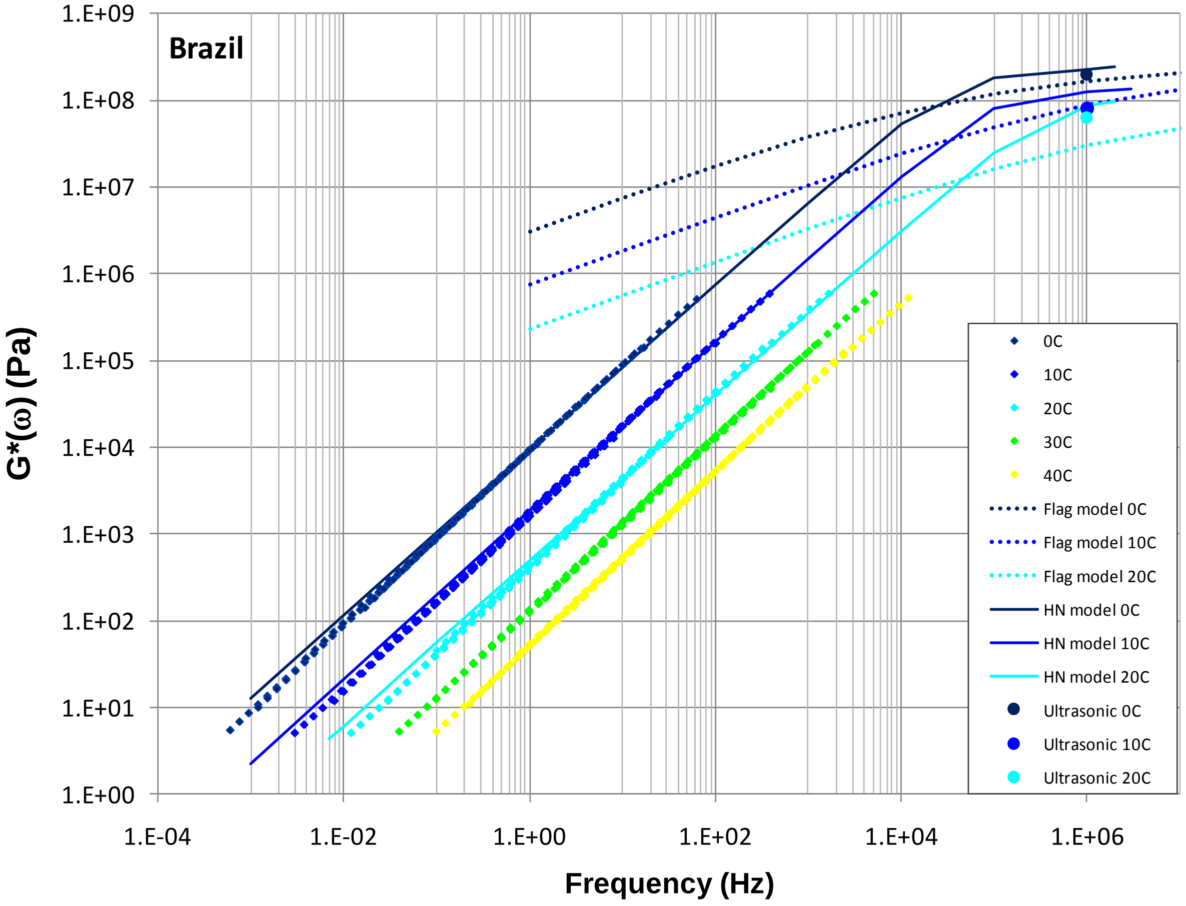

Figure 3.17. Comparison of complex shear modulus at ultrasonic and low frequencies for Brazil heavy oil sample at the same temperatures as rheological measurements were made (0°C, 10°C and 20°C).

The new model is now used to fit the rheological measurements and the result is exhibited in Figure 3.18. The model predicts within the error bars (10%) for frequencies higher than 0.01 Hz to 1000Hz approximately. This model overpredicts complex shear modulus by more than 10% when its magnitude is very small (less than 100Pa). This was observed for all temperatures. In general, the proposed model can fit with very good results (R^2 >0.99) a very broad range of frequency and temperature.

The fitting parameters: alpha (α), gamma (γ), infinite viscosity (η_∞), maximum shear modulus (G_{max}), activation energy (E_a), and isotropic temperature (T_I) are summarized in Table 3.7. Activation energy (E_a) for the Brazil heavy oil sample is the lowest among all the samples based on the results obtained in Part 1; however, once again, tests demonstrated that the estimation of complex shear modulus is almost insensitive to changes in E_a. The isotropic temperature denoted as T_I was again kept equal to 30C (303K) as in the previous sample. The complex shear modulus estimation proved to be almost insensitive to change on this parameter. The G_{max} parameter was decreased in comparison to Venezuela heavy oil sample, due to the significant lower density of the Brazil heavy oil sample. A value of 0.5GPa was chosen as the maximum shear modulus that this sample can achieve at ultrasonic frequencies. The infinite or undisturbed viscosity was estimated based on the rheological measurements showed in Part 1. Again, this parameter will have a significant effect on G* estimation. Finally, both alpha and gamma where constrained between 0 and 1; their variation is very small for the temperature range studied and no definite trend can be concluded.

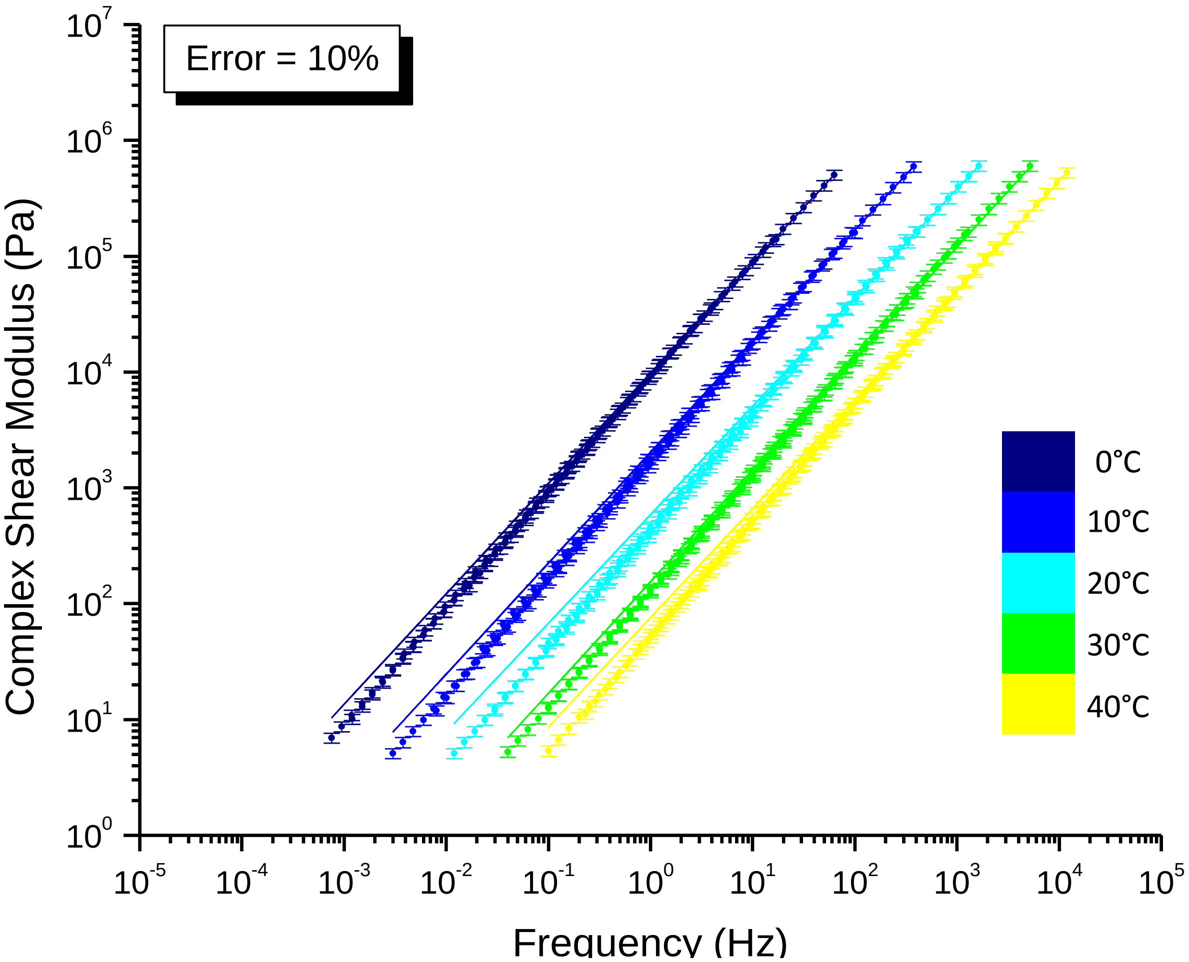

Figure 3.18. Comparison of rheological (low-frequency) measurements and the new frequency dispersion model for Brazil heavy oil sample. Error bars corresponding to 10% were added. The frequency range from 0.01Hz (0°C) to 10000Hz (60°C) approximately is within the error bars.

Table 3.7. Fitting parameters of the new model for Brazil heavy oil sample.

T©	G_{max} (Pa)	η_∞ (Pa.s)	T_l ©	E_a	Alpha (α)	Gamma (γ)	R^2
0	0.5 E+09	1500	30	2400	0.048 ± 0.003	0.595 ± 0.007	0.999
10	0.5 E+09	260	30	2400	0.042 ± 0.003	0.706 ± 0.011	0.999
20	0.5 E+09	75	30	2400	0.063 ± 0.002	0.499 ± 0.007	0.999
30	0.5 E+09	25	30	2400	0.036 ± 0.006	0.559 ± 0.095	0.966
40	0.5 E+09	10	30	2400	0.058 ± 0.001	0.466 ± 0.006	0.999

3.5.3 Canada A Heavy Oil Sample

The new model matches the rheological measurements of Canada A heavy oil sample but at the same time significantly overpredicts the shear modulus obtained from ultrasonic velocity measurements. Shear velocity measurements were carried out at 0.9°C and 22°C which differ from the rheological measurements made at 0°C and 20°C; therefore, certain differences should be expected.

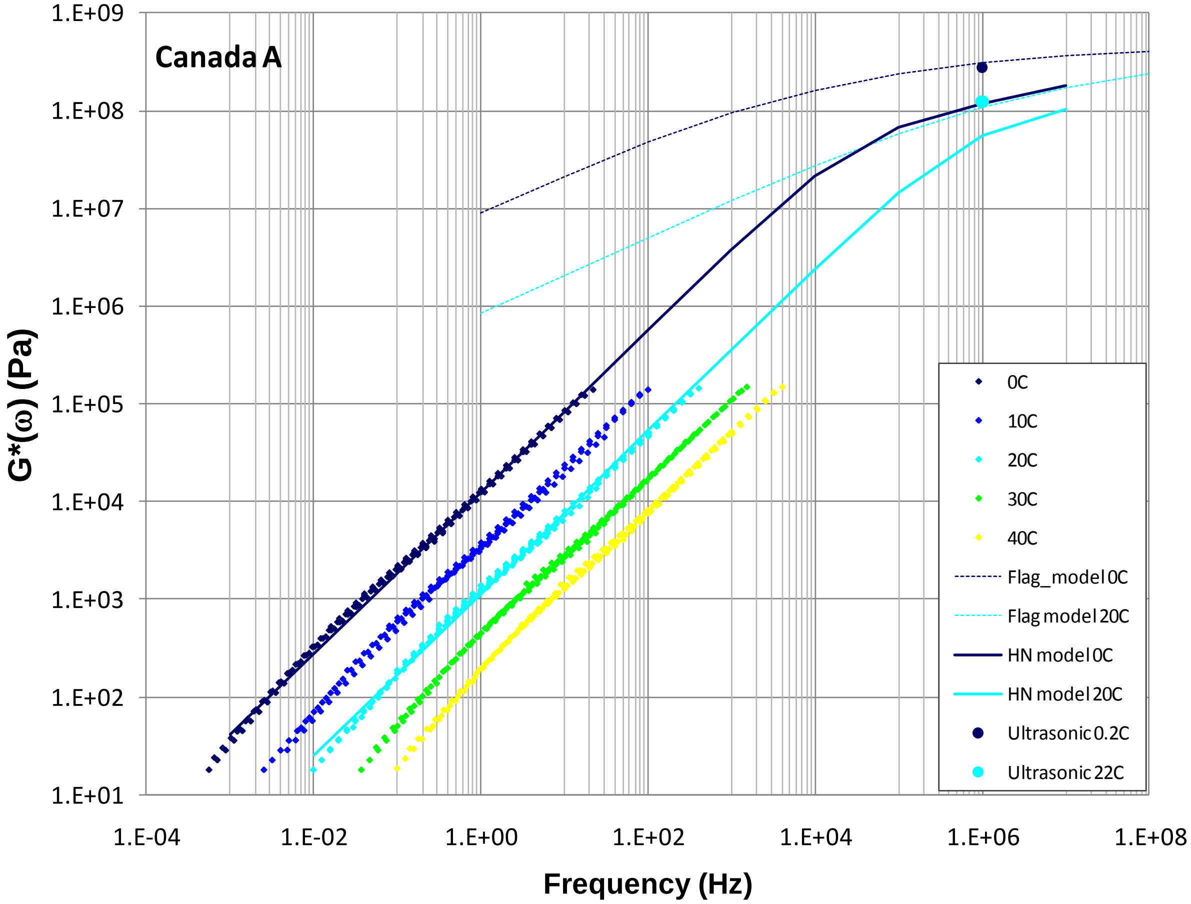

Figure 3.19. Comparison of complex shear modulus at ultrasonic and low frequencies for Canada A heavy oil sample.

The ultrasonic shear modulus was estimated at the same temperatures as the low-frequency measurements were made, that is, at 0°C, 10°C, and 20°C. This was based on the logarithmic function that fits the shear modulus variation with temperature, which was estimated from only two shear velocity measurements (Figure 3.20), from which the error between the ultrasonic (estimated) data and both models can be estimated. The result (Table 3.8) indicates that the FLAG model cannot properly predict shear modulus at sonic and seismic frequencies; the new model also overpredicts G* for ultrasonic frequencies. Figure 3.21 shows the comparison between low-frequency and ultrasonic data estimated at the same temperatures.

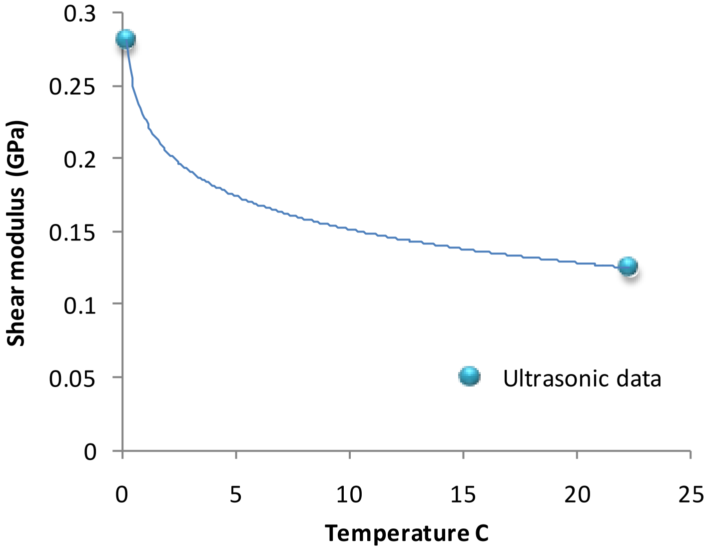

Figure 3.20. Complex shear modulus estimated from ultrasonic velocity measurements with respect to temperature for Canada A heavy oil sample. The logarithmic function was used to obtain G* at 0°C, 10°C and 20°C.

Table 3.8. Comparison of Ultrasonic *(estimated),* FLAG model and the new model at 1MHz. Columns 4 and 5 were calculated based on the difference in percentage between the experimental data, estimated at the same temperature as the rheological measurements were made, and the corresponding models.

Temperature (C)	Ultrasonic *estimated* (Pa)	New model (Pa)	FLAG model (Pa)	Difference % (modified HN)	Difference % (FLAG)
0	2.81 E+08	1.17 E+08	3.07 E+08	9.49	9.49
10	1.52 E+08	8.37 E+08	1.97 E+08	44.81	30.14
20	1.29E+08	5.58 E+07	1.11 E+08	56.68	13.96

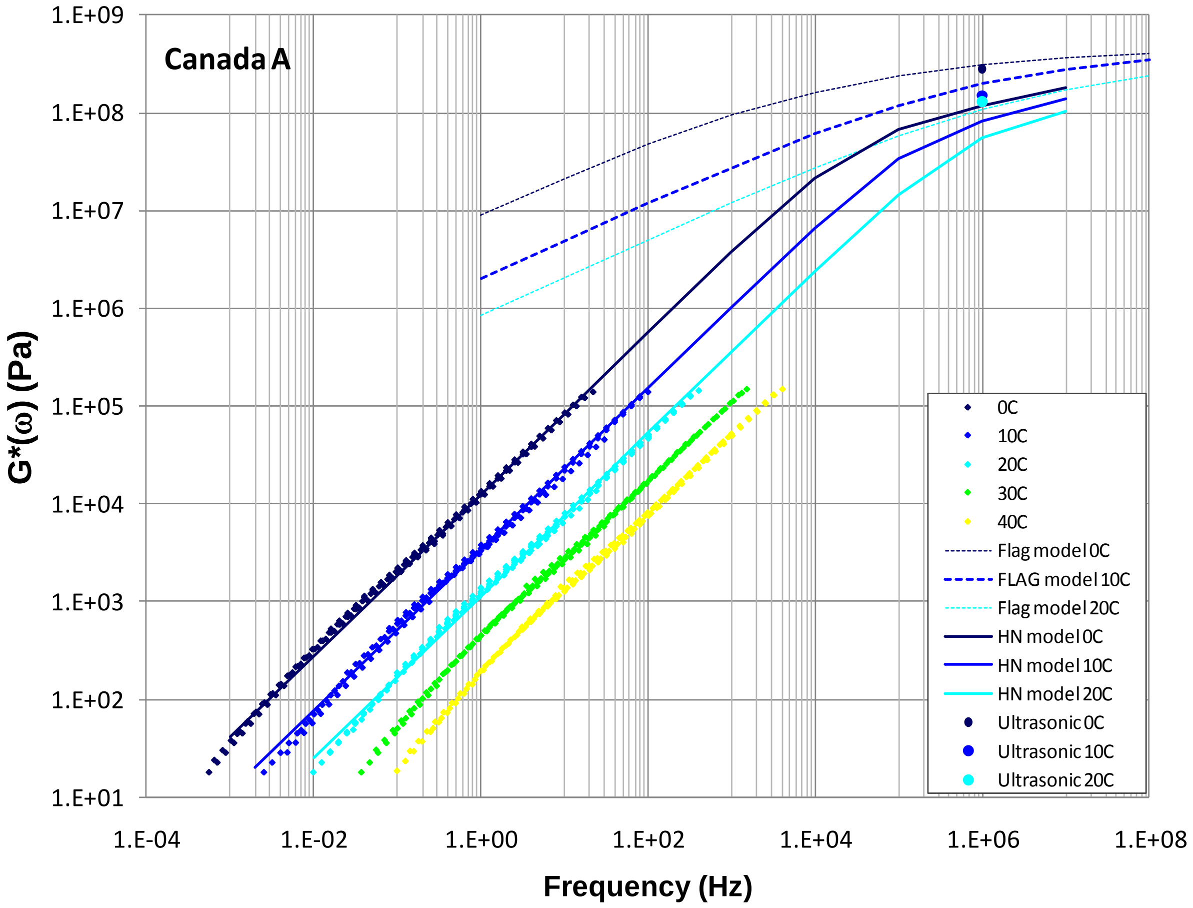

Figure 3.21. Comparison of complex shear modulus at ultrasonic and low frequencies for Canada A heavy oil sample.

The new model predicts the rheological measurements with an error of less than 10% for moduli higher than 100Pa. Once more, this model overpredicts complex shear modulus at very low frequencies for each temperature. The new model matches the experimental data well (R^2 >0.99) in a very broad range of frequencies and temperatures.

The fitting parameters: alpha (α), gamma (γ), infinite viscosity (η_∞), maximum shear modulus (G_{max}), activation energy (E_a), and isotropic temperature (T_I) are summarized in Table 3.9. Activation energy (E_a) for Canada A heavy oil sample is similar to Venezuela heavy oil sample as discussed in Part 2 due to their similar densities. The parameter T_I was again kept equal to 30°C (303K) as in the previous sample. The G_{max} parameter was kept at 1GPa as in the case of the Venezuela heavy oil sample. The infinite viscosity was estimated based on the rheological measurements shown in Part 2. The empirical parameters, alpha and gamma, exhibit a very small variation for the temperature range studied and again no definite trend can be concluded. From all the fitting parameters, only η_∞, G_{max}, α and γ have a significant effect on complex shear modulus estimation.

Table 3.9. Fitting parameters of the modified HN model for Canada A heavy oil sample.

T(C)	G_{max} (Pa)	η_∞ (Pa.s)	T_I (C)	E_a	Alpha (α)	Gamma (γ)	R^2
0	1 E+09	5200	30	3100	0.214 ± 0.006	0.043 ± 0.002	0.996
10	1 E+09	1000	30	3100	0.192 ± 0.006	0.057 ± 0.003	0.996
20	1 E+09	300	30	3100	0.191 ± 0.003	0.050 ± 0.001	0.999
30	1 E+09	80	30	3100	0.200 ± 0.002	0.039 ± 0.001	0.999
40	1 E+09	30	30	3100	0.205 ± 0.001	0.047 ± 0.001	0.999

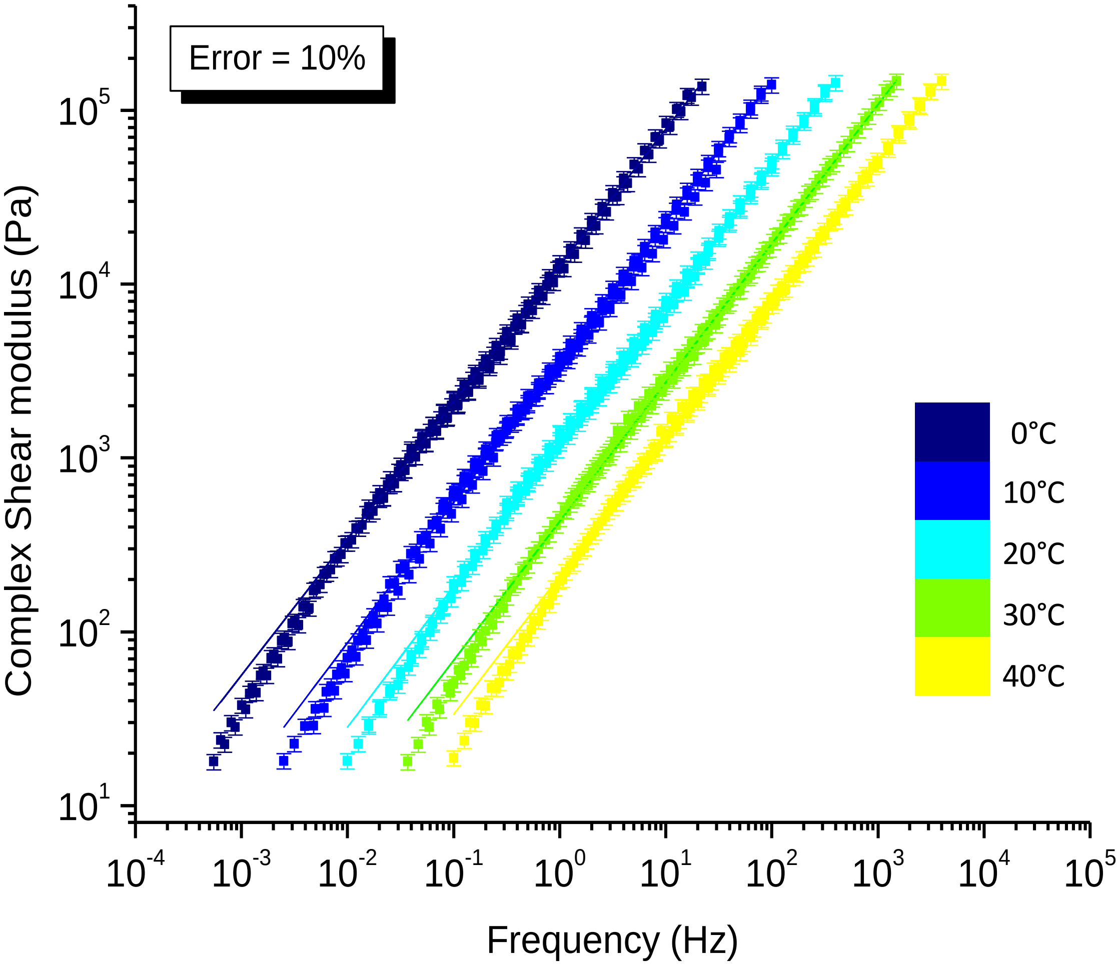

Figure 3.22. Comparison of rheological (low-frequency) measurements and proposed model for Canada A heavy oil sample. Error bars corresponding to 10% were computed for rheological measurements. The frequency range from 0.01Hz (0°C) to 5000Hz (60°C) approximately is within the error bars.

3.5.4 Canada B Heavy Oil Sample

The proposed model fits both low-frequency and ultrasonic measurements for the Canada B heavy oil sample very well. The FLAG model overpredicts the shear modulus for sonic and seismic frequencies as was the case for all previous samples. However, the FLAG model is able to provide a better fit than the proposed model for ultrasonic measurements at 6°C and 22°C due to, in part, to the difference in temperature at which each model was calculated. The proposed model was calculated at 0°C, 10°C, 20°C, 30°C, 40°C, 50°C, and 60°C according to the low frequency measurements.

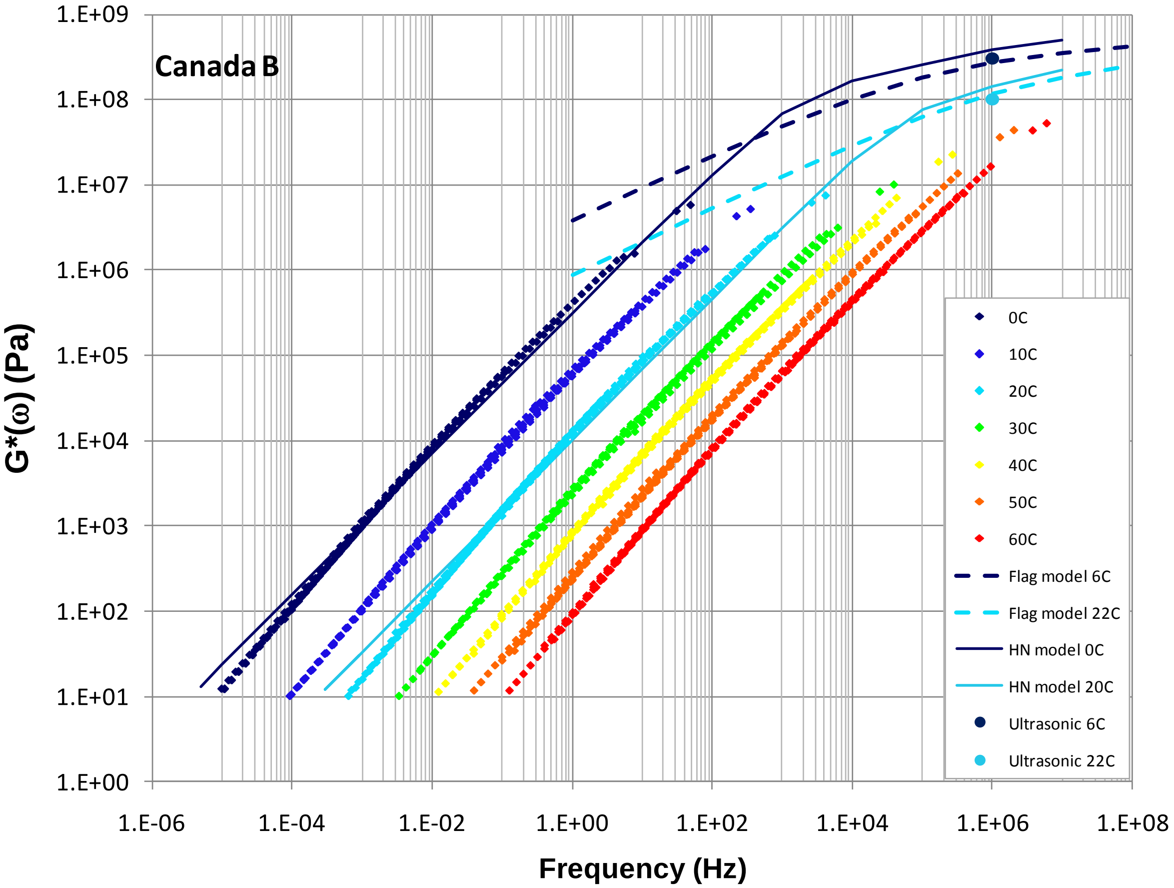

Figure 3.23. Comparison of complex shear modulus at ultrasonic and low frequencies for Canada B heavy oil sample.

For a better comparison between low-frequency and ultrasonic measurements, the ultrasonic shear modulus was estimated at 0°C, 10°C, and 20°C. This was based on the logarithmic function that fits the shear modulus variation with temperature, which was estimated from only two shear velocity measurements (Figure 3.24). The error estimated for each temperature between the ultrasonic (estimated) data and both models reveals that the FLAG model provides a better fit of the ultrasonic data. Figure 3.25 shows the comparison between low-frequency and ultrasonic data estimated at the same temperatures.

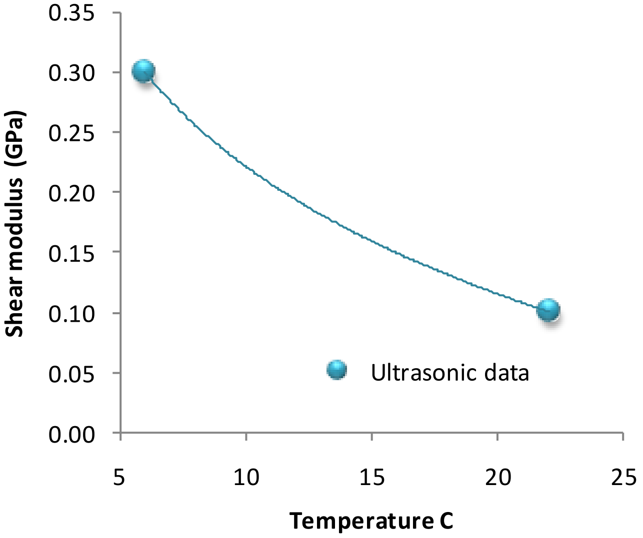

Figure 3.24. Complex shear modulus estimated from ultrasonic velocity measurements with respect to temperature for Canada B heavy oil sample. The logarithmic function was used to obtain G* at 0°C 10°C and 20°C.

Table 3.10. Comparison of Ultrasonic *(estimated),* FLAG model and new model at 1MHz. Columns 4 and 5 were calculated based on the difference in percentage between the experimental data, estimated at the same temperature as the rheological measurements were made, and the corresponding models.

Temperature (C)	Ultrasonic (Pa)	New model (Pa)	FLAG model (Pa)	Difference % (new)	Difference % (FLAG)
0	5.73 E+08	3.78 E+08	2.69 E+08	33.9	53.1
10	2.21 E+08	2.56 E+08	2.13 E+08	15.9	3.8
20	1.15 E+08	1.43 E+08	1.16 E+08	24.4	1.1

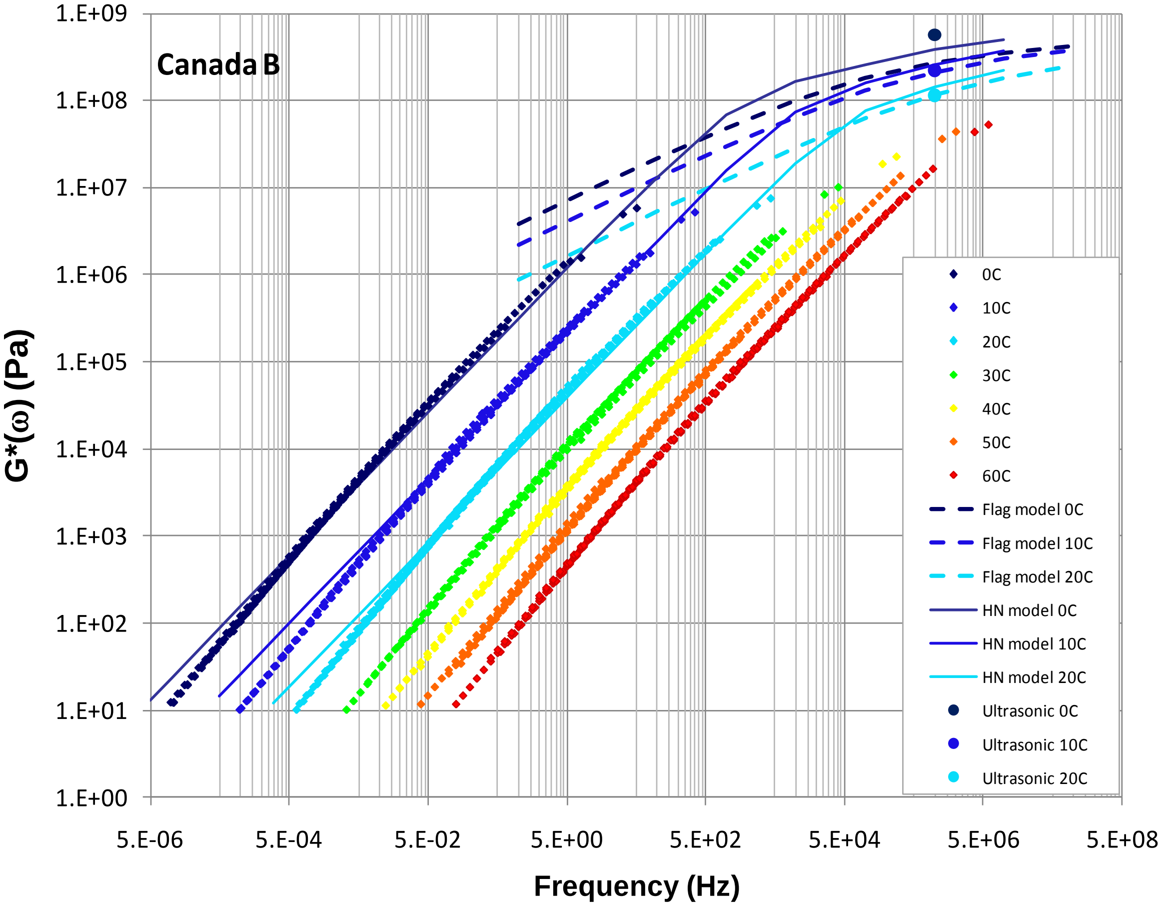

Figure 3.25. Comparison of complex shear modulus at ultrasonic and low frequencies for Canada B heavy oil sample at the same temperatures as the rheological measurements were made (0°C, 10°C and 20°C).

The proposed model in this study predicts accurately the rheological measurements from 0.001Hz to 1MHz with an error less than 10%. Once more, the new model overpredicts complex shear modulus at very low frequencies for each temperature curve. However, the new model fits well (R^2 >0.99) a broad range of frequency and temperature.

The fitting parameters: alpha (α), gamma (γ), infinite viscosity (η_∞), maximum shear modulus (G_{max}), activation energy (E_a), and isotropic temperature (T_I) are summarized in Table 3.11. Activation energy (E_a) for the Canada B sample is the highest of all the samples as is its density. The parameter T_I was again kept equal to 30°C (303K) for all samples. The G_{max} parameter was kept at 1GPa as all samples, except for the Brazil sample. The infinite viscosity was estimated based on rheological measurements. The empirical parameters, alpha and gamma, exhibit a small variation for the temperature range studied and both decrease with temperature. Only η_∞, G_{max}, α and γ parameters have a significant effect on complex shear modulus estimation.

Table 3.11. Fitting parameters of the new model for Canada B heavy oil sample.

T(C)	G_{max} (Pa)	η_∞ (Pa.s)	T_I (C)	E_a	Alpha (α)	Gamma (γ)	R^2
0	1 E+09	101000	30	4300	0.210±0.001	0.110±0.001	0.996
10	1 E+09	14400	30	4300	0.185±0.002	0.101±0.001	0.984
20	1 E+09	2400	30	4300	0.180±0.003	0.091±0.001	0.969
30	1 E+09	500	30	4300	0.176±0.008	0.078±0.001	0.931
40	1 E+09	350	30	4300	0.168±0.007	0.054±0.001	0.976
50	1 E+09	150	30	4300	0.163±0.003	0.040±0.001	0.999
60	1 E+09	35	30	4300	0.157±0.007	0.044±0.001	0.990

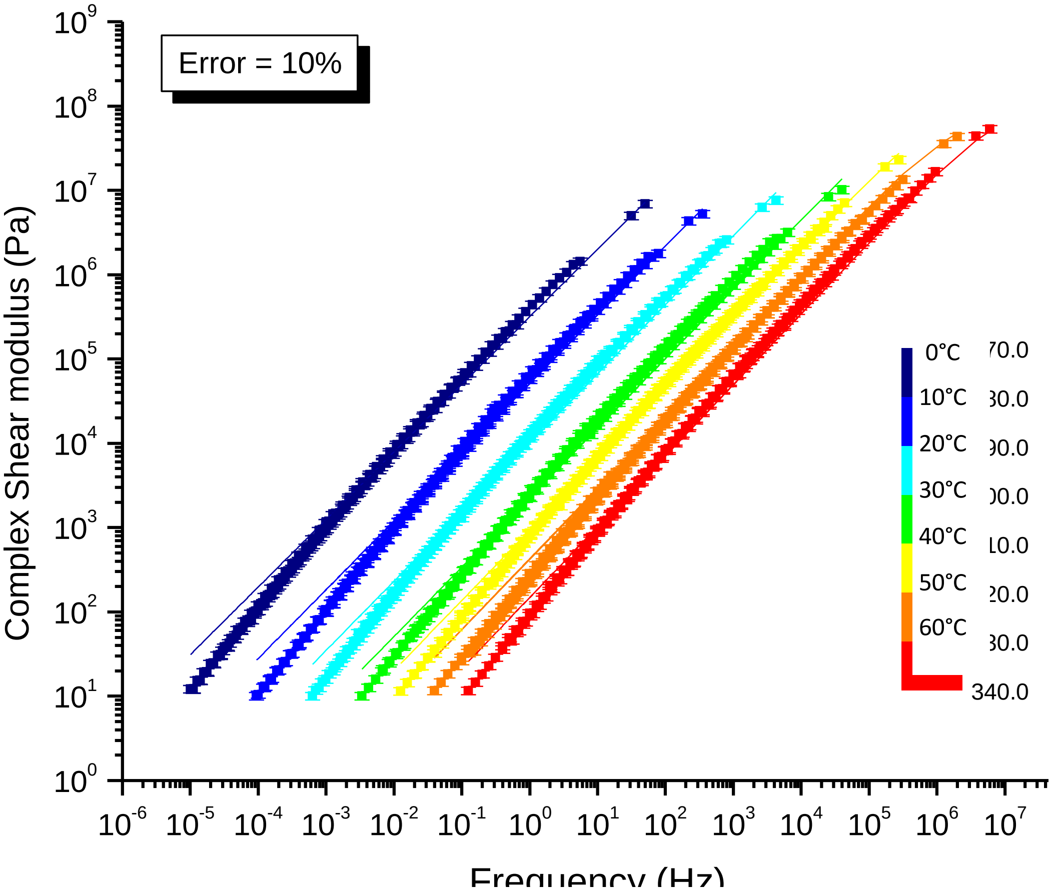

Figure 3.26. Comparison of rheological (low-frequency) measurements and the new model for Canada B heavy oil sample. Error bars corresponding to 10% were computed for the rheological measurements. The frequency range from 0.0001Hz to 1MHz is within the error bars.

3.6 Attenuation Coefficient: Models and Data

Three attenuation models were compared with the low-frequency rheological data: The power-law model, the Azimi 2nd model and the Azimi 3rd model. Of all the models, it seems that the power-law model provides a better fit for all the samples tested (Figure 3.27 – 3.30). The temperature curves to be fitted were chosen randomly: 40°C temperature curve in the case of Venezuela and Canada B heavy oil samples and 20°C temperature curve for Canada A and Brazil heavy oil samples.

The attenuation coefficient (α) was calculated from the rheological measurements following the expression:

$$\alpha = \frac{\omega}{2V_S Q} \qquad (43)$$

where Q was calculated from the ratio of the elastic storage modulus (G') over the viscous loss modulus (G") measured for each temperature and frequency.

On the other hand, equation 24 was used to calculate the attenuation coefficient given by the power-law model, which depends on two (2) constants that are associated with the temperature change: a and γ. However, the parameter γ can be considered as a constant since its variation is very small for the temperature range studied and varied for each sample as shown in Table 3.12. This means that only a needs to be varied in order to fit the measurements of each sample.

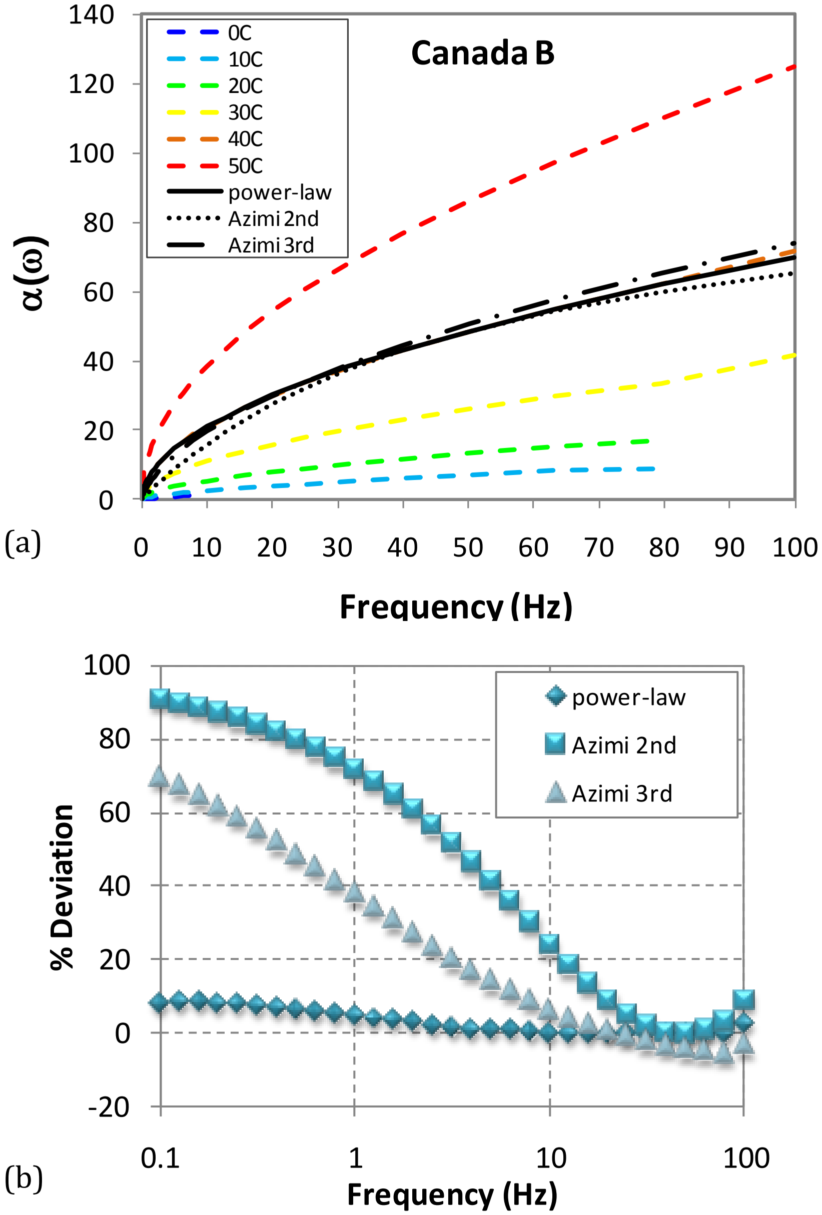

Figure 3.27. (a) Attenuation coefficient versus frequency. (b) Deviation of each model with respect to rheological data of Canada B heavy oil sample. Three models are used to fit the 40°C temperature curve. The best match is obtained using the power-law model.

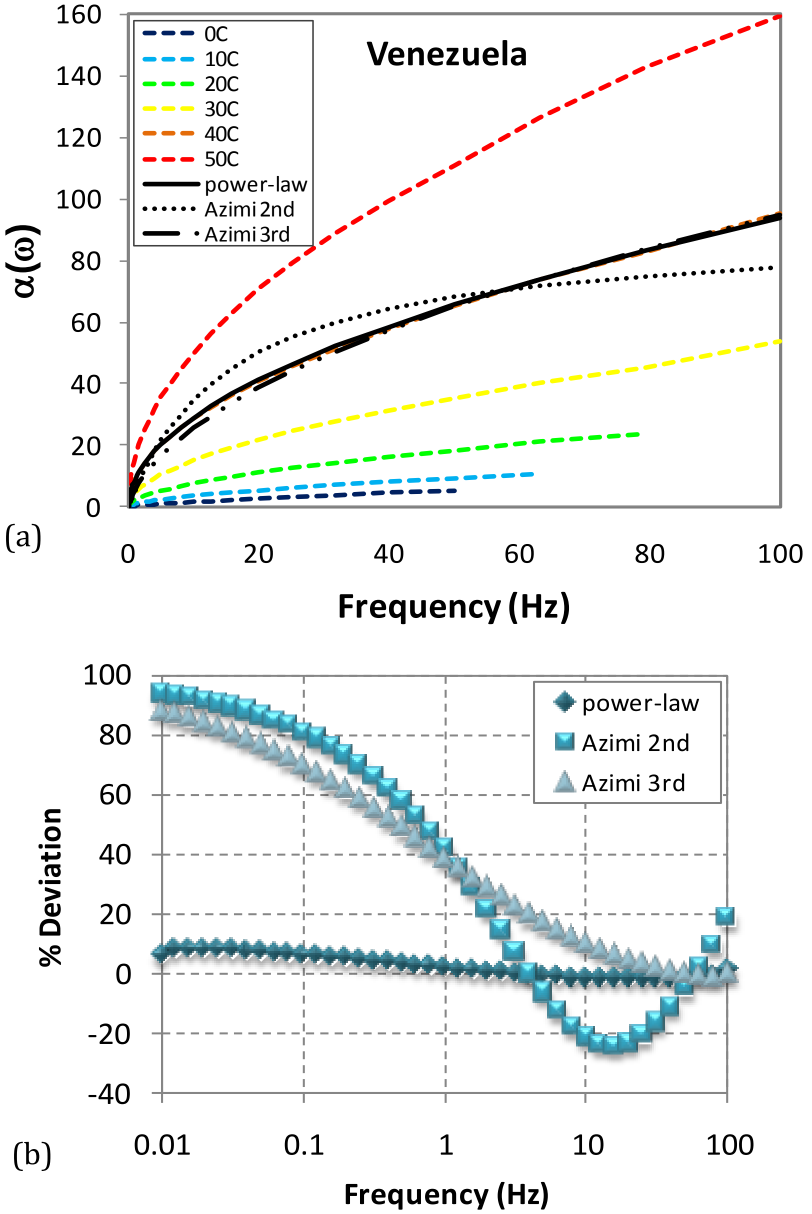

Figure 3.28. (a) Attenuation coefficient versus frequency (b) Deviation of each model with respect to rheological data of Venezuela heavy oil sample.

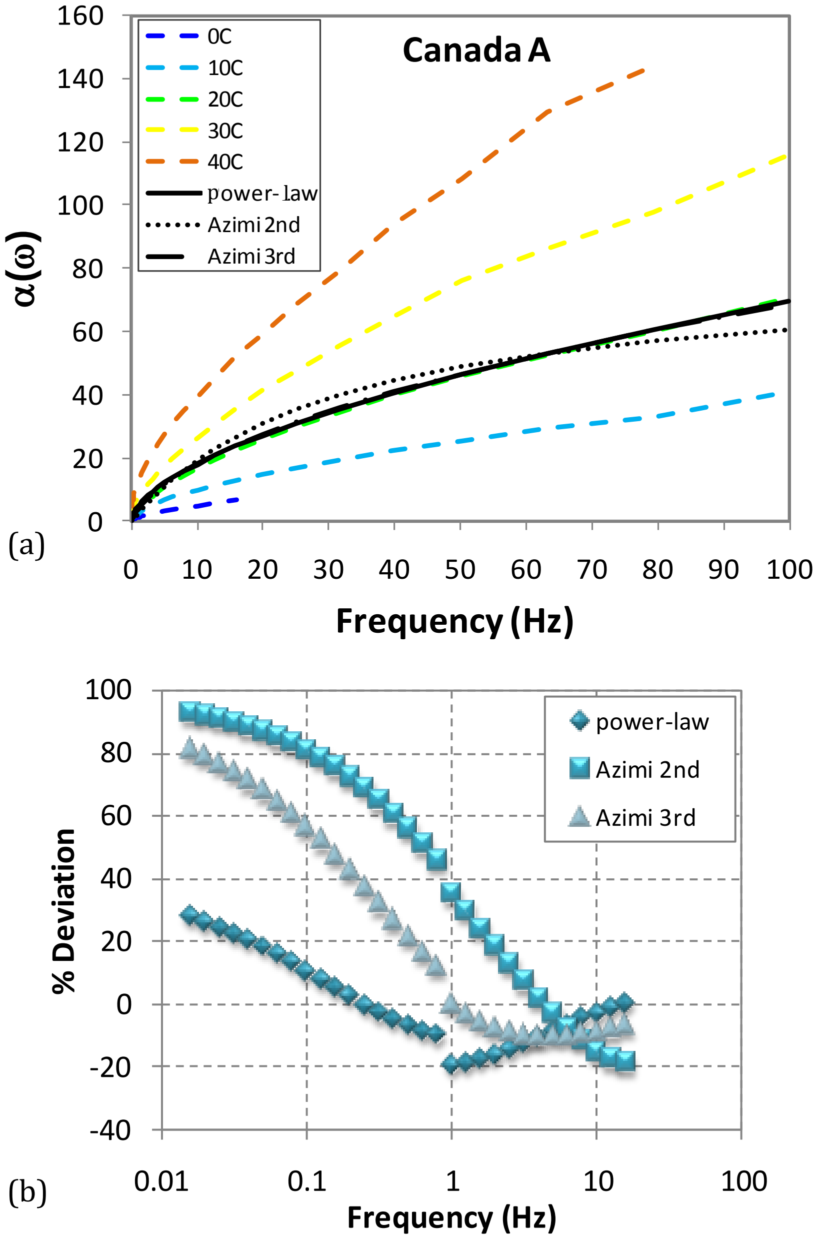

Figure 3.29. (a) Attenuation coefficient versus frequency (b) Deviation of each model with respect to rheological data of Canada A heavy oil sample.

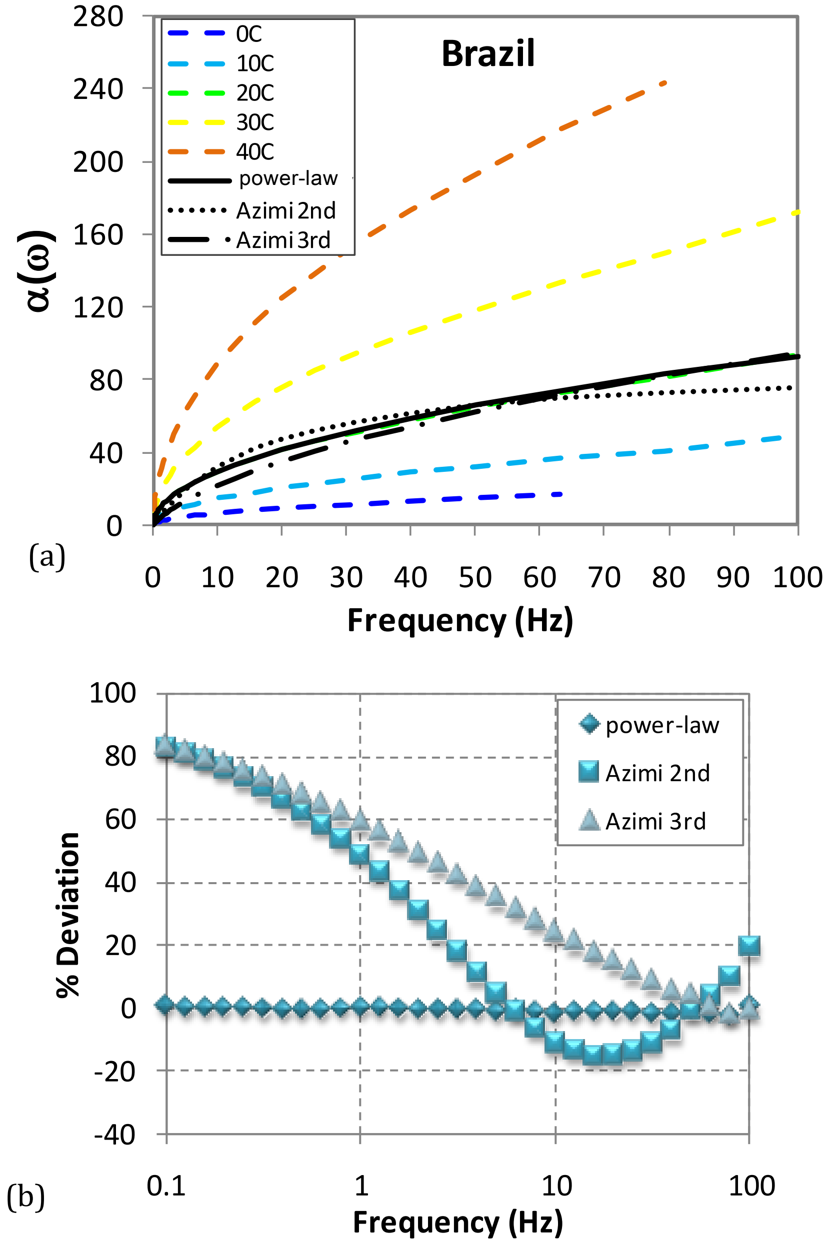

Figure 3.30. (a) Attenuation coefficient versus frequency (b) Deviation of each model with respect to rheological data of Brazil heavy oil sample.

Table 3.12. Gamma parameter for all the heavy oil samples tested.

Sample	gamma
Canada B	0.5
Venezuela	0.48
Canada A	0.39
Brazil	0.5

The parameter a will also vary with respect to temperature (expressed in Kelvin degrees) following a power law type of equation. Figure 3.31 not only shows that all samples except Brazil follow a very similar change of a with respect to temperature but also that this change might be directly affected by the sample density. In other words, samples with lower density such as Brazil, exhibit a drastic temperature effect on the parameter a and viceversa. Clearly, as temperature increases the proportion of the storage versus the loss modulus (Q) decreases, therefore increasing attenuation. It is important to note that attenuation (1/Q) significantly increases with frequency; therefore, attenuation models such as constant Q (Kjartansson, 1979) are not valid for fluids such as these heavy oil samples.

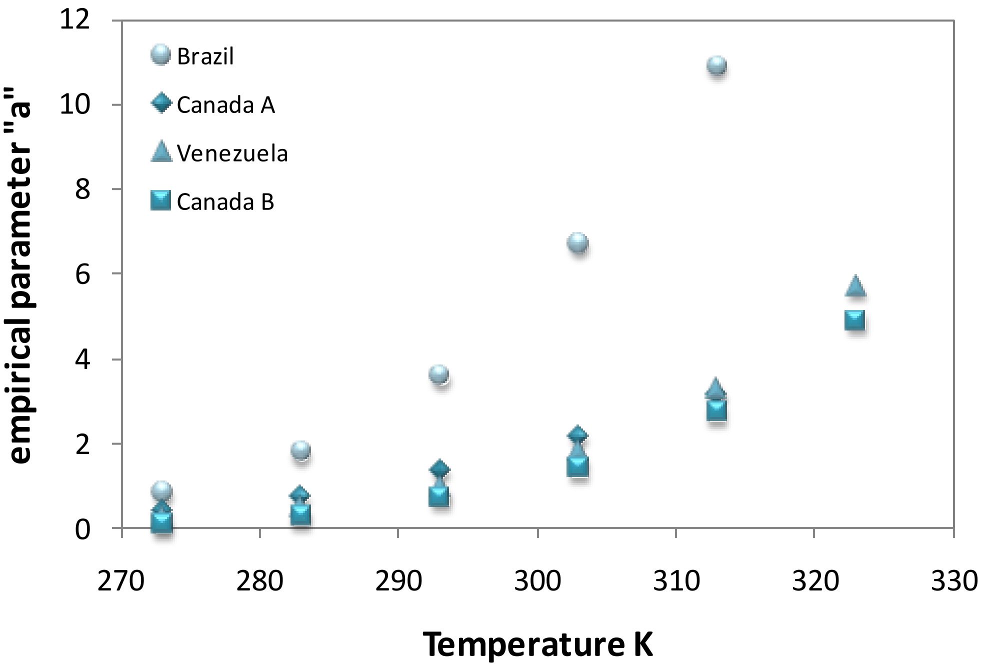

Figure 3.31. Empirical parameter “*a*” versus temperature (°K). Brazil heavy oil sample follows a different trend than the rest of the samples due to its density.

For all the samples studied (Figures 3.32 and 3.33), the attenuation predicted using the power-law attenuation model is not only very accurate ($R^2 > 0.99$) but also very simple since only one parameter is needed.

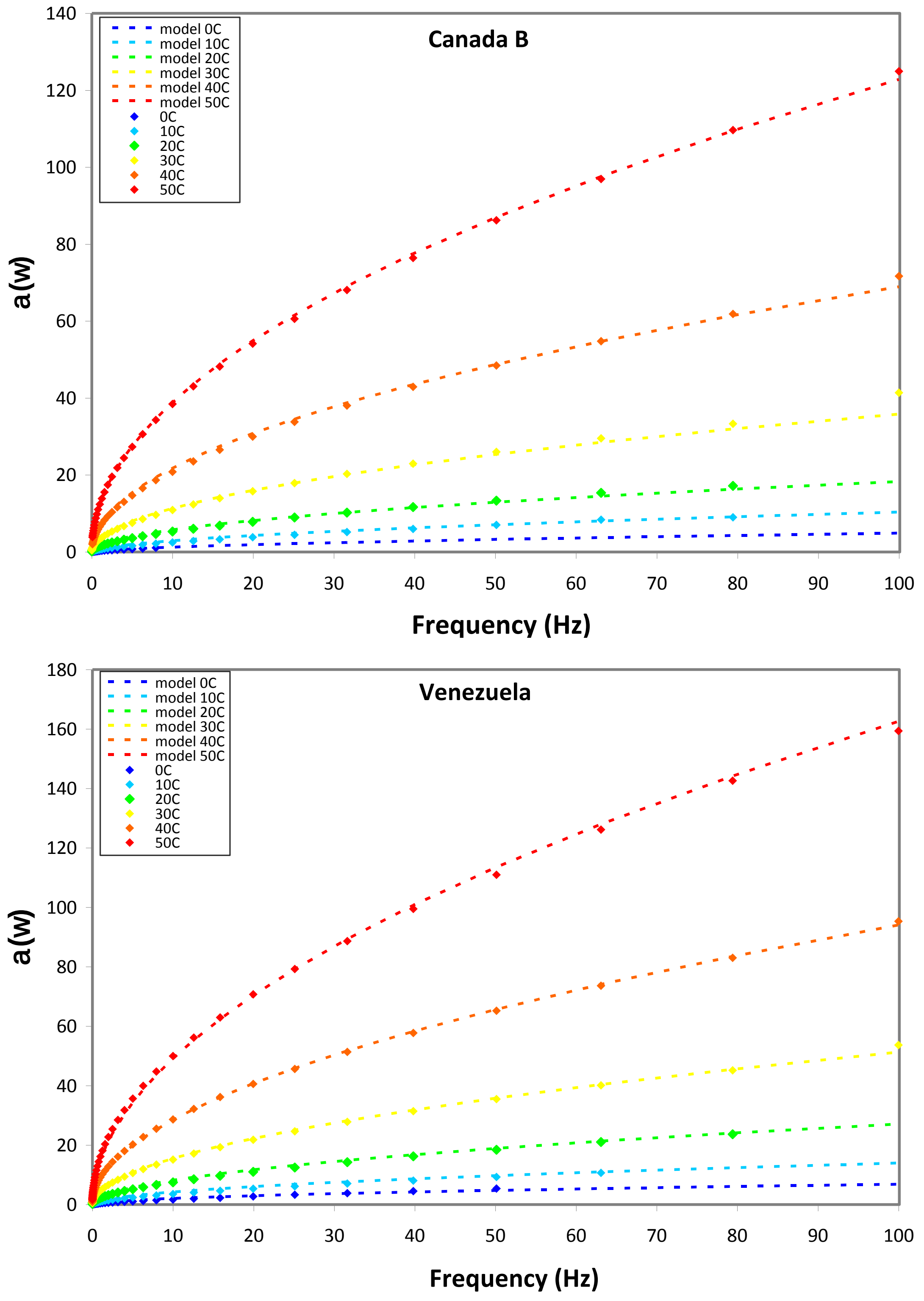

Figure 3.32. Attenuation coefficient versus frequency for (a) Canada B and (b) Venezuela heavy oil samples. The power-law model is applied by keeping “γ” constant and only varying “*a*”.

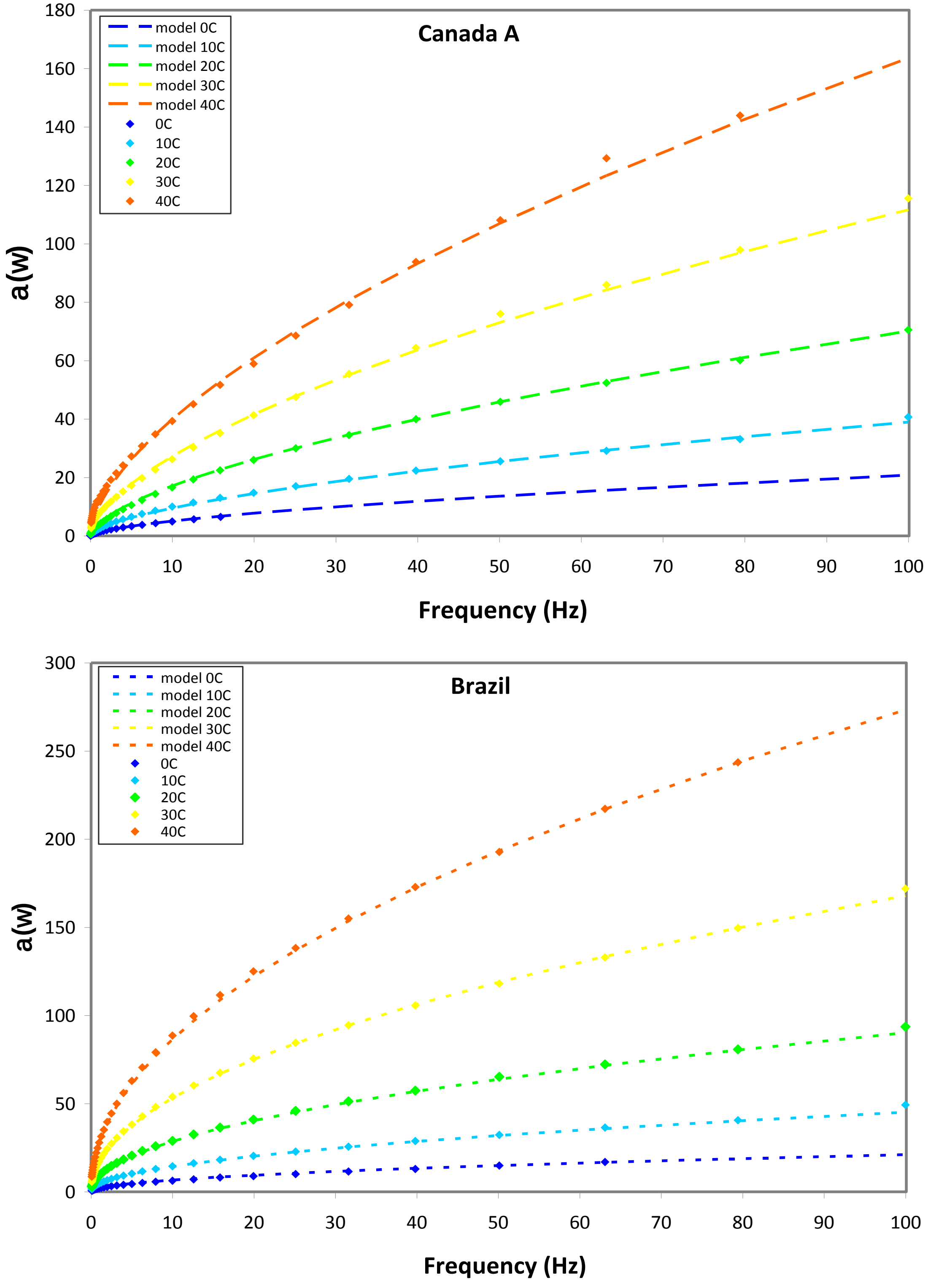

Figure 3.33. Attenuation coefficient versus frequency for (a) Canada A and (b) Brazil heavy oil samples. The power-law model is applied by keeping "γ" constant and only varying "a".

3.7 Causality Link between Attenuation and Shear Modulus

3.7.1 Frequency Effect

The Kramers – Kronig relations theoretically demonstrate the link between the attenuation peak and the maximum slope of the phase velocity, which is usually called the causality link. Basically, if there is no frequency dispersion on the velocity and/or modulus, the attenuation is not frequency dependent (Castagna, 2010 personal communication). This has been observed for a rock saturated with a fluid; however, it seems to be valid also for heavy oils, although an asymmetric peak on the quality factor is observed.

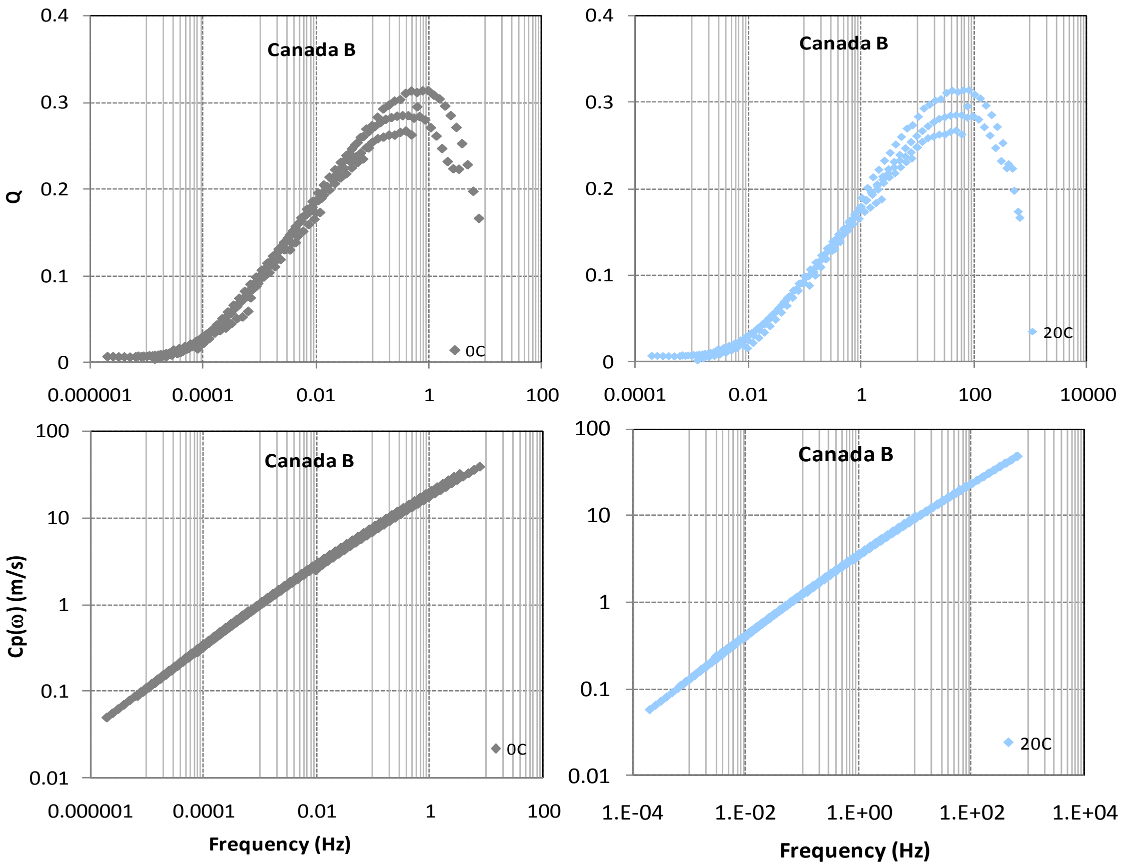

Figure 3.34. Frequency effect on causality: velocity dispersion versus attenuation for Canada B heavy oil sample.

Theoretically, at infinite and very low frequencies the velocity curve remains constant; this helps to determine where the maximum slope of the curve is located. In this study, even after using the time-temperature superposition principle, where I was able to increase (depending on temperature) the original frequency range of the measurements from approximately 10^{-5} Hz to 10^{4} Hz, the region where phase velocity remains constant, was not observed. Figure 3.34 to 3.37 shows the causality link between quality factor and shear velocity at 0°C and 20°C for all the heavy oil samples.

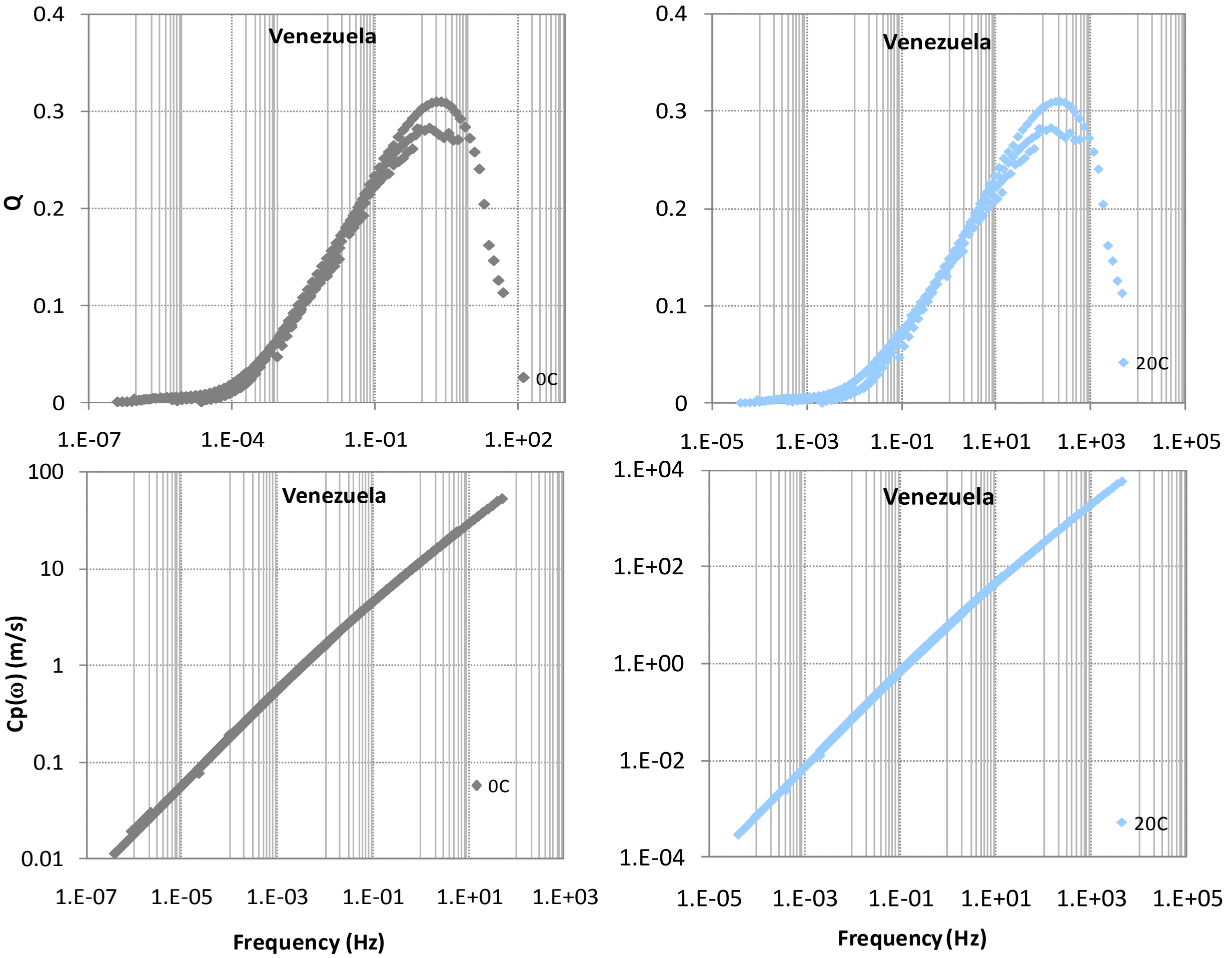

Figure 3.35. Frequency effect on causality: velocity dispersion versus quality factor for Venezuela heavy oil sample.

The peak of quality factor coincides with the frequency at which the elastic component starts decreasing due to the shear thinning phenomenon. The viscous component, on the other hand, seems to not be affected by this frequency. At very low frequencies (or high temperatures), the quality factor approaches to zero since the shear wave cannot “propagate” through the sample. The peak of the quality factor shifts to higher frequencies as temperature is increased, which again confirm that is a thermally activated process and therefore the activation energy can be estimated using Eyring’s equation. Similar results were found by Spencer in 1981.

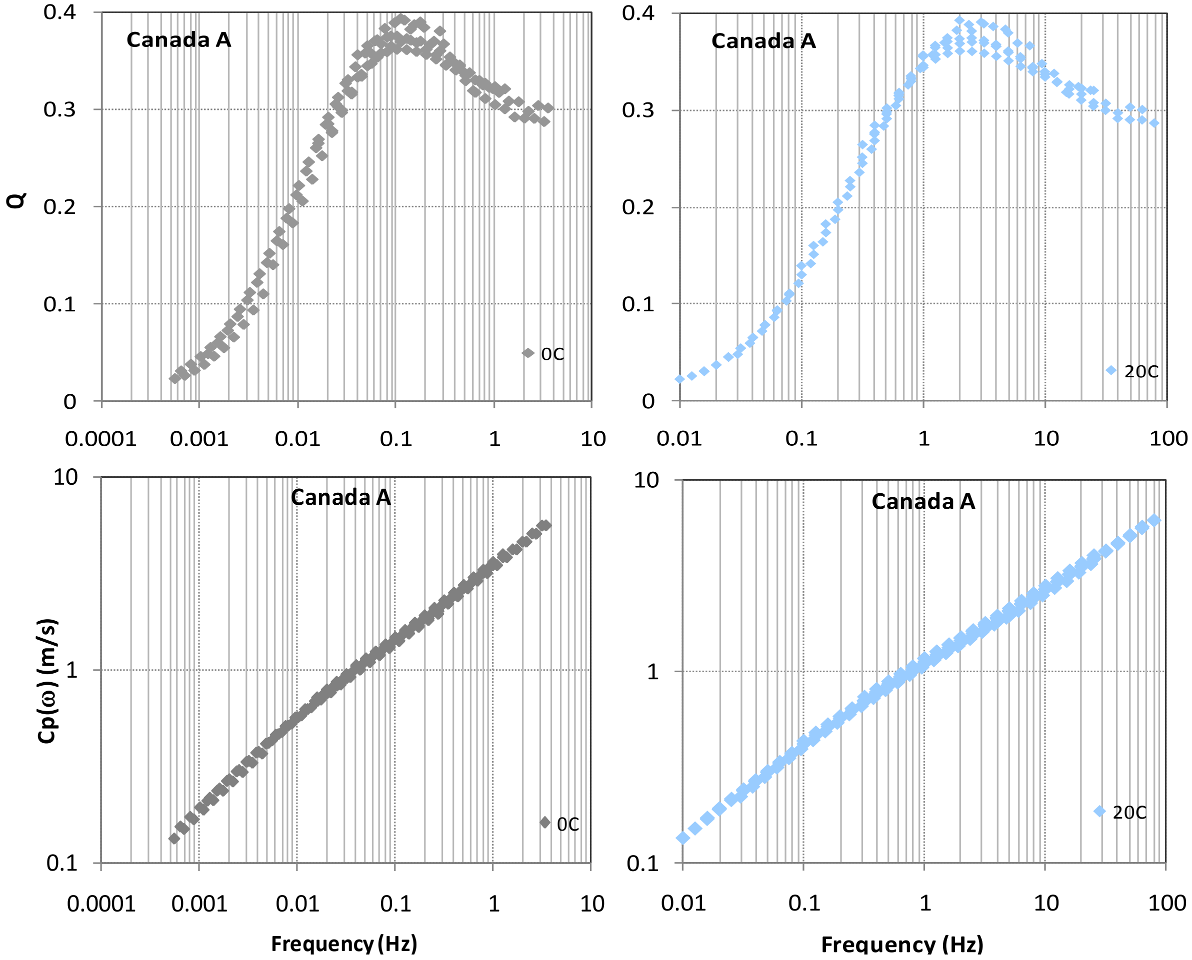

Figure 3.36. Frequency effect on causality: velocity dispersion versus quality factor for Canada A heavy oil sample.

The magnitude of the quality factor and the center frequency presented by Canada B, Venezuela and Canada A heavy oil samples are very similar but once again, the Brazil sample (presumably due to its lower density) has a higher magnitude and center frequency. Dielectrical and electrochemical properties affect these properties besides density (Spencer, 1981); however, no significant differences are expected in that regard between Brazil and the rest of the samples.

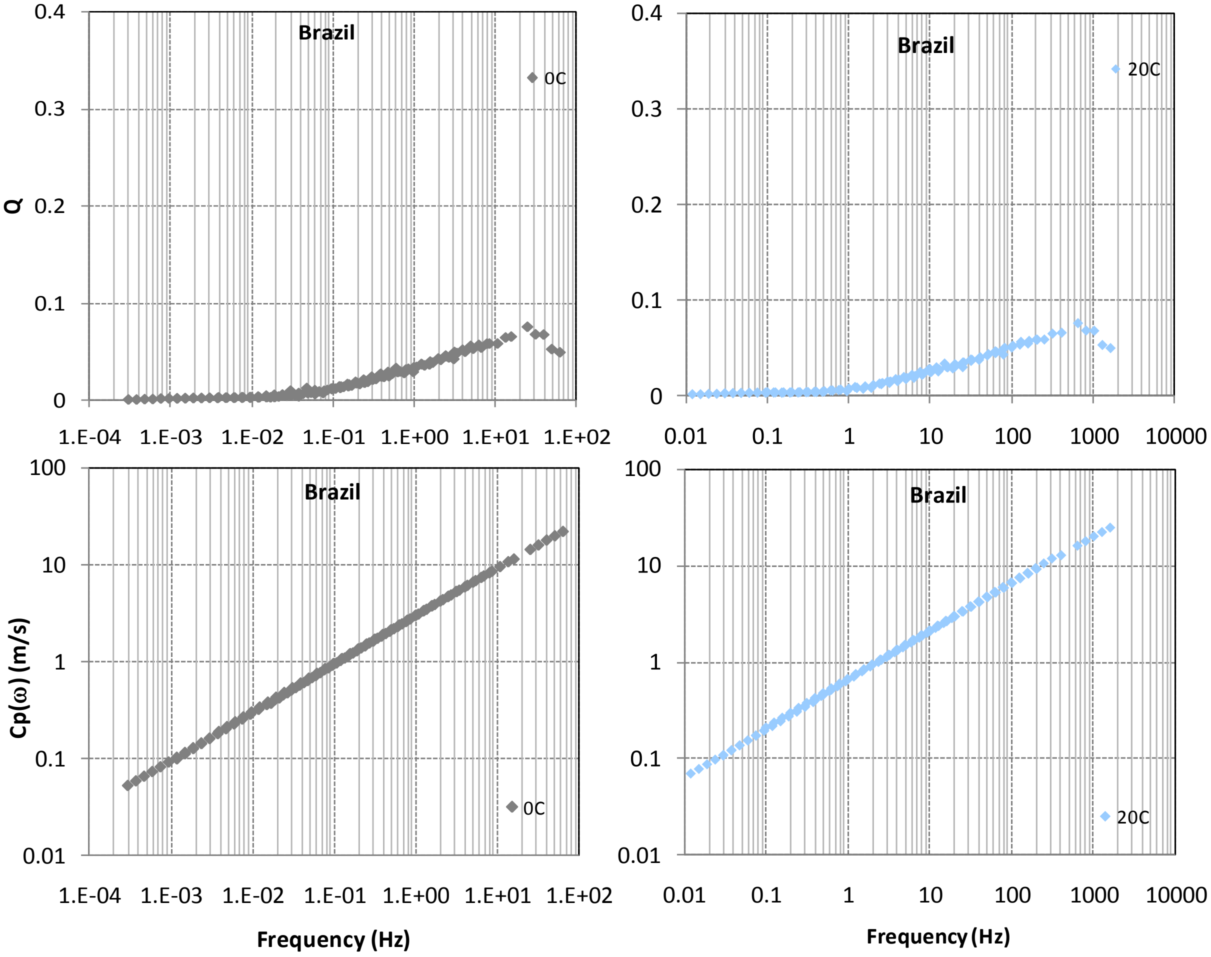

Figure 3.37. Frequency effect on causality: velocity dispersion versus attenuation for Brazil heavy oil sample.

3.7.2 Viscosity and Strain Effect

The Kramers – Kronig relations are theoretical equations that prove the link between stress relaxation and attenuation as both vary with frequency. However, they are not only valid when compared with respect to frequency but also when compared to other properties. Dvorkin (2005) lists over 7 different properties where these equations are still valid: porosity, viscosity, temperature, confining and pore pressure, strain amplitude, scale of inhomogeneity, and water saturation. In this work, heavy oils also comply with the same equations when compared with respect to viscosity and strain. Figures 3.38 and 3.39 show viscosity as another property where causality is observed whereas Figure 3.40 and 3.41 show strain.

In Part 1, it was shown that heavy oils are linear viscoelastic fluids that follow an "Arrhenius behavior" since the correlation between viscosity with respect to temperature can be described (approximately) by one activation energy or relaxation time. This fact is what makes it possible to use the time – temperature superposition principle and therefore use temperature and frequency as exchangeable properties. If viscosity is inversely correlated with temperature and, temperature and frequency are also inversely correlated, then it makes sense that the Kramers – Kronig relations or the causality prevails when plotted against viscosity.

Attenuation decreases as velocity increases but it does not decrease uniformly with frequency when plotted against viscosity, in fact at 80Hz it seems that attenuation increases again but only in the Canada A heavy oil sample this phenomenon is well observed. Velocity on the other hand, always increases with frequency.

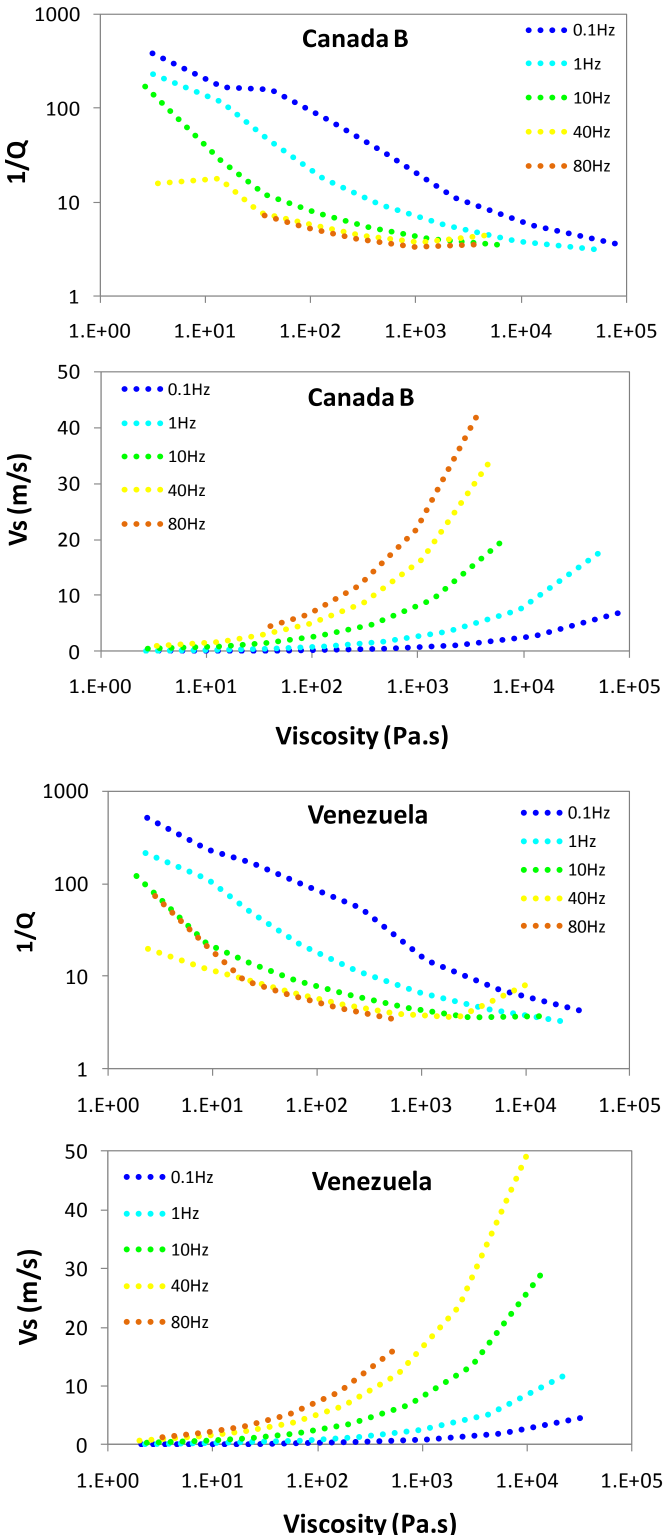

Figure 38. Attenuation (1/Q) and Velocity vs. **viscosity** for Canada B and Venezuela heavy oil samples.

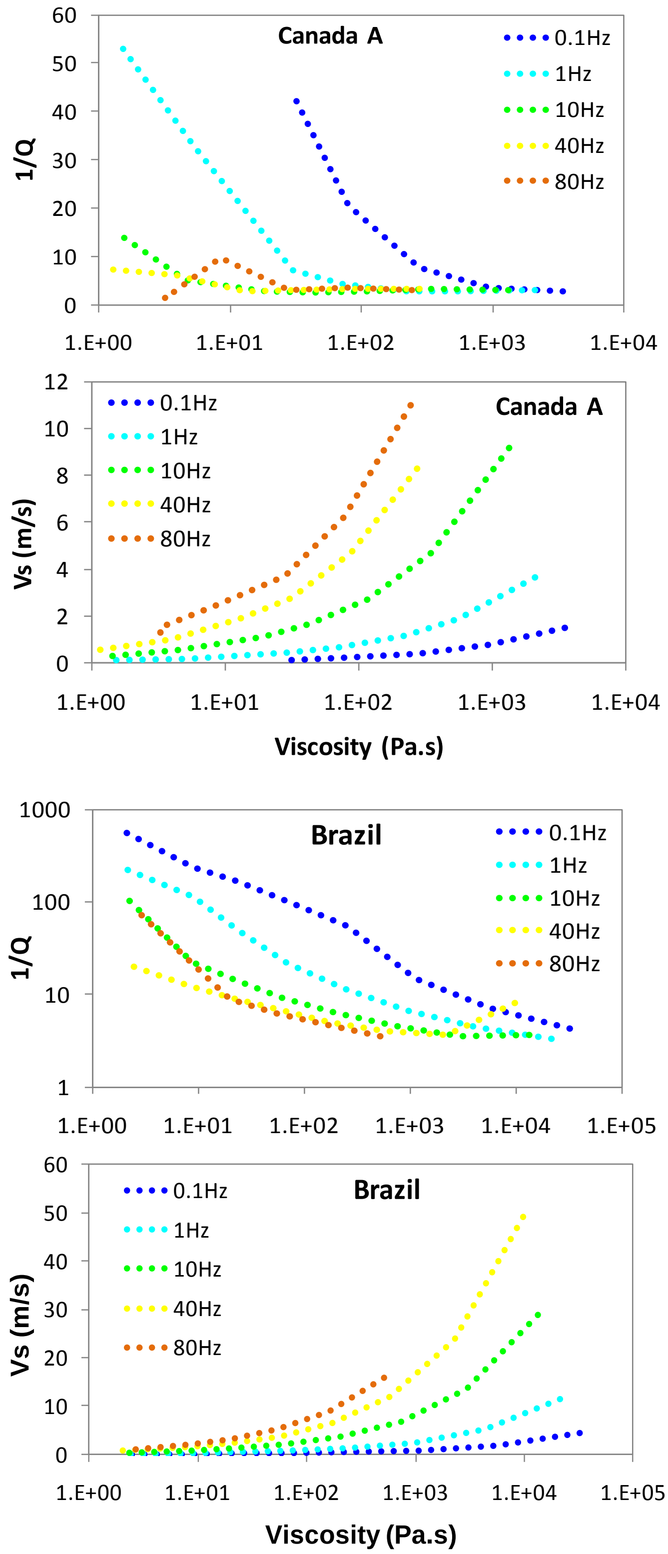

Figure 3.39. Attenuation (1/Q) and Velocity vs. **viscosity** for Canada A and Brazil heavy oil samples.

Figures 3.40 and 3.41 show that attenuation for viscoelastic fluids at strain amplitudes corresponding to seismic wave propagation exists and is approximately constant. On the other hand, the modulus and/or velocity are less dependent on strain for low strain amplitudes. Once again, the link between attenuation and stress relaxation is clear when compared to strain.

It is important to note that in these figures, no time – temperature superposition was applied; therefore, this is the actual data measured for each sample.

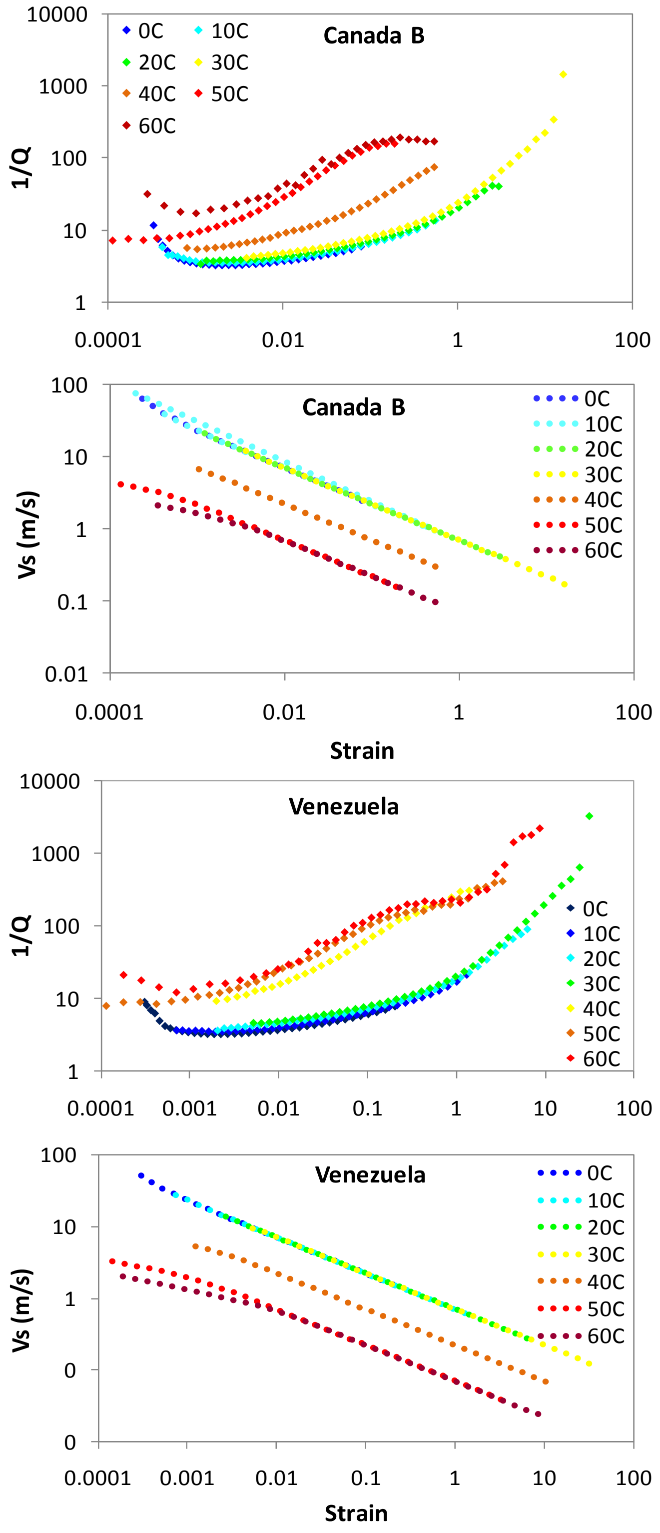

Figure 3.40. Velocity and attenuation (1/Q) versus **strain** for Canada B and Venezuela heavy oil samples.

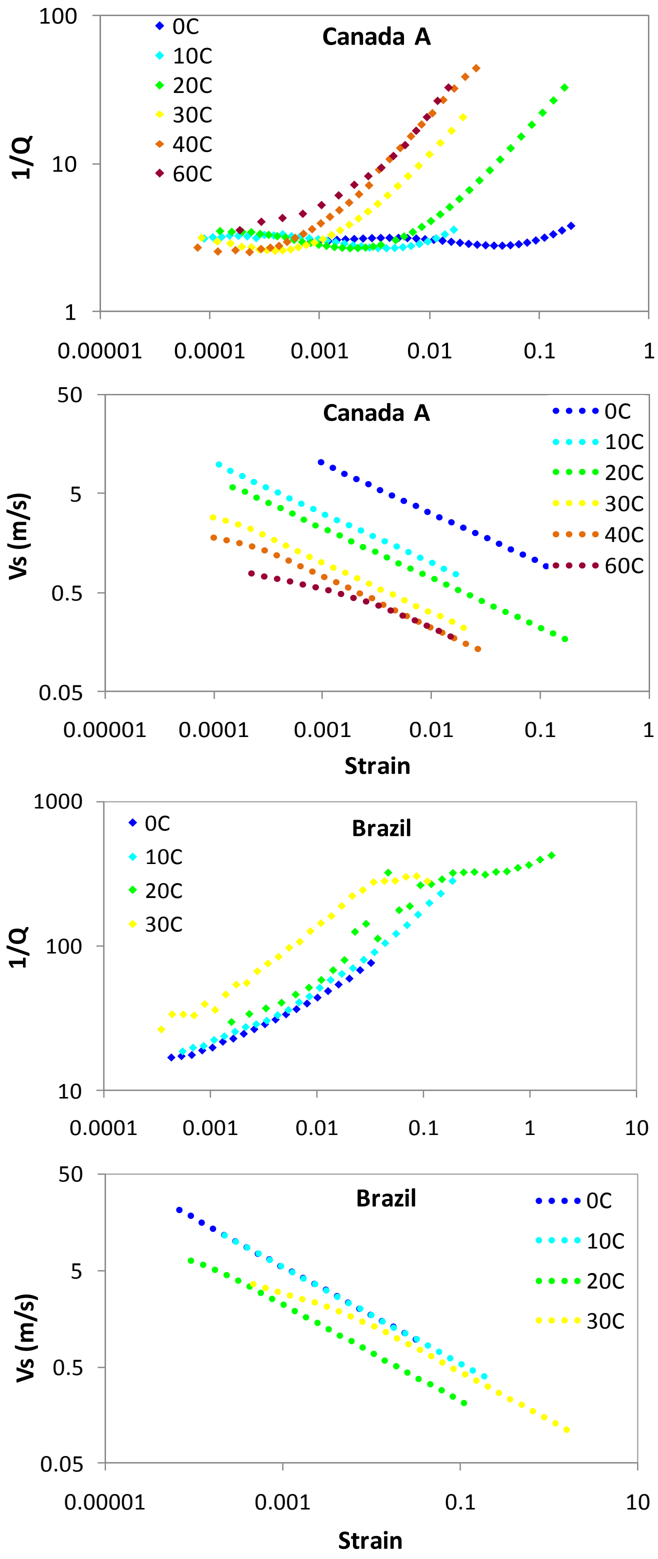

Figure 3.41. Velocity and attenuation (1/Q) versus **strain** for Canada A and Brazil heavy oil samples.

Part 4

Finite Element Modeling of a Heavy Oil Reservoir for Fracture Characterization

This chapter focuses on a new methodology to characterize the porous space (fractures) of a heavy oil carbonate reservoir using the finite element method. The input data consists of well-log information from 18 wells. Some of the logs used are Sonic Scanner, Formation MicroImager (FMI), gamma-ray, porosity, density, and saturation logs. Different geological formations were modeled: shales, limestones, and dolostones.

The finite element modeling, based on the Partition Theorem, estimates the effective properties of fractured media, which can be represented by bulk density, P-wave velocity, shear-wave velocity, and the Thomsen or other anisotropy parameters. This information was used to generate velocity-porosity correlations for each formation, which along with sonic data from each well, can potentially be used to generate fracture porosity logs.

A 3D subsurface model of the carbonate field was generated to map qualitatively the changes of fracture porosity. The model is consistent with the geological model interpreted in the area.

4.1 Finite Element Modeling (FEM)

Mathematically, analytical solutions are only possible for idealized problems, very different from those found in real applications. More complicated geometries, material properties, boundaries conditions etc., require numerical models. The finite element method solves numerically partial differential equations (PDEs) by approximating the equation to be solved with another numerically stable equation.

The advantage of FEM is evident when it is necessary to solve complex elasticity equations over complicated geometries or domains that require discretization into sub-domains or elements (Figure 4.1). This is usually called meshing. The system, which can be, for instance, a reservoir rock, a pipe or any other structure, is divided into **finite elements** interconnected by points called nodes. These elements can have tetrahedral or hexahedral shapes and can also represent physical properties such as elastic moduli, density, temperature, etc.

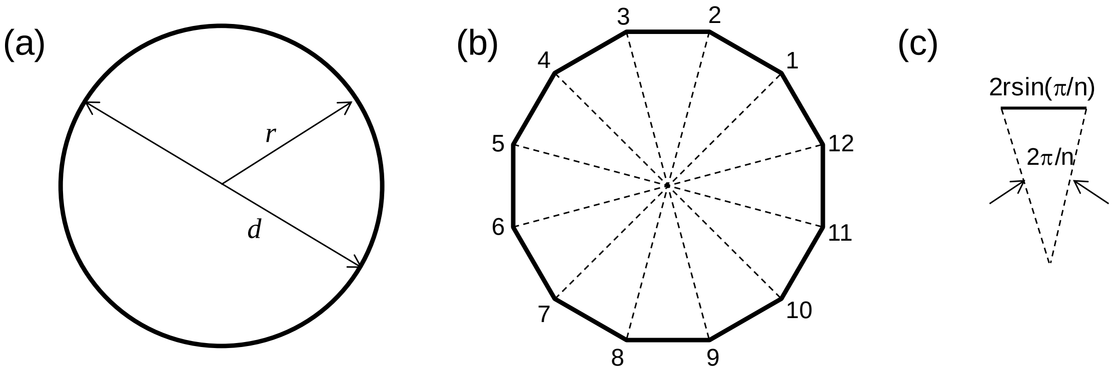

Figure 4.1. FEM basis. (a) A continuum material. (b) A discrete approximation. (c) A generic element (from Zienkiewicz et al., 2005).

The COMSOL Multiphysics software was used to run FEM along with adaptive meshing and error control.

4.1.1 The Effective Medium

The objective of the finite element modeling is to investigate the overall elastic behavior of fractured rocks, or in other words, the effective medium properties that characterize a volume V for a certain scale of interest. The effective stiffness tensor can be described through the Hooke’s Law:

$$\sigma(x,\omega) = C(x)\dot{\varepsilon}(x,\omega) \tag{1}$$

where the stress (σ) and strain (ε) tensors depend not only on position (x) but also on the frequency (ω). Both tensors are described in terms of volume averages (Christensen, 1979; Hudson, 1991; Grechka, 2003) as follows:

$$\langle \boldsymbol{\sigma} \rangle = \tfrac{1}{V}\textstyle\int_V \ \sigma\,(x)dx \tag{2}$$

$$\langle \boldsymbol{\varepsilon} \rangle = \frac{1}{V}\int_V \ \varepsilon\,(x)dx \tag{3}$$

However, in this study the long-wave approximation was assumed; therefore, no frequency dependence is included. The equation of motion can be written as:

$$\frac{\partial}{\partial x_j} C_{ijkl}(x)\frac{\partial u_k}{\partial x_l} + \rho(x)\omega^2 u_i = 0 \tag{4}$$

where i=1,2,3. The elastic stiffness tensor C and the density ρ represent the properties of a heterogeneous solid that occupies a volume V.

The modeling solves the equation of motion numerically by applying homogenous stress (traction) and homogeneous strain (displacement) boundary conditions, which allows the estimation of the upper and lower bounds of the resulting effective properties (Grechka and Rojas, 2007).

In general, a material may appear as homogeneous on a higher scale of observation but at the same time, it may appear as heterogeneous on a lower level or scale of observation. This type of material is usually referred as a composite material that has effective properties (Figure 4.2). However, in a strict sense, the true effective properties can be only estimated for the representative volume element (RVE). According to Gitman (2006), the RVE is the "minimum material volume that contains sufficient (mathematically infinite) information about the microstructure (e.g. pores) in order to be representative but, it is much smaller than the macroscopic body". The RVE is statistically homogeneous and independent of boundary conditions.

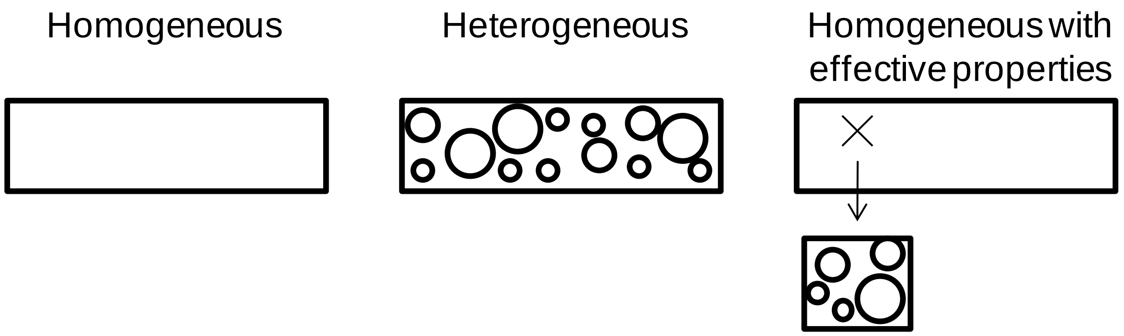

Figure 4.2. An effective medium can be defined as a homogeneous or heterogeneous material depending on the scale of observation (from Gitman, 2006).

4.1.2 Effective Medium Theories

The response obtained from the modeling can be compared with different effective medium theories such as Differential Effective Medium (DEM) and the Non-Interaction Approximation (NIA). Effective medium theories usually agree on the effective properties for low concentration of inclusions; however, large discrepancies are expected once the number of inhomogeneities increases. Most of these theories treat the fractures as cavities.

- **Differential Effective Medium Theory (DEM)**

This theory models two-phase composites by incrementally adding inclusions of one phase to the matrix phase (Zimmerman, 1991) which is represented in Figure 4.3. However, this theory can be generalized to multiple phases. The DEM scheme requires the solution for one crack in the effective matrix; therefore, it is limited to models where such solutions are known: overall isotropy (random orientations) and a single set of parallel cracks in an isotropic matrix. This seems to be too restrictive for typical geophysical applications. The prediction can be expressed by two linear differential equations with initial conditions:

$$\begin{aligned} K^*(\phi) &= K_m \\ \mu^*(\phi) &= \mu_m \end{aligned} \qquad (5)$$

which can be solved numerically (Berryman, 1992):

$$\begin{aligned} (1-\phi)\frac{d}{d\phi}[K^*(\phi)] &= -K^*(\phi)P^* \\ (1-\phi)\frac{d}{d\phi}[\mu^*(\phi)] &= -\mu^*(\phi)Q^* \end{aligned} \qquad (6)$$

where Q and P are functions of the matrix bulk modulus (K_m) and shear modulus (μ_m).

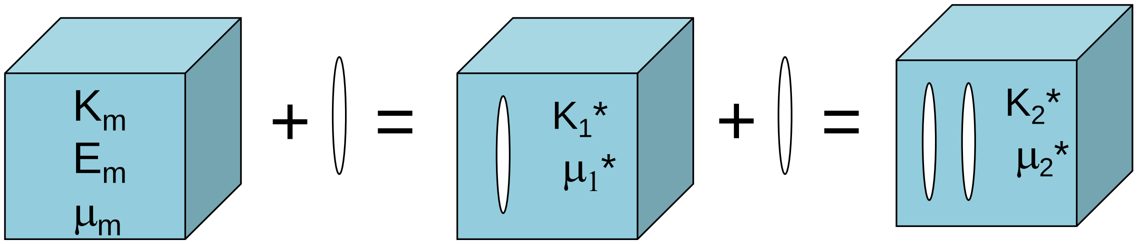

Figure 4.3. Differential effective medium scheme. Effective properties are estimated by adding one inclusion at a time.

Norris (1985) showed that the DEM is always consistent with the Hashin-Shtrikman upper and lower bounds.

- **The Non-Interaction Approximation (NIA)**

The basis of NIA is that stress distributions for each fracture are not affected by the presence of other fractures. Therefore, the contribution to the overall compliance (inverse of stress) can be simply summed up as shown in the following equation (Grechka and Kachanov, 2006):

$$s_e(e) = s_b + \Delta_s \qquad (7)$$

where s_e corresponds to the effective compliance of the rock, s_b is the background compliance (matrix) and Δs is the sum of the compliance of each fracture.

Some of the properties of the theory include:

1. Aspect ratios do not affect the effective properties (dry cracks) but they do affect permeability.
2. It is assumed that geometrical intersection of the fractures as well as fracture shapes and their jaggedness can be safely ignored while computing the effective elasticity (Grechka and Kachanov, 2006).

These properties were, in fact, the result of numerous numerical models (Grechka and Kachanov, 2006; Grechka, 2007; Grechka and Rojas, 2007) that show that the even though the assumption of non-interaction is violated (high concentration and intersecting cracks), the NIA is capable to handle these complexities in some cases, since it remains sufficiently accurate in the entire range of the crack densities employed.

Figure 4.4 shows the normal stress distribution on the x direction (τ_{11}) when using finite element modeling for a group of penny-shaped cracks. Here, we can observe two types of interactions, amplification and shielding. Amplification corresponds to the highest stress that the inclusion can support (usually at the tip of the inclusion) whereas shielding corresponds to the most compliant part of the inclusion. Both interactions interfere partially canceling each other, which turns out to be the reason of the agreement between the modeling and the non-interaction approximation theory.

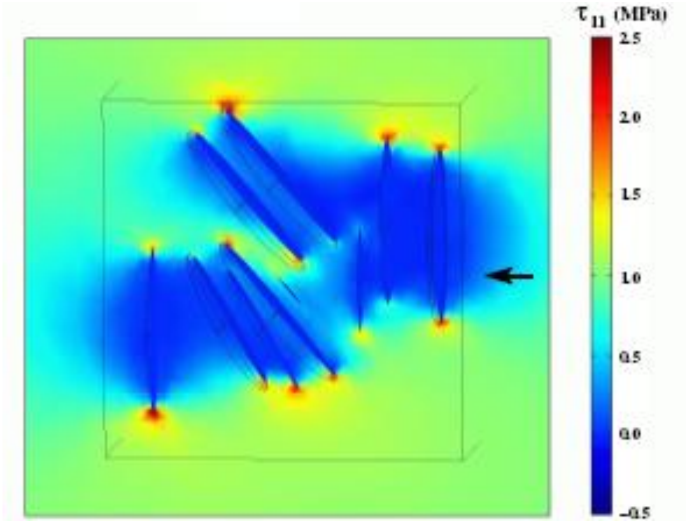

Figure 4.4. Stress distribution. Two types of interaction exist, *shielding* (blue), which correspond to the compliant sector of the inclusion and *amplification* (red) that refers to the stiffest part of the inclusion. Grechka and Kachanov, 2006.

4.1.3 The Numerical Modeling

The numerical modeling is based on the representative volume element (RVE) concept but also on the Partition Theorem (Huet, 1990). This theorem states that different static boundary conditions result in different apparent stiffness tensors (Grechka and Rojas, 2007). However, applying homogeneous stress and homogeneous strain boundary conditions result in the lowest and highest possible value of the stiffness tensor, which will converge to the effective stiffness tensor as the number of inhomogeneities increases and the volume V approaches the RVE (Grechka and Rojas, 2007).

It is important to note that different components of the elastic stiffness tensor will converge at different rates to the effective elastic stiffness tensor (Ostoja-Starzewski, 2006; Grechka and Rojas, 2007). The partition theorem is hierarchical, since each sub-model (partition) not only derives from the whole (parent) model but also each partition is equally representative of the parent model.

The modeling depends on the number, distribution and size of inclusions as well as the stiffness contrast between the host matrix and the inclusions (fractures). Figure 4.5 shows the dependence of the bounds on the number of fractures for a certain elastic coefficient. For a small number of fractures, a high variability of the elastic properties is expected, but as the number of fractures is increased, the rock becomes more homogeneous until the effective medium is achieved. At that point, both bounds converge and no need for averaging the response from the bounds is necessary.

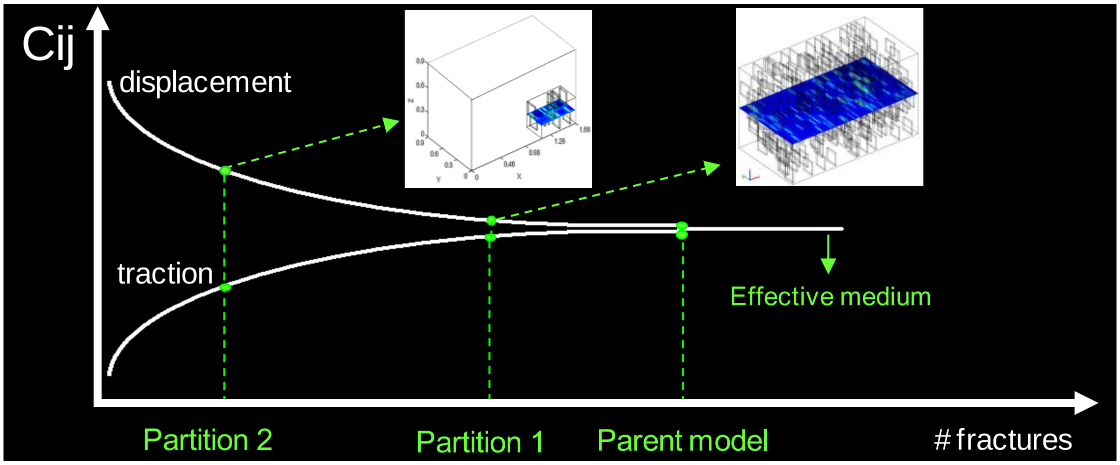

Figure 4.5. Scale dependent bounds (displacement and traction) determine the elastic properties. An example of a parent model as well as a partition model is shown.

The remote stress boundary conditions are simulated by applying constant loads to the faces of a homogeneous cube with matrix properties and envelopes a fractured volume. This approach is called the framing method in computational mechanics (Grechka, 2003).

The modeling requires as input data compressional velocity, shear-wave velocity and density for the rock matrix. Also, it requires the number of fractures, aspect ratio and type of pore infill. It is important to note that the code is able to create different arrays by placing randomly orientated fractures inside of the “digital rock”. Different arrays generate variations of the stiffness tensor; therefore, it is important to average the result for different arrays for more consistent effective properties.

The elastic stiffness tensor obtained is then used to estimate the vertical compressional and shear-wave velocities calculated from the C_{11} and C_{33} stiffness coefficients and the density of the so called digital rock.

The result was compared with the prediction given by the DEM and NIA theories (Figure 4.6). Even though both theories assume a low concentration of inclusions, they both agree with the results obtained from the numerical modeling. Here, it is also evident how both limits converge as the number of fractures increases. However, even for a small number of inclusions the error on P and shear-wave velocities is about 10%.

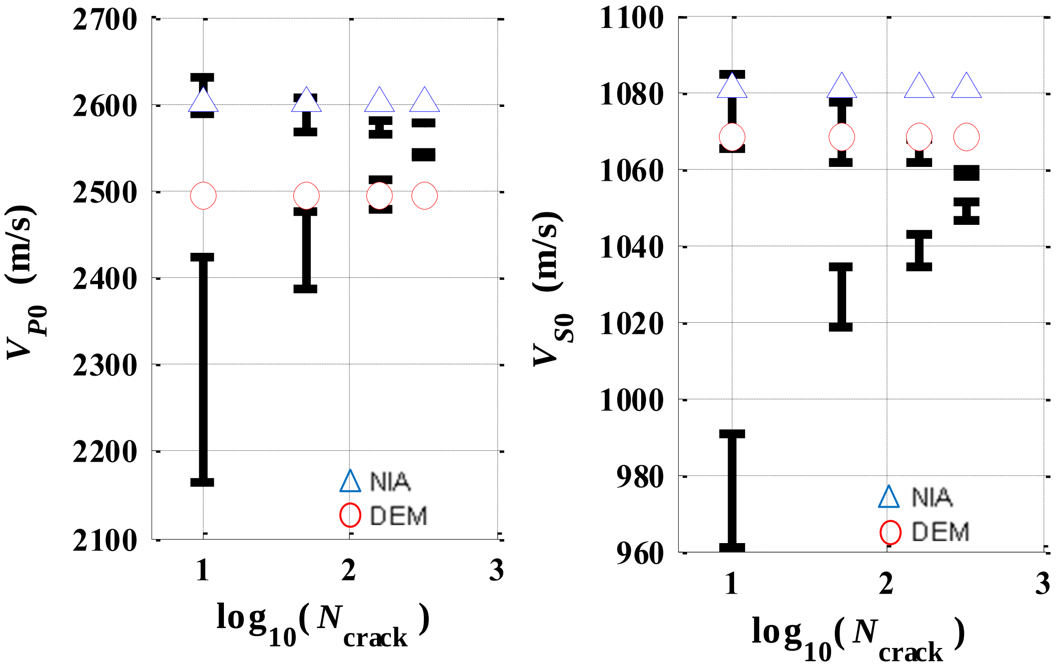

Figure 4.6. Comparison between effective medium theories (NIA and DEM) and numerical modeling for vertical P-wave and S-wave velocity estimation. The error bars (black) correspond to upper and lower bounds resulting from the modeling plus two (2) standard deviations.

Once again, the numerical modeling and the effective medium theories were compared for different scenarios. The best agreement is generally achieved for larger number of inclusions and for fluid-filled fractures, where the stiffness contrast between the matrix and the inclusion properties is lower.

Figure 4.7 shows the modeled effect that different pore fluids have on compressional velocity and anisotropy parameters for a carbonate rock, which will be called Carbonate M.

On the other hand, two types of inclusion (fractures and vugs) were analyzed. The modeling shows that fractures are more sensitive to pore fluid change since they drastically reduce the elastic properties from water or bitumen to gas conditions. However, it is necessary to take into account that the equations to estimate the elastic stiffness tensor, numerically, assume a small aspect ratio, suitable only for fractures. Also, the presence of vugs reduces significantly P-wave and S-wave velocity even for the same porosity.

The effect that fractures and vugs have on the type of matrix was also investigated. Figure 4.8 shows the results of effect that the pore type has on a soft and a hard rock. The matrix properties of Carbonate M were used as an example of a hard rock and the matrix properties of another carbonate rock, namely, Carbonate T were used as a soft rock. Lithologic information about the play analyzed will be given in the next section. Analyzing the results of this modeling, we can conclude that the fracture effect on the elastic properties for a hard rock like Carbonate M is approximately three times the effect on a soft rock like Carbonate T.

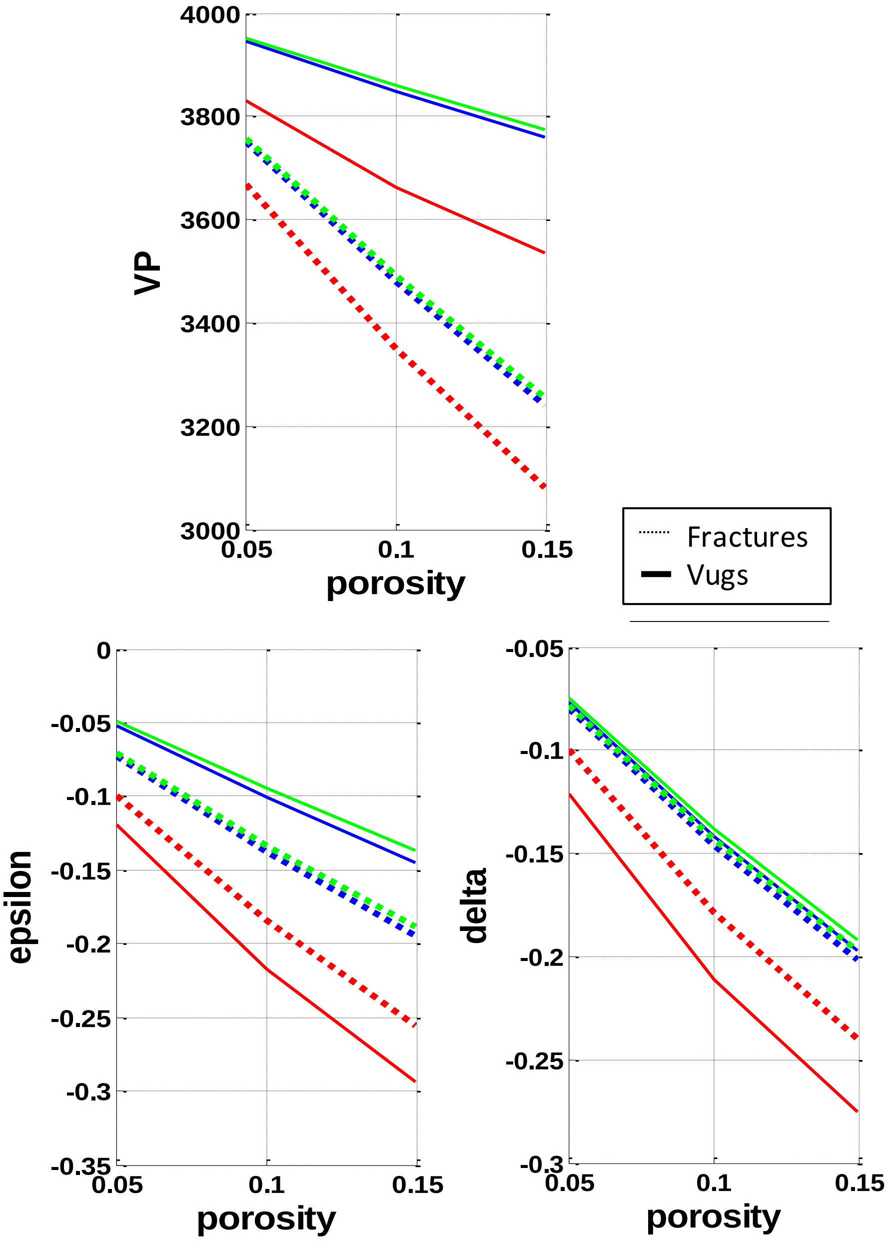

Figure 4.7. Effect on P-wave velocity and anisotropy parameters as pore space (fractures or vugs) is increased. The numerical modeling analyzed three fluid types: gas (red), water (blue), and oil (green).

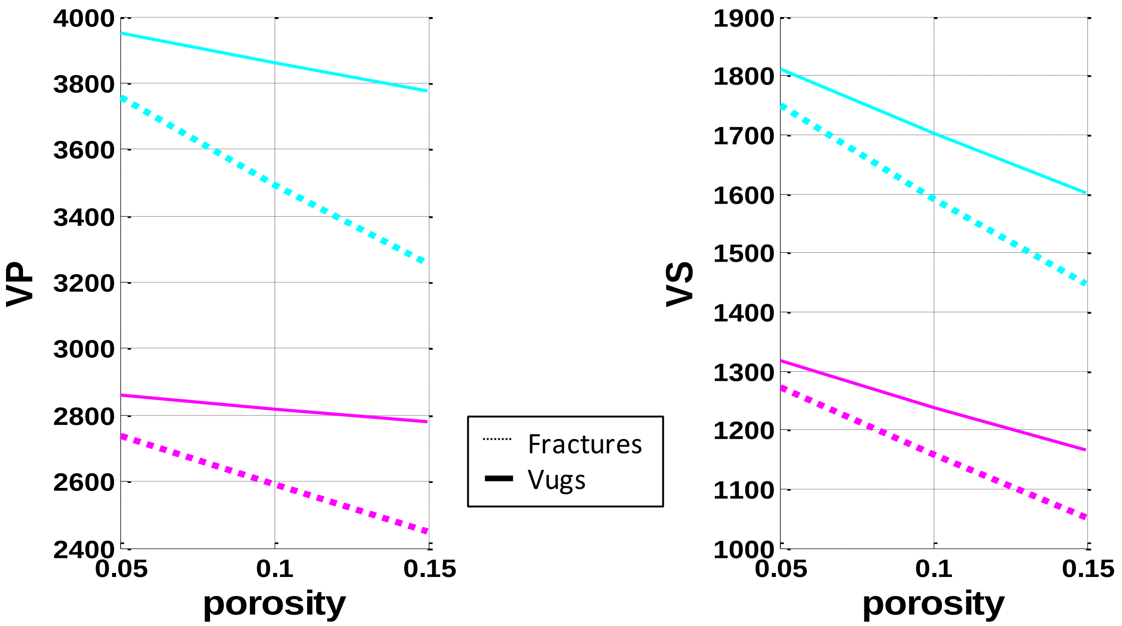

Figure 4.8. Effect of fractures and vugs on a hard rock (Carbonate M) and on a soft rock (Carbonate T). According to the numerical modeling, the vug effect on the elastic properties is higher than the presence of fractures even for the same porosity. Blue color corresponds to Carbonate M whereas pink color refers to Carbonate T.

4.2 Heavy Oil Reservoir

The data to be analyzed belong to a relatively shallow carbonate heavy oil reservoir. The play is mainly characterized by a succession of shales, limestones, and dolostones. Several formations will be analyzed in terms of fracture characterization.

4.2.1 Seal

Shale D acts as the seal and it is lithologically characterized by black and green shales with sandstone interbeds. Several subdivisions (transgressive surfaces of erosion) can be recognized in the shale D formation as a result of the transgression of the sea.

4.2.2 Reservoirs

- Carbonate M is a reservoir dolomite with vuggy porosity and solution – enhanced fracture porosity as a result of the multiple episodes of dolomitization. This unit is heavily karsted. Two subdivisions are interpreted in this unit.
- Carbonate T is a reservoir composed of dolosiltstones and fine-grained dolograinstones. These marine sediments are characterized by intercrystalline and microporosity. It is also heavily karsted. Two subdivisions are interpreted in this unit.
- Carbonate V results from multiple episodes of dolomitization of the original limestone that progressively led to porosity and permeability enhancement. There are 3 main subdivisions in the unit with different porosity development. Microporosity as well as moldic and vuggy porosity can be found on this unit. The karsting increased the porosity and the heterogeneity of the formation.

4.2.3 Well - Log information

The FE modeling requires as input data velocity and density information of the rock matrix. This information was extracted from 18 wells drilled in the area. Some of the logs available are: dipole sonic logs (compressional and shear wave velocity), density logs, resistivity logs, and Formation MicroImager (FMI) logs. FMI logs generate an electrical image of the rocks surrounding the wellbore from microresistivity measurements providing very high resolution (typical resolution is about 5mm).

These logs were vital to decide not only the characteristic fracture density of each formation, but also to select those intervals that were appropriate for the finite element modeling, that is, intervals that include only matrix porosity; large fractures or vugs were excluded since they will exhibit a significant change in the matrix properties (velocity and density) of the formation.

Figure 4.9 shows the FMI log corresponding to two different wells where the porosity is evident. The blue box located in log on the right shows large vugs, whereas the box located in the log in the left shows the matrix properties. It seems obvious that intervals with such large vugs will dramatically change the matrix properties needed for the modeling. It is important to mention once more that the modeling will introduce the fracture porosity and yield the effective properties of fractured rock.

In summary, FMI logs helped to select the intervals used for the modeling while sonic scanner and density logs were used to obtain P-wave velocity, fast and slow shear-wave velocity, and bulk density.

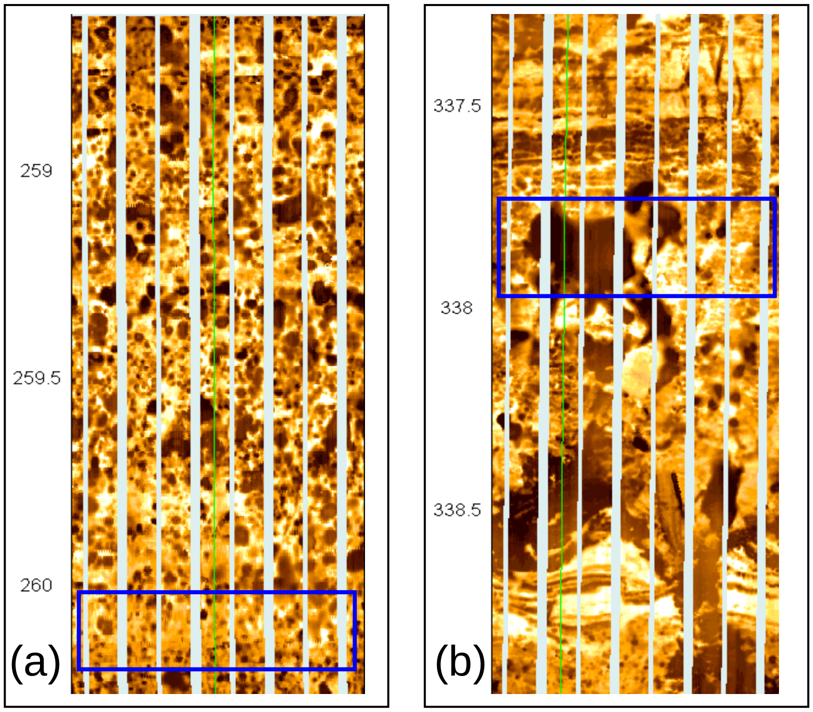

Figure 4.9. Two examples of a FMI log showing (a) an interval selected for the modeling and (b) interval including vugs not used for the modeling.

The following tables collect the P-wave velocity, shear-wave velocity, and density. Based on the distribution of the well-log data on the play, two (2) areas were selected: Area1 that corresponds to wells to the south, and Area 2 that includes the wells located to the north of the field. It was mentioned that the intervals were chosen based on the FMI logs; however, P-wave velocity, S-wave velocity, and density curves were blocked carefully in order to represent with one point an interval sharing similar values. The advantage of this method, besides reducing the amount of repeated information, is eliminating anomalous and spurious values.

The following tables comprise the information needed for the FE modeling, including subdivision of the formations previously described:

Table 4.1. Input data for Area 1.

Formation	VP	VS	ρ
Shale D	2480	1143	2342
Carbonate M2	4200	2150	2430
Carbonate M1	3900	1800	2360
Carbonate T2	3370	1670	2300
Carbonate T1	3350	1610	2300
Carbonate V3	4400	2200	2450
Carbonate V2	4600	2400	2590
Carbonate V1	4200	2100	2480

Table 4.2. Input data for Area 2.

Formation	VP	VS	ρ
Shale D	2480	1143	2342
Carbonate M2	4500	2100	2550
Carbonate M1	4350	2050	2500
Carbonate T2	3550	1900	2370
Carbonate T1	3500	1750	2380
Carbonate V3	4400	2250	2450
Carbonate V2	5150	2640	2600
Carbonate V1	4300	2150	2500

4.2.3.1 Anisotropy Estimation

Anisotropy parameters are also part of the matrix information needed for the finite element modeling, but only in the case of Shale D. It was considered as very important to take into account the anisotropic nature of shales before adding the fractures during the modeling.

Shales are found experimentally to be anisotropic (Thomsen, 1986; Vernik and Liu, 1997; Sayers, 1999). The origin of anisotropy in shales is definitely non-unique and may be attributed to several factors. However, preferred orientation or texture of the shapes of minerals, such as clay platelets (Kaarsberg, 1968; Tosaya, 1982; Sayers, 1994; Johnston and Christensen, 1995; Cholach and Schmitt, 2005) and thin bedding of isotropic or anisotropic layers (Schoenberg and Sayers, 1995) are identified as some of the most important sources of seismic anisotropy. Sayers (1999) includes the effect of stress induced anisotropy to explain the preferred orientation of clay platelets.

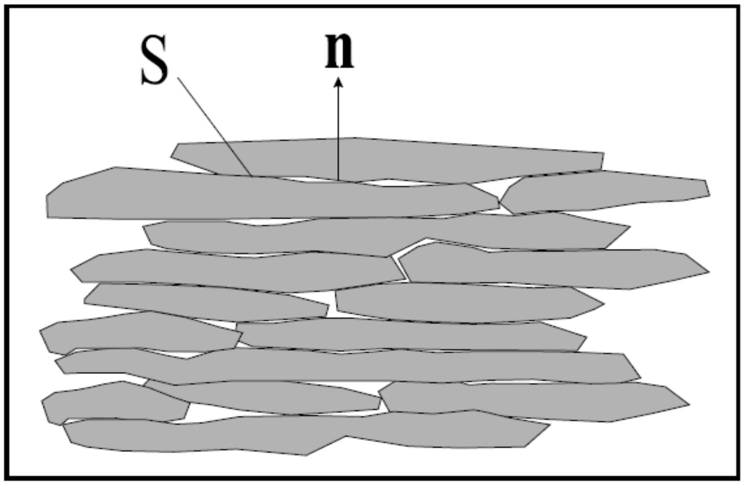

Figure 4.10. Clay particle alignment in shales. Liu et al., 2000.

“Slow sedimentation of clay minerals from suspension favors face-to-face aggregation to form domains of parallel clay platelets” (Sayers, 1999). The vector normal (n) to the clay platelets varies from domain to domain with a preferred orientation resulting from the depositional environment and stress history of the rock (Figure 4.10). Hence, the clay particles vary in orientation but are aligned locally (Hornby et al., 1994; Schoenberg and Sayers, 1995).

One way to quantify the anisotropy is through the anisotropy parameters. Following Thomsen (Thomsen, 1986), they are: **epsilon** (ε), which characterize P-wave anisotropy; **delta** (δ) that relates to NMO and the conversion of energy between P-waves and SV-waves; and **gamma** (γ), which describes S-wave anisotropy. They are estimated from the five independent coefficients of a VTI/HTI elastic stiffness tensor through the following equations:

$$\varepsilon = \frac{C_{11} - C_{33}}{2C_{33}} \tag{8}$$

$$\delta = \frac{(C_{13} + C_{44})^2 - (C_{33} - C_{44})^2}{2C_{33}(C_{33} - C_{44})} \tag{9}$$

$$\gamma = \frac{C_{66} - C_{44}}{2C_{44}} \tag{10}$$

where:

C_{11}: refers to horizontally propagating compressional velocity.

C_{33}: refers to vertically propagating compressional velocity

C_{44}: refers to vertically polarized shear-wave velocity.

C_{66}: refers to horizontally polarized shear-wave velocity.

C_{13}: off-diagonal element that unfortunately lacks of a simple physical basis.

We used two different methods to estimate the anisotropy parameters in Shale D. One method was an inversion/optimization procedure to estimate the elastic stiffness tensor from well-log measurements using deviated boreholes. The other method estimates C_{33} and C_{44} from dipole sonic-log data and C_{66} from Stoneley wave velocity (V_T). At the end, a combination of both techniques was applied since there were not enough deviated boreholes sufficiently distributed in the field to reliably construct phase velocity versus deviation angle plots for each formation.

The basis of the first technique can be summarized as: "if anisotropy is present, deviated well measurements will differ from expected vertical responses" (Furre and Brevik, 1998). The methodology starts by creating a database that includes P-wave and S-wave velocity, deviation angle, and density. Then, group velocities of the three modes of propagation are calculated based on the solution of the Christoffel equation (Musgrave, 1970). Using an inversion (optimization) procedure, the five elastic coefficients are estimated by fitting theoretical and measured velocities (Figure 4.11). Using this result, anisotropy parameters can be calculated.

INPUT	
C11	**28**
C33	**19**
C44	**4.3**
C66	**7**
C13	**13**
ρ	**2461**

OUTPUT	
ε	**0.237**
δ	**0.149**
γ	**0.314**

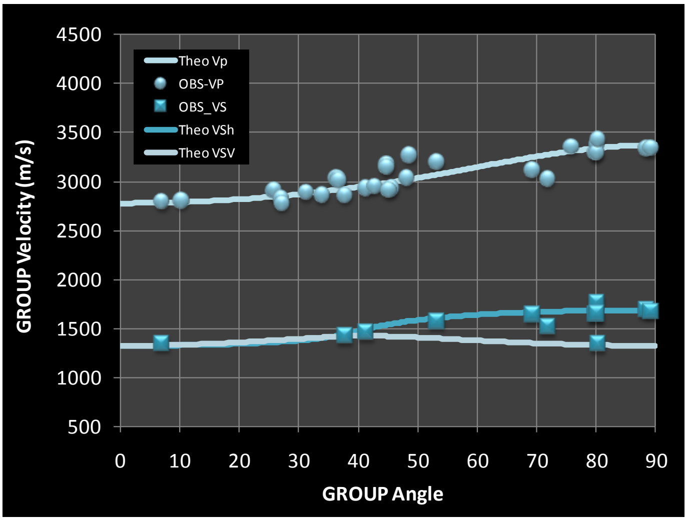

Figure 4.11. Anisotropy parameters are estimated by fitting theoretical and measured velocities.

The other method makes use of the well-log information that is not always available such as Stoneley velocity, and fast and slow shear-wave velocity. First of all, C_{33} and C_{44} are calculated from vertical P-wave and S-wave velocity:

$$C_{33} = \rho V_{P0}^2 \tag{12}$$

$$C_{44} = \rho V_{S0}^2 \tag{13}$$

Then, C_{66} is calculated from Stoneley (tube) wave velocity (V_T) as follows:

$$V_T = v_f \left(1 + \frac{k_f}{C_{66}}\right)^{-1/2} \tag{14}$$

where v_f is fluid (mud) velocity and k_f is the fluid (mud) bulk modulus.

However, the last two elastic coefficients C_{11} and C_{13} are inverted from P-wave and SV-wave group velocity equations:

$$\rho V_P^2 = C_{33}(1 - sin^4\theta) + C_{11} sin^4\theta + (2C_{13} + 4C_{44} - 2C_{33}) sin^2\theta cos^2\theta \tag{15}$$

$$\rho V_{SV}^2 = C_{44} + (C_{11} + C_{33} - 2C_{13} - 4C_{44}) sin^2\theta cos^2\theta \tag{16}$$

Once anisotropy parameters are found for each of the seven (7) subdivisions of Shale D, the next step is to proceed with the finite element modeling in order to understand the effect of fractures on an already VTI formation (Figure 4.12). Once more, in the case of the carbonate formations, it has been assumed that the background or matrix properties are isotropic and anisotropy comes from the presence of fractures.

Since there are seven subdivisions in Shale D with different rock properties, it was necessary to use finite element modeling for *layered rocks* to estimate the induced anisotropy resulting from the layering and finally estimate their effective properties. First, the response from the first two units was modeled and then the result is modeled with the next layer in depth, resembling Backus averaging. The same procedure was made for all the units of Shale D. The resulting effective properties represent the input data for the fracture modeling:

Table 4.3. Effective elastic properties for Shale D taking into account intrinsic and (layer) anisotropy. No fractures have been added to the model at this point.

V_P (m/s)	V_S (m/s)	Density (Kg/m^3)	ε	δ	γ
2480	1143	2342	0.143	0.0105	0.1997

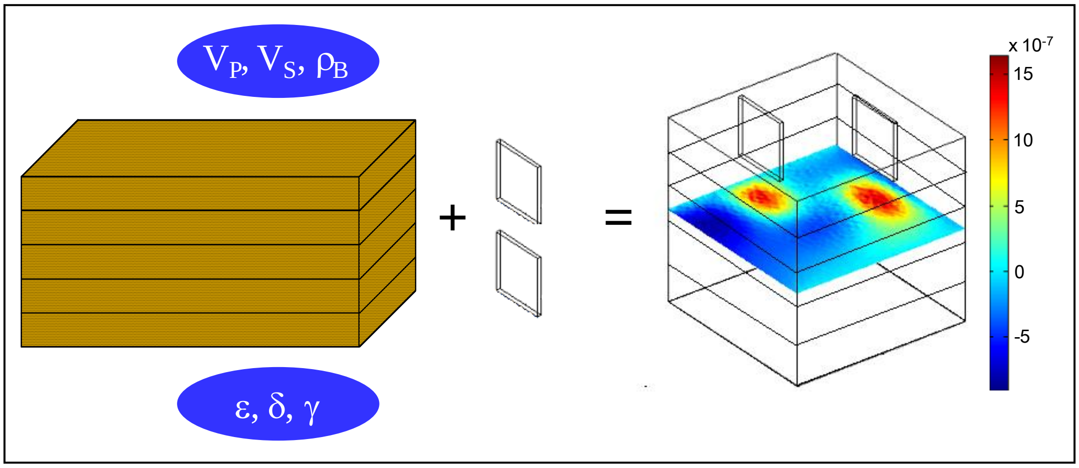

Figure 4.12. Clearwater Shale modeling. An orthorhombic formation is the result of modeling a VTI formation with intrinsic and layer anisotropy and fractures perpendicular to bedding.

4.3 3D Fracture Porosity Modeling

4.3.1 Methodology

In this section, the information contained in Tables 4.1, 4.2, and 4.3 will be used to estimate the effective properties of Shale D and the carbonate reservoirs as fracture porosity is varied. The methodology is summarized as follows:

I. Numerical Modeling

I.1. Input matrix properties according to Tables 4.1 and 4.2.

Intrinsic anisotropy is included for Shale D.

I.2. Select pore fluid and its properties (V_P, V_S and ρ_f) according to formation:

Shale D: water.
Carbonate M: partial saturation between gas and bitumen.
Other formations: bitumen.

I.3. Select boundary condition: displacement or traction.

I.4. Select number of inclusions: 1, 3, 5 and 7. Fracture porosity varies 2 to 20%.

I.5. Select aspect ratio (θ) and size of fractures and/or vugs.

In this study $\theta = 0.08$ for fractures and $\theta = 0.75$ for vugs.

I.6. Select location of inclusions (approximately 10 runs are needed with different inclusion location).

II. Estimation of Velocities and Thomsen's Parameters.

The result of the modeling will be the effective elastic stiffness tensor of matrix plus inclusions as number of inclusions are varied. P-wave and S-wave velocities can be calculated using equation 12 and 13 for each boundary condition. Both values will be averaged following Hill (1963). Figure 4.13 shows an example of stress and strain distributions when traction and displacement boundary conditions are applied.

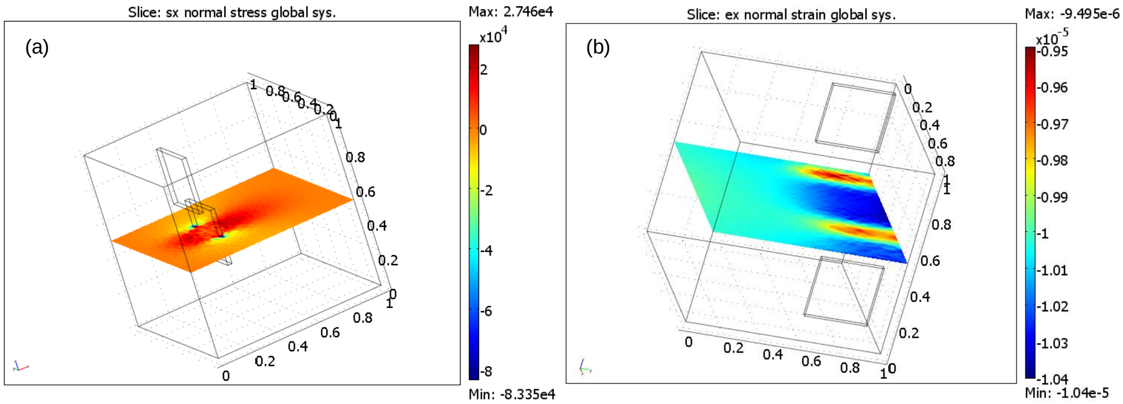

Figure 4.13. 3D fracture modeling applying (a) traction and (b) displacement boundary condition.

III. Interpretation.

Expressions that correlate P-wave velocity, S-wave velocity with fracture porosity were obtained. Fracture porosity logs were created for each well and formation based on sonic data and the previously obtained FEM based V-ϕ_{frac} correlations. Following the geological model interpreted in the area, the fracture porosity logs were interpolated to create a 3D representation of fracture porosity changes in the field.

4.3.2 Results

4.3.2.1 Shale D

In this formation the result is very similar to the initial properties (Figures 4.14 and 4.15) for two main reasons, the fracture density is very small and the contrast between matrix properties and pore-space properties (fractures) is also small. The amount of fractures (2) was decided based on FMI logs. Although the NIA model is outside the bounds of the numerical modeling, the difference is insignificant.

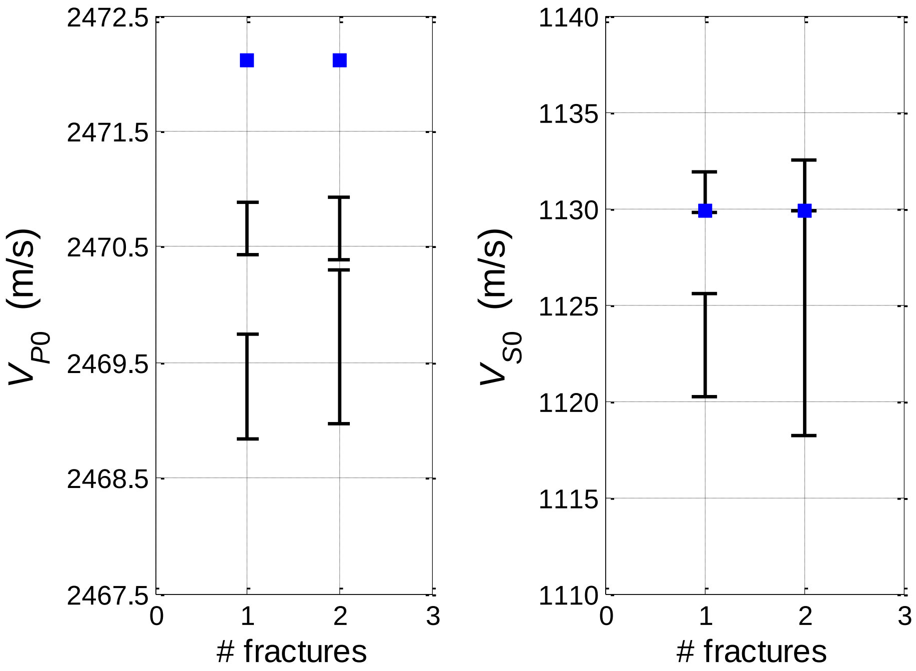

Figure 4.14. Fracture effect on the elastic velocities of Shale D. Numerical modeling (black error bars correspond to traction and displacement boundary conditions) and NIA theory (blue squares) are in perfect agreement.

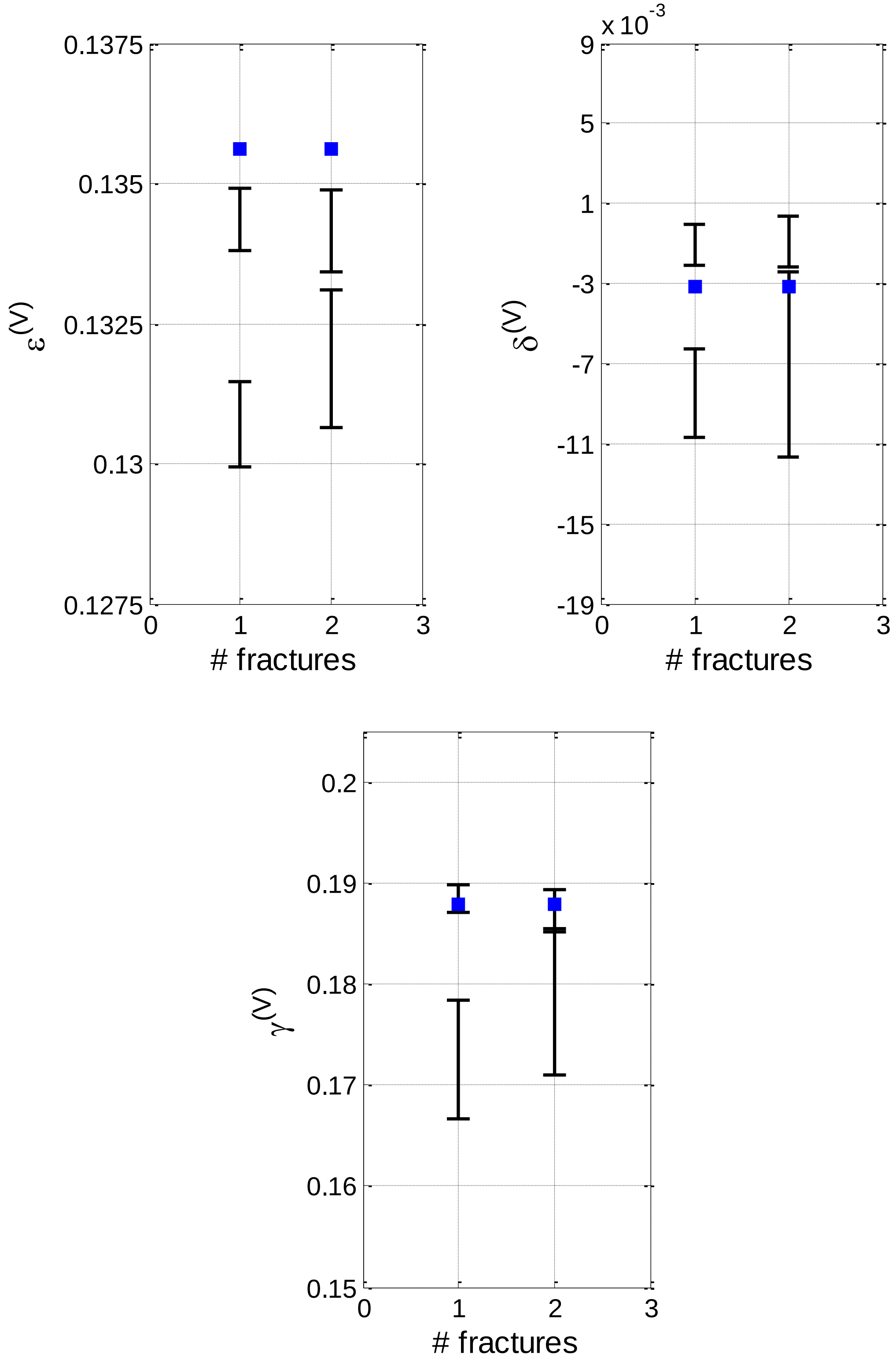

Figure 4.15. Fracture effect on the Thomsen's parameters for Shale D. Numerical modeling (black error bars) and NIA theory (blue squares) are in agreement.

4.3.2. 2 Carbonate Reservoirs

From numerical modeling, V_P modeled and V_S modeled was obtained as a function of fracture porosity, which will enable to generate velocity-porosity correlations for each formation and ultimately generate fracture porosity maps. It is important to mention that the fracture porosity term includes not only the porosity due to fractures but also the primary porosity accounted on the matrix properties. Only vugs were excluded. It seems obvious that the pore fluid effect will be present when analyzing P-wave modeling; however, input S-wave velocities are usually more sensitive to errors associated to the tool itself.

The velocity – porosity correlations found for both areas are very similar, which can be an indication of the robustness of the technique. The Carbonate M formation exhibits a trend slightly different from the rest of the formations when P-wave modeling is analyzed (Figure 4.16). This difference is attributed to a change in the pore fluid: Carbonate M is characterized by having a higher percent of water saturation in comparison to other formations. On the other hand, all formation exhibit the same trend when S-wave velocity is analyzed (Figure 4.17).

The correlation between P-wave velocity and fracture porosity is accurately described by an exponential fitting whereas a logarithmic fitting gives the best results for S-wave velocity. Only in the case of Carbonate M, logarithmic fitting is recommended for P-wave velocity. The expressions were collected in Table 4.4. The correlation coefficient was above 0.99.

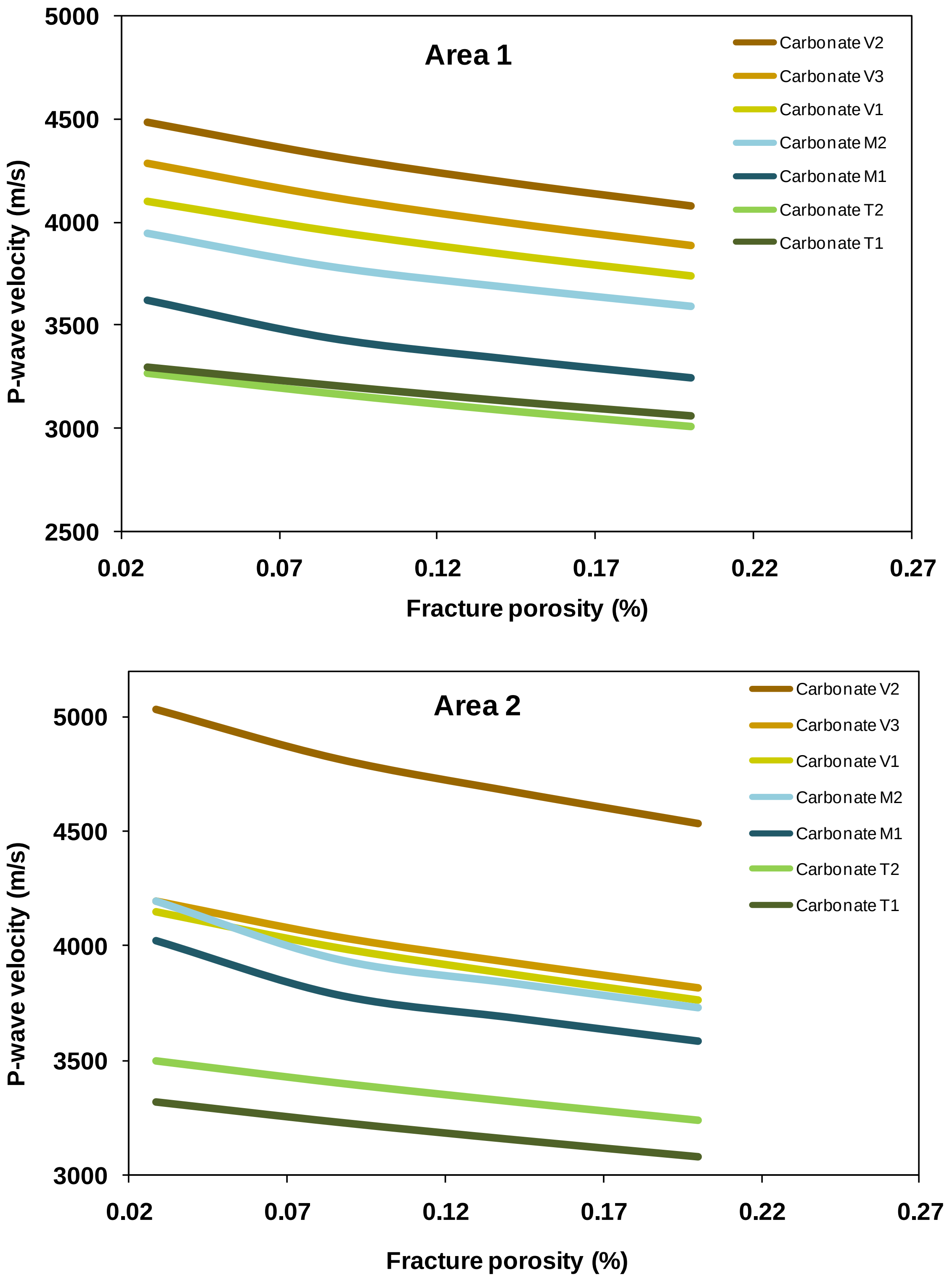

Figure 4.16. V_P vs. ϕ_{frac}. Pore-fluid effect (bitumen-gas partial saturation) is evident on Carbonate M formation in both areas.

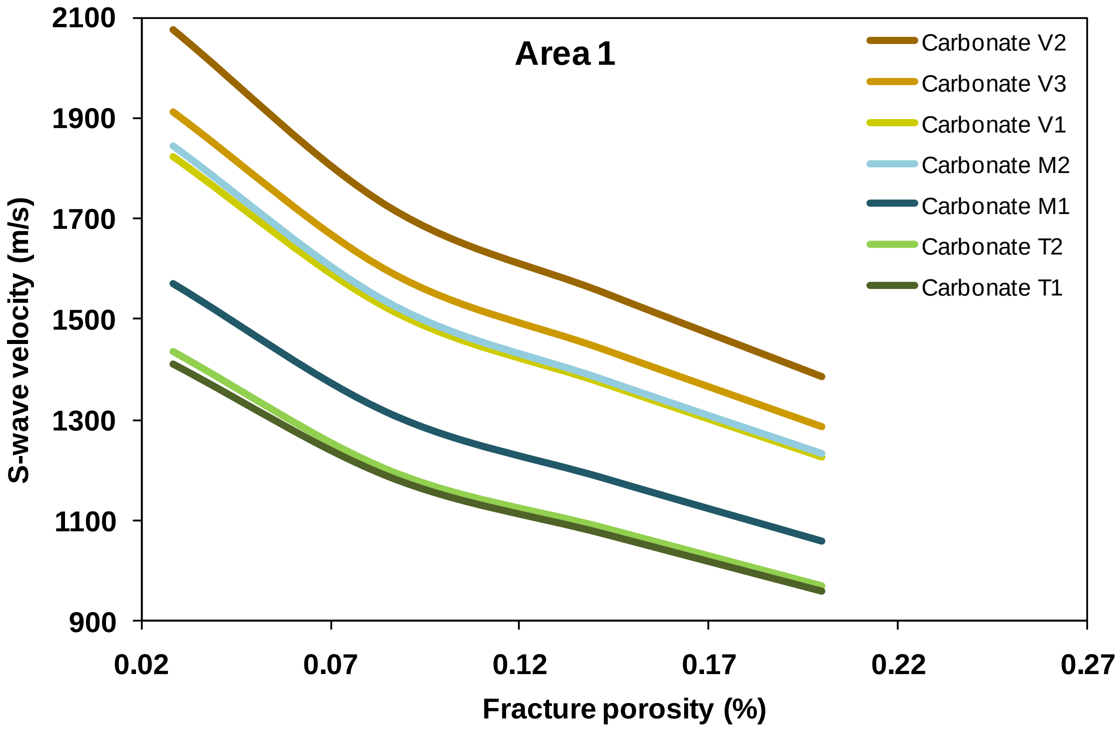

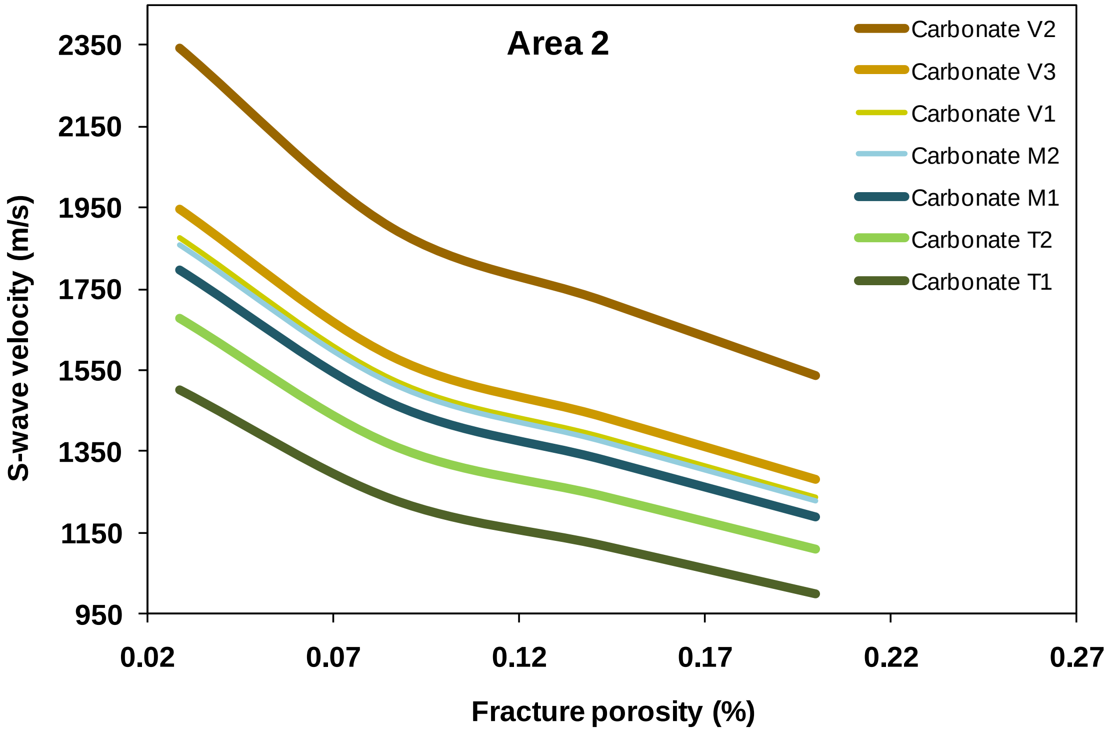

Figure 4.17. V_S vs. ϕ_{frac}. All the correlations follow the same trend since S-wave velocity is insensitive to pore fluid.

Table 4.4. Velocity – Fracture porosity correlations for Area 1 and Area 2. The logarithmic and exponential fitting was very good ($R^2 > 0.99$).

	Area 1	Area 2
Carbonate M2	$V_P = -178 Ln(\phi_F) + 3327$ $V_S = -307 Ln(\phi_F) + 763$	$V_P = -237 Ln(\phi_F) + 3357$ $V_S = -317 Ln(\phi_F) + 737$
Carbonate M1	$V_P = -189 Ln(\phi_F) + 2956$ $V_S = -256 Ln(\phi_F) + 670$	$V_P = -223 Ln(\phi_F) + 3237$ $V_S = -306 Ln(\phi_F) + 713$
Carbonate T2	$V_P = 3310 e^{-0.48\phi_F}$ $V_S = -232 Ln(\phi_F) + 618$	$V_P = 3539 e^{-0.45\phi_F}$ $V_S = -287 Ln(\phi_F) + 662$
Carbonate T1	$V_P = 3338 e^{-0.45\phi_F}$ $V_S = -226 Ln(\phi_F) + 618$	$V_P = 3359 e^{-0.44\phi_F}$ $V_S = -252 Ln(\phi_F) + 609$
Carbonate V1	$V_P = 4159 e^{-0.55\phi_F}$ $V_S = -300 Ln(\phi_F) + 768$	$V_P = 4202 e^{-0.56\phi_F}$ $V_S = -321 Ln(\phi_F) + 739$
Carbonate V2	$V_P = 4543 e^{-0.55\phi_F}$ $V_S = -345 Ln(\phi_F) + 859$	$V_P = 5100 e^{-0.6\phi_F}$ $V_S = -406 Ln(\phi_F) + 905$
Carbonate V3	$V_P = 4342 e^{-0.57\phi_F}$ $V_S = -314 Ln(\phi_F) + 808$	$V_P = 4252 e^{-0.55\phi_F}$ $V_S = -333 Ln(\phi_F) + 764$

Fracture porosity logs were created for each well and formation (only carbonate reservoirs were included) based on sonic data and using the FEM based V-ϕ_{frac} correlations. Figure 4.18 shows the porosity logs for three wells as well as the geological horizons interpreted in the area. Each geological formation was further subdivided to improve vertical and horizontal interpolation and at the same time each of the layers were divided to create a data point every 0.5 m approximately. Overall, the geological model was used to guide the petrophysical model.

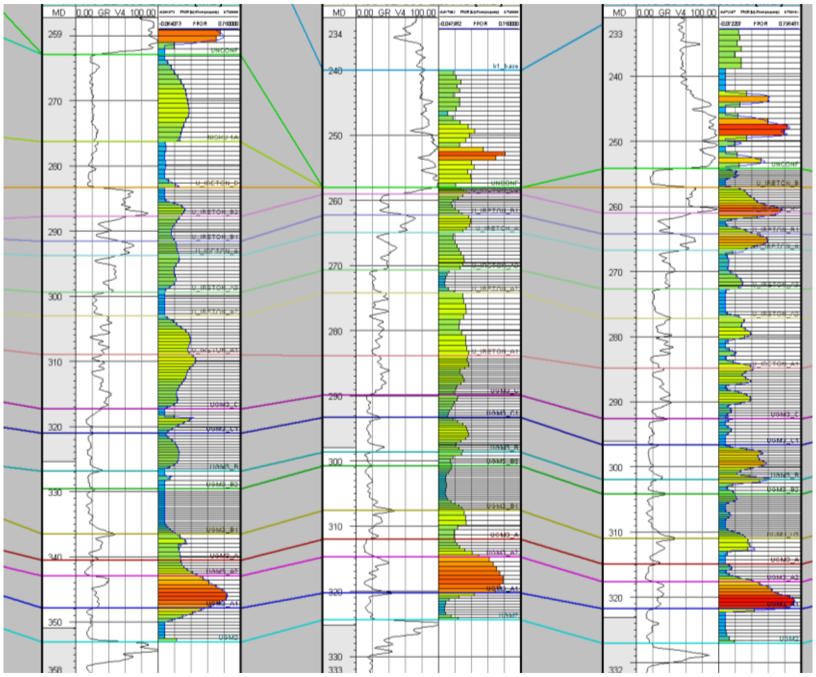

Figure 4.18. Fracture porosity logs obtained from P-wave correlations. High fracture porosity is indicated by orange/red colors while low fracture porosity is given by blue color. Gamma-ray log is also included (black line).

A simple interpolation technique (moving average) was used to create the cube from porosity logs (Figure 4.19). The horizontal cell is 100m and the vertical cell is 0.5m, approximately.

P-wave and S-wave modeling give similar responses; however, P-wave modeling predicts higher fracture porosity values. This is due to the presence of hydrocarbon (gas and bitumen) that lowers the velocity and therefore results in higher estimated fracture porosity.

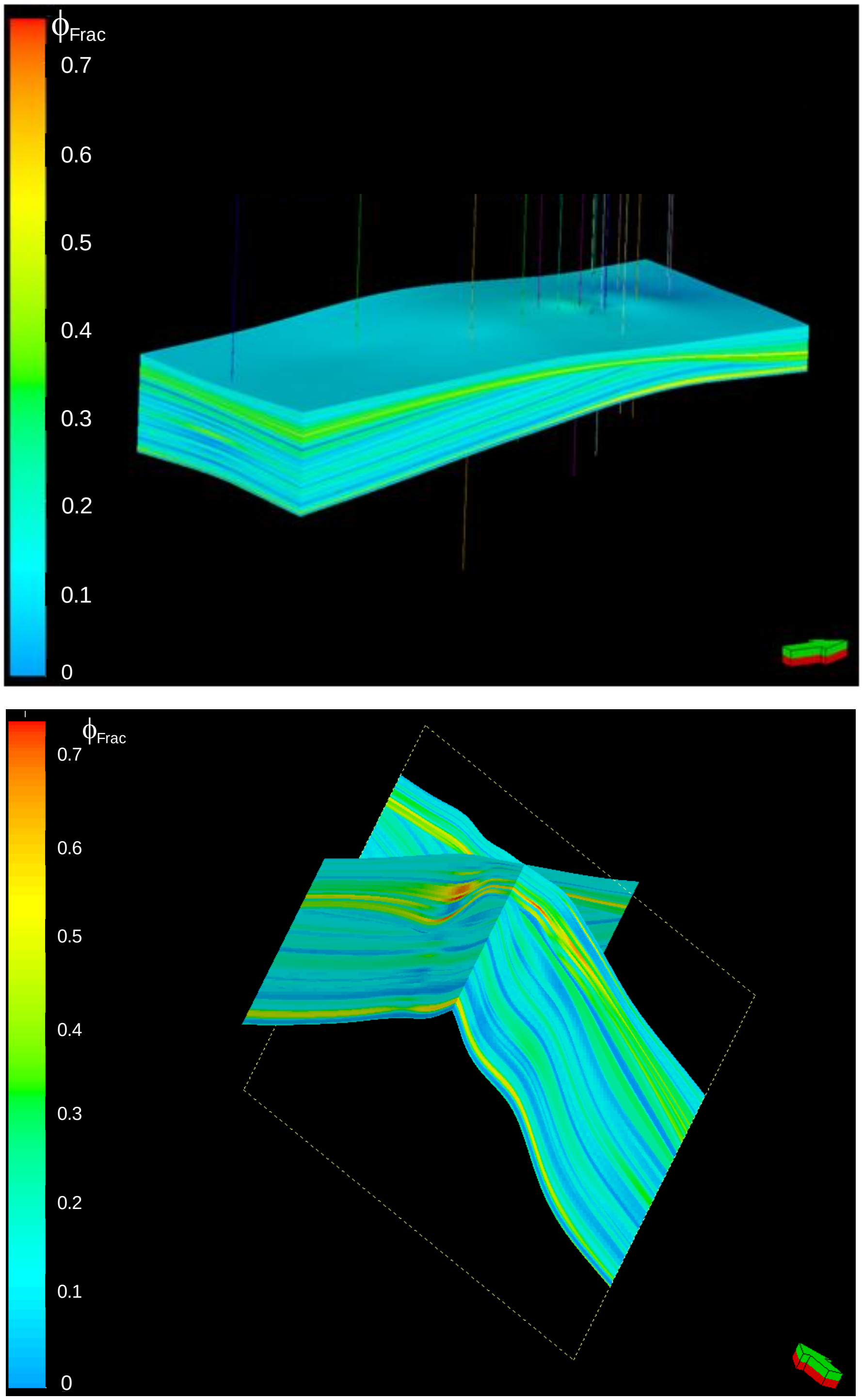

Figure 4.19. 3D Fracture porosity model following P-wave modeling after interpolation. The 3D Fracture porosity model represents an excellent tool to qualitatively determine those areas with high fracture porosity.

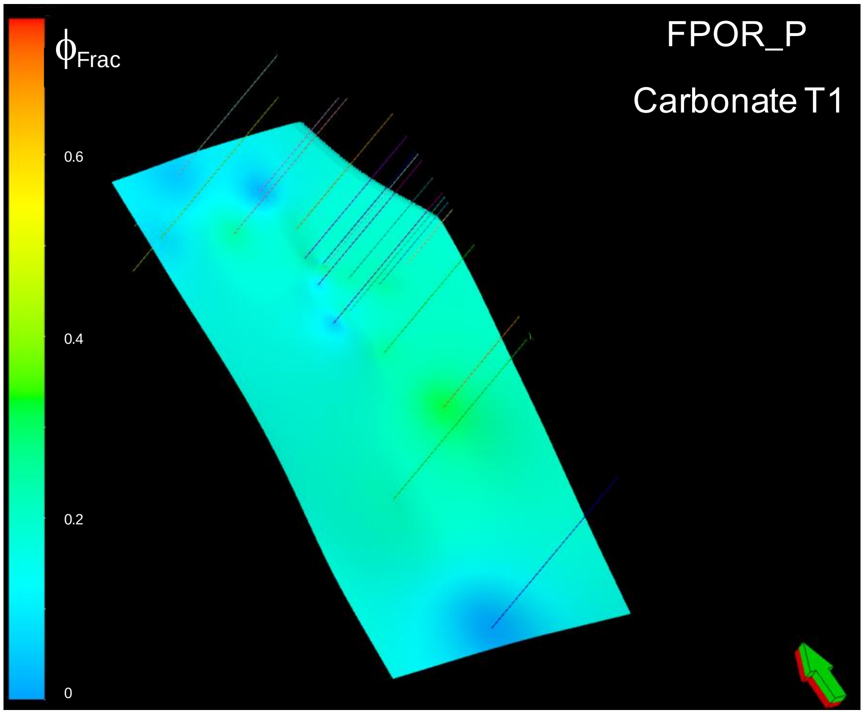

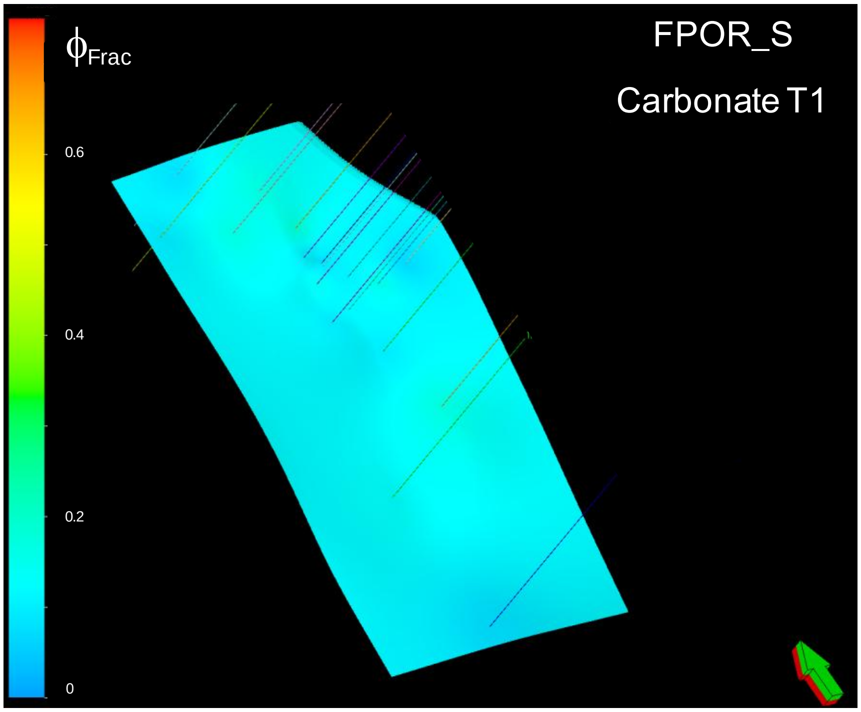

Figure 4.20. Slice of 3D Porosity model for Carbonate T1. (a) P-wave modeling. (b) S-wave modeling.

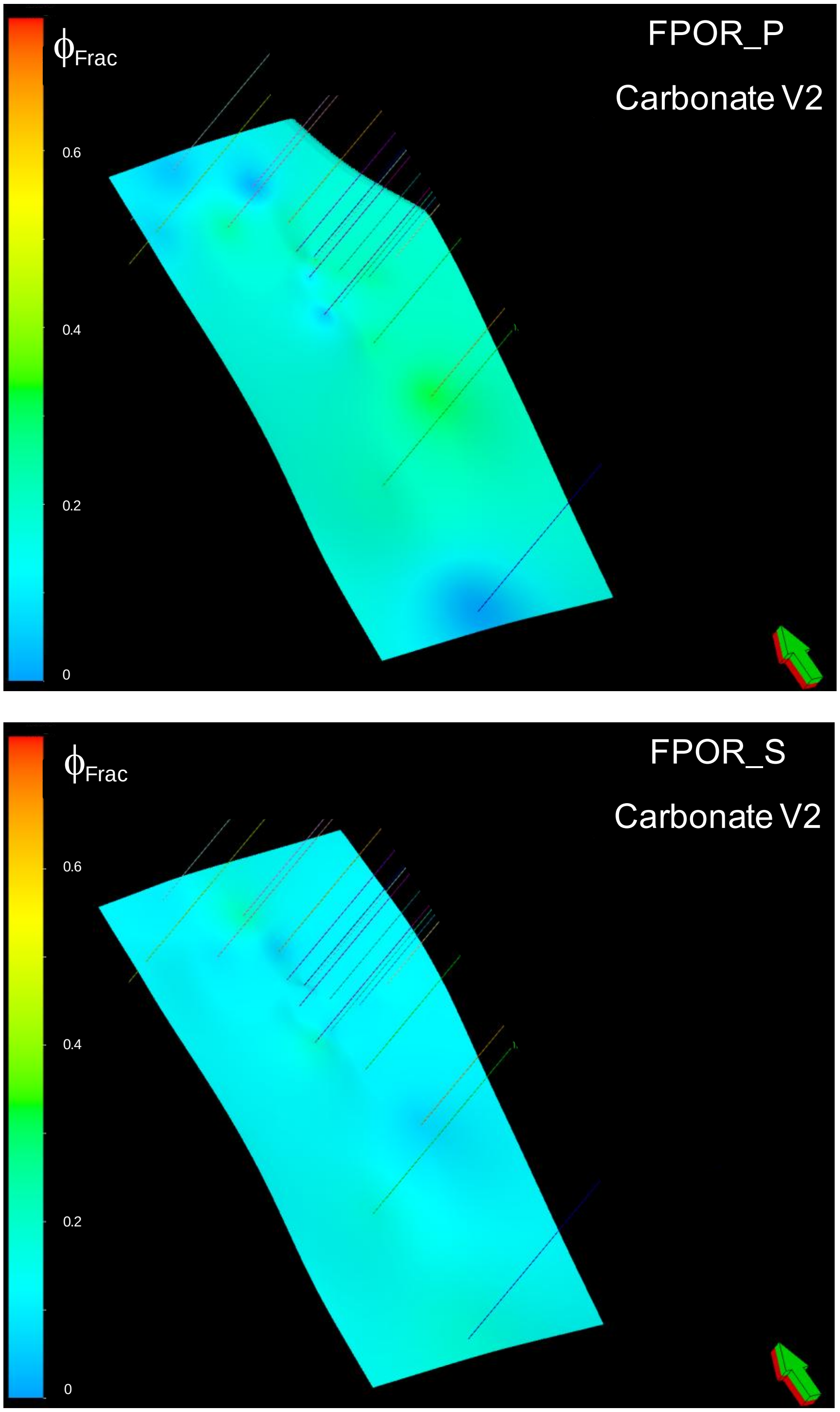

Figure 4.21. Slice of 3D Porosity model for Carbonate V2. (a) P-wave modeling. (b) S-wave modeling.

Comparing the results given by P-wave and S-wave modeling, it is noticeable that they give similar responses; however, P-wave modeling predicts higher fracture porosity values. This is due to the presence of hydrocarbon (gas and bitumen) that lowers the velocity and therefore assumes higher fracture porosity. Shear velocity is less sensitive to pore-fluid changes but responds to changes on the rock frame. Figures 4.20 and 4.21 are slices of the fracture porosity estimated through P-wave and S-wave modeling for some of the formations analyzed in this study.

Similar results were obtained for the other formations. One of the advantages of this method is the excellent vertical resolution provided by the sonic logs; however, to improve the horizontal resolution, it is recommended to integrate other types of input data such as seismic data. This method is also a great tool to map the relative changes on the fracture porosity in a field, which will help to characterize more in depth the areas with the highest fracture porosity.

4.4 3D Vug Porosity Modeling

A similar methodology was applied when investigating the porosity effect due to vugs. The main difference is the aspect ratio of the inclusions, which was increased to 0.75. Previously, numerical modeling showed that vugs greatly affect the effective properties of the medium in comparison to fractures. The vug porosity (ϕ_{vug}) modeling was carried out for Carbonate V1 and Carbonate V2, but can be extended as well to other formations.

Velocity – porosity correlations were found using P-wave and S-wave velocity information (Table 4.5). These correlations are the result of averaging the lower bound (traction boundary condition) and upper bound (displacement boundary condition) generated through numerical modeling. Figure 4.22 shows the numerical modeling result using P-wave and S-wave velocity information for Carbonate V2, as well as the result given by the theories NIA and DEM. The numerical modeling and NIA give similar results; however, the DEM predicts a bigger “vug” effect on the effective properties as porosity is increased. In fact, the DEM response is lower than the lower bound, which is theoretically incorrect. Figure 4.23 shows a similar result for Carbonate V1.

Table 4.5. Velocity – ϕ_{vug} correlations for Area 2. Exponential fitting was very good (R^2 >0.99).

	Area 2
Carbonate V1	$V_P = 4160e^{-2\phi_{vug}}$ $V_S = 2110e^{-2\phi_{vug}}$
Carbonate V2	$V_P = 4955e^{-2.1\phi_{vug}}$ $V_S = 2589e^{-2\phi_{vug}}$

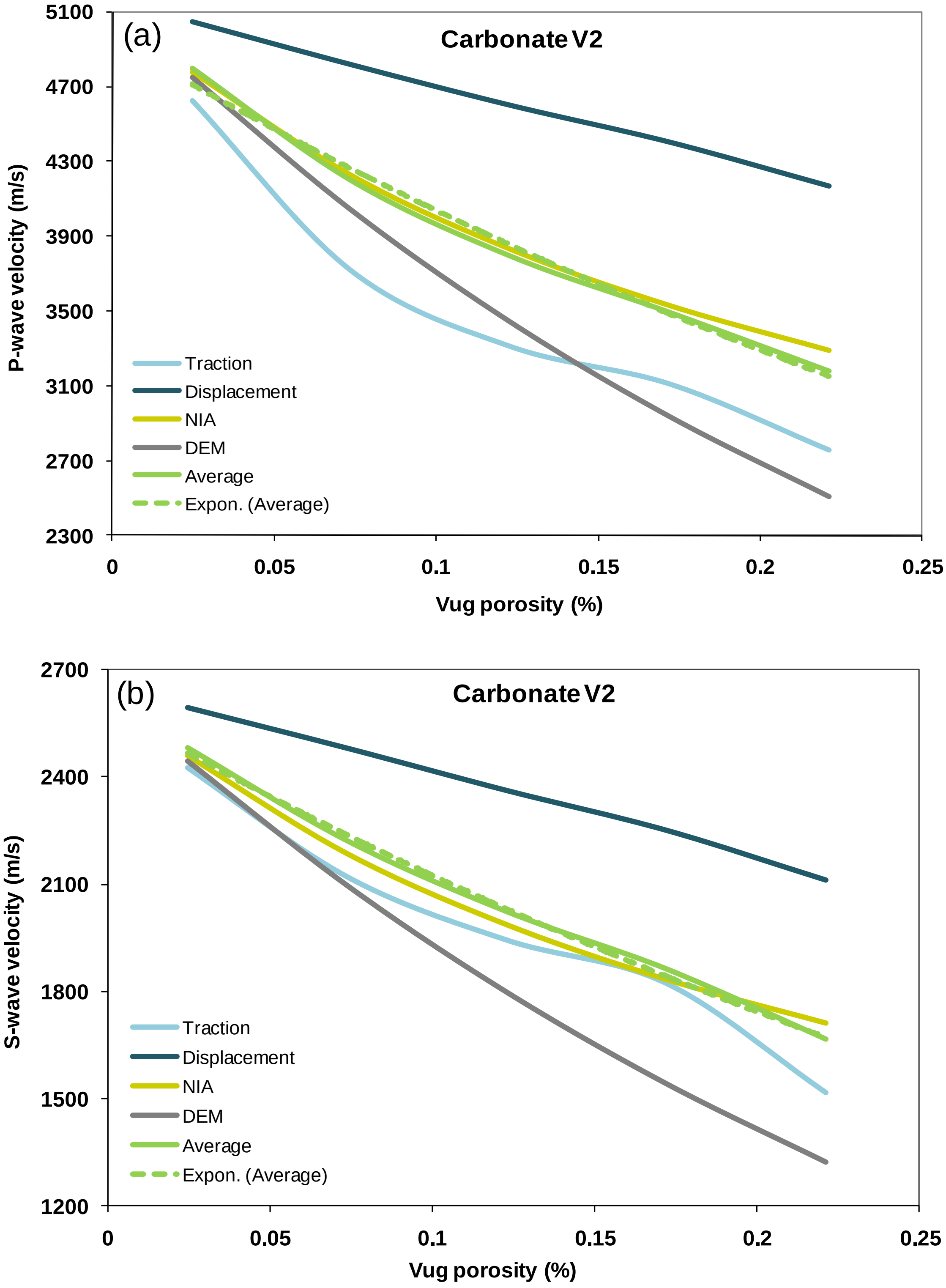

Figure 4.22. Velocity – Vug porosity correlations for Carbonate V2. (a) P-wave modeling. (b) S-wave modeling. DEM theory does not agree with numerical modeling and NIA theory.

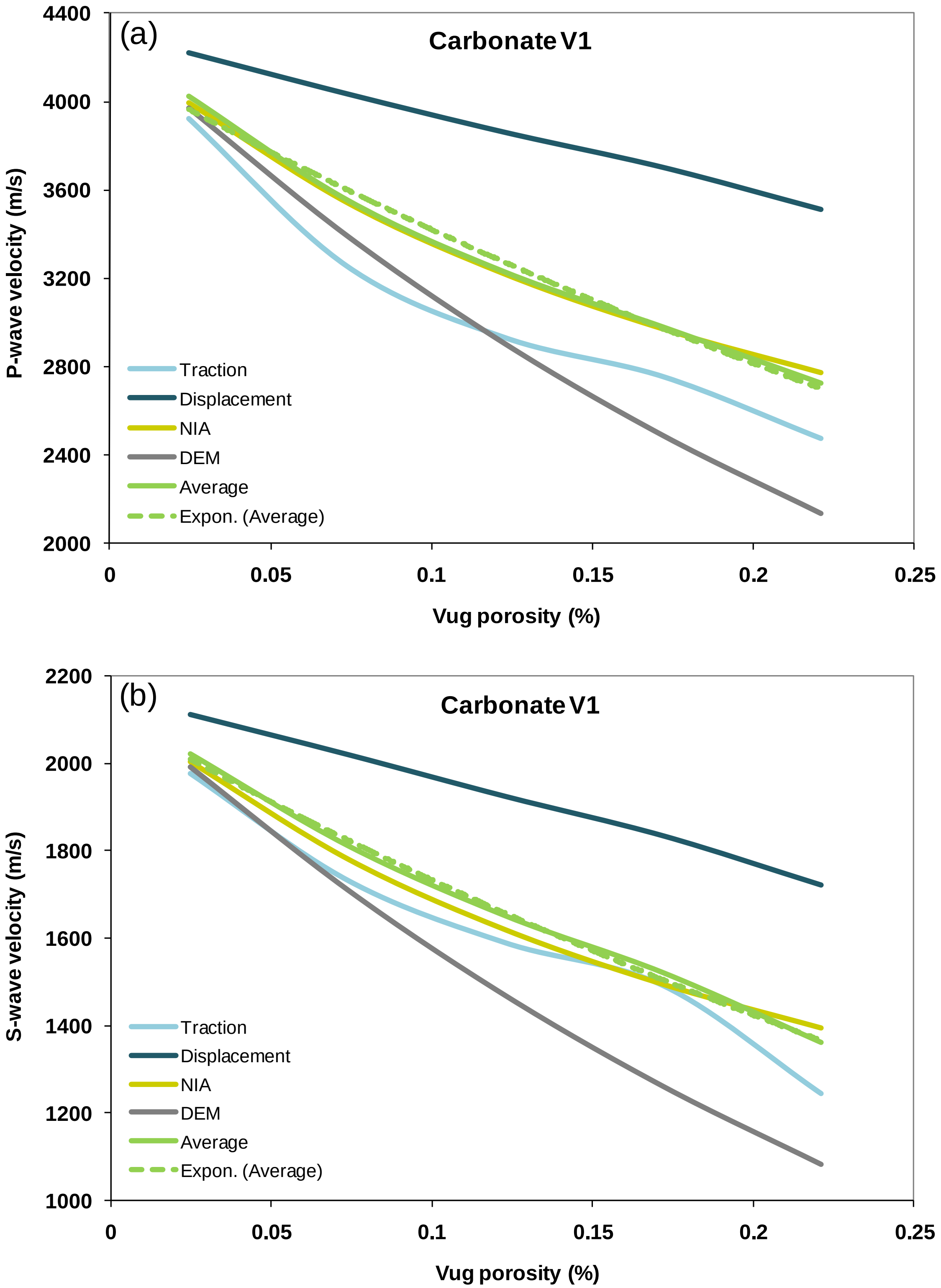

Figure 4.23. Velocity – Vug porosity correlations for Carbonate V1. (a) P-wave modeling. (b) S-wave modeling. DEM theory does not agree with numerical modeling and NIA theory.

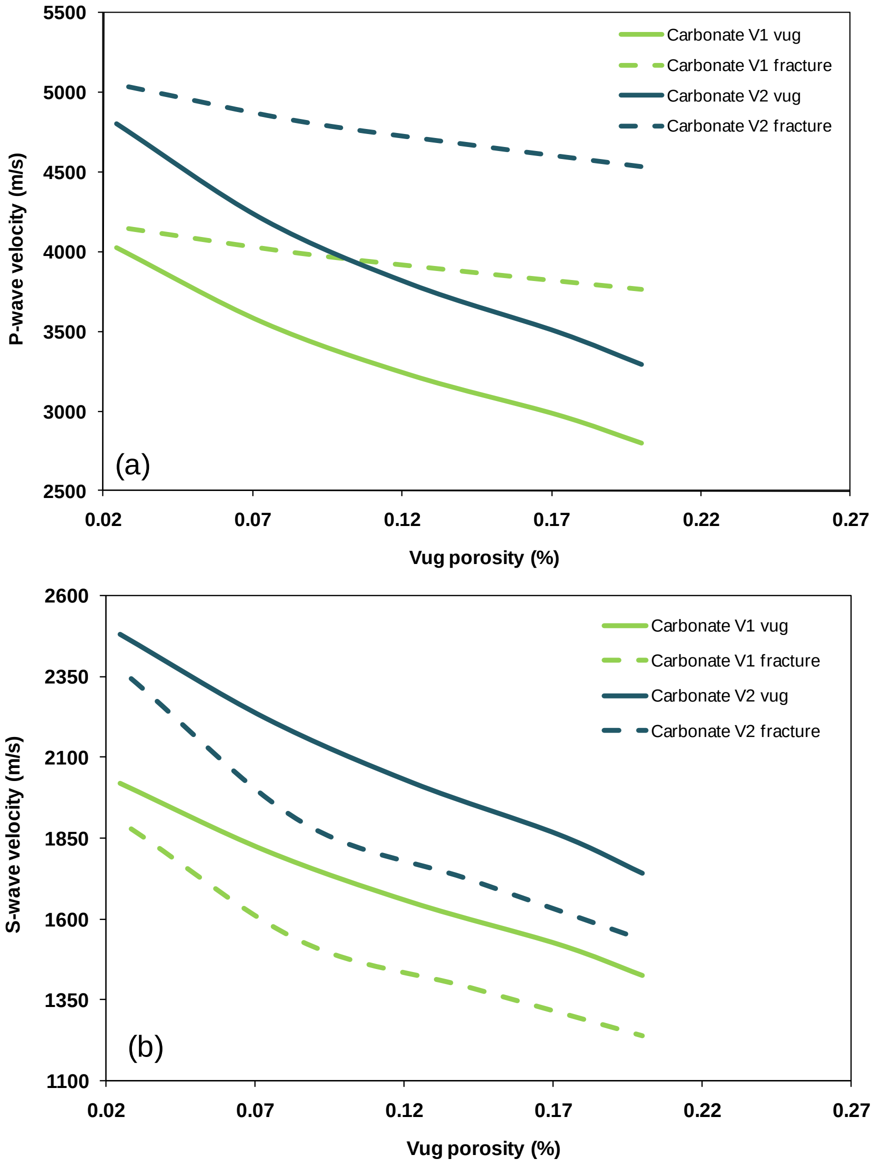

Figure 4.24. Comparison of “fracture” and “vug” correlations corresponding to Carbonate V1 and Carbonate V2. (a) P-wave modeling. (b) S-wave modeling.

Figure 4.24 shows the comparison of vug and fracture modeling for Carbonate V1 and Carbonate V2. The vug modeling as previously mentioned shows a bigger impact on the effective properties than the modeling of fractures even if they occupy the same pore space.

The porosity logs were generated based on the velocity – porosity correlations and an example is shown in Figure 4.25.

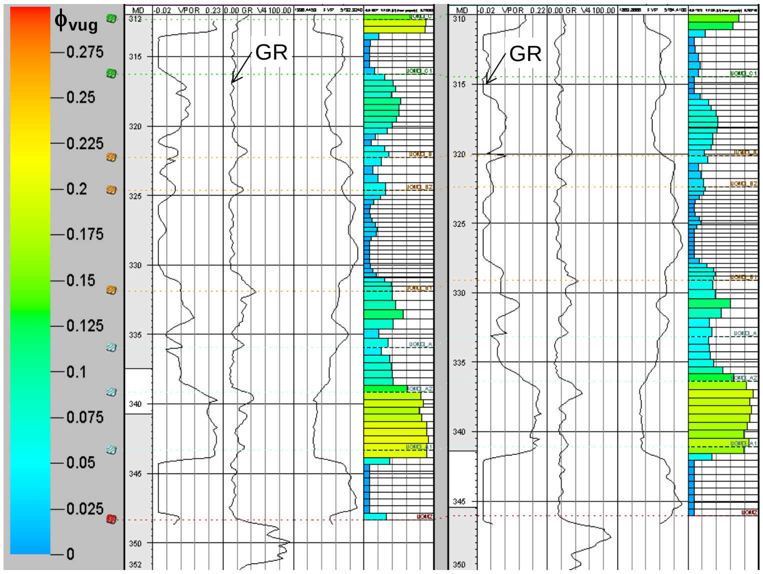

Figure 4.25. "Vug" porosity logs obtained from P-wave correlations. High porosity is indicated by orange/ red colors while low fracture porosity is given by blue color. The Gamma-ray log is also included (black line).

This is a new methodology that involves finite element modeling, well log data and the interpreted 3D geological model to characterize the fracture and vug effect on this heavy oil carbonate reservoir. Empirical correlations of compressional and shear wave velocity with respect to fracture porosity were found for each geological formation and proved to be consistent in different regions of the field. The results obtained from the P-wave modeling showed higher fracture porosity values than those obtained with shear velocity due to the effect of hydrocarbons; however, they both showed similar changes in fracture porosity, constituting in a very good *qualitative* tool. However, lateral resolution of the 3D fracture porosity map is poor.

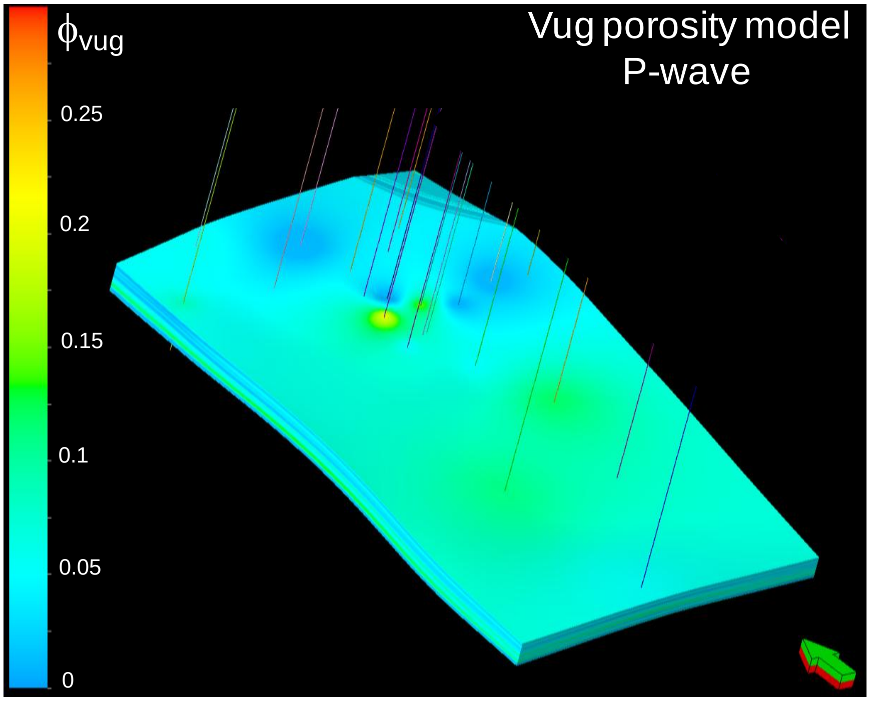

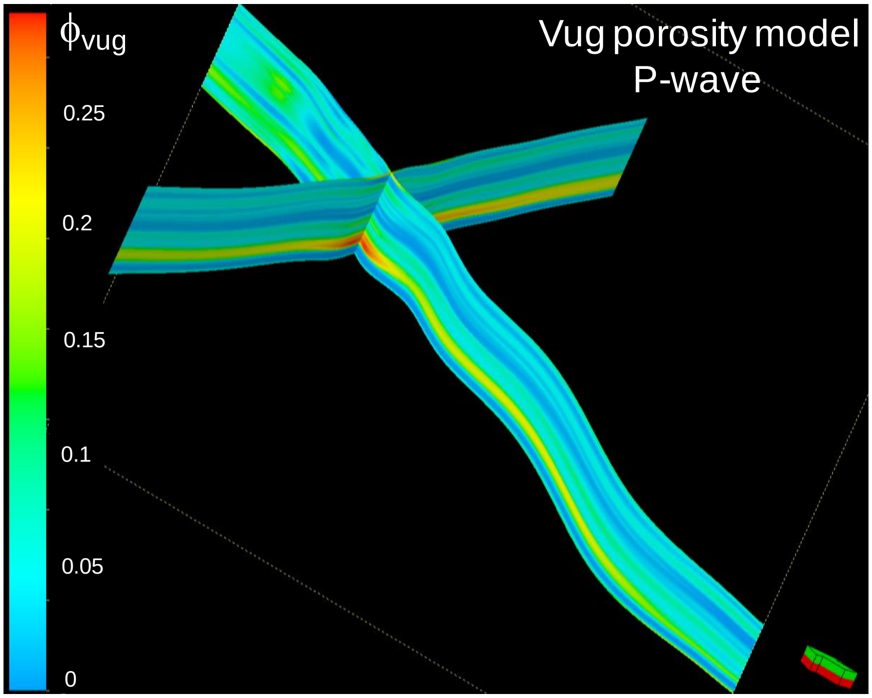

Figure 4.26. 3D Vug porosity model following P-wave modeling after interpolation. This methodology is an excellent tool to qualitatively determine areas with high porosity due to presence of vugs.

Part 5

Conclusions

Heavy and extra-heavy oils analyzed in this study exhibit a non-Newtonian behavior at room temperatures. They exhibit a viscous component (loss modulus) higher than the elastic component (storage modulus), which is typical of a viscoelastic fluid. They also exhibit another non-Newtonian characteristic, usually referred to as the shear thinning phenomenon, where viscosity decreases as shear strain (frequency) increases. The presence of an elastic component is what makes a heavy oil sample different from a Newtonian fluid. According to rheological measurements, the storage modulus becomes very important for seismic, sonic, and ultrasonic frequencies and for temperatures below 30˚C. Above this temperature, the viscous component becomes significantly larger in comparison to the elastic component and, for seismic frequencies, the Newtonian assumption is valid.

The estimation of the glass point temperature of the heavy and extra heavy oil samples analyzed in this study by the Differential Scanning Calorimeter method represented a challenge not only because the glass transition by itself is not an actual phase change but also because heavy oils have a complex structure where each constituent (asphaltenes, resins, saturates, and aromatics) has a different melting point. Overall, all the heavy oil samples exhibit a very subtle glass transition but also a very similar glass point temperature, which was expected since the oils have a similar density. The glass point temperature estimated for these heavy oil samples varies from about -40°C to -50°C.

The changes caused by the loss and storage modulus as temperature varies are responsible of the different phases recognized in a viscoelastic fluid. The liquid point temperature that separates the quasi-solid phase from the liquid phase, varies significantly according to each sample and was corroborated using two different methods. The liquid point is 60°C for samples Venezuela and Canada B, 40°C for Canada A and 20°C for Brazil sample.

The viscoelastic effect seems to be linked to the density of each sample; Canada B has the highest density and exhibit the most noticeable shear thinning phenomenon. Most of the samples do not exhibit this phenomenon for temperatures over 50°C. On the other hand, the Brazil sample has the highest glass point temperature but also exhibits the lowest density. The liquid point, as previously mentioned, decreases as the density of the samples decrease. It is clear that a connection between viscosity and density exists. However, viscosity calculation from density requires the molecular weight of each component.

The power-law model and the Eyring's rate reaction theory were used to derive an expression that accurately predicts complex viscosity in terms of frequency and temperature for temperatures below 50°C - 60°C. Above this temperature, viscosity becomes Newtonian and no shear thinning is observed. One of the key aspects of the expression is given by the activation energy parameter which was found to be independent of temperature but dependent on frequency. The activation energy for the Canada B sample varies between 1250J/mol (high frequency) and 1750J/mol (low frequency); the Venezuela sample varies from 1100J/mol to 1500J/mol; The Brazil sample varies from 1250J/mol to 1350J/mol and, finally, the Canada A sample varies from 800J/mol to 1400J/mol. All the values are approximate.

Other parameters are required when using the new viscosity model: K is the most insensitive parameter when estimating complex viscosity and affects viscosities at different temperatures in the same manner. The next least sensitive parameter is the power-law index, which varies for all samples between 0.8 and 1. Activation energy affects viscosity estimations mostly at low temperatures (high viscosity). Finally, the most important parameters when this model are T_G and T_I; they affect viscosity at all temperatures.

The viscoelastic nature of the heavy oil samples analyzed in this study requires frequency dispersion and attenuation models that predict the variation of the complex shear moduli and attenuation coefficient with frequency. The Havriliak – Negami model was modified to include the temperature effect by expressing the relaxation time as a thermally activated process. None of the existing models reviewed were suitable for heavy oils since they do not take into account the temperature factor.

The new frequency temperature dispersion model properly described the variation of G* measured by low frequency (rheological) measurements with a correlation coefficient of 0.99. The major errors (about 10%) were found when predicting G* at very low frequencies for each temperature. On the other hand, the model usually overpredicted G* at ultrasonic frequencies. It is important to take into account that measurements were available only at one frequency (1MHz), which made it more difficult to accurately fit the model. The parameters most sensitive to G* estimation are: G_{max} (G* at infinite frequencies), η_∞ (undisturbed viscosity) and the fitting parameters α and γ. For samples Venezuela, Canada A and Canada B, α varies from 0.15 to 0.21 and γ varies from 0.04 to 0.12. Both represent a very small variation. However, the Brazil sample varied from 0.04 to 0.06 and from 0.47 to 0.7 for α and γ respectively. Once again, the different behavior seems to be related to the anomalous density of the Brazil sample.

The power-law is an attenuation model that accurately (correlation coefficient above 0.99) predicted, for all samples, the attenuation coefficient measured through the rheological measurements. This simple model depends on only one parameter that is directly correlated through a power law equation to temperature and indirectly correlated to sample density. The peak of the quality factor indicates the elastic component decreases for a certain cut-off frequency; however viscous component remains unaltered. The variation of quality factor with temperature and frequency shows that the heavy oils are dominated by a thermally activated process since the peak of quality factor shifts to higher frequencies as temperature is increased. This agrees with the results found by Spencer (1981) for saturated sandstones.

Strain and viscosity are two other factors besides frequency where the shear modulus dispersion is evident as well as the link between stress relaxation and attenuation. Attenuation decreases as viscosity increases but it does not decrease uniformly with frequency. Velocity on the other hand, always increases with frequency.

Attenuation when compared against strain amplitudes shows diverse results depending on temperature. For low temperatures, where the heavy oil sample better approximates a viscoelastic solid, attenuation is almost constant for strain amplitudes similar to those for seismic wave propagation. On the other hand, at high temperatures, attenuation varies significantly with strain amplitude.

The viscoelastic properties discussed in Part 2 and Part 3 were applied to finite element modeling of a heavy oil carbonate reservoir. It was found that fractures on a carbonate rock are more sensitive to pore fluid than vugs. The results obtained using P-wave data showed higher fracture porosity values than those obtained with S-wave data due to the effect of hydrocarbons; however, in a qualitative sense both results showed similar changes in fracture porosity, over the field.

Part 6

References

Aki, K., and P. G. Richards, 2002, Quantitative Seismology. University Science Books, 2 edition.

Aklonis, J. J., and W. MacKnight, 1983, Introduction to Polymer Viscoelasticity. John Wiley and Sons.

Avramov, I., 2005, Viscosity in disordered media. Journal of Non-Crystalline Solids, v. 351, p. 3163–3173.

Azimi, S. A., A. V. Kalinin, V. V. Kalinin and B. L. Pivovarov, 1968, Impulse and transient characteristics of media with linear and quadratic absorption laws. Physics of Solid Earth, v. 2, p. 42-54.

Barnes, H.A, J.F. Hutton, and K. Walters, 1989, An Introduction to Rheology. Elsevier Science Publishers.

Barton, N., 2007, Rock Quality, Seismic Velocity, Attenuation and Anisotropy. Taylor & Francis.

Beggs H.D. and J. R. Robinson, 1975, Estimating the viscosity of crude oil systems. Journal of Petroleum Technology, v. 27, p. 1140-41.

Behura, J., M. Batzle, R. Hofmann, and J. Dorgan, 2007, Heavy oils: Their shear story. Geophysics, v. 72, 5, p. E175–E183.

Bennison, T., 1998, Prediction of Heavy Oil Viscosity. IBC Heavy Oil Field Development Conference, London.

J. G. Berryman, 1992, Effective stress for transport properties of inhomogeneous porous rock. Journal of Geophysical Research, v. 97, p. 17409-17424.

Cadoret T., G. Mavko and B. Zinsner, 1998, Fluid distribution effect on sonic attenuation in partially saturated limestones. Geophysics, v. 63, p. 154.

Charm, S.E., 1962, The nature and role of fluid consistency in food in engineering applications. *In:* E. M. Mrak, and G. F. Stewart, (eds.), Advances in Food Research: Academic Press Inc.

Cheeke, J. D., 2002, Fundamentals and Applications of Ultrasonic Waves. CRC Press.

Cholach, P. and Schmitt, D., 2003, Intrinsic anisotropy of shales. 73rd Ann. Internat. Mtg.: Soc. of Expl. Geophysics, v. 22, p.149-152.

Christensen, R. M., 1971, Theory of Viscoelasticity: An Introduction. Elsevier Science & Technology Books.

Christensen, R. M., 1979, Mechanics of Composite Materials. Wiley, New York.

Christensen, R. M., 2005, Mechanics of Composite Materials. Dover Publication Inc.

Cole, K.S. and R. H Cole, 1941, Dispersion and absorption in dielectrics, Journal of Chemical Physics, v. 9, p. 341–351.

Crawford, R. J., 1998, Plastics Engineering. Elsevier 3rd Edition.

Davidson, D. W., and R.H. Cole, 1950, Dielectric relaxation in glycerine. Journal of Chemical Physics, v. 18, p. 1417.

De Ghetto G., F. Paone, and M. Villa, 1995, Pressure-Volume-Temperature Correlations for Heavy and Extra Heavy Oils. International Heavy Oil Symposium, SPE 30316, p. 647-662.

Dvorkin, J., 2005, Attenuation and Velocity dispersion – Causality link? Rainbow in the Earth, 2nd International Workshop. Lawrence Berkeley National Laboratory.

Dyre, J.C, T. Hechsher, and K. Niss, 2009, A brief critique of the Adam–Gibbs entropy model. Journal of Non-Crystalline Solids, v. 355, p. 624–627.

Ehrenstein, G., G. Riedel, and P. Trawiel, 2004, Thermal Analysis of Plastics: Theory and Practice. Carl Hanser Verlag.

Fan, Y., S. Dai, and R. I. Tanner, 2003, Rheological properties of some thermotropic liquid crystalline polymers. Korea-Australia Rheology Journal, v. 15-3, p. 109–115.

Ferry, J. D., 1980, Viscoelastic Properties of Polymers. Wiley.

Findley, W. N., Lai, J. S., and K. Onaran, 1989, Creep and Relaxation of Nonlinear Viscoelastic Materials: with an Introduction to Linear Viscoelasticity. Dover Publications Inc.

Frisillo, A. L., and T. J. Stewart, 1980, Effect of partial gas/brine saturations on ultrasonic absorption in sandstone (abstract). Stanford University Publications in Geological Sciences, v. 17, p. 24.

Furre, A., and Brevik, I., 1998, Characterization of angle dependency in sonic logs. 68th Ann. Internat. Mtg: Soc. of Expl. Geophysics, p. 292-295.

Futterman, W. I., 1962, Dispersive body waves. Journal of Geophysical Research, v. 67, p. 5279 – 5291.

Gabitto, J., and M. Barruffet, 2003, Experimental and theoretical determination of Heavy Oil viscosity under reservoir conditions. Final progress report DE-FG26-99FT40615.

Gitman, I.A., 2006, Representative Volumes and Multi-scale Modeling of Quasi-brittle Materials. Master in Science thesis, Perm State Technical University.

Glasstone, S., K. J. Laidler, H. Eyring, 1941, Theory of Rate Processes. McGraw-Hill.

Gordon, R. B and L. A. Davis, 1968, Velocity and attenuation of seismic waves in imperfectly elastic rock. Journal of Geophysical Research, v. 73, p. 3917 – 3935.

Grechka V., 2003, Effective media: A forward modeling view. Geophysics, v. 68, p. 2055–2062.

Grechka V., 2007, Multiple cracks in VTI rocks: Effective properties and fracture characterization. Geophysics v. 72, p. D81.

Grechka, V., and M. Kachanov, 2006, Effective elasticity of fractured rocks. The Leading Edge v. 25, p. 152.

Grechka, V., and M. A. Rojas, 2007, On the ambiguity of elasticity measurements in layered rocks. Geophysics, v. 72, p. D51.

Gurevich, B., K. Osypov, and R. Ciz, 2007, Viscoelastic modeling of rocks saturated with heavy oil. SEG Technical Program Expanded Abstracts, v. 26, p.1614-1618.

Han, D., J. Liu, and M. Batzle, 2007, Shear velocity as the function of frequency in heavy oils. SEG Technical Program Expanded Abstracts, v. 26, p. 1716-1719.

Havriliak, S. and S. Negami, 1967, A complex plane representation of dielectric and mechanical relaxation processes in some polymers: Polymer, v. 8, p. 161–210.

Hilbert, L. B., T. K. Hwong, N. G. W. Cook, K. T. Nihei, and L. R. Myer, 1994, Effects of strain amplitudes on the static and dynamic nonlinear deformation of Berea sandstone. *In:* Nelson and Laubach (eds.), Rock Mechanics: Model and Measurements, Challenges from Industry, p. 497.

Hill, R., 1963, Elastic properties of reinforced solids: some theoretical principles. Journal of Mechanics and Physics of Solids, v. 11, p. 357–372.

Hongkui, G., L. Yingsong, M. Shanzhou, and S. Li, 2001, Difference of rock elastic parameters under static and dynamic loading. University of Petroleum (East China) Dongying, Shandong, China. *In:* F. Bingjun, S. Wang and L. Zhonkui (eds.), Frontiers of Rock Mechanics and Sustainable Development in the 21st Century, p. 69-71.

Hornby, B.E., Schwartz, L.M. and Hudson, J.A., 1994, Anisotropic effective-medium modelling of the elastic properties of shales. Geophysics, v. 59, p.1570-1583.

Hudson, J. A., 1991, Overall properties of heterogeneous material. Geophys. J. Internat., v. 107, p. 505–511.

Huet, C., 1990. Application of variational concepts to size effects in elastic heterogeneous bodies. J. Mech.Phys. Solids, v. 38, p. 813–841.

Ide, J., 1936, Comparison of statically and dynamically determined Young's modulus of rocks. Proceedings of National Academic Sciences, v. 22, p. 2.

Johnston, D. H., and M. N. Toksöz, 1980, Thermal cracking and amplitude dependent attenuation. Journal of Geophysical Research, v. 85(B2), p. 937–942.

Johnston, D. H., and M. N. Toksöz, 1981, Seismic Wave Attenuation. Geophysics Reprint Series.

Johnston, D. H., 1981, Attenuation: a state of the art summary. *In:* Johnston, D. H., and M. N. Toksöz (eds.), Seismic Wave Attenuation. Geophysics Reprint Series.

Johnston, J.E. and Christensen, N.I., 1995, Seismic anisotropy of shales. Journal of Geophysical Research, v. 100(B4), p. 5991-6003.

Kaarsberg, E. A., 1968, Elastic studies of isotropic and anisotropic rock samples: Trans. Am Inst Min Metallurg Eng, v. 241, p. 470-475.

Kjartansson, E., 1979, Attenuation of seismic waves in rocks and applications in energy exploration. Ph.D. thesis, Stanford University.

Knopoff, L., 1964, Q. Rev Geophysics Space Physics, v. 2, p. 625 -660.

Kolsky, H., 1956, The propagation of stress pulses in viscoelastic solids. Philosophical Magazine, v. 1, p. 693-710.

Kowar, R., 2009, Causality analysis of waves and wave equations obeying attenuation. Photoacoustic imaging in Medicine and Biology, Report 6.

Kramers, H. A., 1956, La diffusion de la lumiere par les atomes, Atti Cong. Intern. Fisica, (Transactions of Volta Centenary Congress), v. 2, p. 545-557.

Krönig, R. L., 1926, On the theory of the dispersion of X-rays. Journal of the Optical Society of America, v. 12, p. 547-557.

Leuzzi, L., and T. M. Nieuwenhuizen, 2007, Thermodynamics of the Glassy State. Taylor and Francis Group.

Liu, E., J. A. Hudson, and Pointer, T., 2000, Equivalent medium representation of fractured rock, Journal of Geophysical Research, v. 105, p. 2981-3000.

Macias-Salinas, R., C. Duran-Valencia, S. Lopez-Ramirez, and C. Bouchot, 2009, Eyring-theory-based model to estimate crude oil viscosity at reservoir conditions. Energy & Fuels, v. 23, p. 464–470.

McKavanagh, B., and F. D. Stacey, 1974, Mechanical hysteresis in rocks at low strain amplitudes and seismic frequencies. Physics of the Earth and Planetary Interiors, v. 8, p. 246 -250.

Menard, K. P., 1999, Dynamic Mechanical Analysis: A Practical Introduction. CRC Press.

Meyer, R. F., E. D. Attanasi, and P. A. Freeman, 2007, Heavy Oil and Natural Bitumen Resources in Geological Basins of the World. USGS 2007-1084.

Mobley, J., K. Waters, M. S. Hughes, C. S. Hall, and J. N. Marsh, 2000, Kramers–Kronig relations applied to finite bandwidth data from suspensions of encapsulated microbubbles. Journal of Acoustical Society of America, v. 108, 5, p. 2091-2106.

Musgrave, M. J. P., 1970, Crystal Acoustics. Holden Day.

Norris, A. N., 1985, A differential scheme for the effective moduli of composites. Mechanics of Mater, v. 4, p. 1-16.

Nur, A., and R. Winkler, 1980, The role of friction and fluid flow in wave attenuation in rocks. Geophysics, v. 45, p. 591-592.

Olsen, C., I. L. Fabricius, A. Krogsboll, and M. Prasad, 2004, Static and dynamic Young's Modulus for Lower Cretaceous chalk: A low frequency scenario. AAPG International Conference, 6 p.

Ostoja-Starzewski, M., 2006, Material spatial randomness: From statistical to representative volume element. Probabilistic Engineering Mechanics, v. 21, p. 112-132.

Pandit, B. I., and M. S. King, 1979, The variation of elastic wave velocities and quality factor Q of a sandstone with moisture content. Canadian Journal of Earth Sciences, v. 16, p. 2187 - 2195.

Peselnick, L., and W. F. Outerbridge, 1960, Internal friction in shear modulus of Solenhofen Limestone over a frequency range of 10^7 cycles per second. Journal of Geophysical Research, v. 66, p. 581 - 588.

Plona, T. J. and J. M. Cook, 1995, Effects of stress cycles on static and dynamic Young's moduli in Castlegate sandstone. *In:* Daemen, J.J.K. & Schulz, R. A. (eds.) Proceedings of the 35th U. S. Symposium on Rock Mechanics, p. 155-160.

Rühl, W., 1982, Tar (extra heavy oil) sands and oil shales, *In:* Beckmann, Heinz, (ed.) Geology of Petroleum: Stuttgart, Enke, v. 6.

Sadoway, D., 2009, Theory of Reaction Rates. Lecture Notes. Department of Materials Science and Engineering, Massachusetts Institute of Technology.

Sayers, C. M., 1994, The elastic anisotropy of shales. Journal of Geophysical Research, v. 99(B1), p. 767-774.

Sayers, C. M., 1999, Stress-dependent seismic anisotropy of shales. Geophysics, v. 64, p. 93-98.

Scherer, G. W., 1986, Relaxation in Glasses and Composites: Wiley, New York.

Schoenberg, M., and Sayers, C. M., 1995, Seismic anisotropy of fractured rock. Geophysics, v. 60, p. 204–211.

Sharkov, E. A., 2003, Passive Microwave Remote Sensing of the Earth: Physical Foundations. Springer - Praxis.

Speight, J. G., 1999, The Chemistry and Technology of Petroleum. Marcel Dekker Inc.

Spencer, J.W., 1981, Stress relaxations at low frequencies in fluid-saturated rocks. Journal de Physique, C5, Tome 42, p.1175-1180.

Stacey, F. D., M. T. Gladwin, B. McKavanagh, A. T. Linde, and L. M. Hastie, 1975, Anelastic damping of acoustic and seismic pulses. Geophysical Surveys, v. 2, p. 133 - 151.

Stewart, R. R. M. N. Toksöz, and A. Timur, 1983, Strain dependent attenuation: observations and a proposed mechanism. Journal of Geophysical Research, v. 88, B1, p. 546-554.

Strick, E., 1967, The determination of Q, dynamic viscosity and creep curves from wave propagation measurements. Geophysical Journal of the Royal Astronomical Society, v. 13, p. 197 – 218.

Thomsen, L., 1986, Weak elastic anisotropy. Geophysics, v. 51, p. 1954-1966.

Tissot, B. P., and T. H. Welte, 1984, Petroleum Formation and Occurrence. Springer-Verlag Telos.

Toksöz, M.N., D. H. Johnston, and A. Timur, 1979, Attenuation of seismic waves in dry and saturated rocks: Laboratory measurements. Geophysics, v. 44, p. 681 - 690.

Tosaya, C., 1982, Acoustical properties of clay bearing rocks. PhD thesis, Stanford University.

Tutuncu A.N., T. Podio, and M.M. Sharma, 1998a, Nonlinear viscoelastic behavior of sedimentary rocks: I. Effect of frequency and strain amplitude. Geophysics, v. 63, p. 184-194.

Tutuncu A.N., T. Podio, A. R. Gregory and M.M. Sharma, 1998b, Nonlinear viscoelastic behavior of sedimentary rocks: II. Hysteresis effect and influence of type of fluid on elastic moduli. Geophysics, v. 63, p. 195-204.

Tutuncu A.N and M.M. Sharma, 1992, The influence of fluids on grain contact stiffness and frame moduli in sedimentary rocks. Geophysics, v. 57, p. 1571-1582.

Tutuncu A.N. and M.M. Sharma, 1994, Grain contact adhesion hysteresis: A mechanism for attenuation of seismic waves in sedimentary granular media. Geophysical Research Letters, v. 21, p. 2323-2326.

Ursin, B., and T. Toverud, 2005, Comparison of seismic dispersion and attenuation models. CREWES Research Report, v. 408.

Vernik, L., and Liu, X., 1997, Velocity anisotropy in shales: A petrophysical study. Geophysics, v. 62, p. 521-532.

Walsh, J. B., 1966, Seismic wave attenuation in rock due to friction. Journal of Geophysical Research, 71, v. 2591 – 2599.

Wang, Z. 2000. Dynamic versus static elastic properties of Reservoir rocks. *In:* Wang, Z., and Nur, A. (eds.). Seismic and Acoustic Velocities in Reservoir Rocks*.* Society of Exploration Geophysicists, Tulsa, v. 19, p. 531-539.

Wang, S., Y. Huang, and F. Civan, 2005, Experimental and theoretical investigation of the Zaoyuan field heavy oil flow through porous media. Journal of Petroleum Science and Engineering, v. 50, p. 83-101.

Waters, K. R., M. S. Hughes, J. Mobley, G. H. Brandenburger, and J. G. Miller, 2000, On the applicability of Kramers–Krönig relations for ultrasonic attenuation obeying a frequency power law. Journal of Acoustical Society of America, v. 108-2, p. 556-563.

Webb, S. L., and Stacey, F. D., 1982, A simple demonstration of the frequency dependences of elastic moduli and the damping of stress waves at seismic frequencies. Bulletin Aust. Society of Exploration Geophysicists, v.13, No 2, p. 23-25.

Wilson, J. M. R., 1985, The dynamic properties of soil, PhD dissertation, Cambridge University.

Wilson, H. J., 2006, Polymeric fluids. Lecture Notes. Department of Mathematics, University College London.

Winkler, K.W., A. Nur, and M. Gladwin, 1982, Friction and seismic attenuation in rocks. Nature, v. 277, p. 528 – 531.

Winkler, K.W., and Nur, A., 1982, Seismic attenuation: Effects of pore fluids and frictional sliding. Geophysics, v. 47, p. 1 -15.

Yu, R., W. Yu, C. Zhou, and J. J. Feng, 2007, Rheology and relaxation processes in a melting thermotropic liquid–crystalline polymer. Journal of Applied Polymer Science, v. 104, p. 3780–3787.

Zhang J.J., and L. R. Bentley, 2005, Factors determining Poisson's ratio. CREWES Research Report, v. 17, p. 1 -15.

Zienkiewickz, O.C., R.L. Taylor, J. Z. Zhu, 2005, The Finite Element Method: Its Basis and Fundamentals. Elsevier Science.

Zimmer, M. A., 2003, Seismic velocities in unconsolidated sands: Measurements of pressure, sorting, and compaction effects. Ph.D dissertation, Stanford University.

Zimmerman, R. W., 1991, Compressibility of Sandstones. Elsevier Science, Amsterdam.

Appendix A: Viscoelastic properties and their units

Symbol	Name	CSG Units	SI Units
σ	Shear stress	dynes/cm2	Pascals
γ	Shear strain	dimensionless	
γ	Shear strain rate	1/sec	1/sec
f	Frequency	1/sec	1/sec
ω	Angular frequency	rad/sec	rad/sec
η'	Shear viscosity (real part)	Poise	Pascals-sec
η''	Shear viscosity (imaginary part)	Poise	Pascals-sec
η^*	Complex shear viscosity	Poise	Pascals-sec
τ	Relaxation time	sec	sec
σ'	Elastic stress	dynes/cm2	Pascals
σ''	Viscous stress	dynes/cm2	Pascals
G'	Storage modulus	dynes/cm2	Pascals
G''	Loss modulus	dynes/cm2	Pascals
G^*	Complex shear modulus	dynes/cm2	Pascals
δ	Phase angle	radians	radians

Appendix B: Viscoelastic models

- **Cole-Cole model (1941)**

$$G^{*}(\omega) = G^{'}(\omega) + G^{''}(\omega)$$

$$G^{'}(\omega) = G_{\max} + \frac{(G_0 - G_{\max})\left[1 + (\omega\tau)^{1-\beta}\sin\left(\frac{\beta\pi}{2}\right)\right]}{1 + 2(\omega\tau)^{1-\beta}\sin\left(\frac{\beta\pi}{2}\right) + (\omega\tau)^{2(1-\beta)}}$$

$$G''(\omega) = \frac{(G_0 - G_{\max})\left[(\omega\tau)^{1-\beta}\cos\left(\frac{\beta\pi}{2}\right)\right]}{1 + 2(\omega\tau)^{1-\beta}\sin\left(\frac{\beta\pi}{2}\right) + (\omega\tau)^{2(1-\beta)}}$$

where G_0 is the shear modulus at zero frequency and β is a parameter that varies between 0 and 1.

- **Cole and Davidson model (1951)**

$$G^{*}(\omega) = G^{'}(\omega) + G^{''}(\omega)$$

$$G^{'}(\omega) = \left\{1 - \left(\cos(\phi)^{\gamma}\cos(\phi\gamma)\right)\right\}G_{\max}$$

$$G''(\omega) = \left\{[\cos(\phi)]^{\gamma}\sin(\phi\gamma)\right\}G_{\max}$$

$$\phi = \arctan(\omega\tau)$$

where γ is a parameter that varies between 0 and 1.

- **Havriliak and Negami model (1967)**

$$G^{*}(\omega) = G^{'}(\omega) + G^{''}(\omega)$$

$$G'(\omega) = \left(1 - R^{\frac{-\gamma}{2}} \cos(\theta\gamma)\right) G_{\max}$$

$$G''(\omega) = \left(R^{\frac{-\gamma}{2}} \sin(\theta\gamma)\right) G_{\max}$$

$$R = \left(1 + (\omega\tau)^{1-\alpha} \sin\left(\frac{\pi\alpha}{2}\right)\right)^{2} + \left((\omega\tau)^{1-\alpha} \cos\left(\frac{\pi\alpha}{2}\right)\right)^{2}$$

$$\theta = \arctan\left(\frac{(\omega\tau)^{1-\alpha} \cos\left(\frac{\pi\alpha}{2}\right)}{1 + (\omega\tau)^{1-\alpha} \sin\left(\frac{\pi\alpha}{2}\right)}\right)$$

where α and γ are parameters that vary between 0 and 1.